Dissertation

submitted to the

Combined Faculty of Natural Sciences and Mathematics
of Heidelberg University, Germany

for the degree of

Doctor of Natural Sciences

Put forward by

Victor Marian

born in

Dresden, Germany

Oral examination: 28th April, 2021

The Intricate Connection Between Major Mergers and AGN with the Highest Eddington Ratios

Victor Marian

Referees: Dr. Knud Jahnke
Prof. Dr. Luca Amendola

The history of astronomy
is a history of receding horizons.

EDWIN POWELL HUBBLE,
THE REALM OF THE NEBULÆ

Abstract

Over the past decade, research has revealed contradictory results on whether mergers of galaxies of similar mass, so-called major mergers, are the dominant or at least an essential mechanism for the formation of active galactic nuclei (AGN) and the growth of supermassive black holes (SMBH) in galaxies. In this work, it is investigated whether such a connection exists for the 'most plausible' objects – broad line AGN with the highest Eddington ratios λ_{Edd}. The first sample is based on *HST*/WFC3 observations and focuses on these objects that possess an $\lambda_{\mathrm{Edd}} > 0.7$ at $z \simeq 2$, the peak epoch of black hole activity. To validate the results and to identify possible discrepancies between observations and simulations, a comparison study is performed on similar objects modeled by the large-scale cosmological simulation IllustrisTNG. An additional sample consists of local $z \lesssim 0.2$ AGN with $\lambda_{\mathrm{Edd}} > 0.3$, observed with the *VLT*/FORS. All AGN samples are compared to inactive galaxies of similar stellar mass and redshift. For all three individual studies, the applied methodology is identical: sources are visually identified and classified into merging and unperturbed galaxies. An excess for the respective AGN host galaxies in the subsequently derived major merger fractions would then indicate that AGN are predominantly triggered by such galaxy mergers.

The analysis of the observed galaxies at $z \simeq 2$ yields merger fractions of $f_{\mathrm{m,\,AGN}} = 0.24 \pm 0.09$ and $f_{\mathrm{m,\,Ina}} = 0.19 \pm 0.04$ for the AGN hosts and inactive galaxies, respectively. In addition to the visual assessment, the IllustrisTNG data set is analyzed by evaluating the galaxies' merger histories and accounting for typical observational uncertainties. The resulting best estimates give $f_{\mathrm{m,\,AGN}} = 0.27 \pm 0.07$ and $f_{\mathrm{m,\,Ina}} = 0.22 \pm 0.01$, indicating an excellent agreement between the two studies at this redshift. In contrast, with $f_{\mathrm{m,\,AGN}} = 0.41 \pm 0.12$ and $f_{\mathrm{m,\,Ina}} = 0.08 \pm 0.06$, the fractions at $z \lesssim 0.2$ show a clear excess in the incidence of major mergers for the AGN host galaxies.

The results are analyzed extensively, including an investigation of possible influences due to selection effects, a time lag between the visibility of galaxy mergers and the AGN, as well as the methodology used. While there is no significant evidence that such major mergers are the dominant process for the existence of the studied AGN at $z \simeq 2$, such gravitational encounters appear to be an important mechanism for comparable AGN at $z \lesssim 0.2$. This may be due to the fact that the gas required for SMBH to achieve such high accretion rates is less abundant in galaxies at low redshifts, leading to major mergers playing a more dominant role in the local Universe. Nevertheless, regardless of redshift, for a minimum of 50% of this particular AGN population, the origin remains unclear.

Zusammenfassung

Die Forschung des letzten Jahrzehnts hat widersprüchliche Ergebnisse darüber offenbart, ob Verschmelzungen von Galaxien ähnlicher Masse, sogenannte major mergers, der dominante oder zumindest ein essentieller Mechanismus für die Bildung aktiver galaktischer Kerne (AGN) und das Wachstum supermassereicher Schwarzer Löcher (SMBH) in Galaxien sind. In dieser Arbeit wird untersucht, ob ein solcher Zusammenhang für die „plausibelsten“ Objekte besteht – AGN mit den höchsten Akkretionsraten im Bezug zur Eddington-Akkretionsrate. Die erste Stichprobe basiert auf Aufnahmen durch das *HST*/WFC3 und untersucht diese Objekte bei $z \simeq 2$, der Epoche, in der die Aktivität Schwarzer Löcher ihr Maximum hatte. Um die Ergebnisse zu validieren und mögliche Diskrepanzen zwischen Beobachtungen und Simulationen zu identifizieren, wird eine Vergleichsstudie an ähnlichen, mittels der kosmologischen Simulation IllustrisTNG modellierten Objekten, durchgeführt. Eine weitere Stichprobe besteht aus lokalen AGN bei $z \lesssim 0.2$, die mit dem *VLT*/FORS beobachtet wurden. Alle AGN Stichproben werden mit inaktiven Galaxien ähnlicher stellarer Masse und Rotverschiebung verglichen. Für alle drei Einzelstudien ist die angewandte Methodik identisch: Die Quellen werden visuell identifiziert und in verschmelzende und ungestörte Galaxien klassifiziert. Ein Überschuss für die jeweiligen AGN in den daraufhin abgeleiteten major merger Anteilen, würde darauf hindeuten, dass AGN ihren Ursprung überwiegend in Galaxienverschmelzungen haben.

Die Analyse der beobachteten Galaxien bei $z \simeq 2$ ergibt für Quellen, die AGN beherbergen bzw. inaktive Galaxien die folgenden major merger Anteile: $f_{\mathrm{m,\,AGN}} = 0.24 \pm 0.09$ und $f_{\mathrm{m,\,Ina}} = 0.19 \pm 0.04$. Zusätzlich zur visuellen Beurteilung inkludiert die Analyse der IllustrisTNG-Daten unter anderem eine Auswertung der „Stammbäume“ der Galaxien und die Berücksichtigung typischer Unsicherheiten der Beobachtungen. Die resultierenden besten Schätzungen ergeben $f_{\mathrm{m,\,AGN}} = 0.27 \pm 0.07$ und $f_{\mathrm{m,\,Ina}} = 0.22 \pm 0.01$, was auf eine ausgezeichnete Übereinstimmung zwischen den beiden Studien bei dieser Rotverschiebung hinweist. Im Gegensatz dazu zeigen die Anteile bei $z \lesssim 0.2$ mit $f_{\mathrm{m,\,AGN}} = 0.41 \pm 0.12$ und $f_{\mathrm{m,\,Ina}} = 0.08 \pm 0.06$ einen deutlichen Exzess in der Inzidenz von major mergers für die Galaxien, die einen AGN beherbergen.

Die Ergebnisse werden umfassend analysiert, einschließlich einer Untersuchung möglicher Einflüsse aufgrund von Selektionseffekten, einer zeitlichen Verzögerung zwischen der Sichtbarkeit von Galaxienverschmelzungen und der AGN sowie der verwendeten Methodik. Während es keine signifikanten Hinweise gibt, dass solche major mergers der dominante Prozess für die Existenz der untersuchten AGN bei $z \simeq 2$ sind, scheinen solche gravitativen Begegnungen ein wichtiger Mechanismus für vergleichbare AGN bei $z \lesssim 0.2$ zu sein. Dies könnte darauf zurückzuführen sein, dass das Gas, das SMBHs benötigten, um solch hohe Akkretionsraten zu erreichen, in Galaxien bei niedrigen Rotverschiebungen weniger reichlich vorhanden ist, was dazu führt, dass major mergers eine dominantere Rolle im lokalen Universum spielen. Nichtsdestotrotz bleibt unabhängig von der Rotverschiebung für ein Minimum von 50% dieser speziellen AGN Population der Ursprung ungeklärt.

Contents

List of Figures

List of Tables

Part I.

Introduction

1. The Fundamentals on AGN

Black holes (BH) are among the most intriguing, enigmatic, daunting, and interesting objects in the universe, and even people who have only the slightest interest in astronomy are fascinated by these cosmological phenomena[1]. Due to their sheer density, these points in space exert such a great gravitational pull that not even light can escape it.

The insight that at least every massive galaxy ($M_\star \approx 10^{10} - 10^{12}\mathrm{M}_\odot$) and potentially the majority of dwarf galaxies host a supermassive black hole (SMBH; $M_{\mathrm{BH}} \approx 10^{6} - 10^{10}\mathrm{M}_\odot$) in their center, is certainly one of the most significant astronomical discoveries of the past few decades (e.g. Kormendy & Richstone 1995; Magorrian et al. 1998; Kormendy & Ho 2013). Such SMBHs show tight correlations with various host galaxy properties, indicating a strong link between the formation and growth of the central BHs and the evolution of the respective galaxies, in the form that both follow the commonly accepted theory of hierarchical structure formation (Jahnke & Macciò 2011). Numerous studies have found distinct trends of BH mass with the bulge velocity dispersion and mass, stellar host mass, velocity dispersion, or luminosity of galaxies (e.g. Marconi & Hunt 2003; Häring & Rix 2004; Jahnke et al. 2009; Bennert et al. 2010, 2011; Beifiori et al. 2012; Graham & Scott 2013; McConnell & Ma 2013; Davis et al. 2018, 2019; de Nicola et al. 2019; Sahu et al. 2019b; Ding et al. 2020; Shankar et al. 2020; Zhu et al. 2021). These findings are confirmed by state-of-the-art cosmological hydrodynamical simulations (Weinberger et al. 2018; McAlpine et al. 2018, 2020; Habouzit et al. 2019; Li et al. 2020b; Terrazas et al. 2020).

SMBHs are widely assumed to grow by accreting mass from rotating disk-like structures. In such accretion phases, they appear as active galactic nuclei (AGN), outshining their host galaxy by many orders of magnitude. The feedback of an active (i.e. matter accreting) SMBH in the form of emitted radiation, winds, jets, or a combination thereof may have a wide range of effects on the host galaxy, depending on the physical nature, geometry, and/or scale of these various outflow mechanisms (Silk & Rees 1998; Harrison et al. 2018). These feedback effects could range from the total quenching to the enhancement of star formation by a variety of processes that affect the interstellar and circumgalactic medium (Husemann & Harrison 2018; Weinberger et al. 2018; Nelson et al. 2019a; Davies et al. 2020; Oppenheimer et al. 2020; Truong et al. 2020;

[1] Source: Empirical study by the author.

Valentini et al. 2020). In addition, individual AGN feedback processes can also have an impact on larger scales, by affecting satellite galaxies and the surrounding intracluster or intragroup medium (Blanton et al. 2010; Chowdhury et al. 2019; Dashyan et al. 2019; Martin-Navarro et al. 2019; Li et al. 2020a).

In light of this interaction between galaxies and their central SMBH in its active phase, it is imperative to understand the mechanisms responsible for triggering such a period of strong mass accretion. Thus, this work contributes another piece to the puzzle of understanding the growth of SMBHs. To provide the necessary context for this work, the following sections contain a brief historical review and introduce the relevant underlying physics of AGN and the connection to their host galaxies described by various scaling relations. The subsequent sections outline the current state of research on the triggering of AGN across cosmic time and present the statistical framework for determining and analyzing the relevance of mergers with respect to the growth of SMBHs in the form of merger fractions.

1.1. A Concise History on AGN and Their Classification

More than 100 years ago astronomers were debating whether the patchy islands of stars they saw through their telescopes were actually part of our galaxy or independent structures. During this period, in 1908, Edward A. Fath observed the 'spiral nebula' NGC 1068 and unwittingly discovered the first active galaxy (Fath 1909). In addition to the expected absorption lines, his spectral analysis revealed emission lines similar to those found in the spectra of ionized gas nebulae, such as planetary nebulae. In the following years, several astronomers confirmed the presence of emission lines in about a dozen structures that we now know are the nuclei of galaxies.

However, it took about another 30 years until Carl Seyfert published his fundamental study of six galaxies whose nuclei show strong emission lines (Seyfert 1943). In his work, he compared the spectra of these sources to the emission lines observed in areas that are nowadays characterized as H II-regions, i.e. areas with active star formation. He found that the emission lines and also the forbidden lines of these galactic nuclei are broader than the corresponding lines in the 'normal' nebulae. Eventually, his study led to the classification of Seyfert galaxies, which in turn were divided into Type I and Type II, depending on the width of the emission lines. While Seyfert's work is recognized today, it did not lead astronomers at that time to focus their attention on these extraordinary objects.

The following decades saw the advent of radio astronomy and with it the discovery of several strong radio sources at high redshifts[2]. Optical counterparts were identified for some of these sources, but interpreted as peculiar stars – therefore referred to as quasi-stellar objects or quasars – rather than being of extragalactic origin. This changed, with the study of Schmidt (1963), who identified the lines of 3C 273 as broadened Balmer lines redshifted to $z \simeq 0.16$. In the same year, Greenstein & Matthews (1963) determined an even higher redshift of $z \simeq 0.37$ for the similar object 3C 48, confirming the extragalactic nature of these sources, which turned out to be extremely luminous and distant objects. Based on influential works such as those of Hoyle & Fowler (1963), Salpeter (1964), Zel'dovich (1964) and especially Lynden-Bell (1969), it became clear that these objects were powered by accretion onto a central SMBH. The term Active Galactic Nucleus describing this phenomenon was first coined by Victor Ambartsumian in the early 1950s.

Although it was not accepted at the time of discovery, there is now a consensus that these quasars and Seyfert galaxies are different incarnations of the same type of object, just observed under varying viewing angles and at different redshifts and luminosities with the latter parameter depending on the BH mass and mass accretion rate. This theory culminated, in two unification models of AGN, one focusing on the radio properties of an AGN (Antonucci 1993), the other mainly on the appearance in the optical wavelength range (Urry & Padovani 1995). However, the distinction has become increasingly blurred in recent decades, since the axis of symmetry is basically identical for both models, resulting in the synonymous use of the two models (Figure 1.1, left panel). This model not only unifies quasars and Seyfert galaxies, but also a considerable number of further AGN classes that have emerged over time, including fairly well-known AGN types, such as Blazars and BL Lac objects (Giommi et al. 2012), which are interpreted as observing (almost) along the axis of the jet, or the Fanaroff-Riley classes I and II, which distinguish the extent of a possible radio emission (Fanaroff & Riley 1974). To provide an impression regarding the multitude of different AGN classes: The recent publication by Padovani et al. (2017), for example, cites ~ 50 different (sub)classes of diverse AGN.

Although in place for nearly 30 years and subject to modifications (e.g. Trump et al. 2011; Hönig 2019) and repeated reviews (e.g. Urry 2004; Ramos Almeida et al. 2011; Netzer 2015; Almeida & Ricci 2017; Spinoglio & Fernández-Ontiveros 2019) (Figure 1.1, right panel), the basic components of the unified model have remained essentially unchanged. In this model, AGN consist of a central SMBH, an accretion disk ($r \simeq 10^{-3}\mathrm{pc}$) and the broad line region (BLR, $10^{-2} \lesssim r[\mathrm{pc}] \lesssim 10^{-1}$) at small radii, the narrow line region (NLR, $10 \lesssim r[\mathrm{pc}] \lesssim 10^{3}$) and a torus of dust and gas ($1 \lesssim r[\mathrm{pc}] \lesssim 100$) at larger radii, as well as in some cases a jet, which separates the AGN into radio-loud and radio-quiet sources (Figure 1.1, left panel). The different

[2] High redshift in this context means $z \lesssim 0.5$.

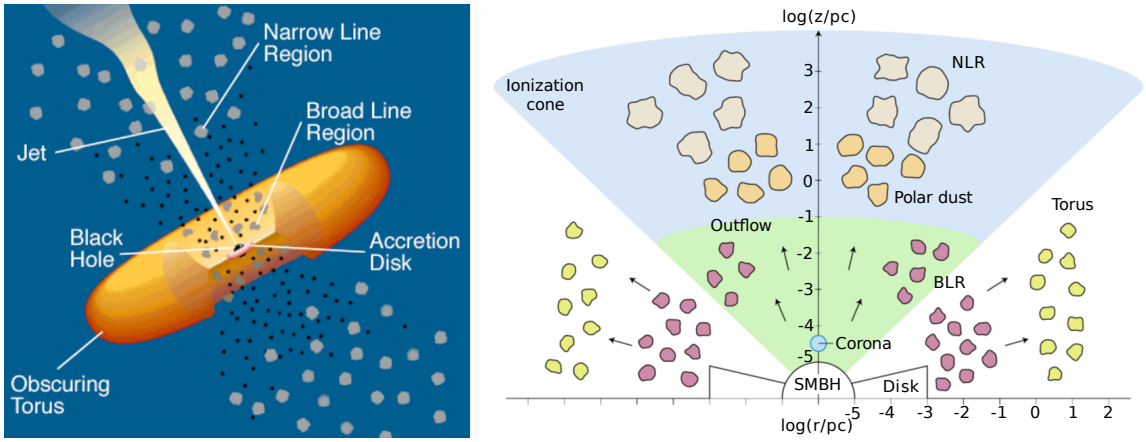

Figure 1.1.: *Left:* An adapted illustration of the unified model of AGN as described by Antonucci (1993) and Urry & Padovani (1995). While the presence of a jet is not mandatory and serves as the criterion for whether an AGN is classified as radio-loud or radio-quiet, all other components are identical in all AGN. In principle, only the viewing angle determines the class of the observed AGN. *Right:* Reviewed version of the unified model as presented in Almeida & Ricci (2017), highlighting the patchy structure of the components.

observational features of individual AGN classes are the result of simple orientation effects. Type I AGN are observed along viewing angles that are identical or similar to the rotational axis. As a result, both the BLR and the SMBH are unobscured, allowing the observation of very broad permitted emission lines, such as Hα, Hβ, CIV λ1549 or MgII λ2798 with respective FWHM of $\sim 1000 - 10000\,\mathrm{km\ s^{-1}}$. In contrast, the SMBH and the BLR of type II AGN are obscured by the optically thick torus region, with only the NLR visible, which emits permitted but also forbidden lines with significantly smaller FWHM of generally $\sim 200 - 1000\,\mathrm{km\ s^{-1}}$. This work adopts this simplistic distinction between type I and type II AGN, considering all observed sources studied in this work to be type I AGN.

A more detailed history of AGN can be found, for example, in Shields (1999) or Ferrarese & Ford (2005). Although there has been considerable progress in the 20 years since these studies were published, these reviews still provide a good reference and starting point for readers interested in the history of AGN.

1.2. The Essential Physics of AGN

1.2.1. Accretion onto BHs

The central engine of an AGN is the accreting SMBH. According to current knowledge, BHs are described completely by their mass, angular momentum and electric charge, where the latter is

assumed to be zero, since an electrically charged BH would soon neutralize by attracting charge of the opposite sign. One of the most fundamental properties is the gravitational radius r_g,

$$r_{\rm g} = \frac{GM_{\rm BH}}{c^2}, \tag{1.1}$$

where G is the gravitational constant, c is the speed of light, and $M_{\rm BH}$ is the mass of the BH. This parameter can be used to define the angular momentum s and the specific angular momentum s/M of a rotating, electrically neutral BH. Another, closely-related parameter, is the spin $a = \frac{s}{Mr_g c}$, which can take values between -1 and 1, specifies the direction of rotation, and is required to define the radius of the event horizon. For a stationary (non-rotating) BH $a = 0$ and the radius of the event horizon is described by the Schwarzschild radius $r_s = 2r_g$, whereas for $a \neq 1$ the radius of the event horizon is given by,

$$r_{\pm} = r_{\rm g}\left[1 \pm (1 - a^2)^{1/2}\right]. \tag{1.2}$$

This implies that for the extreme case of a BH with $a = 1$ the radius of the event horizon is equal to the gravitational radius, i.e. $r = r_g$, meaning that orbiting matter can approach much closer the BH before falling into the singularity. Another important and similar quantity is the radius which describes the size of the sphere of influence. First described by Peebles (1972), it is defined as

$$r_{\rm h} = \frac{GM_{\rm BH}}{\sigma_\star^2} \simeq 10.8\left(\frac{M_{\rm BH}}{10^8 {\rm M}_\odot}\right)\left(\frac{\sigma_\star^2}{200{\rm km\ s}^{-1}}\right){\rm pc}, \tag{1.3}$$

where $\sigma_\star$ is the stellar velocity dispersion of the bulge component. A more simplistic definition (Merritt 2004) relates to the enclosed stellar mass in the form of

$$M_\star(r < r_{\rm h}) = 2M_{\rm BH}. \tag{1.4}$$

Within this region, the gravitational force of the black hole exceeds that of the host galaxy, with the typical sizes being of the order of $1 - 10$pc. One requirement to determine dynamically the BH mass is to resolve this sphere of influence.

Considering that the specific angular momentum of a BH is a factor of $\sim 10^6$ smaller than the specific angular momentum on kpc scales, any gas that is to be accreted by the BH must first lose its excess angular momentum. Mechanisms to accomplish this may include galaxy interactions and mergers, bar instabilities, or secular processes. Recent scientific results regarding the different ways to fuel a SMBH are presented in Section 1.4.

In the immediate vicinity of the BH with a distance $r \lesssim 10^5 r_g$, the material is exposed to various physical forces, including the gravitational effect by the BH, but also by the gas on itself,

radiation and gas pressure, as well as magnetic and gas viscosity. Most likely, stellar winds and supernova explosions also play a relevant role in most instances. Gas that has relatively low angular momentum may be more likely to be accreted by spherical accretion (i.e. Bondi accretion), while material with higher angular momentum will initially settle into an accretion disk where viscosity effects remove any excess angular momentum until this gas is also accreted.

However, not all of the material will ultimately fall into the BH because gas and, in particular, radiation pressure will counteract the accretion or may even accelerate the material outwards. Radiation pressure, in particular, is required to derive a fundamental property in the description of accretion onto a BH, the Eddington luminosity[3]. Assuming a BH with mass M, total (i.e. bolometric) luminosity L, as well as a fully ionized gas at a distance r, the radiation pressure force per single electron is given by,

$$F_{\rm rad} = \frac{L\sigma_{\rm T}}{4\pi r^2 c}, \tag{1.5}$$

where σ_T represents the Thomson cross section[4]. Considering the difference in proton and electron mass, the counteracting gravitational force can be approximated as

$$F_{\rm g} = -\frac{GMm_{\rm p}}{r^2}, \tag{1.6}$$

The accretion proceeds as long as $|F_{\rm g}| > |F_{\rm rad}|$. However, the moment $|F_{\rm g}| \leq |F_{\rm rad}|$, the accretion comes to a halt. The luminosity, at which this occurs, is the Eddington luminosity and is defined as

$$L_{\rm Edd} = \frac{4\pi G c m_{\rm p}}{\sigma_T} M_{\rm BH} \simeq 1.5 \times 10^{38} \frac{M_{\rm BH}}{\rm M_\odot} \left[\frac{\rm erg}{\rm s}\right]. \tag{1.7}$$

The factor 1.5×10^{38} converges to this value for a gas with solar metallicity. For a gas consisting of pure hydrogen, the factor is 1.3×10^{38}. The luminosity L of the gas accreted onto the black hole is given by

$$L = \dot{M}\eta c^2, \tag{1.8}$$

where η is the radiative efficiency, which defines the fraction of the released rest mass energy of the infalling matter. The actual value of this parameter depends on the radius of the innermost

[3] The concept of accretion and Eddington luminosity is not limited to BHs, but applies to any case of a massive object accreting matter, e.g. stars in various states

[4] The Thomson cross section for an electron is

$$\sigma_{\rm T} = \frac{8\pi}{3} r_e^2 \simeq 6.65 \times 10^{-29}\,{\rm m}^2,$$

where r_e is the electron radius

stable circular orbit (ISCO) and thus on the spin of the BH, since the amount of energy that can be converted increases with decreasing distance to the BH. As described in Thorne (1974), this yields $0.06 \lesssim \eta \lesssim 0.42$ for $0 \leq a \leq 1$. This means that theoretically, up to 42% of the rest mass energy of the infalling matter can be released via radiation, making the accretion onto BHs the most efficient radiative source in the Universe. By comparison, the efficiency of the nuclear fusion of hydrogen to helium is only 0.7%. Considering the argument put forward by Soltan (1982) and observational studies, such as the seminal works of Yu & Tremaine (2002) or Marconi et al. (2004), that constrain the BH mass density, the most commonly adopted value for the radiative efficiency is $0.1 \leq \eta \leq 0.2$ (e.g. Shankar et al. 2019, 2020). Given this consensus value, even $\sim 2 \mathrm{M}_{\odot}\,\mathrm{yr}^{-1}$ are sufficient to fuel a luminous AGN.

Inserting now L_{Edd} into Equation (1.8) allows to define the Eddington accretion rate

$$\dot{M}_{\mathrm{Edd}} = \frac{L_{\mathrm{Edd}}}{\eta c^2}, \tag{1.9}$$

and finally the Eddington ratio

$$\lambda_{\mathrm{Edd}} = \frac{L}{L_{\mathrm{Edd}}} = \frac{\dot{M}}{\dot{M}_{\mathrm{Edd}}}, \tag{1.10}$$

which returns the luminosity L and accretion rate $\dot{M}$ normalized to the corresponding Eddington luminosity and Eddington accretion rate, respectively. In the spherical accretion model that is the basis of the formulas derive above, $\dot{M}$ represents the maximum possible accretion rate. However, by assuming, for example, a non-spherical geometry, this limit can be exceeded, resulting in Super-Eddington accretion rates.

1.2.2. BH Mass Measurements

In order to find suitable control galaxies with similar stellar masses as the respective AGN host galaxies (see next Section 1.3), reliable estimates of the BH masses are required. The most robust method to measure the mass of a BH is to evaluate the dynamics of stars and/or gas within the BH's gravitational well. Particularly worth mentioning here are the studies focusing on the SMBH in the center of our Milky Way, which were also honored with last year's Nobel Prize (e.g. Ghez et al. 1998, 2008; Genzel et al. 2010). However, the fact that only type I AGN are considered in this study is not coincidental. Due to the extremely high resolution needed to resolve the sphere of influence, only spectral measurements of the lines emitted from the BLR allow a statistically sufficient number of BH mass estimates.

Assuming that the gas clouds of the BLR are in Keplerian orbits around the BH and in a virialized state, the BH mass can be inferred via

$$M_{\mathrm{BH}} = f(R_{\mathrm{BLR}}) \frac{R_{\mathrm{BLR}} v^2}{G}, \tag{1.11}$$

where R_{BLR} is the radial distance of the BLR and v is the velocity of the emitting gas. The velocity is typically approximated by a measure describing the width of the used emission line, most commonly the FWHM. The factor $f(R_{\mathrm{BLR}})$ depends on the properties of the BLR, such as geometry, inclination and kinematics and is of the order of unity (e.g. Onken et al. 2004). However, it is also one of the main sources of uncertainty in this calculation, since a constant value is usually assumed for all AGN types for a chosen emission line, regardless of e.g. AGN luminosity, R_{BLR} or inclination.

The parameter R_{BLR} can be measured by determining the time difference between the variability in continuum and emission line flux. Studies using this reliable method, referred to as reverberation mapping, have also revealed a correlation between R_{BLR} and luminosity L (Kaspi et al. 2000, 2005; Peterson et al. 2004; Bentz et al. 2006). Since this approach is considerably demanding in terms of observation time, and therefore not suitable for large AGN surveys, R_{BLR} is typically approximated by the continuum luminosity at a comparable wavelength close to the used emission line. For the emission lines that are most commonly used in BH mass determinations, Hβ, MgII, and CIV, this corresponds to 5100Å, 3000Å, and 1350Å, respectively. Referencing Shen et al. (2011), Equation (1.11) can thus be replaced by an empirical relation such as

$$\log\left(\frac{M_{\mathrm{BH}}}{\mathrm{M}_\odot}\right) = a + b \log\left(\frac{\lambda L_\lambda}{10^{44}\ \mathrm{ergs\ s^{-1}}}\right) + 2 \log\left(\frac{\mathrm{FWHM}}{\mathrm{km\ s^{-1}}}\right), \tag{1.12}$$

where a and b are calibrated by empirical studies for different emission lines, such as those mentioned above (e.g. McLure & Dunlop 2004; Vestergaard & Peterson 2006; Vestergaard & Osmer 2009; Shen et al. 2011). Since BH masses can thus be derived with single measurements of L and an emission line width, this method is also referred to as 'single epoch measurement'. In the observational studies presented in this work, such BH measurements are used. Further details on the BH masses of the specific AGN samples can be found in the corresponding chapters.

1.3. The Connection Between AGN and Host Galaxy

The connections between SMBH masses and the properties of their host galaxies have been studied extensively for about three decades (for comprehensive reviews see e.g. Ferrarese & Ford 2005; Kormendy & Ho 2013; Graham 2016). The most prominent correlations that have been studied first, and on which the focus has remained until today, are the correlations of

SMBH mass with spheroid mass, which serves as a proxy for the total or bulge mass, mostly depending on whether early- or late-type galaxies are being studied (e.g. Kormendy & Richstone 1995; Magorrian et al. 1998; McLure & Dunlop 2002; Marconi & Hunt 2003; Häring & Rix 2004; Schramm et al. 2008; Jahnke et al. 2009; Bennert et al. 2011; Sani et al. 2011; Schulze & Wisotzki 2011; Beifiori et al. 2012; Graham & Scott 2013; McConnell & Ma 2013; Reines & Volonteri 2015; Shankar et al. 2016; Davis et al. 2019; Sahu et al. 2019a; Schutte et al. 2019; Ding et al. 2020; Habouzit et al. 2020; Suh et al. 2020), and the stellar velocity dispersion or luminosity of the bulge (e.g. Ferrarese & Merritt 2000; Gebhardt et al. 2000; Merritt & Ferrarese 2001; Tremaine et al. 2002; Wyithe 2006b,a; Graham 2007; Lauer et al. 2007; Gültekin et al. 2009; Bennert et al. 2010; Beifiori et al. 2012; Vika et al. 2012; McConnell & Ma 2013; Shankar et al. 2016; Sahu et al. 2019b; Sexton et al. 2019; Baldassare et al. 2020; Caglar et al. 2020; Bennert et al. 2021). On larger scales, scaling relations between BH mass and galaxy characteristics such as total luminosity (e.g. Bennert et al. 2010; Beifiori et al. 2012), Sérsic index n (e.g. Graham & Driver 2007; Beifiori et al. 2012; Vika et al. 2012), mass of the dark matter halo (e.g. Schulze & Gebhardt 2011; Volonteri et al. 2011), number and velocity dispersion of globular clusters (e.g. Burkert & Tremaine 2010; Harris & Harris 2011; Sadoun & Colin 2012), pitch angle of the spiral arms (e.g. Seigar et al. 2008; Berrier et al. 2013; Davis et al. 2017) or even galaxy cluster mass (e.g. Bassini et al. 2019; Phipps et al. 2019) have also been tested.

A combination of these tight scaling relations with the observation of a similar cosmic evolution of the BH accretion density (Aird et al. 2015; Hickox & Alexander 2018) and the star formation rate density (e.g. Madau & Dickinson 2014), with both trends peaking at $z \simeq 2$, may suggest a physically codependent evolution that is primarily regulated by AGN feedback processes. However, such trends do not necessarily imply causality, but only imply that both SMBHs and host systems follow a hierarchical merger growth scheme, where the central limit theorem can explain the tight correlations Jahnke & Macciò (e.g. 2011).

Figure 1.2 illustrates a compilation of selected results showing the variety of the M_{BH}–$M_{\star}$ scaling relation. For guidance, the 2D density distribution of the parental sample of simulated galaxies at $z = 2$ that is part of this work and described in more detail in Section 5.1 is included as well. The displayed scatter is not only due to selection and systematic effects, but it should also be noted that the referenced studies examine different sources in terms of nuclear activity, redshift, and morphology. To visualize this fact, sources from (Reines & Volonteri 2015) and Suh et al. (2020) are presented in the corresponding colors to the respective scaling relation as well. In the chapters describing the observational studies, more information is given on the particular scaling relations that are used to infer the stellar masses of the AGN host galaxies.

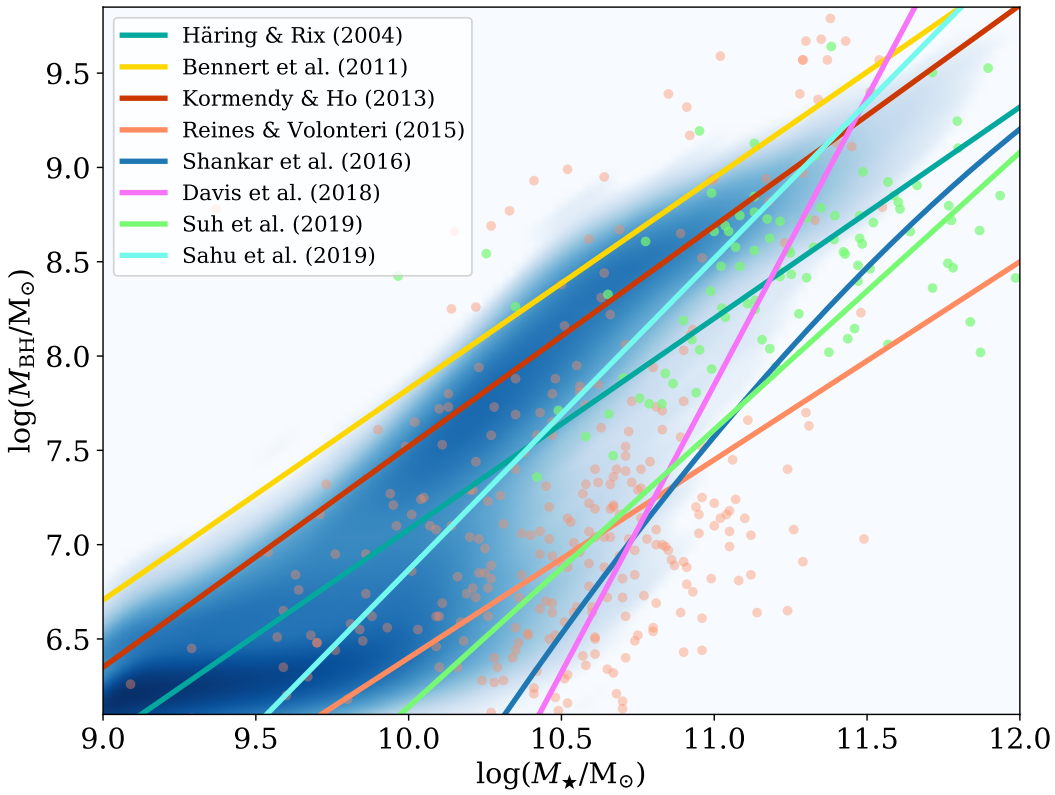

Figure 1.2.: Various selected $M_{\rm BH}$–$M_\star$ scaling relations superimposed on the 2D density distribution of the simulated parent data of galaxies at $z = 2$ that is used in Chapter 5. In addition, sources from Reines & Volonteri (2015) and Suh et al. (2020) which are used to derive the respective relations are shown in the corresponding color.

1.4. The Dissent on SMBH Growth

For decades astrophysicists have assumed that galaxies follow an evolutionary path that involves at least one merger event with another galaxy of similar mass (i.e. a *major* merger). This gravitational encounter could remove most of the angular momentum of the gas, funneling it into the most central regions where the SMBH is located. (Barnes & Hernquist 1992; Sanders & Mirabel 1996). Such an incident would ultimately lead to the AGN phase, in which the coalescing galaxy hosts at least one active SMBH at its center. This theoretical scenario was comprehensively presented in the seminal work of Sanders et al. (1988), and further explored with numerous simulations (Springel et al. 2005; Hopkins et al. 2006a, 2008; Somerville et al. 2008; McAlpine et al. 2018, 2020; Weigel et al. 2018; Bhowmick et al. 2020) and observations (e.g. Yue et al. 2019; Gao et al. 2020). This causal connection between major mergers and the presence of an

active SMBH has been found especially for AGN populations at low redshift (Koss et al. 2010; Cotini et al. 2013; Sabater et al. 2013; Hong et al. 2015; Ellison et al. 2019), and luminous partially obscured AGN at different cosmic epochs (Urrutia et al. 2008; Schawinski et al. 2012; Treister et al. 2012; Glikman et al. 2015; Fan et al. 2016; Donley et al. 2018; Goulding et al. 2018; Urbano-Mayorgas et al. 2019; Secrest et al. 2020).

In recent years, however, numerous studies have found contradictory results. While some works find a slight, but insignificant enhancement in the incidence of major mergers in AGN host galaxies (Silverman et al. 2011; Rosario et al. 2015; Hewlett et al. 2017; Shah et al. 2020), the majority of these studies report comparable merger rates for a wide range of AGN host galaxies when compared to samples of matching inactive control galaxies. No causal relationship with major mergers has been detected for either the general population of AGN, generally detected in the X-ray regime and observed in the optical domain (Gabor et al. 2009; Georgakakis et al. 2009; Cisternas et al. 2011; Silva et al. 2021), or specific AGN, such as those with the highest BH masses (Mechtley et al. 2016). The same conclusion has been inferred for obscured (Schawinski et al. 2012; Zhao et al. 2019a; Zakamska et al. 2019) or young AGN (Villforth et al. 2019). Also luminosity-selected AGN with low or moderate luminosities of $L_{\rm X} \leq 10^{43}$erg s^{-1} (Grogin et al. 2005; Allevato et al. 2011; Schawinski et al. 2011; Kocevski et al. 2012; Böhm et al. 2013) show no signs of an enhanced merger rate. Finally, even for the most controversial population – luminous AGN with $L_{\rm X} \geq 10^{43}$erg s^{-1}– evidence against a correlation between major mergers and these objects has been found (Karouzos et al. 2014; Villforth et al. 2014, 2017; Sharma et al. 2021).

These studies, which examined AGN at various redshifts and with a variety of luminosities and masses, consistently find that the fraction of host galaxies that are part of a major merger is significantly less than 50%, implying that major mergers are not the dominant trigger of AGN. Therefore, the unanimous conclusion is that mergers should be considered as only one of several possible mechanisms for initiating SMBH growth and AGN activity. Thus, it is necessary to consider alternative processes and/or differences in the lifetimes of merger features and AGN.

Recent works examining secular processes (Smethurst et al. 2019; Man et al. 2019), such as supernova feedback (Chen et al. 2009; Kumar & Johnson 2010) or gas inflow driven by instabilities (Bournaud et al. 2011), suggest that one of these processes may actually be the dominant mechanism to trigger AGN activity. On the other hand, other studies find no significant evidence that large-scale bars play an important role in the growth of SMBHs (Cheung et al. 2015; Cisternas et al. 2015; Goulding et al. 2017).

A possible time lag between the actual major merger event and the advent of the observable AGN phase seems to be an insufficient explanation for the contradictory findings regarding the

role of major mergers in the growth of SMBHs (Cisternas et al. 2011; Mechtley et al. 2016). Instead, Goulding et al. (2018) propose an intriguing alternative that might alleviate this tension: Although AGN are indeed triggered by major mergers, their activity, and hence luminosity, during the merger process depends on the merger stage and can therefore vary considerably. Thus, at larger separations between the two galaxies, the resulting torques are not sufficient to provide enough gas to trigger an AGN phase or fuel the BH(s). However, at close passages, both torques and gas inflow increase, boosting AGN activity as long as the distance between the two galaxies is sufficiently small. Prior to coalescence, this would lead to a periodic AGN variability, while the morphological features of this encounter, such as tidal tails, shells, or asymmetries, would be continuously visible, explaining the lack of observed AGN in merging systems. Based on the findings of the observational studies presented in this work, this aspect and its influence on the results will be discussed in the respective chapters.

2. Statistical Framework

2.1. Applied Electoral Systems

In the course of determining the major merger fractions of the AGN host galaxies, as well as the control sources, experts create individual rankings based on their visual classifications of the respective samples and the objects they contain. One step of the analysis is to combine these individual assessments into an overall ranking. A task that appears trivial at first glance turns out to be much more complex upon closer examination. The reason for this can be found by delving into the field of social choice theory and electoral systems, and considering Arrow's impossibility theorem (Arrow 1950). It states that no existing method that combines two or more individual votes into a consensus ranking satisfies the following three axioms: (1) non-dictatorship, such that all individual votes are considered to be equal; (2) unanimity or the weak Pareto principle, which states that if all voters agree on $X > Y$, this also applies to the overall ranking; and (3) the independence of irrelevant alternatives, such that the consensus relationship between X and Y only depends on the individual preferences between those two entities and not any additional option(s). Additional conditions considered are the Condorcet paradox and the Condorcet criterion (Condorcet 1785; Condorcet et al. 1989). The former states that an overall sequence can be cyclic – e.g., X wins over Y, which wins over Z, which in turn wins over X – although the individual votes are not. The latter declares that an overall top-ranked candidate wins in every pairwise comparison with every other candidate.

In order to test if and how the violation of a criterion affects the final result, the same three different methods are applied in each analysis to combine the individual rankings, since each of these methods satisfies a different set of criteria.

The first technique, from here on referred to as the average method, adopts the same approach that is used in Mechtley et al. (2016). The initial step is to calculate the mean rank for each candidate from the individual rankings and discard any individual vote that differs by more than 2σ from the respective average rank. The respective mean ranks are recalculated and used to create the final consensus ranking, by ordering the candidates in an ascending order according

to their final average rank. However, since this algorithm weighs individual votes, it apparently violates the non-dictatorship criterion.

In contrast, the second method employed, the Borda count (Emerson 2013), satisfies this condition, but violates the independence of irrelevant alternatives in exchange. The original version of this approach, in which the first-ranked option receives n points, the second placed $n-1$ and so on, with n being the total number of candidates, is adapted by applying the Dowdall system (Reilly 2002). With this modification, candidates receive the reciprocal value of their respective ranks, i.e. the first-ranked option is given $1/n = 1$ point, the next 0.5 points, and so on. This variation reduces the influence of low-ranked candidates, who may be ranked more randomly due to a lack of significant features.

While the Borda count avoids the Condorcet paradox, only the third approach, the Schulze method (Schulze 2011, 2018), also satisfies the Condorcet criterion. In this method, all pairwise comparisons between two candidates X and Y are calculated for all individual rankings and put in relation to each other, resulting in an overall ranking in which the top-ranked candidate indeed wins over all other candidates, i.e. the so-called Condorcet winner. For lower ranks within the resulting consensus sequence, the second-placed candidate loses only to the top-ranked option, and so on. More detailed information and also a variety of extensive examples can be found in Schulze (2018).

2.2. The Beta Distribution

The derivations of the merger fractions in this work are based on various methods that ultimately count how many galaxies are classified as merging and inactive within a given subsample of sources. The merger fraction is then simply defined as the number of distorted galaxies over the total number N of objects,

$$f_m = \frac{a}{a+b}, \tag{2.1}$$

where a represents the number of merging galaxies, b counts the sources that are undisturbed, i.e. all remaining objects, and $N = a + b$. From a statistical point of view, the merging fraction can be interpreted as the probability that a random galaxy from the sample is a merger. A merger fraction of $f_m = 0$ and $f_m = 1$ would result in no or all galaxies being classified as mergers, respectively.

Since only samples of limited size are examined, it is essential to quantify the uncertainties introduced by shot noise for the resulting merger fractions. Based on the two parameters a and b, the probability densities for the resulting merger fractions can be continuously quantified within the feasible domain $[0, 1]$ by using the beta distribution,

$$f(x) = \begin{cases} \frac{1}{B(a,b)} x^{a-1}(1-x)^{b-1} = \frac{\Gamma(a+b)}{\Gamma(a)\Gamma(b)} x^{a-1}(1-x)^{b-1} & \text{if } 0 < x < 1 \\ 0 \text{ otherwise} \end{cases} \tag{2.2}$$

where Γ is the Gamma function and

$$B(a,b) = \int_0^1 x^{a-1}(1-x)^{b-1} dx \tag{2.3}$$

is the beta function that is used to normalize the beta distribution. This function is similar to the binomial distribution, which has the following form: $f(k,n,p) = \binom{n}{k} p^k (1-p)^{n-k}$, where n is the number of trials, k is the number of successes and p is the probability of success. However, the difference between the binomial and beta distribution is that the former models the probability k based on the parameters n and p, while the latter models the probability p itself. Therefore, the beta distribution can be interpreted as a probability distribution of probabilities, in the sense that for an unknown probability p it provides the probability densities of all the possible values that p can take. This is precisely what is required to assess the uncertainties of the inferred merger fractions (i.e. merger probabilities).

Depending on a and b, the probability density function (PDF) of a beta distribution can have very different shapes, from u-shaped over a straight line to a bell shape, which resembles the appearance of a normal distribution. As examples relevant to this work, Figure 2.1 shows only PDFs of beta distributions whose mean values could also conceivably be merger fractions based on similar sample sizes. Thus, no extreme cases such as $a, b < 1$ are shown, which would correspond to less than one merging and one unperturbed galaxy, respectively. The formula for the mean of a beta distribution is identical to Equation (2.1). From left to right, the panels in the top row show the corresponding distributions for sample sizes of $N = \{10, 50, 100, 500\}$, each for a mean of $\mu = \{0.2, 0.4, 0.9\}$. Clearly visible is how the shape and uncertainty in the form of the standard deviation,

$$\sigma = \sqrt{\frac{ab}{(a+b)^2(a+b+1)}}, \tag{2.4}$$

depends on a and b, and the sum of these two parameters, i.e. the sample size. The panels in the bottom row show how the corresponding σ decrease with sample size N for each of the three chosen values of μ. Although the absolute value of σ depends on the respective values of a and b, the value of this parameter decreases only slowly for $N \gtrsim 50$. This implies that excessively large sample sizes do not enhance the statistical significance considerably.

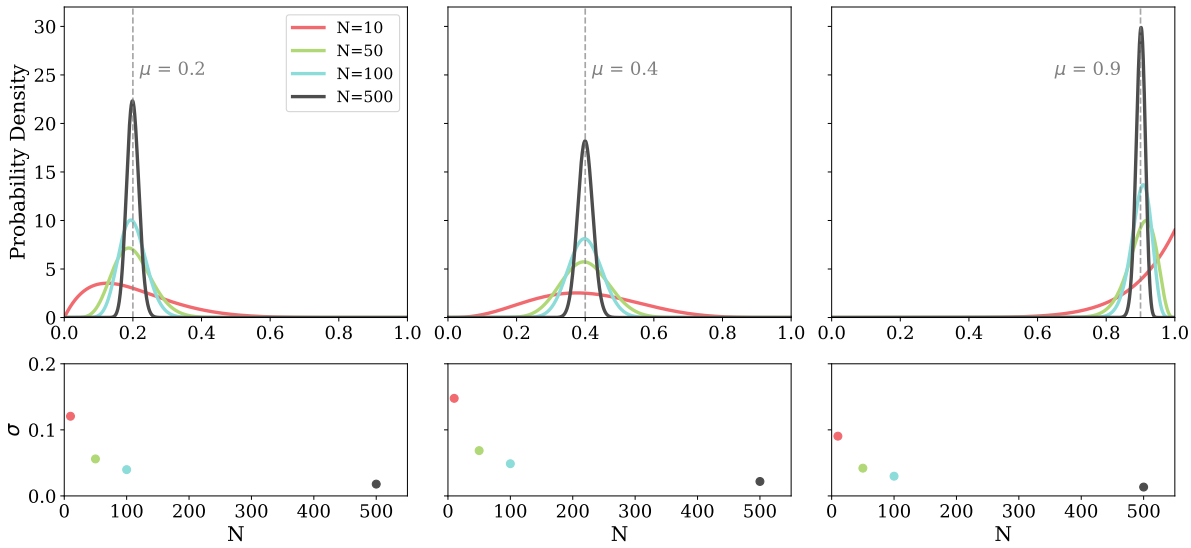

Figure 2.1.: *Upper row:* Probability density functions for various examples of beta distributions. While the means are identical for each distribution within each panel, the same four sums of $N = a + b$ are shown in all panels, illustrating how the shape of the functions depend on the parameters a and b and thus the sample size N. *Lower row:* Trend of standard deviation σ with increasing sample size N for each of the chosen means μ.

In a theoretical scenario where this experiment could be repeated several times with comparable data sets, one could update the previous result each time by simply adding the newly derived numbers of mergers and unperturbed galaxies – or more generally the numbers of successes and failures – to the corresponding existing parameters a and b. This would, most probably, shift the derived mean toward the true mean, and would also narrow the distribution by effectively increasing the sample size. Such an approach of constantly updating a and b, is what is actually done when dealing with a constant stream of new available data and modeling the posterior probability by Bayesian inference. In this case, the beta distribution is well suited as a prior since it is the conjugate prior for the Bernoulli, binomial, negative binomial, and geometric distributions. As a result, the posterior distribution is again described by a beta distribution, which in turn can be used as an updated prior. However, for this particular application – determining the merger fractions of observed or modeled galaxies – such a procedure is not realistic, since a statistically meaningful number of independent trials or an excessively large sample is not feasible due to limitations in observing time or even suitable sources.

3. Thesis Outline

In contrast to preceding studies, investigating the role of major mergers in triggering AGN, this work focuses on a key part of the parameter space that has remained untested so far, AGN with the highest Eddington ratios $\lambda_{\mathrm{Edd}} = L/L_{\mathrm{Edd}}$. It appears intuitive and plausible that at least AGN with the highest specific accretion rates are predominantly triggered by major mergers, since the amounts of gas required to achieve such high accretion rates may only be supplied by gravitational interactions of two gas-rich galaxies of similar mass.

As in almost all of the above studies that reject major mergers as the dominant triggering mechanism of AGN, the individual samples of AGN host galaxies are compared to a suitable sample of inactive comparison galaxies that are matched in redshift, stellar mass, observed wavelength, depth, and signal-to-noise ratio (S/N). Only by considering such a matched comparison sample, a statement about a possible enhancement of the merger fraction for AGN host galaxies is actually valid. Hence, this work consists of thorough, separate analyses of the major merger fractions for three different samples of AGN with the highest Eddington ratios. In Part II the focus lies on such AGN at redshift $z \simeq 2$, a period that is now typically referred to as cosmic noon. Chapter 4 presents an observational study comparing the merger fractions of AGN and a sample of matched control galaxies. In order to assess the validity of the observational results at $z \simeq 2$, a comparable analysis for simulated AGN at this redshift is featured in Chapter 5 using the state-of-the-art magnetohydrodynamical cosmological simulation IllustrisTNG. In Part 6, a similar sample of local AGN at $z \lesssim 0.2$ is studied, allowing for a test of any redshift dependence within the same AGN subpopulation. Part IV consolidates the results of the three independent analyses and discusses them with regard to each other and previous studies. In addition, the results are summarized and potential future projects are discussed, which also includes an outlook on future challenges and still unanswered questions.

Part II.

AGN with the Highest Eddington Ratios at the Cosmic Peak of Black Hole Growth

4. Probing the Major Merger-AGN Connection with Observations

The combination of the increased total merger rate of galaxies at $z \simeq 2$ relative to the local Universe and the peak of cosmic AGN activity at this redshift (Boyle et al. 2000; Aird et al. 2015; Hickox & Alexander 2018) makes it very plausible that at this cosmic time, in particular, AGN with Eddington ratios close to unity or even above show an excess of merger events.

In order to test this conjecture, 21 AGN host galaxies are compared to a matched sample of 92 inactive comparison galaxies at this particular redshift. Since major merger features of the sources in the CANDELS sample (Grogin et al. 2011; Koekemoer et al. 2011) are visible up to $z \simeq 2.5$ (Kaviraj et al. 2013, and references therein), and the observations of the AGN host galaxies provide the same depth and signal-to-noise ratio (S/N), the existence of a potential causal sequence between major mergers and SMBH growth can be tested. These signatures of major mergers, such as tidal torques and tails or asymmetries, serve as a proxy to determine whether a particular source was recently or is still part of a gravitational interaction. After accounting for the AGN nuclei in the images and a combination of both samples, experts rank the combined sample according to the strength of the distortions. The repeated separation into AGN and non-AGN allows to determine the individual fractions of the distorted galaxies.

Attention is also drawn to two questions that inevitably arise when considering possible differences in merger fractions: First, whether there is the possibility of a time lag between the visibility of merger features and an AGN that would eventually lead to the observation of the latter while signs of the gravitational encounter are no longer detectable; second, how it would affect the results if the opposite were true in the sense that merger features are clearly visible but an AGN associated with this process is explicitly not. As suggested by Goulding et al. (2018), precisely such cases could explain the inconclusive results regarding the role of major mergers in the emergence of AGN. Finally, a possible link between post-starburst galaxies and AGN is

also being investigated, since such galaxies show clear signs of recent mergers, but also require a mechanism to stop the recently increased star formation.

The adopted cosmological parameters are $\Omega_\Lambda = 0.7, \Omega_0 = 0.3$, and $h = 0.7$. All magnitudes are given in the AB system (Oke & Gunn 1983).

4.1. Data

4.1.1. AGN Host Galaxies

The initial parent sample is constructed by selecting targets from the SDSS DR7 Quasar catalog (Abazajian et al. 2009; Schneider et al. 2010; Shen et al. 2011), which have been uniformly selected by the target algorithm described in Richards et al. (2002) (see also Richards et al. 2006). Further constraints are adopted by using the broad line MgII measurements of the virial BH masses by Shen et al. (2011) and selecting only sources within a mass range of $8.5 \leq \log(M_{\rm BH}/{\rm M}_\odot) \leq 8.7$. Moreover, only AGN within the redshift interval of $1.8 \leq z \leq 2.2$ and an Eddington ratio $\lambda_{\rm Edd} \geq 70\%$ are selected.

Proceeding to even higher redshifts than $z \simeq 2$ would impede reliable BH mass determination due to a lack of available AGN SDSS spectra with sufficient quality of MgII line measurements. Combined with the fact that limits have been reached in terms of resolution and point spread function (PSF) stability, this is therefore likely to be the highest redshift range in which highly accreting AGN can be reliably studied for galaxy properties with the *Hubble Space Telescope (HST)*. The presented selection criteria allow to avoid the lower mass limit of SDSS, which lies at $\log(M_{\rm BH}/{\rm M}_\odot) \simeq 8.3$ (Shen et al. 2008; Vestergaard et al. 2008), and still investigate the AGN population that provides at least half of the total BH mass accretion in the early Universe and has the highest Eddington ratios, i.e. the highest specific accretion rates (Figure 4.1, left panel). Using the bolometric luminosities $L_{\rm bol}$ provided in the SDSS DR7 quasar catalog and assuming an efficiency parameter of $\eta = 0.1$, the respective mass accretion rates $\dot{M}$ are calculated (Figure 4.1, right panel).

The experiment is designed in such a way that the sample sizes allow a significant discrimination between a $\geq 50\%$ merger fraction for the AGN sample and an assumed 20% fraction for the inactive galaxies. For this objective and ∼90 comparison galaxies (see below), 21 AGN are sufficient to detect a difference at a $> 99.7\%$ probability level, i.e. $> 3\sigma$ confidence. Therefore, to avoid any biased selection, the resulting initial sample of 147 targets satisfying the aforementioned conditions is reduced to 21 randomly selected AGN. These limits in BH mass and Eddington ratio/mass accretion rate are shown as blue boxes in Figure 4.1, and the initial 147 AGN and

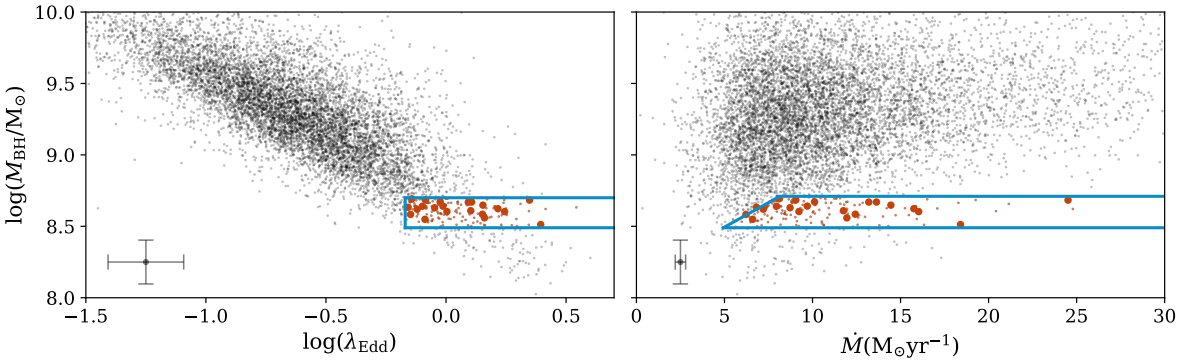

Figure 4.1.: Left: Black hole mass $M_{\rm BH}$ vs. Eddington ratio $\lambda_{\rm Edd}$ for the complete sample of AGN at redshift $1.8 \leq z \leq 2.2$ (black points). Overplotted are the selection limits (blue box) as well as the parent sample (small red points) and the final selection of AGN (large red points). Right: $M_{\rm BH}$ vs. mass accretion rate $\dot{M}$ for the same samples, showing that the final selection consists of AGN possessing the highest specific accretion rates. The error bars display the corresponding average uncertainties in BH mass, Eddington ratio and mass accretion rate.

final 21 selected AGN are shown as small and large red points, respectively. A visual inspection of the spectra of these targets confirms the robustness of the BH mass determinations.

The error bars in Figure 4.1 represent the mean uncertainties of the black parent sample in BH mass $M_{\rm BH}$, Eddington ratio $\lambda_{\rm Edd}$, and mass accretion rate $\dot{M}$. While the uncertainty in $M_{\rm BH}$ is approximately the expected value of ~ 0.4 dex for single-epoch BH mass determinations (e.g. Shen 2013, and references therein), the uncertainty in $\dot{M}$ is significantly smaller, since this parameter is based solely on the estimates of the bolometric luminosity. Thus, since the uncertainty in $M_{\rm BH}$ is the dominant component, the uncertainty in $\lambda_{\rm Edd}$ is of the same order of magnitude.

The 21 final selected sources have been observed with *HST*/WFC3 in the F160W band, corresponding to *V* in the rest frame (*HST* program ID 14262, PI K. Jahnke). The exposure time for each target observation is one orbit (∼40min) split into a 6×400s dithering pattern. The resulting lower magnitude limit of 24 mag is sufficient to detect features of major mergers, such as tidal tails or asymmetries at $z \simeq 2$ (van Dokkum & Brammer 2010; Ferreras et al. 2012).

Table 4.1 summarizes the properties of the investigated AGN. Apart from the SDSS source designations, the corresponding redshifts z are listed, as well as the *k*-corrected (Richards et al. 2006) absolute I-band magnitudes, normalized to $z = 2$, the bolometric luminosities $L_{\rm bol}$, the rest frame luminosities at 3000Å L_{3000}, the FWHM of the single-epoch measurements of MgII in km s^{-1}, and the respective BH masses $M_{\rm BH}$. All these values are drawn from the catalog presented in Shen et al. (2011). Furthermore, the last two columns provide the calculated

Target AGN (SDSSJ) (1)	Redshift z (2)	M_I mag (3)	L_{bol} ergs^{-1} (4)	L_{3000} log($L_\odot$) (5)	FWHM (km s^{-1}) (6)	M_{BH} log($M_\odot$) (7)	λ_{Edd} (8)	$\dot{M}$ $M_\odot yr^{-1}$ (9)
0832+4347	1.8	–26.51	46.58	12.28	2100	8.5	–0.09	6.6
0846+2723	2.0	–27.71	47.15	12.65	1900	8.7	0.35	24.6
0915+2947	2.1	–27.14	46.76	12.47	2100	8.7	–0.02	10.2
1014+4041	2.0	–27.21	46.92	12.56	2000	8.6	0.15	14.3
1025+2204	2.1	–27.10	46.88	12.54	2000	8.7	0.09	13.1
1106+1044	1.9	–26.85	46.72	12.43	2000	8.6	0.00	9.2
1144+4524	1.9	–26.48	46.61	12.32	2200	8.6	–0.12	7.2
1236+2811	2.0	–27.00	46.89	12.55	2000	8.7	0.11	13.7
1304+2409	1.9	–27.45	46.96	12.67	1700	8.6	0.24	15.9
1309+3817	1.8	–26.61	46.66	12.36	2200	8.6	–0.10	7.9
1414+4216	1.8	–26.63	46.59	12.29	2300	8.6	–0.16	6.8
1415+1103	1.9	–27.18	46.85	12.56	1800	8.6	0.15	12.4
1418+2711	2.0	–27.05	46.55	12.43	2000	8.6	–0.15	6.2
1426+2959	1.9	–26.80	46.74	12.39	2200	8.6	–0.01	9.8
1427+5338	2.0	–26.84	46.83	12.42	1900	8.6	0.16	12.0
1513+3035	1.9	–26.69	46.71	12.31	2400	8.7	–0.09	9.0
1530+0704	2.0	–26.57	46.66	12.30	2500	8.7	–0.14	8.1
1539+2711	2.1	–27.23	46.83	12.45	2000	8.6	0.10	11.7
1546+2236	2.0	–27.04	46.95	12.66	1800	8.6	0.22	15.9
1556+0800	1.9	–27.25	47.02	12.64	1600	8.5	0.39	18.2
1624+2204	2.0	–26.72	46.70	12.37	2200	8.6	–0.05	8.7

Table 4.1.: Properties of the sampled AGN: Columns 1-6 are taken from the catalog of Shen et al. (2011). Column 1: SDSS object designation (J2000.0); Column 2: redshift, determined by the SDSS DR7 (Schneider et al. 2010); Column 3: *k*-corrected (Richards et al. 2006) absolute I-band magnitude, normalized to $z = 2$; Column 4: bolometric luminosity; Column 5: luminosity at 3000 Å; Column 6: FWHM of MgII in the broad component; Column 7: BH virial mass using MgII; Column 8: Eddington ratio λ_{Edd}; Column 9: mass accretion rate $\dot{M}$ in solar masses per year.

corresponding Eddington ratios λ_{Edd} and mass accretion rates $\dot{M}$, with the latter being based on the assumption of a radiative efficiency of $\eta = 0.1$.

4.1.2. Inactive Galaxies

To construct the comparison sample of inactive galaxies, the exhaustive observations of the CANDELS Multi Cycle Treasury program (Grogin et al. 2011; Koekemoer et al. 2011) are used. In order to ensure the best possible match with the AGN sample, galaxies with the same properties as the AGN host galaxies are selected within the GOODS-S, GOODS-N, AEGIS, COSMOS, and UDS fields. This entails selecting sources that lie in the same redshift and mass range and were observed with the same instrument and filter. For this purpose, the same redshift cuts are applied and *HST*/F160W observations are used that have similar or higher S/N than the single-orbit AGN observations. If necessary, noise is added to these images to match the limiting sensitivity in the

AGN sample. To estimate the required stellar masses of the AGN host galaxies, the $M_{\rm BH}$–$M_{\star}$ scaling relation by (Bennert et al. 2011) is adapted by a small normalization factor of 2 to account for a potential redshift evolution out to $z = 2$ (Bennert et al. 2010; Schulze & Wisotzki 2011). Due to the uncertainties in the BH mass measurements, this relation would also be applicable in the case of no evolution with redshift (Suh et al. 2020).

Subsequently, out of a few thousand potential candidates (van der Wel et al. 2014), 92 galaxies with $9.2 < \log(M_{\star}/\mathrm{M}_{\odot}) < 11.7$ are randomly selected to comprise the final sample of inactive galaxies, with the individual mass estimates drawn from the catalog presented by the 3D-HST survey (Brammer et al. 2012; Skelton et al. 2014; Momcheva et al. 2016).

This rather wide mass range accounts for the uncertainties in the BH mass determinations, which in turn affect the host mass estimates. Considering these uncertainties, an identical range in stellar mass is examined for both the AGN host galaxies and the comparison sample. However, to determine a possible impact of stellar mass on the results, the analysis is repeated with a mass-restricted subsample ($10.4 < \log(M_{\star}/\mathrm{M}_{\odot}) < 11.5$) of inactive galaxies.

4.1.3. Reduction and Modeling

Since the interest is to detect potential merger features of AGN host galaxies, it is mandatory to subtract the central AGN light component, which is superimposed on the host galaxy stellar light and can be a factor of 5-40 brighter than the underlying host galaxy (Jahnke et al. 2004b,a, 2009; Sanchez et al. 2004; Kotilainen et al. 2007; Schramm et al. 2008; Mechtley 2014). Therefore, a good PSF model is essential to achieve a satisfactory subtraction of the central AGN component. In general, it is best to create a PSF model from stars in the same frame and with the same color as the AGN to avoid influences of optics and different spectral energy distributions (SED). However, because this is not possible for all exposures, and because WFC3 suffers from optical imperfections such as coma or astigmatism, additional PSF models are constructed from archival data of high S/N stars (see Mechtley et al. 2016). It is ensured that these observations match the AGN observations in resolution, readout-mode, and dithering pattern. Ultimately, the final set consists of eight different PSF models.

In a next step, the individual images of each object of the two samples and the selected PSFs are combined using the software package drizzlepac (following approaches outlined in Koekemoer & et al. 2002; Gonzaga & et al. 2012), resulting in a pixel scale of $0\farcs060$, corresponding to ~ 0.5 kpc at $z \simeq 2$. Variance maps, which are mandatory for the subsequent modeling, are produced for all images as well as for the PSF models. Excluding the variance maps from the modeling process would lead to an underestimation of the errors, since the flux contribution of the central point source is significantly higher than that of the sky.

By applying the Markov Chain Monte Carlo (MCMC) fitting algorithm PSFMC[1], first described and used in Mechtley (2014) and Mechtley et al. (2016), 2D two-component models of the objects are created. Contrary to most tools dedicated to fitting galaxies in 2D, PSFMC allows the user to define fixed values or prior probability distributions for the model parameters, such as position in x and y, total magnitude, Sérsic index n, or position angle, while the output is the posterior probability distributions for these same parameters based on the observational input image. Figure 4.2 illustrates one of the resulting corner plots, showing the 2D covariances between each pair of parameters and the histograms for each parameter. The user also chooses number of samples that should be drawn from the posterior distributions, with PSFMC creating a model image, a PSF convolved model image and a variance map based on each drawn sample. The joint probabilities of each observed pixel flux value yield the likelihood function, which is then multiplied by the prior probabilities resulting in the posterior probability of the drawn sample. The sample is then rejected or accepted via the Metropolis criterion (Metropolis et al. 1953; Hastings 1970).

Additionally, the algorithm does not assume an error-free PSF, but implements the respective PSF variance maps during the convolution process. For this purpose, the *HST* focus model (Cox & Niemi 2011) is employed to determine the time-dependent telescope focus for each source and to find the best fitting PSF within the PSF library.

By using PSFMC, one also avoids the problem of the algorithm getting caught in a false minimum. For example, GALFIT (Peng et al. 2002, 2010), a tool that is most commonly used to decompose galaxies, minimizes the least squares by applying the Levenberg-Marquardt algorithm. Especially for models with small effective radius $r_{\rm e}$ and a large Sérsic index n, most of the information for the next iteration in the minimization process is stored within a single pixel. If such pixels now contain wrong flux values resulting e.g. from a PSF mismatch, the algorithm may be led into a false minimum.

Via a point source model and a Sérsic profile, the central AGN component and the underlying host galaxy are fitted simultaneously. Although the host galaxies may not be perfectly described by a Sérsic profile, it is a sufficient approximation since one can still determine potential asymmetries or tidal features. Moreover, the use of this two-component approach has a twofold advantage: first, it ensures that the contributing flux from the central source is not overestimated, which avoids a possible PSF over-subtraction. Second, while the fitting of multiple components is supported, the use of only two components keeps the required computation time within reasonable limits.

For the actual fits, neighboring galaxies whose central flux peaks do not coincide with the central source in the respective images are masked and excluded. To remove the AGN, the

[1] See https://github.com/mmechtley/psfMC for additional information, examples and documentation.

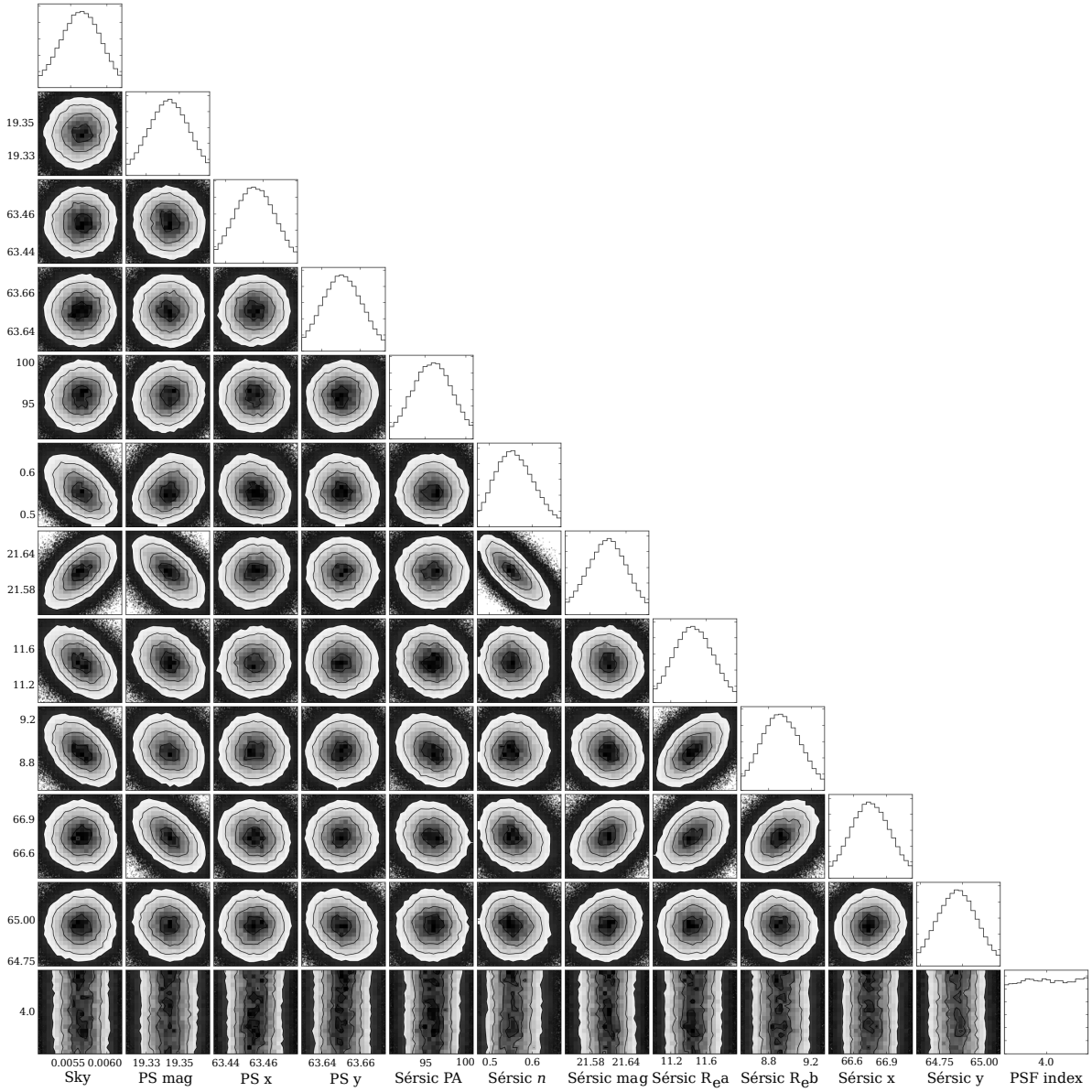

Figure 4.2.: Posterior probability distributions for SDSS J083253.96+434712.5 showing the 1D distributions of each modeled parameter as well as the 2D covariances between each pair of parameters.

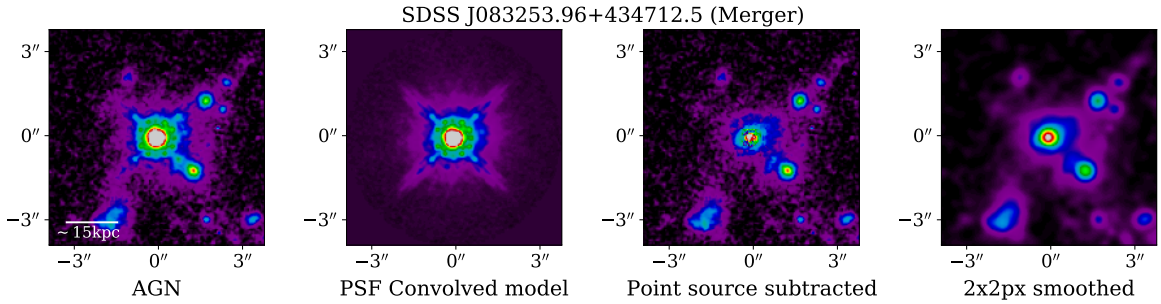

Figure 4.3.: Different steps of the AGN/host galaxy modelling process for an example source are shown. The first image depicts the original, processed *HST*/WFC3 image, the second displays the PSF convolved point source model, and the third and fourth show the host galaxy after point source subtraction with the original sampling and smoothed by an $\sigma = 2$ px Gaussian, respectively. This particular source is one of the five AGN host galaxies classified as a merger (see Section 4.2 for more details). All images are displayed with the same arcsinh scaling. The remaining 20 AGN of the sample are shown in Appendix A.

resulting point source model, i.e. the PSF convolved point source component, is then subtracted from the original image which shows then only the underlying host galaxy. Figure 4.3 presents, from left to right, for one of the 21 AGN sources, the original drizzled *HST*/WFC3 image, the convolved point source model, and the point source-subtracted model revealing the host galaxy, once with the original sampling, and once smoothed by an $\sigma = 2$ px Gaussian. All four images are shown in the same arcsinh scaling. Comparable plots for the remaining 20 AGN are shown in Appendix A.

To achieve the goal of galaxies in both samples exhibiting the same nuclear residuals, synthetic point sources are added over the position of the flux center of the inactive galaxies. This is done by randomly selecting one of the PSFs and excluding it from the subsequent modeling for that particular inactive galaxy. If necessary, additional noise is added to match the observed AGN. The same fitting process as for the AGN sample is then performed. Similar to Figure 4.3 and Appendix A, Appendix B presents both the 11 comparison galaxies that are classified as mergers in all three consensus rankings and, for comparison, a selection of 10 randomly drawn control galaxies classified as undisturbed. The final result yields now two samples that are not only matched in mass, redshift, S/N, instrument, and filter, but also have the same central residuals at the center due to the point source subtraction.

4.2. Morphological Analysis and Merger Fractions

After the modeling process, the final joint sample comprises of 113 images of AGN hosts and inactive galaxies. As a next step to derive the merger fractions, ten experts with extensive

experience in working with imaging data of galaxies are asked to visually analyze the images and identify possible features indicative of major mergers[2]. Based on their assessment, they should then rank the galaxies from most to least distorted. Such an approach to visually detect features due to gravitational interactions has been successfully applied in previous studies (e.g. Cisternas et al. 2011; Kocevski et al. 2012; Mechtley et al. 2016). It should be noted that there are an increasing number of machine learning algorithms that can classify galaxies based on their morphologies and possibly their merger state (e.g. Bottrell et al. 2019; Cheng et al. 2019; Snyder et al. 2019). However, due to the manageable sample size and the high time and logistical cost of learning an automatic classification routine with a suitable "external" training set, human interpretation and judgment, has been preferred over this automatic approach.

Each expert will have his or her own subjective interpretation of what a major or minor perturbation might look like, but the 'blind' analysis forces the criteria to be applied equally to both active and inactive galaxies within the combined sample. Therefore, personal biases regarding the appearance of mergers do not play a significant role in the analysis. To eliminate further systematic bias, each classifier has been given a sample with random order and naming. In addition, they are requested to flag the images that they believe show an unresolved source, due to the image being noise dominated or displaying only artifacts from the point source subtraction. To this end, images of eight point source-subtracted stars are provided as reference. Four of them are eventually also included in the joint sample of galaxies to assess the 'quality' of the individual rankings.

While only one galaxy has been flagged as unresolved by five experts and all other galaxies receiving fewer flags, the point source-subtracted star images have been flagged five to nine times each. In total, 165 of 1170 individual scores are flagged as unresolved (of which 96 are attributed by two experts), with 35 flags referring to the five objects mentioned above (one galaxy and four stars). For the subsequent creation of the consensus ranking, this one galaxy is excluded, leaving a final sample of 112 sources.

To determine if and how strongly the combination method affects the results, three different techniques are applied to combine the individual rankings. The first approach follows Mechtley et al. (2016) and weighs the individual ranks of each galaxy. The second and third methods adopted are the Borda count (Emerson 2013) and the Schulze method (Schulze 2011, 2018) (see Section 2.1). Individual entries that are flagged as unresolved are treated as unranked votes with no preferred order among them.

[2] The classifiers are: Seth Cohen, Bernd Husemann, Knud Jahnke, Victoria Jones, Anton Koekemoer, Victor Marian, Andreas Schulze, Arjen van der Wel, Carolin Villforth, and Rogier Windhorst.

The merger fractions are derived by splitting the three combined rankings at a particular rank, from here on referenced as cutoff rank. Galaxies below this limit in the ranking, i.e. with a higher rank do not show an obvious presence of gravitational interaction features upon visual inspection and vice versa. For consistency, the same cutoff rank is chosen for each of the consensus sequences. After detailed visual analysis, position 22 is identified as the cutoff rank. Separating the combined sample at this point into a set of galaxies with obvious merger features and a sample without such features, and again into AGN and inactive control galaxies, all three consensus rank sequences yield identical numbers. Quantitatively, the three consensus rankings provide the following numbers:

- 5 AGN host galaxies and
- 17 inactive galaxies show merger features;
- 16 AGN host galaxies and
- 74 inactive galaxies show no such features.

It should be noted that between the three different combined lists, the objects and their order do not necessarily have to be, and are in fact, not the same. Nevertheless, the objects above the chosen cutoff rank at position 22 vary only slightly: all five AGN and 11 of the 17 comparison galaxies that have been classified as mergers are identical in the three consensus rankings.

As described in Section 2.2, the probability density distributions of the inferred merger fractions can be described by a beta distribution, where a represents the number of galaxies with merger features and b denotes the number of not-distorted galaxies. Figure 4.4 shows the PDFs for the inferred merger fractions in red and blue for the sample of inactive galaxies and the AGN host galaxies, respectively. The solid lines display the expected values, i.e. the means for both samples; the dashed lines and shaded regions show the associated 68% confidence intervals. The merger fractions are interpreted as the respective means of the distributions and are $f_{\mathrm{m,\,AGN}} = 0.24 \pm 0.09$ for the AGN host galaxy sample and $f_{\mathrm{m,\,Ina}} = 0.19 \pm 0.04$ for the inactive galaxies. This difference is indistinguishable within 1σ. A Welch's t-test testing the hypothesis that both samples have identical means yields a *p*-value of $\simeq 0.12$.

4.2.1. Influences by Choice of Combination Method or Cutoff Rank.

The influences resulting from the applied method for combining the individual ranks or the choice of cutoff rank are examined by recalculating the merger fractions for a sequence of cutoff ranks between 15 and 50 and evaluating the resulting values for each of the three methods. The resulting trends in merger fractions with cutoff rank are shown in Figure 4.5. The gray

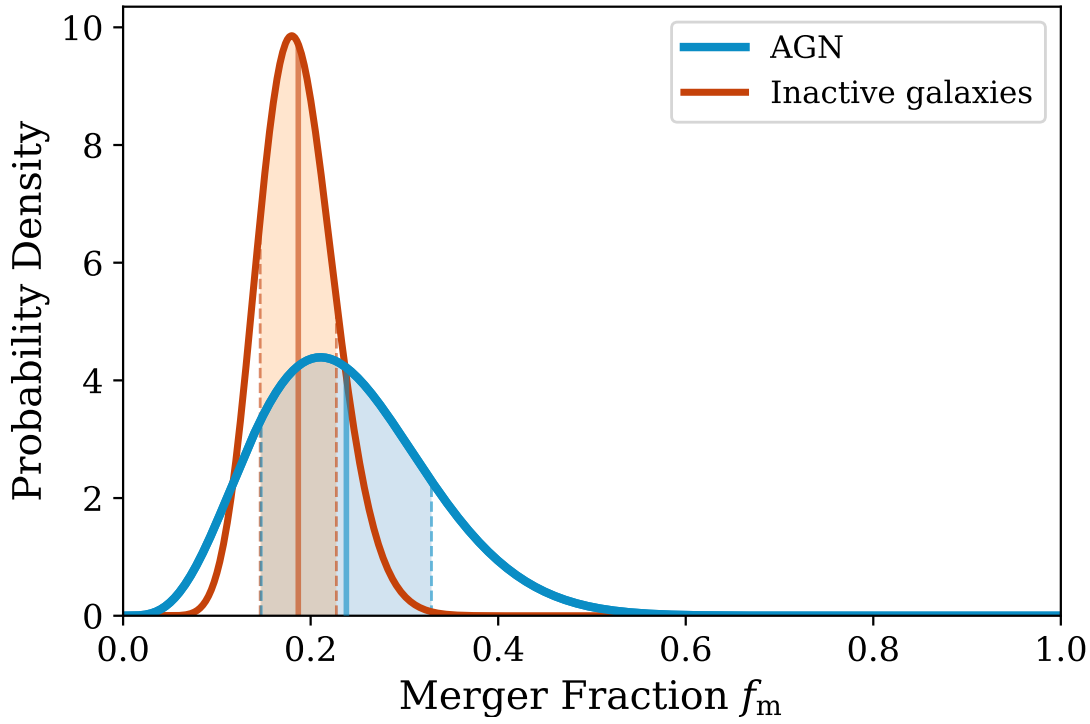

Figure 4.4.: Probability density distributions for the inferred merger fractions of the AGN host galaxies at $z \simeq 2$ (blue) and a matched control sample of inactive galaxies (red). The solid lines show the means of the respective merger fractions, while the dashed lines denote the central 68% confidence intervals.

dotted vertical lines denote the selected cutoff rank at position 22, the color scheme describes the respective sample, blue for AGN and red for the comparison sample, and the line type represents the respective method: solid for the average method, dashed for the Borda count approach and dotted for the Schulze method. Thus, the three plots on the left show the evolution of the merger fractions for both samples as a function of the selected cutoff rank, broken down for each method. Supplementary, the two plots on the right show the results of the respective merger fractions summarized for each method, but separated with respect to AGN activity. By definition, the fractions increase the higher the selected cutoff rank. However, with the exception of the Borda count for cutoff ranks between 40 and 50, the merger fractions for both samples differ by less than 1σ for each individual method.

While there appears to be a slight but not significant lack of enhancement at cutoff ranks $\gtrsim 38$ for the AGN merger fraction derived using the Borda method, the fractions for the inactive galaxies are virtually identical over the entire range of cutoff ranks studied. The consistent results

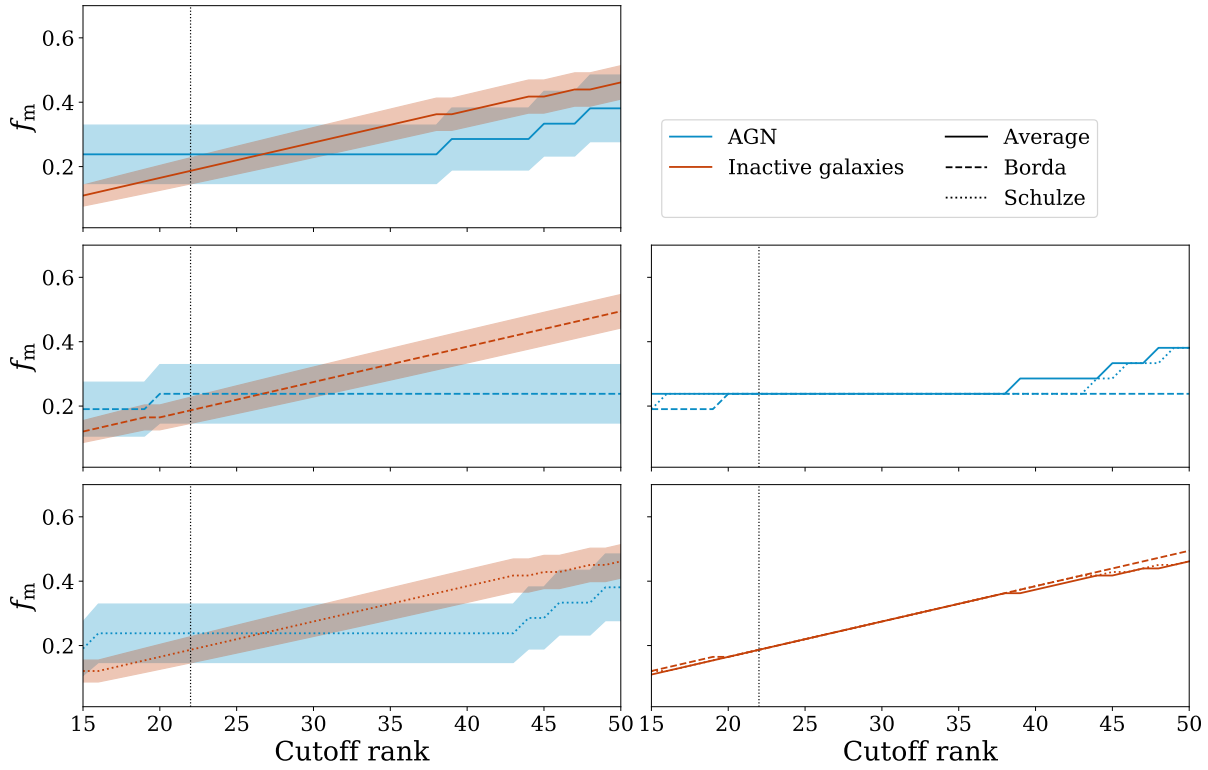

Figure 4.5.: Distributions of the merger fractions of AGN host galaxies and inactive galaxies as a function of cutoff rank and methods used to derive the consensus rankings. The blue and red colors represent the AGN and comparison sample respectively. The line style indicates the respective combination method. The shaded regions give the 1σ interval. The plots on the left display the evolution in merger fraction with cutoff rank for both samples, separated by applied combination method. From top to bottom the individual panels show the average, Borda count, and Schulze method. The two plots on the right present the three methods combined for the two respective samples (AGN sample in blue in the upper plot, comparison sample in red in the lower panel).

for the three combination methods between ranks 20 and 40 emphasize two facts: First, there is a very good overall agreement between the individual rankings with respect to the classification of targets into merging galaxy and undisturbed systems. Otherwise, one would detect slightly different merger fractions over the entire evaluated cutoff rank range, as it is the case for ranks $\gtrsim 38$ for the AGN merger fractions. However, these slight deviations are simply explained by the fact that each expert ranks the inconspicuous galaxies marginally differently, since they do not exhibit any noticeable merger features. As a consequence, the different algorithms of the three combination methods provide slightly different results. Second, this already implies that - even without visual examination of the objects - the cutoff rank must lie between ranks 20 and 40. Therefore, the initial choice of cutoff rank is well suited, as it places the separator in a

range where the merger fractions are indeed identical, confirming that the choice of combination method does not affect the final results. In addition, it should be noted that for the inactive galaxies, a cutoff rank at position 50 corresponds to a merger fraction of $\sim 50\%$, a value that has not been found in any observation or simulation that studies cosmic merger rates for the general galaxy population. Since the determined merger fractions are insensitive to the combination method or cutoff rank, pure Poisson noise is considered the dominant source of uncertainty. Under this assumption, the cumulative distribution function provides a $\sim 99.4\%$ confidence for the absolute merger fraction of the AGN sample being $\leq 50\%$.

4.2.2. Morphological Sample Comparison

Since the two samples are randomly selected, it can be assumed that the morphologies of the inactive and AGN host galaxies are equally distributed. To test this hypothesis and to determine the fraction of disk-dominated host galaxies, the mean Sérsic indices $\langle n \rangle$ are derived by averaging over each of the individual Sérsic profile fits of the AGN host galaxies and control galaxies recovered by PSFMC. Both samples reveal almost identical values for the mean Sérsic indices, with the AGN host galaxies and inactive galaxies yielding $\langle n_{\mathrm{AGN}} \rangle = 5.42 \pm 3.46$ and $\langle n_{\mathrm{Ina}} \rangle = 5.24 \pm 3.2$, respectively. Assuming that the galaxies are only either disk- or bulge-dominated, one can again use the beta distribution (see Section 4.2) to infer the corresponding fractions and their uncertainties. Using a Sérsic index of $n = 2.5$ (Shen et al. 2003) to distinguish galaxies into disk or bulge-dominated objects yields fractions of disk-dominated sources of $f_{\mathrm{disk,AGN}} = 0.29 \pm 0.10$ and $f_{\mathrm{disk,Ina}} = 0.22 \pm 0.04$ for the AGN sample and the comparison sample, respectively. While these absolute estimates should be treated with caution, since only a single Sérsic profile is used to describe each galaxy, the relative difference in the fractions of the AGN sample and the comparison sample is representative, since both samples are fitted using the same approach. Although the ratio of the total numbers of the two samples is almost 1:5, a subsequent two-sample Kolmogorov-Smirnov (KS) test with a resulting $p = 0.62$ supports the assumption that both samples are drawn from the same parent distribution.

The statistically identical fractions of disk-dominated galaxies are another argument against the merger scenario, since one would expect a smaller fraction of disk-like AGN host galaxies due to the merger process. The results are consistent with those of Georgakakis et al. (2009), who found that at $z \simeq 1$ relative to the total AGN space density and to the total luminosity density, $30 \pm 9\%$ and $23 \pm 6\%$ of AGN host galaxies are dominated by a disk-like structure, respectively. Nevertheless, the high percentage ($\sim 80\%$) of disk-like host galaxies that Schawinski et al. (2011) describe for their intermediate-luminosity AGN sample at $z \sim 2$ cannot be reproduced. Still,

when performing a two-sample KS test, they also found no difference between the distributions of the Sérsic indices of their AGN sample and the matching comparison sample.

Since it is a primary proxy for galaxy mass, the fitted magnitudes of the Sérsic components returned by the modeling process are also examined. Although this parameter should be treated with caution, since the primary goal of including this component was to avoid an over-subtraction by the point source, the average Sérsic magnitudes for the AGN sample and the inactive galaxies are in excellent agreement. Quantitatively, these yield $m_{\mathrm{Sérsic,AGN}} = 21.4 \pm 0.6$ mag and $m_{\mathrm{Sérsic,Ina}} = 21.7 \pm 0.6$ mag, respectively. This consistent result verifies that both samples are indeed well matched in stellar mass (see also the following section).

4.2.3. Impact of Stellar Mass and Eddington Ratio

To rule out any impact of the initial selection in stellar mass on the results, the calculations are repeated with a mass-constrained subsample of the comparison galaxies, with the mass range narrowed down to $10.4 < \log(M_\star/\mathrm{M}_\odot) < 11.5$. Such a mass range corresponds to the range of stellar masses of the AGN host galaxies, if any uncertainties in the BH mass estimates are not considered when applying the scaling relation presented in Section 4.1.2. This approach reduces the number of inactive galaxies by 18, discarding 14 galaxies with lower masses and four with higher masses.

By applying the same cuts with respect to the number of flags (see Section 4.2) and an identical cutoff rank at 22, the merger fractions for the AGN sample remain unchanged, while the fraction for the comparison galaxies increases to $f_{\mathrm{m,\,Ina}} = 0.23 \pm 0.05$. This value can now be assumed to be identical to the value derived for the AGN sample and could be explained in two ways: Since 14 of the 18 excluded galaxies are at the low-mass end, their surface brightnesses and S/N are correspondingly lower, making the detection of merger features more difficult. In addition, due to their apparently smaller size, they are also more affected by the point source subtraction, which only increases the probability of misclassification.

However, excluding these galaxies also changes the overall rankings, which in turn means that it is essential to quantify how many of these sources were actually in the merger bin, i.e. above a cutoff rank of 22. For the averaging approach and the Schulze method, the number of galaxies equals four, while only two are considered merging when considering the consensus ranking compiled via Borda counts. Adjusting the total cutoff rank accordingly, i.e. lowering it by 3 to arrive at a cutoff rank at position 19, the resulting merger fraction for the inactive galaxies yields $f_{\mathrm{m,\,Ina}} = 0.19 \pm 0.05$. This number is consistent with the initial result for the merger fraction of the comparison sample, leading to the conclusion that there is only an insignificant dependence of the merger fraction on stellar mass.

An additional test examines whether the merger fraction depends on the Eddington ratio by splitting the AGN sample into two subsets. The cut is made at $\lambda_{\mathrm{Edd}} = 1$, which, except for one source, corresponds to a separation at $\dot{M} = 10\mathrm{M}_{\odot}\mathrm{yr}^{-1}$. Coincidentally, this bisects the sample, with 10 AGN having an Eddington ratio $\lambda_{\mathrm{Edd}} < 1$. If major mergers are indeed responsible for transporting large gas masses to the center and therefore supporting such high accretion rates, a majority of the five AGN host galaxies that have been classified as mergers should also belong to the subset that shows accretion rates $\dot{M} > 10\mathrm{M}_{\odot}\mathrm{yr}^{-1}$. However, only two of these five host galaxies are above this threshold, while in contrast the five AGN with the highest absolute accretion rates are classified as non-disturbed. Nevertheless, it is noted at this point that neither the sample size is actually statistically representative, nor different merger stages are taken into account.

Since it is also very likely that some unperturbed sources are identified as mergers and vice versa, the absolute values of the merger fractions should be treated with caution. However, assuming that a misclassification bias applies equally to both samples, the relative differences can be examined without restriction. With a ratio of $f_{\mathrm{m,\,AGN}}/f_{\mathrm{m,\,Ina}} = 1.26 \pm 0.43$, the AGN merger fractions show a slight enhancement. Nonetheless, this result is not significantly different from unity and, combined with the finding that the AGN merger fraction is most probably well below 50% and the lack of a trend of merger features with accretion rate, this leads to the conclusion that major mergers are not predominantly responsible for the triggering and growth of SMBHs with the highest specific accretion rates at $z \simeq 2$.

4.3. Potential Caveats and the Connection to Compact Galaxies

4.3.1. Undetectable Merger Features: Time Lag and Offset AGN

A caveat often discussed is a possible time lag between a major merger process and the putative onset of AGN activity. Such a discrepancy would wash out all merger features before the AGN can be detected, implying that the AGN may have been triggered by the gravitational encounter but is obscured as long as the features of a merger are still visible.

However, considering recent observations and simulations one can argue against this point. The usual lifetimes of AGN is described to be $10^6 - 10^8$ yr (Martini 2004; Hopkins et al. 2005; Shen et al. 2007; Hopkins & Hernquist 2009; Conroy & White 2013; Cen & Safarzadeh 2015) with 50-75% of this period – which is inversely correlated with X-ray luminosity – spent in an obscured state (Gilli et al. 2007). In contrast, other recent observations show that the visibility of the features of a major merger is on the order of $10^8 - 10^9$ yr (Conselice 2006; Lotz et al. 2008b; Ji et al. 2014; Solanes et al. 2018).

As a result, even for the longest-lived AGN with maximum obscuration and a minimum lifetime for the merger features, there is an overlap of at least a few 10^7 yr in which the AGN phase and galaxy distortions are visible simultaneously. It is reasonable to expect that this conservative estimate also applies to host galaxies with lower masses and thus shorter merger timescales.

For the AGN sample of this work, with eminently high bolometric luminosities and large host galaxy masses, an AGN lifetime of $t_{\mathrm{AGN}} = 10^8$ yr is assumed, with the AGN spending 50% of this period in an obscured state. The merger timescale is considered to be $t_{\mathrm{m}} = 10^9$ yr. Even with a delay of 200 – 300 Myr between the merger and the onset of the AGN phase (Hopkins et al. 2006b; Wild et al. 2010), such conditions result in an overlap in visibility of at least 500 Myr for the selected sample of AGN. Additionally, as noted above, instead of observing comparable fractions of disk-dominated galaxies in both samples, one would expect an increase in bulge-dominated galaxies for the AGN host galaxy sample, as they would have undergone a higher number of major mergers.

As a test to detect possible post-merger features, analyses of the elliptical isophotes (Astropy Collaboration et al. 2013, 2018; Bradley et al. 2019) of the AGN host galaxies as well as the point source-subtracted inactive galaxies are performed followed by a comparison of the resulting centroid positions with the corresponding point source positions returned by the modeling process. To determine the latter, Gaussian functions are fitted to the posterior probability distributions of the *x* and *y* positions of the point source. The mean values of the respective Gaussian distributions are then used as the corresponding positions of the modeled point sources. For the comparison, the mean of the absolute radial distances between the modeled point source coordinates and the central positions determined by the outer isophotes are now calculated for both samples, i.e. $\langle r \rangle_{\mathrm{dist,\,AGN}}$ for the AGN host galaxies and $\langle r \rangle_{\mathrm{dist,\,Ina}}$ for the comparison sample.

In the case of an increased fraction of major merger events for the AGN sample, $\langle r \rangle_{\mathrm{dist,\,AGN}}$ would be expected to be larger than $\langle r \rangle_{\mathrm{dist,\,Ina}}$ due to possible merger-induced shifts between the AGN positions and the actual flux centers of the underlying host galaxies. For a robust measurement of the central positions, the elliptic isophotes are fitted out to ∼15 kpc. It is then visually verified that the central *x* and *y* coordinates remain constant within the last measurements. In all cases, the coordinates converged to their final value as early as ∼5 kpc. Additionally, sigma clipping is applied to account for any nearby sources.

The resulting average radial distance for the AGN is $\langle r \rangle_{\mathrm{dist,\,AGN}} = 0.4 \pm 0.2$ kpc, while the analysis for the comparison sample yields $\langle r \rangle_{\mathrm{dist,\,Ina}} = 0.5 \pm 0.2$ kpc. Figure 4.6 shows the corresponding distributions of radial distances for the AGN and control samples in blue and red, respectively. To allow a direct comparison, both histograms are normalized to their maximum amplitude and the solid lines represent the mean radial distances referred to above.

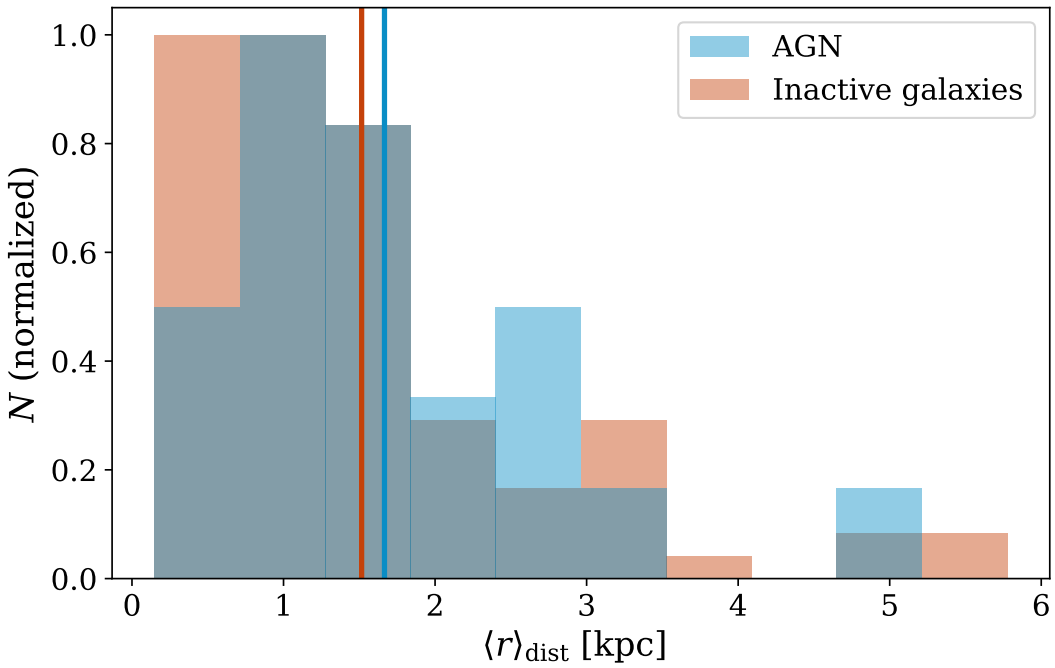

Figure 4.6.: Distributions of the radial distances in kpc between the centroid positions of the elliptic isophotes and the point source coordinates from the models. The blue and red histograms show the AGN sample and the comparison sample of inactive galaxies, respectively. Both histograms are normalized to the total number of sources in the sample, N/N_{max}. The solid lines in the corresponding colors denote the mean radial distances for $\langle r \rangle_{\mathrm{dist,\,AGN}}$ and $\langle r \rangle_{\mathrm{dist,\,Ina}}$.

Considering that for the inactive galaxies the synthetic point sources are added at the position of the flux-weighted centers of each galaxy, one might expect $\langle r \rangle_{\mathrm{dist,\,Ina}} = 0$ in the perfect case. However, the analyses of the isophotes are performed on images after subtracting the point sources - a process that introduces inevitable residual artifacts. The distribution of distances for the inactive galaxies therefore represents the error for this measurement. The results suggest that, on average and within the error introduced by the point source subtraction, the AGN sample shows no evidence of distinct nuclear offsets, since $\langle r \rangle_{\mathrm{dist,\,AGN}} \sim \langle r \rangle_{\mathrm{dist,\,Ina}}$. Therefore, within the resolution limit, this test also yields no enhancement of merger events for the AGN sample.

4.3.2. Intermittent AGN Activity

In contrast to the scenario described in the previous section, where the AGN lifetime appears longer compared to the observability of the merger features, the other extreme case and its

impact on the merger fractions should also be considered. In this sequence of events, there is a merger-induced AGN phase with clearly visible merger features, but no AGN is detectable since the accretion is suspended. Such an approach would resolve the contradictory findings regarding a possible connection between major mergers and AGN and is presented in Goulding et al. (2018). They explain the inconclusive results presented by the previous studies[3] by suggesting that these findings are dependent on the stage of the merger and a directly resulting AGN variability. During the close passages of the galaxies, the resulting torques are sufficient to feed the AGN, but as the separation increases, the AGN activity also subsides. As a result, the tidal features are still visible, but the central SMBH is not fueled sufficiently to be active and is only re-ignited during later passes. This implies that in this scenario some of the inactive sources classified as merging actually host an active but intermittent AGN. That is, the SMBH currently appears or is indeed inactive, but has already had a period of high accretion and will reach such high accretion rates again in the future, which would then place it within the selection limits of the AGN sample. In the following, the term "intermittent" is used to describe this particular subpopulation of AGN.

Thus, having estimated the number of AGN misclassified as unperturbed and their effect on the merger fraction in the previous section, the number of merging inactive galaxies that host an intermittent AGN and are therefore misclassified as inactive should now be determined. To quantify this aspect in terms of expected limits and to investigate dependencies, the fraction of merging inactive galaxies currently hosting such an AGN, $f_{\mathrm{m,\,Ina\,\&\,AGN}}$, is expressed by

$$f_{\mathrm{m,\,Ina\,\&\,AGN}} = f_{\mathrm{AGN}} \times f_{\mathrm{m,\,AGN}} \times \frac{t_{\mathrm{m}}}{t_{\mathrm{AGN}}}. \tag{4.1}$$

Here, f_{AGN} describes the fraction of sources with accretion rates $\geq 70\%$ of the Eddington accretion rate during a single major merger event with respect to the overall galaxy population in the same redshift and mass range. Accordingly, t_{AGN} represents the cumulative period of a source accreting above this threshold in accretion rate. The merger fraction of the AGN subpopulation is given by $f_{\mathrm{m,\,AGN}}$, and finally the parameter t_{m} describes the duration in which merger features are distinctly visible.

The value of the parameter f_{AGN} is constrained by the logarithmic number densities of the total galaxy population and the AGN with comparable Eddington ratios at $z \simeq 2$. For the AGN, a representative value of $\log(\Phi) = -6.2$ Mpc^{-3} mag^{-1} is adopted by taking the mean I-band magnitude of the AGN sample (see Table 4.1), which yields $m_I = -27.0$ mag, and using the *i*-band quasar luminosity function published by Ross et al. (2013). To derive a comparable number density for the total galaxy population at $z \simeq 2$ and suitable for the selected mass range, the stellar mass function presented in Henriques et al. (2015) is used. With the mean stellar

[3] see Section 1.4

host mass from the BH mass estimates (see Section 4.1.2), the logarithmic number density yields $\log(\Phi) = -3.4^{+0.1}_{-0.2}$ Mpc^{-3} mag^{-1}. Taking finally the ratio of the two number densities, the result is $f_{\mathrm{AGN}} = 1.6 \times 10^{-3}$. To account for the scatter in the BH masses and hence the uncertainty in the stellar masses, the analysis is repeated with $f_{\mathrm{AGN}} = 10^{-3}$ and $f_{\mathrm{AGN}} = 2 \times 10^{-3}$, derived from the lower and upper limit of the number density of the general galaxy population. It should be noted, however, that the uncertainties introduced by the use of different stellar mass functions (Conselice et al. 2016, and references therein) are not quantified.

For $f_{\mathrm{m,\,AGN}}$ the derived value of $f_{\mathrm{m,\,AGN}}$=0.24 $\pm$ 0.09 is used, but the calculations are also reiterated for $f_{\mathrm{m,\,AGN}}$ = {0.10, 0.40, 0.50, 0.60, 0.70}. The assumed values for t_{m} are $t_{\mathrm{m}} = 10^8$ yr and $t_{\mathrm{m}} = 10^9$ yr. As with f_{AGN}, $f_{\mathrm{m,\,Ina\,\&\,AGN}}$ refers to the total galaxy population in the same redshift and stellar mass range. The upper limit of $f_{\mathrm{m,\,Ina\,\&\,AGN}}$ is identical to the determined merger fraction of inactive galaxies, $f_{\mathrm{m,\,Ina}} \simeq 0.2$, which would imply that 100% of the inactive galaxies currently undergoing a detectable major merger actually host an intermittent AGN. Conversely, $f_{\mathrm{m,\,Ina\,\&\,AGN}} = 0.0$ would be the lower limit and would correspond to the nonexistence of intermittent AGN.

Figure 4.7 presents the results of the calculation for different $f_{\mathrm{m,\,AGN}}$ with $f_{\mathrm{AGN}} = 1.6 \times 10^{-3}$ and $t_{\mathrm{m}} = 10^8$ yr. The lower *x*-axis displays the total time t_{AGN} of a source accreting with $\lambda_{\mathrm{Edd}} \geq 0.7$, while the upper abscissa shows the merger time scale normalized over this characteristic AGN timescale, $t_{\mathrm{m}}/t_{\mathrm{AGN}}$. The *y*-axes depict the total fraction of inactive, merging galaxies hosting an intermittent AGN $f_{\mathrm{m,\,Ina\,\&\,AGN}}$, as well as this parameter normalized to the total subpopulation of inactive merging galaxies, $f_{\mathrm{m,\,Ina\,\&\,AGN}}/f_{\mathrm{m,\,Ina}}$. The solid blue line illustrates the evolution for the AGN merger fraction presented in this work, $f_{\mathrm{m,\,AGN}} = 0.24$, while the blue shaded region displays the 1σ interval. The dashed lines, ranging from purple to black, correspond to the values for $f_{\mathrm{m,\,AGN}}$ mentioned above.

Clearly visible is a trend of increasing $f_{\mathrm{m,\,Ina\,\&\,AGN}}$ with decreasing t_{AGN}. This is not surprising, since a higher fraction of intermittent and thus hidden AGN requires shorter AGN timescales. For a constant t_{AGN}, $f_{\mathrm{m,\,Ina\,\&\,AGN}}$ grows with increasing $f_{\mathrm{m,\,AGN}}$. This behaviour is also to be expected, since a higher number of AGN allows for a higher number of intermittent AGN. Conversely, for the reported value of $f_{\mathrm{m,\,AGN}}$ = 0.24, the cumulative time scale limits lie in the range of $2 \times 10^5 \lesssim t_{\mathrm{AGN}}[\mathrm{yr}] \lesssim 4 \times 10^6$ for $0.20 \geq f_{\mathrm{m,\,Ina\,\&\,AGN}} \geq 0.01$.

Considering now, in addition to $f_{\mathrm{m,\,AGN}}$ = 0.24 $\pm$ 0.09 and $f_{\mathrm{AGN}} = 1.6 \times 10^{-3}$, a rather short AGN timescale of $t_{\mathrm{AGN}} = 10^6$ yr, corresponding to 1% of the merger time (or 0.1% for $t_{\mathrm{m}} = 10^9$), this assumption yields a fraction of inactive, merging galaxies that host an intermittent AGN of $f_{\mathrm{m,\,Ina\,\&\,AGN}} = 0.04^{+0.01}_{-0.02}$. This result implies that only approximately 20% of the comparison galaxies that display distinct merger features host an intermittent AGN, which is currently

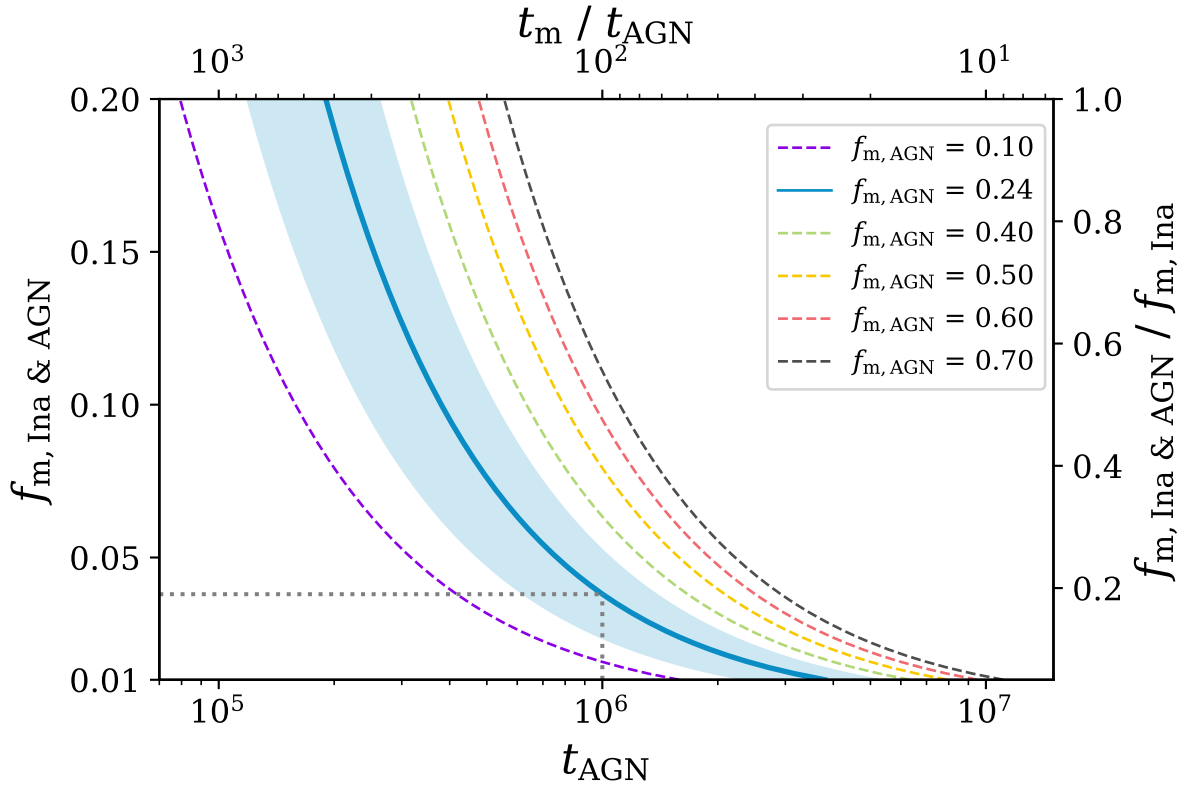

Figure 4.7.: Fraction $f_{\mathrm{m,\,Ina\,\&\,AGN}}$ of inactive galaxies with distinct merger features that host an intermittent AGN (see the text for a definition) versus the cumulative time t_{AGN} that an AGN is accreting above 70% of the Eddington accretion rate. The secondary axes present the merger visibility time t_{m} as multiples of t_{AGN}, and $f_{\mathrm{m,\,Ina\,\&\,AGN}}$ normalized to the total fraction of inactive merging galaxies $f_{\mathrm{m,\,Ina}}$. The solid blue line, as well as the shaded region show the results for AGN merger fraction determined in this work, $f_{\mathrm{m,\,AGN}} = 0.24 \pm 0.09$. The dashed lines correspond to $f_{\mathrm{m,\,AGN}} = \{0.10, 0.40, 0.50, 0.60, 0.70\}$.

undetectable. For reference, Figure 4.7 displays the estimated $t_{\mathrm{AGN}} = 10^6$ yr and the resulting $f_{\mathrm{m,\,Ina\,\&\,AGN}} \simeq 0.04$ via the dotted gray lines.

Unfortunately, to date, there are no detailed simulations that could model specific accretion rate histories and thus put a hard constraint on t_{AGN}. Accordingly, one must resort to small-scale simulations that trace the growth of SMBHs in a more global context (Di Matteo et al. 2005; Johansson et al. 2009a,b; Hopkins & Quataert 2010; Jung et al. 2018). The assumed cumulative time scale of $t_{\mathrm{AGN}} = 10^6$ yr for a BH that accretes at more than 70% of the Eddington accretion rate lies within the uncertainties provided by such simulations, but at the lower end of the expected value (see also Section 4.3.1). Assuming an AGN timescale that is an order of magnitude larger – i.e. $t_{\mathrm{AGN}} = 10^7$ yr – already results in a fraction of inactive merging galaxies

hosting an intermittent AGN that converges to zero, independent of the AGN merger fraction $f_{\mathrm{m,\,AGN}}$.

To be consistent with the theory proposed in Goulding et al. (2018), and if therefore a significant part of the merging inactive galaxies should host an AGN at some point during the merger process (i.e. $f_{\mathrm{m,\,Ina\,\&\,AGN}} \sim 0.20$), the ratio of $t_{\mathrm{AGN}}/t_{\mathrm{m}}$ would need to be a factor of 5-10 smaller, with the exact value depending on f_{AGN} and assuming the derived value for $f_{\mathrm{m,\,AGN}}$ is correct. This would result in relatively short and therefore rather improbable AGN timescales of $1.2 \times 10^5 \lesssim t_{\mathrm{AGN}}[\mathrm{yr}] \lesssim 2.4 \times 10^5$. However, to better constrain these estimates from a physical point of view, more detailed measurements and in particular, simulations of merger timescales, accretion rates, AGN populations and AGN populations classified by their accretion rates are essential.

4.3.3. Testing the Prevalence of Compact Galaxies Hosting AGN

In recent years, several studies have found that post-starburst galaxies are small and often show evidence of a recent merger in the form of tidal tails and distortions (Pawlik et al. 2016; Wild et al. 2016; Almaini et al. 2017). It is reasonable to assume that this particular population of galaxies is more prone to host AGN, with the feedback from an active SMBH possibly being the dominant process to quench the increased star formation. The validity of this theory can be tested by comparing the number densities of such galaxies and AGN, which are the focus of this work, and deriving the resulting AGN timescale.

For the AGN, the same number density as presented in Section 4.3.2 is assumed, i.e. $\log(\Phi) = -6.2\,\mathrm{Mpc}^{-3}\mathrm{mag}^{-1}$ (Ross et al. 2013). The corresponding number density for post-starburst galaxies at $z \simeq 2$ and in a suitable stellar mass range yields $\log(\Phi) = -4.4\,\mathrm{Mpc}^{-3}\mathrm{mag}^{-1}$ (Wild et al. 2016). The evident difference of two orders of magnitudes increases when it is considered that not all AGN can be hosted in post-starburst galaxies or their progenitors, since AGN hosted in non-distorted or disk-dominated systems are clearly detected. This leads to an estimated overall difference in number density between the specific population of AGN and post-starburst galaxies by a factor of $2 - 4 \times 10^2$. That result, combined with an assumed visibility of post-starburst signatures of $10^9\mathrm{yr}$ (Wild et al. 2016), leads to a timescale of $\sim 2.5 - 5\,\mathrm{Myr}$, in which the AGN accretes above the threshold of 70% Eddington ratio. As described in the previous two subsections, such a short timescale seems improbable, implying that even in post-starburst galaxies, where AGN could understandably play a prominent role due to the obvious merger processes and the need to quench the enhanced star formation, active SMBHs still play only a minor role. Even if lower accretion rates of approximately a few percent of the Eddington ratio, and thus lower luminosities are considered, the corresponding number density and the resulting AGN timescale

would increase by only a factor of $\sim$3, still implying a very improbable lifetime for AGN with such or higher accretion rates.

In the context of compact galaxies, an attempt is also made to estimate the influence of such galaxies on the AGN merger fraction. In their study, Kocevski et al. (2017) show that AGN detected in X-ray at z $\simeq$ 2 are most abundant in compact star-forming galaxies, which have on average effective radii of $r_e \sim 1$ kpc. It could be argued that this small size makes it impossible to resolve these sources and thus detect unique merger features. Ultimately, this would imply an underestimation of the merger fraction for the AGN host galaxies. Unfortunately, at the current state of research focusing on this particular type of galaxy, quantified estimates of the fraction of these objects with respect to the total galaxy population at the redshift and, in particular, mass range studied in this work are difficult. Therefore, a possible impact on the recovered AGN merger fraction cannot be unambiguously quantified.

However, considering the best available estimates of the number densities for compact star-forming galaxies at $z \simeq 2$ (van der Wel et al. 2014; van Dokkum et al. 2015), it is unlikely that a significant fraction of AGN is hosted in such galaxies. This leads to the conclusion that the fraction of AGN host galaxy mergers, if not unchanged, is well below $f_{\mathrm{m,\,AGN}} = 0.5$, implying that major mergers are not the dominant mechanism for triggering AGN. Furthermore, even if AGN are mainly hosted by compact galaxies, the overall result would not change significantly, since only the possible presence of large-scale merger signatures, which can extend to sizes of several effective radii, is considered. Finally, such features could also stem from the companion galaxy, which may not necessarily be compact, further mitigating the effect of a potential compact AGN host galaxy.

5. The Role of Mergers in a Cosmological Simulation

Simulated galaxies from TNG300, which is part of the collection of cosmological simulations in IllustrisTNG (Springel et al. 2018; Pillepich et al. 2018a; Nelson et al. 2018, 2019b; Naiman et al. 2018; Marinacci et al. 2018), are used to verify the results presented in Chapter 4. Finding consistent merger fractions would dismiss the often voiced caveat that the results are the consequence of observational limitations, such as merger features that are too faint to detect or that are hidden behind the (subtracted) PSF features. Using mock images of the modeled galaxies similar to the observations at $z \simeq 2$, a comparable population of highly accreting AGN and a selection of inactive control galaxies are examined. This allows

- to examine the merger fractions of both samples within the simulation using the same visual classification approach as in the observational studies,

- to compare the derived absolute merger fractions and the relative difference with the results from the observational study at $z \simeq 2$, and

- to verify the method of deriving the merger fractions by visually classifying the galaxy morphologies by (a) analyzing the true merger histories provided by the simulation, given that the full merger trees are available for each galaxy, and (b) automatically determining the key parameters of the galaxy morphologies using the software package statmorph (Rodriguez-Gomez et al. 2019), a tool to automatically determine the morphology of a galaxy.

To test a trend of significance of (major) mergers with the BH mass, two additional samples each of AGN and inactive control galaxies are selected. Furthermore, the analysis includes an investigation of the influence due to the selection, possible different AGN or galaxy populations, and the resolution limit of the simulation.

5.1. Data

5.1.1. IllustrisTNG

The IllustrisTNG[1] project (Springel et al. 2018; Pillepich et al. 2018a; Nelson et al. 2018, 2019a; Naiman et al. 2018; Marinacci et al. 2018) describes a suite of magneto-hydrodynamical cosmological simulations with different resolutions and volumes and is the direct successor of the successful Illustris[2] project (Genel et al. 2014; Vogelsberger et al. 2014b,a; Sijacki et al. 2015). Based on the AREPO code (Springel 2010; Pakmor & Springel 2013), numerous observed results over a wide redshift range have been reproduced, such as the relations of BH mass versus stellar mass (at $z = 0$) (Weinberger et al. 2018), the gas phase mass versus metallicity (Torrey et al. 2019), the bimodality of galaxy color (Nelson et al. 2018), or the optical morphologies of the local galaxy population (Rodriguez-Gomez et al. 2019). The series of simulations consists of three publicly available main installments, TNG50, TNG100, and TNG300[3]. The respective designations refer to the approximate side length of the corresponding modeled volume in comoving Mpc. For each of these simulation boxes, three to four runs have been realized at different resolutions. Table 5.1 lists the key parameters for each of the three versions with the highest resolution. The cosmology adopted in IllustrisTNG and used throughout this chapter is based on the results presented by the Planck Collaboration et al. (2016), with $\Omega_\lambda = 0.6911$, $\Omega_\mathrm{m} = 0.3089$, $\Omega_\mathrm{b} = 0.0486$ and $H_0 = 67.74\,\mathrm{km\ sec^{-1}Mpc^{-1}}$.

The Friends-of-Friends (Davis et al. 1985) and Subfind (Springel et al. 2001; Dolag et al. 2009) algorithms are used to identify the halos and subsequently the subhalos they contain, where the latter correspond to galaxies in real observations. The most detailed runs of TNG100 and TNG50 yield $\sim 4.3 \times 10^6$ and $\sim 5.7 \times 10^6$ subhalos at $z = 0$, respectively. In contrast, the TNG300 realization with the highest resolution contains $\sim 1.4 \times 10^7$ subhalos at $z = 0$. At $z \simeq 2$, these numbers increase to $\sim 5.6 \times 10^6$ and $\sim 1.9 \times 10^7$ for TNG100 and TNG300, respectively. Considering the comparatively large range in redshift ($1.8 \leq z \leq 2.2$) chosen to select suitable AGN in the observational study, TNG300 is adopted for the following analysis because this simulation provides the box with the largest volume. Nevertheless, it should be noted that this simulated volume is still smaller by a factor of $\sim 10^3$.

[1] https://www.tng-project.org/
[2] https://www.illustris-project.org/
[3] While TNG100 and TNG300 have already been released in December 2018, TNG50 is only available since February 2021.

Run name	Volume [Mpc^3] (1)	$L_{\rm box}$ [Mpc/h] (2)	$N_{\rm Gas}$ (3)	$N_{\rm DM}$ (4)	$m_{\rm baryon}$ [$\mathrm{M}_\odot/h$] (5)	$m_{\rm baryon}$ [$10^6\mathrm{M}_\odot$] (6)	$m_{\rm DM}$ [$\mathrm{M}_\odot/h$] (7)	$m_{\rm DM}$ [$10^6\mathrm{M}_\odot$] (8)
TNG50	51.7^3	35	2160^3	2160^3	5.7×10^4	0.08	3.1×10^5	0.45
TNG100	106.5^3	75	1820^3	1820^3	9.4×10^5	1.4	5.1×10^6	7.5
TNG300	302.6^3	205	2500^3	2500^3	7.6×10^6	11.0	4.0×10^7	59.0

Table 5.1.: Key characteristics of the three main IllustrisTNG runs. The parameters are the simulation's comoving volume and box side-length in columns (1) and (2), the number of initial gas and dark matter particles in columns (3) and (4), and the mean mass resolution of the baryons in columns (5) and (6) as well as of the dark matter particles in columns (7) and (8).

5.1.2. BHs in IllustrisTNG

Throughout the entire simulation run, each time a halo exceeds a mass of $7.38 \times 10^{10}\mathrm{M}_\odot$ and does not yet host a BH, a BH with a mass of $1.18 \times 10^6\mathrm{M}_\odot$ is seeded. Subsequently, these BHs grow according to an Eddington-limited Bondi-Hoyle accretion rate (Weinberger et al. 2018) described by

$$\dot{M} = \min(\dot{M}_{\rm Bondi}, \dot{M}_{\rm Edd}), \tag{5.1}$$

where the Bondi accretion rate $\dot{M}_{\rm Bondi}$ is defined as

$$\dot{M}_{\rm Bondi} = \frac{4\pi G^2 M_{\rm BH}^2 \rho}{c_{\rm s}^3} \tag{5.2}$$

and the Eddington accretion rate $\dot{M}_{\rm Edd}$ is given by

$$\dot{M}_{\rm Edd} = \frac{4\pi G M_{\rm BH}^2 m_{\rm p}}{\eta \sigma_{\rm T}}. \tag{5.3}$$

In the formulas above G represents the gravitational constant, $M_{\rm BH}$ the BH mass, ρ the local gas density, c_s the local sound speed of the gas, $m_{\rm p}$ the proton mass, $\sigma_{\rm T}$ the Thompson scattering cross section, and η the radiative efficiency, which is assumed to be $\eta = 0.2$[4]. The bolometric luminosity depends on the Eddington ratio $\lambda_{\rm Edd} = \dot{M}/\dot{M}_{\rm Edd}$ and accounts for a decreasing radiative efficiency at low accretion rates (Weinberger et al. 2018; Nelson et al. 2019a):

$$L_{\rm bol} = \begin{cases} \eta \dot{M} c^2, & \text{for } \lambda_{\rm Edd} \geq 0.1 \quad (5.4) \\ 10\lambda_{\rm Edd}^2 L_{\rm Edd} = 10\lambda_{\rm Edd}^2 \dot{M}_{\rm Edd} c^2, & \text{for } \lambda_{\rm Edd} < 0.1. \quad (5.5) \end{cases}$$

[4] Please note the difference with observational studies where $\eta = 0.1$ was used.

Due to the limited resolution inherent to cosmological simulations and other systematic effects, the BHs may drift away from the central position of the respective halos. In IllustrisTNG, this behavior is prevented by computing the minimum gravitational potential in a region around the BH that includes 1000 mass resolution elements. If it is not already at this location, the BH is then positioned at this potential minimum.

Depending on λ_{Edd}, the feedback from accreting SMBHs in IllustrisTNG is implemented twofold. As long as

$$\lambda_{\mathrm{Edd}} < \min\left[0.002\left(\frac{M_{\mathrm{BH}}}{10^8 \mathrm{M}_\odot}\right)^2, 0.1\right], \tag{5.6}$$

the feedback is periodically injected and directed as kinetic energy into the surrounding gas at the rate of $\dot{E}_{\mathrm{kin}} = \epsilon_{f,\mathrm{kin}} \dot{M} c^2$, where $\epsilon_{f,\mathrm{kin}} \leq 0.2$ is the gas density dependent coupling efficiency. Whenever λ_{Edd} exceeds this threshold, the feedback switches to the 'thermal mode' and energy is continuously injected via $\dot{E}_{\mathrm{therm}} = 0.02 \dot{M} c^2$. For more detailed information on the implementation of the formation, evolution, and feedback of BHs in IllustrisTNG, the reader may refer to the studies by Weinberger et al. (2017, 2018) and Nelson et al. (2019a).

5.1.3. Sample Selections

With a box length of ∼300 comoving Mpc, TNG300 provides a volume large enough to study the rarely occurring population of AGN with the highest Eddington ratios in a statistically meaningful way. At the same time, the resolution is still sufficiently high to resolve large-scale distortions and to allow a comparison with the observational study at $z \simeq 2$, especially considering that the focus is on massive galaxies with $M_\star \sim 10^{11} \mathrm{M}_\odot$. For the construction of an initial sample, all sources at $z = 2$ (corresponding to snapshot 33) and with BH masses $M_{\mathrm{BH}} \geq 10^7 \mathrm{M}_\odot$ and stellar masses $M_\star \geq 10^{9.3} \mathrm{M}_\odot$ are selected. This lower limit on the stellar mass is determined by applying the same scaling relation that has been used to derive the stellar host masses of the observed AGN (see Section 4.1.1). Based on the rather reasonable assumption that the most massive BHs are located in the centers of the galaxies, only the respective BH particles with the highest mass are considered for each subhalo, ignoring possible additional, less massive BH particles.

This initial selection yields about $\sim 1.6 \times 10^5$ sources. To account for the noise in the observed parameters, characteristic observational uncertainties that are based on the SDSS DR7 catalog of Shen et al. (2011) are added to the BH masses and Eddington ratios of the simulated sources. For this purpose, the uncertainties in these two parameters are first determined for the observed AGN that are part of the parent sample in Section 4.1.1 and hence lie in a redshift interval of $1.8 \leq z \leq 2.2$. For each of the simulated sources, a value is then drawn randomly from the

distribution of uncertainties which is then used to scale a normal distribution from which the final uncertainty is again drawn randomly. The resulting numbers then correspond to the uncertainties that are eventually added to the BH masses and Eddington ratios of the simulated subhalos.

To investigate any difference in merger incidence with BH mass, three AGN samples are defined by adopting consistently the same Eddington ratio interval but three different BH mass bins (Figure 5.1). The three BH mass bins in $\log[M_{\rm BH}/{\rm M}_\odot]$ are $[7, 7.75]$, $[7.75, 8.5]$ and $[8.5, 8.7]$. Adopting a lower cutoff in BH mass would gain no information as real observations are limited to BH masses of a similar value. In addition, a lower cutoff would get close to the seed mass of $1.18 \times 10^6 {\rm M}_\odot$. The boundaries of the highest mass bin are identical to the BH mass limits of the observational study that is presented in Chapter 4.

Identical to this investigation, a lower limit in the Eddington ratio is defined at $\lambda_{\rm Edd} = 0.7$. Since the Eddington ratio in ILLUSTRISTNG is initially constrained to $\lambda_{\rm Edd} = 1$ and to avoid the influence of statistical outliers caused by the addition of uncertainties, the Eddington ratio is also limited to an upper bound of $\lambda_{\rm Edd} = 10$. The three samples, ordered from low to high mass, receive the designations "Low Mass" (LM), "Intermediate Mass" (IM), and "High Eddington" (HE). The final number of sources within each sample is 2078, 722, and 44 for the LM, IM, and HE samples, respectively.

For comparison, three corresponding samples of inactive control galaxies within the same BH mass bins and an Eddington ratio interval of $10^{-4} \leq \lambda_{\rm Edd} \leq 10^{-3}$ are defined. The number of sources within the LM, IM, and HE samples are 146, 1126, and 1033, respectively. A summary of the selection process is shown in Figure 5.1. The blue points show the parent sample of the TNG300 sources after adding the uncertainties, while the gray and green points represent the parent sample of the SDSS DR7 sources and the AGN examined in Chapter 4. The three AGN and corresponding control samples are shown in orange (LM), red (IM), and purple (HE), respectively. Finally, the blue cross visualizes the median of the SDSS DR7 observational uncertainties in BH mass and Eddington ratio. The AGN and inactive galaxies in the HE subsamples serve as sources for the direct comparison with the samples studied in Chapter 4.

5.2. Determining the Merger Fractions

One of the advantages in dealing with simulated data is the fact that one can access the true (i.e. simulated) merger history. This allows to objectively determine whether a galaxy is part of a merger. If that is the case, the mass ratio of the two interacting galaxies can also be determined, and thus whether it is possibly a major or minor merger. This analysis is performed for all six samples (i.e. the three active plus the corresponding three inactive).

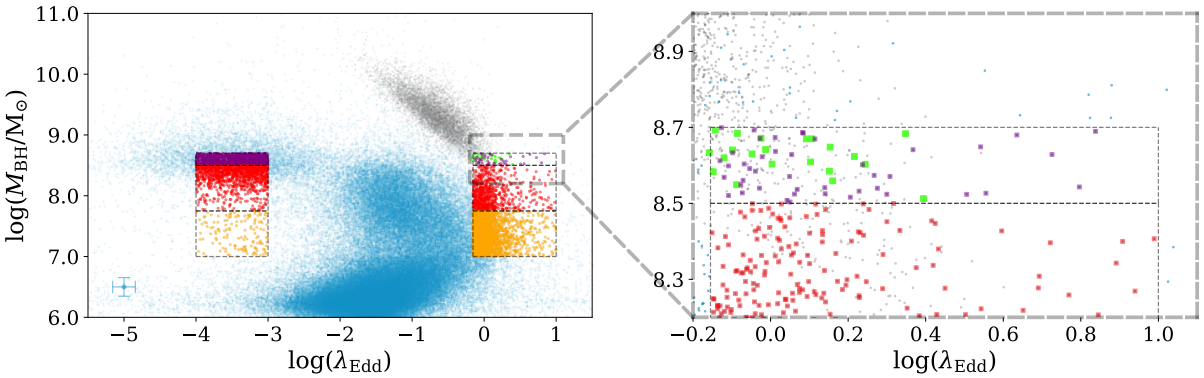

Figure 5.1.: Selection of the high Eddington (HE, violet), intermediate mass (IM, red) and low mass (LM, orange) AGN (right boxes) and control galaxies (left boxes). The AGN investigated in Chapter 4 are given in green. Shown as blue points are all TNG300 sources at $z = 2$ after applying uncertainties that are based on SDSS DR7 AGN observations at $1.8 < z < 2.2$ (grey points). The blue cross displays the median of the SDSS DR7 observational uncertainties in BH mass and Eddington ratio.

To provide a more detailed and direct comparison with the observational results, two additional techniques are used to find the merger fractions of the HE subsamples: The visual classification approach, as described in the previous Chapter 4 and in the following Section 5.2.3, and a method that uses an automatic determination of the morphological parameters. For both, synthetic images of the HE AGN host galaxies and the HE inactive galaxies are generated and analyzed. These synthetic images are created using the radiative transfer code SKIRT (Baes et al. 2011; Camps & Baes 2015, 2020) and the GALAXEV stellar population synthesis code (Bruzual & Charlot 2003) while following the recipe outlined in Rodriguez-Gomez et al. (2019). In addition to the stellar component and star-forming regions this approach takes the influence of dust attenuation and scattering into account. The randomly oriented output images are tuned to have the same S/N, pixel scale (0.″06/pixel), field of view, and filter band (*HST*/WFC3 F160W) as the observations. The publication of Rodriguez-Gomez et al. (2019) and the references therein provide more detailed information about the inner workings and implementation of the SKIRT and GALAXEV codes.

The results of this process are idealized images as if the objects had been observed with a point-like PSF (i.e. a Dirac delta function) and an infinite S/N. Therefore, to perfectly replicate the observations, Gaussian noise is added and the images are convolved with an appropriate PSF. To determine the background noise, the same observations from the CANDELS survey (Grogin et al. 2011; Koekemoer et al. 2011) of the objects that serve as control galaxies in Chapter 4 are used. In each image, the source is first masked, and then the individual background noise value σ_{bg} is determined. The median of the resulting distribution of these values is then

used to scale a Gaussian distribution from which a random value is drawn for each pixel of each of the synthesized images, which is finally added to the respective flux values. Finally, the simulated images are matched with the observations by randomly convolving each of the images with one of the eight PSFs used to model the point sources in the observational study. In Section 5.2.3, Figure 5.5 shows an example of the post-processing procedure and a comparison with the observations.

In all three approaches, the merger fractions and their uncertainties are calculated by determining the number of merging and undisturbed sources, a and b, and assuming a beta distribution.

5.2.1. Simulated Merger Histories

The use of simulations provides a complete access to the evolutionary path of a galaxy. This fact is exploited by examining the merger histories of all sources within the six samples. The merger histories for IllustrisTNG are generated analogously to the merger histories for its predecessor simulation Illustris by using the Sublink algorithm (Rodriguez-Gomez et al. 2015). The algorithm determines the descendant of a subhalo by analyzing the membership of all particles of that subhalo in the next snapshot. A merger is then defined by two subhalos having the same descendant. The main progenitor of any merger is the one with the most massive history (De Lucia & Blaizot 2007). Correspondingly, the main progenitor branch is then the branch that traces these main progenitors back in time.

All provided timescales since the last merger (250 Myr, 500 Myr, 1 Gyr, 2 Gyr) and stellar mass ratios, which are based on the stellar masses of the progenitor galaxies M_1 and M_2, are considered. A merging event classifies as a major merger when the mass ratio $M_2/M_1 > 1/4$. Any interaction with a mass ratio of $1/10 < M_2/M_1 \leq 1/4$ is categorized as a minor merger. Finally, the merger fractions are also determined by considering all mergers, regardless of mass ratio. To avoid an underestimation of the stellar mass of the secondary progenitor galaxy and thus of the mass ratio, and to allow for a valid comparison with observations, the mass ratio is determined at the time when the less massive progenitor galaxy reaches its maximum stellar mass (Rodriguez-Gomez et al. 2015).

It is important to be aware that the mass ratio categories are not exclusive, as a source can have both a major and minor merger within a chosen time period. Therefore, a galaxy could contribute simultaneously to the merger fractions for both major and minor mergers, regardless of the chosen combination of lookback times. This implies that the cumulative merger fraction for mergers in a mass range $M_2/M_1 > 1/10$ would not be the sum of the respective merger fractions for major and minor mergers for a given lookback time t_{lb} and sample of sources. To account for this effect, minor merger events occurring within the next 0.5 Gyr of a major merger

are neglected, as the potential impact of such mergers on SMBH growth within this period is expected to be comparatively insignificant (Steinborn et al. 2018). Furthermore, as of yet, only evidence of major mergers can be observed at $z \sim 2$. Since the observational comparison study focuses on such events and estimates the visibility of merger features (at $z \sim 2$) to be of the order of 1 Gyr, the merger fractions for this specific combination of merger category and t_{lb} are considered in particular.

For each combination of merger type and lookback time, the sources that have been part of a merger are counted and likewise the number of undisturbed sources are determined. These values then serve as parameters a and b for the calculations of the merger fractions. Figure 5.2 presents the results of this analysis. The top and bottom row of panels display the merger fractions and uncertainties for the AGN and control galaxies, respectively. Within each panel, from top to bottom the merger fractions are shown for major mergers, minor mergers and all mergers. From left to right, the columns represent the subsamples with decreasing BH mass. Considering major mergers, AGN host galaxies show an enhancement in merger fractions, independent of t_{lb} or subsample and thus the mean BH mass. However, with increasing t_{lb} and thus decreasing impact of the major merger event, this excess decreases. Compared to the observational result, the major merger fractions of the HE samples for $t_{\mathrm{lb}} = 1\,\mathrm{Gyr}$ show a larger relative difference, but are consistent when uncertainties are taken into account. The corresponding merger fractions are highlighted by a red square in Figure 5.2.

A similar result is found for the minor mergers. In particular, for $t_{\mathrm{lb}} = 500\,\mathrm{Myr}$ and $t_{\mathrm{lb}} = 1\,\mathrm{Gyr}$, a significant excess in the corresponding merger fractions for AGN host galaxies can be detected across all subsamples. For $t_{\mathrm{lb}} = 250\,\mathrm{Myr}$, this is only true for the two less massive subsamples, but not for the HE sample. Since higher BH masses also imply higher stellar mass within these systems, this suggests that minor mergers, unlike the more vigorous major mergers, have not yet had time to affect the SMBH in these more massive systems, but will eventually do so, since the HE sample also shows an excess for $250\,\mathrm{Myr} < t_{\mathrm{lb}} < 1\,\mathrm{Gyr}$. Considering mergers with any given mass ratio, at a lookback time of 250 Myr systems in the HE and LM bin, show a notable difference in the merger fractions, as do galaxies in the LM bin and a lookback time of 500 Myr.

To account for any selection bias that may have been introduced by applying the SDSS observational uncertainties to the BH mass and Eddington ratio, the random addition of uncertainties, sampling, and calculations are iterated 1000 times. The resulting merger fractions are then the average of the 1000 individual results. Similar to Figure 5.2, the results are presented in Figure 5.3. Although some of the individual absolute values have changed, they are within the uncertainties of the results based on the original single draw. Therefore, the general statements remain the same, although overall the relative differences in the respective pairs of merger

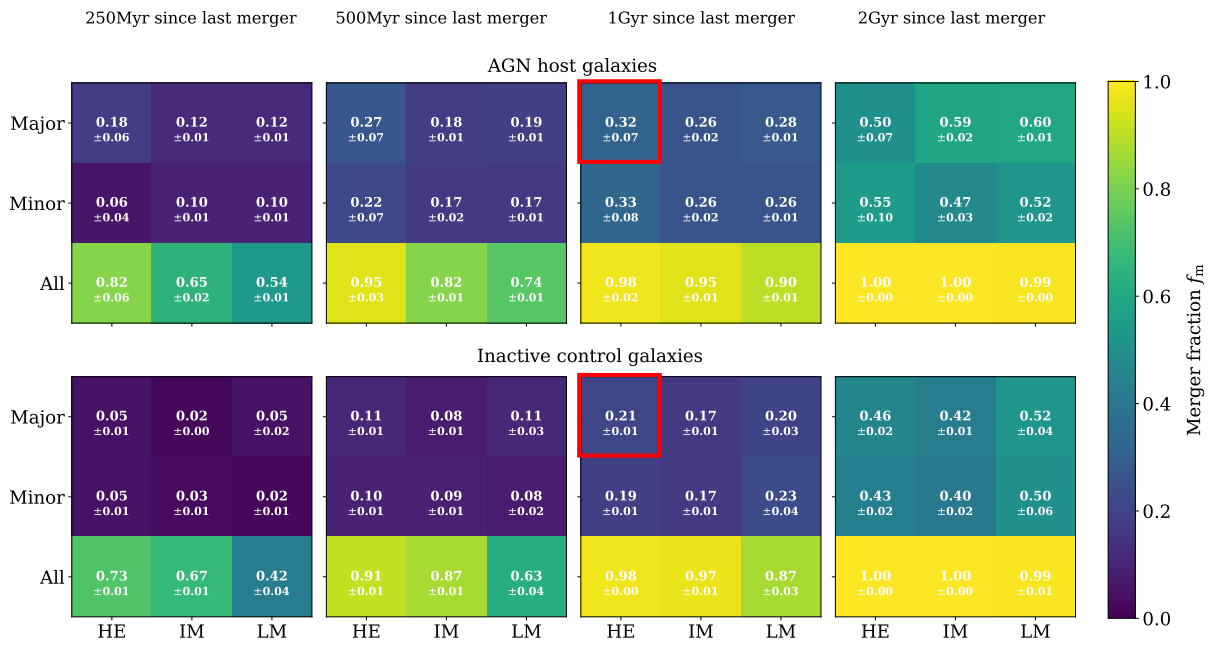

Figure 5.2.: Merger fractions for major, minor and all mergers for all the six samples and lookback times between 250 Myr and 2 Gyr. The top and lower panels show the merger fractions for the AGN host galaxies and inactive control galaxies, respectively. For guidance, the merger fractions of the combination that is best suited for a comparison with the observational results in Chapter 4 are highlighted: AGN with the highest Eddington rates or matching control sources, major mergers and a lookback time of 1 Gyr.

fractions have decreased. Regardless of the subsample or $t_{\rm lb}$, AGN host galaxies appear to have, at best, a slight excess in the major merger incidence. Again, the combination of $t_{\rm lb} = 1{\rm Gyr}$, major mergers, and HE samples is highlighted in Figure 5.3.

Also for minor mergers, the initial conclusions remain essentially unchanged. For $t_{\rm lb} = 500\,{\rm Myr}$ and $t_{\rm lb} = 1\,{\rm Gyr}$, the AGN hosts still show a slight excess in merger fraction. The same is true for the minor merger rates for a time of 250 Myr since the last merger. However, this time the sources in the HE AGN sample also show an increase for this $t_{\rm lb}$, although it should be noted that due to the corresponding uncertainty, the originally outlined scenario that minor mergers take their time to affect massive systems cannot be completely discarded. Considering all mergers, regardless of mass ratio, the calculations reveal no obvious relative difference for all $t_{\rm lb}$ and subsamples.

In summary, although there is on average a mild excess in AGN major merger fractions for all lookback times and subsamples, the results are still consistent with previous studies (see Section 7.2) and also with the observational study and its results. Also, the relative difference for a given $t_{\rm lb}$ is comparable among the subsamples, suggesting that there is no correlation of merger fractions with BH mass. Despite this slight increase in AGN merger rate, major mergers

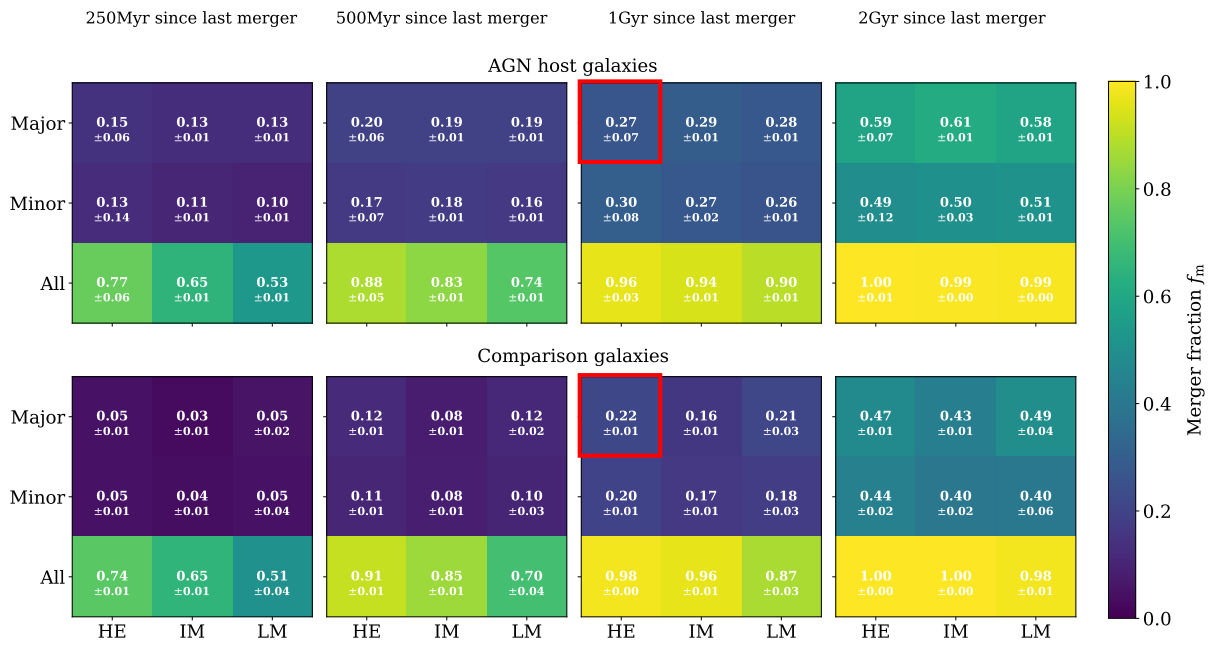

Figure 5.3.: Analogously to Figure 5.2 the merger fractions for all the combinations of merger type, lookback time and sample are shown. In contrast to Figure 5.2, the merger fractions are averaged over 1000 iterations of sample selection. Again, the merger fractions that are most suitable for comparison with the observational results at $z \simeq 2$ are highlighted.

still do not appear to be the dominant cause of SMBH growth, as simulated merger fractions are also well below 50%. Therefore, this confirms the conclusion of the observational study that even the particular subpopulation of AGN with the highest Eddington ratios at $z \simeq 2$ require alternative processes to be triggered. In fact, the ratio of the merger fractions best suited for a comparison with the observational study yield with $f_{\mathrm{m,\,AGN}}/f_{\mathrm{m,\,Ina}} = 1.23 \pm 0.39$ almost an identical result. For convenience, the interested reader will find a figure in Appendix C showing the relative differences in the merger fractions of AGN hosts and comparison galaxies, based on the iteratively sampled merger histories.

5.2.2. Non-parametric Diagnostics of Galaxy Morphology

Mock images are created exclusively for the HE subsamples to allow direct comparison with the observations by adopting the same visual classification approach to determine the merger fractions (see the following Section 5.2.3). In addition, the post-processed synthetic images of the two HE subsamples are classified using statmorph (Rodriguez-Gomez et al. 2019). This

python package[5] allows the computation of various parameters suited to assess the individual galaxy morphologies, such as Gini and M_{20} (Lotz et al. 2004) or concentration, asymmetry, and smoothness (CAS, Conselice 2003). In addition, the tool also creates and provides the parameters of a best-fit 2D Sérsic profile (Sérsic 1963, 1968; Graham & Driver 2005) and also determines the multimode intensity deviation statistic (MID, Freeman et al. 2013).

Similar to other tools that model observations, such as the widely used GALFIT, statmorph requires three input arguments: The actual (background subtracted) image, an associated segmentation map, and a weightmap or, if this is not provided, the value of the gain. Contrary to other solutions, the weightmap should store the standard deviation of each pixel value. Additionally, a mask as well as a PSF can be specified. While the former defines the pixels that will be excluded from the subsequent calculations, the latter is needed for the fitting of the Sérsic profile. After rejecting pixels whose flux values differ by more than 10σ, all the aforementioned morphological diagnostics are performed.

The positions of the sources in the $G-M_{20}$ space serve as a proxy to identify mergers (Lotz et al. 2004, 2008a). The Gini coefficient G essentially maps the uniformity of the surface brightness of a galaxy and is given by

$$G = \frac{1}{|\overline{f}|} n(n-1) \sum_{i=1}^{n} (2i - n - 1)|f_i|, \tag{5.7}$$

where n is the number of pixels that have the absolute flux values $|f_i|$, where $i = 1, 2, ..., n$, and $|\overline{f}|$ is the corresponding mean. The parameter M_{20} measures the second-order spatial moment of the brightest quintile of pixels and is normalised over the total spatial moment of a galaxy. It is defined as

$$M_{20} = \log_{10}\left(\frac{\sum_i M_i}{M_{\rm tot}}\right), \text{while } \sum_i f_i < 0.2 f_{\rm tot} \tag{5.8}$$

and

$$M_{\rm tot} = \sum_i^n M_i = \sum_i^n f_i \left[(x_i - x_c)^2 + (y_i - y_c)^2\right], \tag{5.9}$$

where x_i and y_i are the coordinates of the i-th pixel and (x_c, y_c) is the position of the galaxy's center where $M_{\rm tot}$ has its minimum.

These parameters and the approach have first been applied by Lotz et al. (2004) for low-redshift galaxies at $z < 0.25$. However, Lotz et al. (2008a) have updated the relation to be applicable also to galaxies at $0.2 < z < 1.2$ and Snyder et al. (2015) have successfully employed it to mock

[5] https://statmorph.readthedocs.io

images for galaxies from the original ILLUSTRIS simulation up to $z \sim 3$. Following these earlier studies, the two HE samples are split into late-type, early-type and merging sources by

$$S(G, M_{20}) = \begin{cases} \text{Mergers :} & G > -0.14M_{20} + 0.33 \\ \text{E/S0/Sa :} & G \leq -0.14M_{20} + 0.33, \text{and} \\ & G > 0.14M_{20} + 0.80 \\ \text{Sb/Sc/Sd/Irr :} & G \leq -0.14M_{20} + 0.33, \text{and} \\ & G \leq 0.14M_{20} + 0.80. \end{cases} \tag{5.10}$$

In Figure 5.4 the results of this classification are shown. The points represent the control galaxies, while the stars display the AGN. All sources are color-coded according to their shape asymmetry A_S. To derive this parameter, the same formula is used as for the asymmetry parameter A in the CAS system, which is simply the subtraction of a galaxy image rotated by 180° from the original image. It is given by

$$A = \frac{\sum_{i,j} |f_{ij} - f_{ij}^{180}|}{\sum_{i,j} |f_{ij}|} - A_{\text{bg}}, \tag{5.11}$$

where f_{ij} and f_{ij}^{180} are the pixel flux values of the original and rotated image, while A_{bg} is the mean asymmetry of the background. The only difference from A is that for A_S this calculation is performed on the corresponding segmentation map and not on the galaxy image itself, allowing a more sensitive detection of low surface brightness features (Rodriguez-Gomez et al. 2019).

While the distribution of inactive galaxies is consistent with the overall distribution of morphological types at $z = 2$ (e.g. Mortlock et al. 2013; Huertas-Company et al. 2015), the AGN are predominantly hosted in late-type galaxies, which tend to have on average slightly lower values of G and, in particular, a considerably higher M_{20}. This suggests that the morphologies of AGN hosts appear to have a much patchier structure than those of the control galaxies. Quantitatively, 29.3% of the inactive galaxies are classified as bulge dominated, while 54.8% appear to be disk-dominated or irregulars. In comparison, the corresponding numbers for the AGN host galaxies are 4.6% and 72.7%.

As expected, the values of shape asymmetry A_S are on average highest in the merger bin. The corresponding values are $\langle A_S \rangle = 0.56 \pm 0.24$ and $\langle A_S \rangle = 0.46 \pm 0.17$ for the AGN and inactive galaxies, respectively. In contrast, the respective means of A_S are much lower in the late-type and early-type bins. For disk-dominated galaxies and irregulars, the mean A_S values yield $\langle A_S \rangle = 0.34 \pm 0.12$ (AGN) and $\langle A_S \rangle = 0.29 \pm 0.13$ (control galaxies). With $\langle A_S \rangle = 0.29 \pm 0.11$ (AGN) and $\langle A_S \rangle = 0.32 \pm 0.11$ (control galaxies), the spheroidal galaxies have on average similar values.

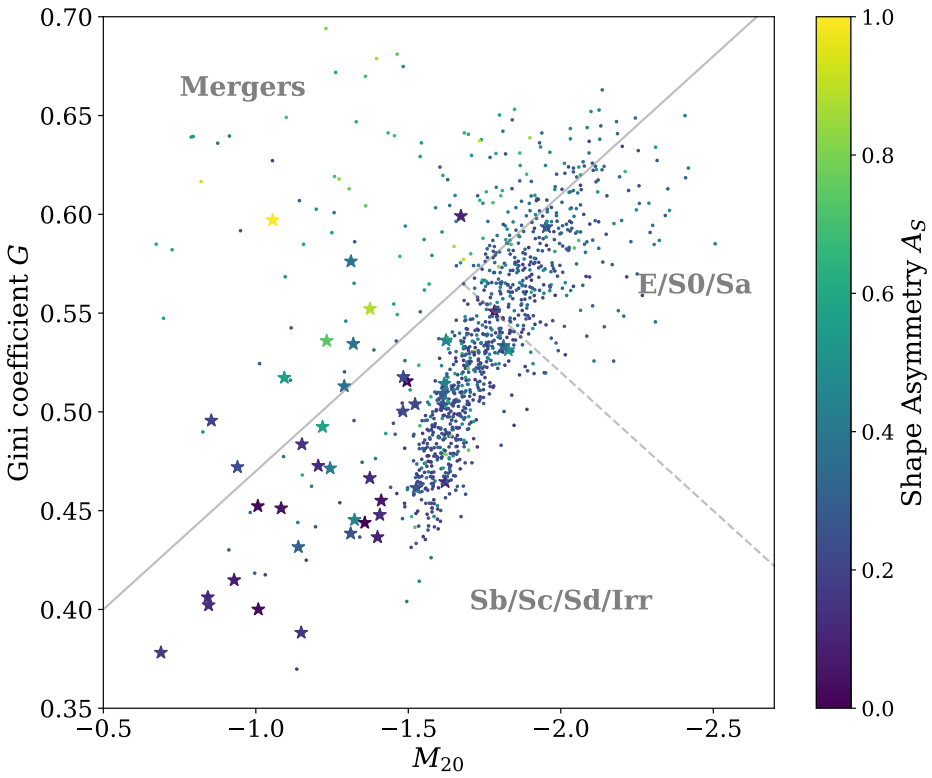

Figure 5.4.: Inactive (dots) and AGN host galaxies (stars) from the HE samples in G-M_{20} space. The classifying relations by Lotz et al. (2008b) are used to identify the galaxies into late-, early-type and mergers. The colour-coding of the sources is based on the value of the shape asymmetry A_S.

As before, the respective merger fractions are derived by counting how many sources are classified as mergers and non mergers, respectively. Those numbers are then used as parameters a and b for the formulas presented in Section 2.2 to determine the probability densities and uncertainties. The resulting merger fractions yield $f_{\mathrm{m,\,AGN}} = 0.23 \pm 0.06$ for the HE AGN sample and $f_{\mathrm{m,\,Ina}} = 0.16 \pm 0.01$ for the corresponding control sample. This result is in excellent agreement with both the findings based on the simulated merger histories as well as the merger rates reported by the observational study in Chapter 4.

5.2.3. Visual Classification

To allow for the most direct comparison with the observations, the same approach of visual classification of galaxy morphology that is used in Chapter 4 is adopted as the third method to derive the major merger fractions of the HE samples.

As a reminder, to make the sources in the AGN and control samples of the observational study indistinguishable, the presence of a central AGN source was simulated by adding a synthetic point source onto the flux center of the inactive galaxies. In a next step, 2D two-component models of all sources are created using PSFMC. The resulting models consist of a point source model for the central AGN and a model following a Sérsic profile for the underlying host galaxy. The point source models are then subtracted from the original AGN observations or the point source added images of the inactive sources. This ultimately yields only the stellar light contributions from the host galaxies, revealing possible asymmetries or tidal features that are used as a visual proxy for a recent or ongoing merger event.

As a result of this modeling process and subsequent point source subtraction, all sources in the observational study show randomly distributed residuals. The only differences between an original observation of one of the control galaxies (i.e. before the addition of the synthetic point source) and its point source-subtracted image are the residuals introduced by the addition of the synthetic point source and its removal by its (imperfect) model. To mimic this appearance for the simulated galaxies, the individual point source-subtracted images of the observed control galaxies are subtracted from their respective original exposures, resulting in a library of 250 unique residual patterns[6]. Since the simulated observations of AGN host galaxies do not contain an artificial central AGN component, the synthetic images of AGN and control galaxies are comparable. Consequently, it is not necessary to first remove a point source in the simulated AGN images. Therefore, for each of the simulated and post-processed galaxy images, one of the residual patterns is randomly selected and added to the image. Before addition, the residuals are scaled according to the ratio of the maximum flux value between each simulated image and the original galaxy observation whose residuals are used. In the end, the two HE samples are not only indistinguishable from each other, but also resemble the analyzed images in Chapter 4.

Figure 5.5 shows a comparison between the simulations and the real observations. Panels (a) and (b) illustrate the original, idealized image of one of the simulated sources and the same image after PSF convolution and addition of Gaussian noise. Panels (c) and (d) show the same source after adding a residual pattern in the original sampling and after smoothing by a $\sigma = 2\,\mathrm{px}$ Gaussian kernel. Since real observations obviously cannot provide idealized images, panel (e) shows the original observation of a control galaxy from Chapter 4, corresponding to panel (b) for the simulated source. Similarly, panels (f) and (g) show the real inactive galaxy after modeling and point source subtraction, without and with smoothing, respectively.

[6] As stated in Section 4.1.2 only 92 control galaxies are used. However, in an initial analysis, some of them were modeled not only in the original but also in a rotated or mirrored version, resulting in a sample of 250 inactive sources.

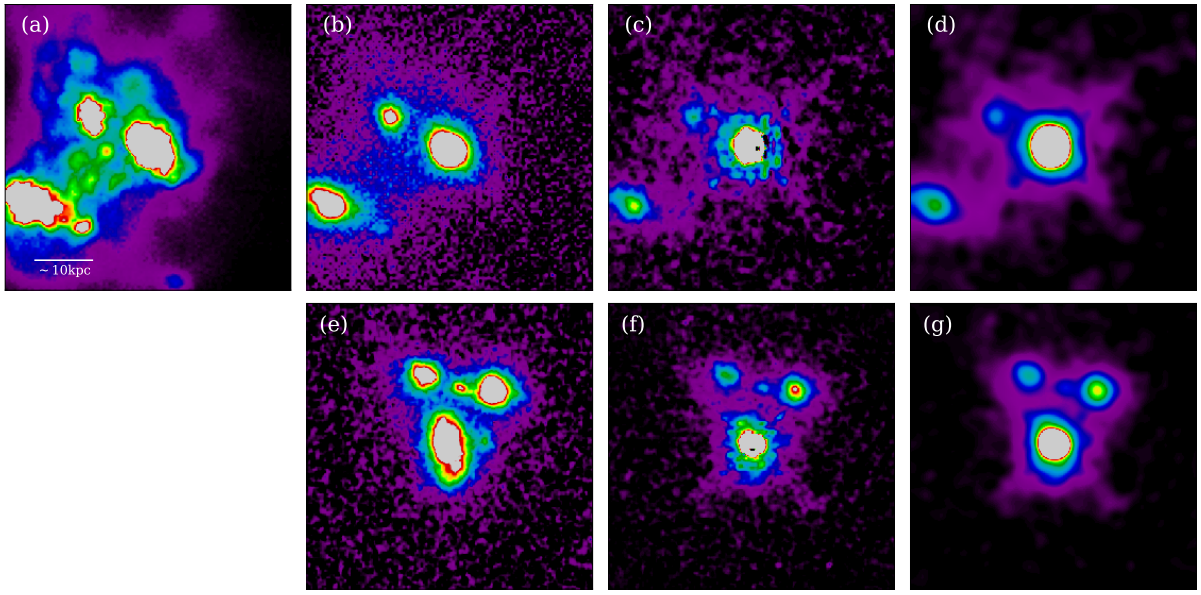

Figure 5.5.: Comparison between synthetic image and observation. The top row displays, from left to right, for one of the simulated sources, the original synthetic image (a), the same image with background noise added and after convolution with a PSF (b), and the final image after adding characteristic residuals introduced by point source modelling in the observational study without (c) and after a $\sigma = 2$ px Gaussian smoothing (d). The bottom row shows an example of a similarly structured observed galaxy with the same pixel scale, comparable field of view, and identical scaling. Analogously the original observation (e) and the same image after the modelling process are presented in the original sampling (f) and after smoothing (g).

Following the analysis strategy of the observational study, eight experts are asked to rank a joint randomly distributed sample consisting of both HE samples according to the degree of distortion and thus the probability of the presence of a recent or ongoing merger[7]. In addition, the classifiers are requested to choose the cutoff that separates the sources into mergers and unperturbed objects. Again, any personal preference regarding the classification of a galaxy as merging or non-merging affects AGN and inactive galaxies equally. Accordingly, personal perceptions do not play a significant role in determining merger fractions.

The same three methods introduced in Section 2.1 and used in the observational study are also employed here to create consensus rankings from the individual rankings. For the average method, out of a total of 8616 votes (1077 sources times eight classifiers), 191 votes are discarded.

The median is calculated from the individual cutoff rank estimates, yielding a cutoff at rank 244 as the threshold for dividing the consensus rankings into merging and unperturbed galaxies.

[7] The classification has been performed by Irham Andika, Knud Jahnke, Anton Koekemoer, Victor Marian, Mira Mechtley, Masafusa Onoue, Arjen van der Wel, and Carolin Villforth.

Again, the appearance and, more importantly, the order of the galaxies in each overall ranking is not necessarily the same. Nevertheless, 209 sources (i.e. 86%) are identical in all three overall rankings, confirming that the choice of method for combining the individual rankings is not significant. Eventually, the calculation yields the results presented in Table 5.2. Taking the respective averages of these values (which happen to be identical to the classifications via the Schulze method) as a and b, the resulting merger fractions are $f_{\mathrm{m,\,AGN}} = 0.52 \pm 0.07$ and $f_{\mathrm{m,\,Ina}} = 0.21 \pm 0.01$ for the AGN host galaxies and inactive control galaxies, respectively. While the merger fraction for the inactive sample is consistent with the results of the other approaches described in this Chapter and also with the findings of the real observations, a significant excess is found for the merger fraction of the AGN.

To test whether the choice of cutoff rank affects the results, the respective merger fractions are calculated for cutoff ranks ranging from 10 to 500 for all three methods (Figure 5.6, left panels). As expected, the merger fractions increase with higher cutoff rank as more galaxies, independent whether AGN or inactive sources, are classified as mergers. Nevertheless, a clear excess in the AGN merger fractions is consistently present, regardless of cutoff rank. This fact, together with the fact that the merger fractions for all cutoff ranks between 10 and 500 are well within the uncertainties of the respective other methods, confirms not only the initial conclusion that the choice of combination method does not affect the final results, but also that the choice of cutoff rank does not bias the results. Interestingly, however, the relative difference between the merger fractions increases up to a rank of ~ 110, while remaining relatively constant thereafter (Figure 5.6, right panels). This suggests that comparatively more AGN host galaxies show the most distinct features in the visual analysis, which could be interpreted as a consequence of an ongoing or recent merger event. To find out the underlying cause for these results, a deeper analysis will be performed, especially with respect to the visual classification.

5.3. Evaluation of Resulting Merger Fractions

Table 5.3 compares the simulated merger fractions derived by the different methods with the results of the observational study. With the exception of the simulated AGN merger fractions that are based on the visual analysis, all merger rates agree with each other in relative, as well as absolute terms. This again suggests that major mergers are not the predominant driver of SMBH growth for the studied subpopulation of AGN with the highest Eddington ratios at $z \simeq 2$. However, the significant increase in the simulated merger fraction of AGN host galaxies based on visual classification of galaxy morphologies is unexpected. Rather, one would have predicted that the results of the visual classifications of the observed and simulated data would yield similar

AGN		
Method	No. of mergers	No. of non-mergers
Average	22	22
Borda	24	20
Schulze	23	21

Inactive galaxies		
Method	No. of mergers	No. of non-mergers
Average	221	812
Borda	219	814
Schulze	220	813

Table 5.2.: Number of mergers and undisturbed sources for the two HE samples based on visual classification.

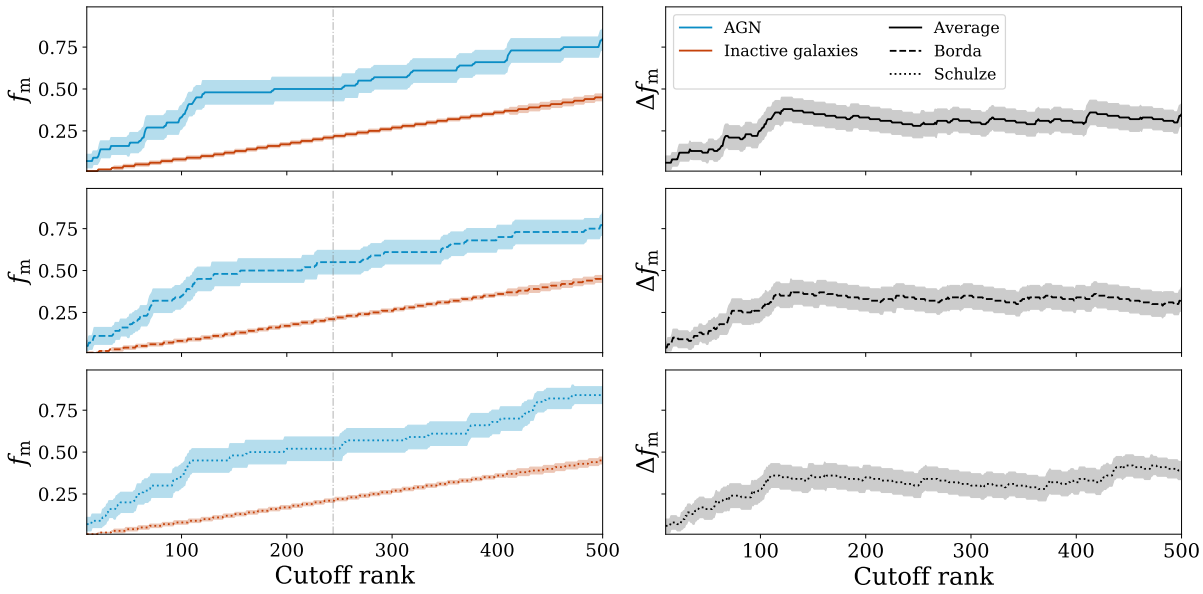

Figure 5.6.: The left panels show the evolution of the merger fractions with cutoff rank for all three methods implemented to combine the individual rankings. The blue and red lines represent the merger fractions for the AGN and inactive galaxies, respectively. The dash-dotted vertical grey line depicts the selected cutoff at rank 244. The right panels display the corresponding differences in the merger fractions between the two samples for each cutoff rank.

	AGN	Inactive galaxies	$\Delta f_{\mathrm{m}} = f_{\mathrm{m,\,AGN}} - f_{\mathrm{m,\,Ina}}$
Observational study	0.24 ± 0.09	0.19 ± 0.04	0.05 ± 0.10
Merger histories	0.32 ± 0.07	0.21 ± 0.01	0.11 ± 0.07
Merger histories (1000 iterations)	0.27 ± 0.07	0.22 ± 0.01	0.05 ± 0.07
Automatic classification	0.23 ± 0.06	0.16 ± 0.01	0.07 ± 0.06
Visual classification	0.52 ± 0.07	0.21 ± 0.01	0.31 ± 0.07

Table 5.3.: Comparison of the merger fraction at $z \simeq 2$ that is based on the observational study with those that are derived from the ILLUSTRISTNG data.

results, while the other methods, and in particular the true merger history, could reveal a possible excess in the AGN merger rates. This would imply that the visual classification is not suited to determine the AGN merger fractions at $z \simeq 2$ and other techniques are needed to achieve this goal. However, the results are quite the opposite, suggesting that the results based on the visual classification approach need to be reviewed.

5.3.1. Accuracy of Galaxy Morphology Classifications

To test the validity of the visual classification, the first step is to determine the false positives FP, false negatives FN, true positives TP, and true negatives TN for both HE samples by examining for each source whether the respective visual and automatic classifications of galaxy morphologies match the true simulated merger histories. True positives (negatives) refer to galaxies that are categorized as mergers (non-mergers) using both the merger history and one of the other two classification methods. Accordingly, sources are classified as false positives (negatives) if they are defined as mergers (non-mergers) in one of the galaxy morphology analyses, but actually belong to the other class when the simulated merger history is considered. To be consistent with the observational study, only major mergers and a lookback time of $t_{\mathrm{lb}} = 1\,\mathrm{Gyr}$ are considered for the simulated merger history.

The analysis shows that the fraction of correctly classified AGN and inactive galaxies (i.e. the sum of the respective true positives and true negatives) is comparable between the visual and automatic classification methods, with accuracies of 50-60% and $\sim 70\%$, respectively. However, while for the automatic classification the number of false positives and false negatives is almost equal, thus balancing out and not affecting the final result, the visual classification approach results in significantly more false positives than false negatives, regardless of the combination method. For the automatic classification approach, the corresponding ratios of false positives over false negatives are $\mathrm{FP/FN} \simeq 0.6$ for the AGN and $\mathrm{FP/FN} \simeq 0.7$ for the inactive galaxies. These ratios, while not unity, are at least similar to each other and therefore affect at most

the absolute values of the respective merger fractions, but not the relative difference. For the visual classification, the associated fractions are significantly different. For the inactive sample, the FP/FN ratio gives $\simeq 1.1$, implying that the resulting merger fraction is not affected by misclassified sources. However, depending on the combination method, FP/FN for the AGN host galaxies ranges from 2.1 to 3.0, implying that at least a factor of 2 more AGN are misclassified as mergers than vice versa.

As a consequence of these findings, every single AGN that is a false positive is identified and subject of a repeated visual analysis. Most of them appear to have a patchy, asymmetric structure, regardless of whether the original idealized mock images or the same images after a certain step of post-processing are examined. This visual perception is also confirmed by the automatic classification analysis. While the average difference for the Gini coefficient G between the false positives and all other AGN is $\Delta G = 7 \times 10^{-3} \pm 0.078$, the mean values of M_{20} and A_S diverge. The corresponding values for the false positive AGN are $\langle M_{20} \rangle = -1.13 \pm 0.29$ and $\langle A_S \rangle = 0.45 \pm 0.23$, while all other AGN have $\langle M_{20} \rangle = -1.42 \pm 0.25$ and $\langle A_S \rangle = 0.36 \pm 0.15$.

In addition, for each of the 24 AGN classified as a merger in at least one consensus ranking, we examine which features are the primary reasons for inclusion in the merger category. Several partially mutually exclusive criteria are considered, such as the presence of large and/or small neighbors, weak or strong asymmetries in the core region and/or outskirts, asymmetric diffuse halos, or the presence of tidal tails or bridges. The analysis identifies only two AGN that meet either the neighborhood and/or core asymmetry criterion. One source has a small neighbor, and the other shows weak asymmetries in the core. Moreover, the latter object is not classified as a merger in all consensus rankings, since it is listed above the selected cutoff rank only in the overall ranking based on the Borda method. This implies that at most in these two cases a possible projection or residuals in the center introduced by post-processing could actually be responsible for a classification as a merging source. Conversely, this means that 22 of 24 AGN visually classified as merging have at least one of the large-scale features that are unlikely to be affected by post-processing, such as a tidal bridge or asymmetries in the outskirts or halo. For comparison, the same analysis is applied to the 29 top ranked inactive galaxies. Again, only one of them has a large neighbor and weak nuclear asymmetries as its only criteria. All other 28 control galaxies show large-scale distortions.

An ancillary analysis examines whether the AGN host galaxies are on average intrinsically brighter than the sources in the inactive sample. This would imply that post-processing, in particular the addition of a residual pattern, has a smaller effect on the images in the active sample than on the inactive sources. As a result, possible distortions and asymmetries in the images of the AGN are easier to detect because they are not as strongly obscured by residuals

and background noise. To test this hypothesis, the mean intensities of the AGN and the control sources are measured. No differences are found between the two HE samples or between the false positive, false negative, or correctly classified AGN. This conclusion is also independent of the post-processing stage, as this test is performed on the idealized images, the noisy and PSF-convolved images, as well as on the final post-processed images.

In summary, the high AGN merger fraction based on visual classification is not due to a true merging nature in most of the AGN. Rather, this is simply a consequence of the presence of asymmetric, apparently non-relaxed sources that only mimic the appearance of a merging system. The following sections discuss possible cause(s) for such an appearance.

5.3.2. Influence of Selection Effects

Since a population of sources with peculiar properties, rather than directly the visual classification approach, is responsible for the significantly higher AGN major merger fraction found with this technique, it is tested whether the selection process and the addition of uncertainties based on the SDSS observations could be responsible for this deviating result.

As a first step, the stellar masses of the objects in both HE samples are checked and verified to be comparable. If this were not the case, one can assume that different galaxy populations are indeed being studied, which would clearly discourage a direct comparison between AGN and inactive galaxies. Analyzing the sources after adding the uncertainties, the AGN host galaxies appear to be less massive than the control galaxies. Nevertheless, the mean values of the stellar masses of both samples are well within their respective uncertainties, and this difference is not expected to have a significant impact on the results.

However, when focusing on the distribution in BH mass-stellar mass space for the selected sources, the AGN host galaxies and the control galaxies partially populate a different region. While the addition of the uncertainties to the BH masses leads to the inactive galaxies being uniformly scattered up and down into the final selection limits, the BH masses of the AGN host galaxies are almost exclusively scattered upward, except for the sources with the highest stellar masses. Since luminous AGN with high stellar masses are quite rare, this is likely the result of the limited simulation volume, although TNG300 is one of the simulations with the largest box size currently available. Since these sources with highly up scattered BH masses could consequently be in a very different state of evolution, we test whether the false-positive AGN are the ones that show the largest difference between the true BH mass and the BH mass after the addition of a random uncertainty value. As it turns out, the false-positive AGN show, on average, a slightly higher but negligible difference in BH mass with respect to the rest of the sources in the AGN sample.

With an additional test, the AGN merger fraction is recalculated by incrementally excluding AGN with a difference between true and uncertainty added BH mass of $-1.5 \leq \Delta M_{\rm BH}\,[\rm dex] \leq 0.1$ by using a step size of $\Delta M_{\rm BH} = 0.1$. The minimum in the merger fraction is obtained when excluding all sources with a BH mass difference of $\Delta M_{\rm BH} > 0.3\,\rm dex$. However, in this case the merger fraction is still $f_{\rm m,\,AGN} \simeq 0.44$, which is not significantly lower than the original result. Therefore, it is likely that the large scatter of the true AGN BH masses does not affect the result. This confirms also the assessment that the merger fractions that are derived via the merger histories do not depend on the choice of the subsample, i.e. BH mass.

As a consequence of the detection of the partially large difference in the true BH mass, the location of all objects in the parameter space spanned by BH mass versus Eddington ratio is re-examined. As described in Section 5.1.3, these are the properties used to select the sources. Because the accretion rates in IllustrisTNG are limited to the respective Eddington mass accretion rates (see Section 5.1.2), it is possible that a combination of sources simultaneously up scattered in $M_{\rm BH}$ and $\lambda_{\rm Edd}$ can explain the excess of false-positive classified AGN. The analysis reveals that several sources in the HE AGN subsample indeed have Eddington ratios that are smaller by a factor of $10 - 40$ in reality. However, no source has both a large difference in true BH mass and Eddington ratio because, if anything, the difference in Eddington ratio tends to be inversely proportional to the difference in BH mass. Nevertheless, to test whether the selection affects the results, a fiducial relationship is derived, given by

$$M_{\rm BH} = -\frac{1}{2}\lambda_{\rm Edd} + \alpha, \tag{5.12}$$

which is used to recalculate the AGN merger fraction by gradually excluding specific AGN that show the highest combined deviations. In each iteration step of the recalculations, objects are progressively discarded that have BH masses below this relation, assuming $7.5 \leq \alpha \leq 8.2$ and a step size of $\Delta\alpha = 0.1$. With $f_{\rm m,\,AGN} \simeq 0.48$, the minimum of the AGN merger fraction occurs at $\alpha = 7.9$. Such a result for the AGN merger fraction is still significantly different from the merger fractions derived using the other two methods and deviates negligible from the original result that includes all sources.

Figure 5.7 summarizes the analysis presented in this subsection. The panels *(a)* and *(b)* show all sources with added uncertainties in BH mass versus stellar mass and Eddington ratio, respectively. The same is illustrated for the true simulated values in the *(c)* and *(d)* subplots. Panels *(e)* and *(f)* compare only the AGN before and after adding the uncertainties, while finally *(g)* and *(h)* present the same for the sources in the control sample. The dashed lines and boxes indicate the selection limits in BH mass and Eddington ratio. The shaded parts represent the

smallest and largest regions in parameter space from which objects are progressively excluded to recalculate the AGN merger fractions.

In a final test that examines the impact of selection effects, the validity of the derived merger fractions is checked by reselecting the sources for all six subsamples, this time ignoring any SDSS uncertainties in BH mass and Eddington ratio. The resulting numbers of AGN in the LM, IM, and HE samples are 2067, 553, and 22, respectively. The corresponding numbers for the control galaxies are 32, 1002, and 1589. Strikingly, the number of objects decreases by a factor of ~ 0.5 and ~ 0.2 for the AGN in the HE sample and for the comparison galaxies within the LM sample, respectively.

Based on the merger histories of each object, the corresponding merger fractions are recalculated. As a comparison to Figures 5.2 and 5.3, the newly derived merger fractions are shown in Figure 5.8. Once again, the merger fractions most suitable for comparison with the observational study are framed in red. Compared to the initially derived merger fractions in Section 5.2.1, some AGN subsamples show a more pronounced increase in the merger fraction for a given combination of merger type and lookback time. For instance, the resulting minor merger fraction for HE AGN and the major merger fraction of IM AGN, both for a lookback time of 1 Gyr, are $f_{\mathrm{m,\,AGN}} = 0.41 \pm 0.12$ and $f_{\mathrm{m,\,AGN}} = 0.36 \pm 0.02$, respectively. However, for the former merger fraction, note that this value is still consistent with the original result due to the large uncertainty range. Despite the absolute increase in some values, the merger fractions are still not large enough to accept major mergers as the dominant trigger for SMBH growth. Therefore, despite some selection effects, the final source selection does not substantially affect the results.

5.3.3. Past and Future Evolution of Active and Inactive Galaxies

Evidently, neither the visual classification approach nor the source selection are the cause of the large discrepancies in the inferred AGN merger fractions. Therefore, to explain the irregular appearance of AGN misclassified as mergers, the possibility of actually studying distinctly different populations of AGN host galaxies is explored.

Influence of uncoalesced mergers

First, it is checked whether the false-positive AGN are actually part of a merger that has not yet coalesced. Consequently, although these sources are not yet registered as a merger in the examined snapshot, they will be registered as such in the subsequent ones. This scenario is tested by accessing the simulated merger histories and examining at what point in the simulated future the next major or minor merger occurs for each AGN. Only three of 15 AGN misclassified as

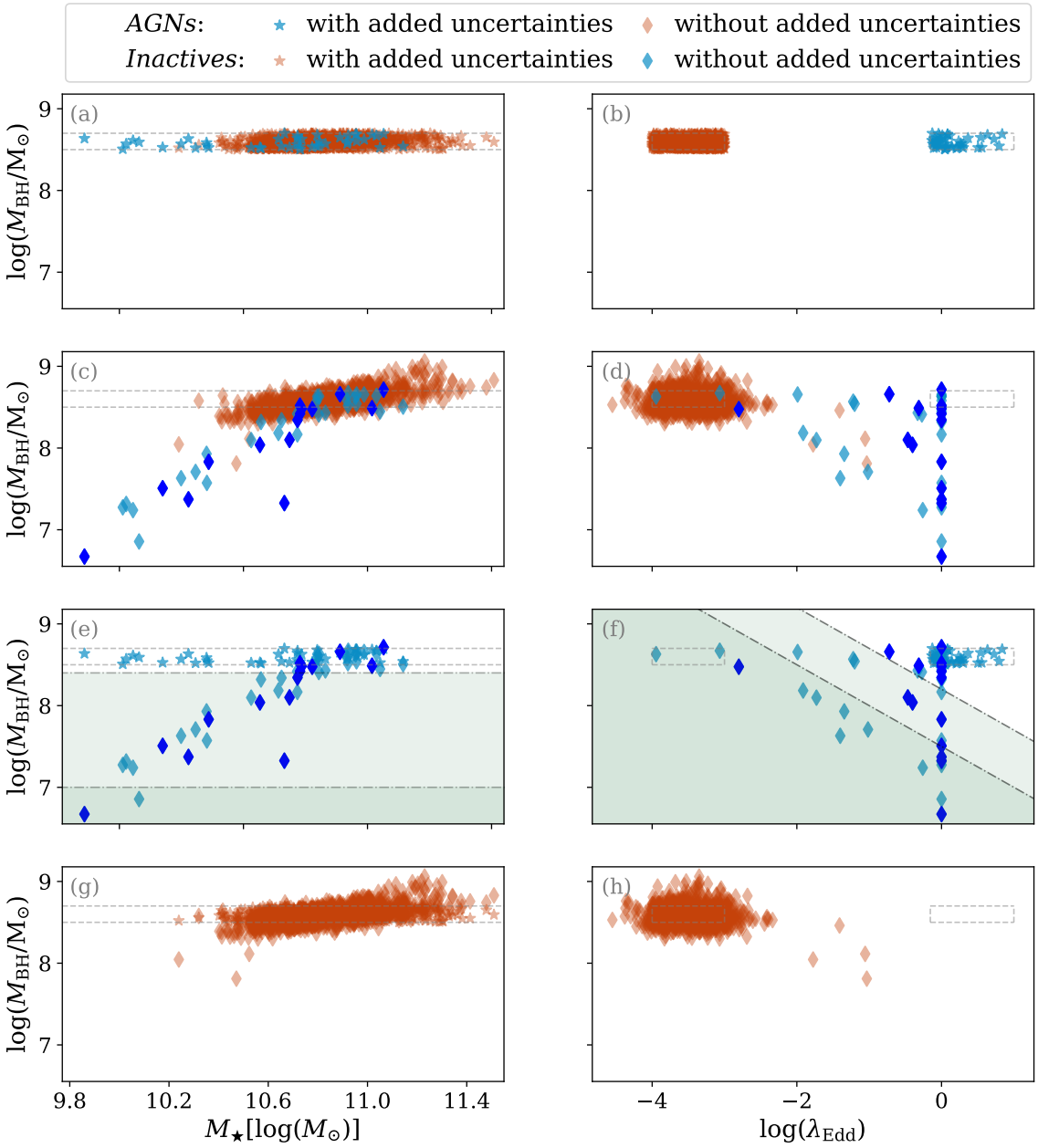

Figure 5.7.: Visualization of possible selection effects. The panels in the left column show the HE objects in BH mass versus stellar host mass, while the right panel shows the same objects in BH mass versus Eddington ratio space. The panels *(a)* and *(b)*, as well as *(c)* and *(d)* show the sources after and before the addition of the random SDSS uncertainties. The respective lower panels *(e)* - *(h)* show the same only for AGN and inactive control galaxies separately. The shaded regions in *(e)* and *(f)* visualize the minimum and maximum parameter space from which AGN are incrementally rejected in order to recalculate the merger fraction.

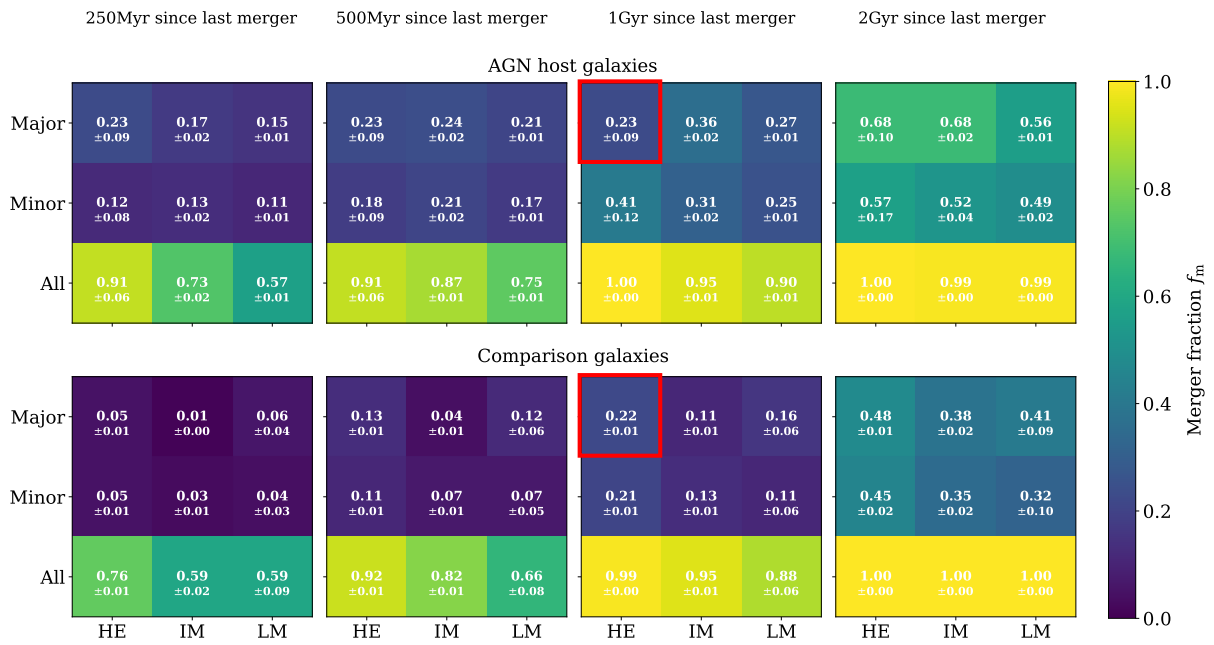

Figure 5.8.: Merger fractions of all the subsamples, which this time consist of sources that are selected on their true simulated values of BH mass and Eddington ratio. As in all the other comparable diagrams, the merger fractions that compare best with the findings of the observational study are highlighted.

a merger are registered as part of a major merger at the next snapshot, which corresponds to $z = 1.9$ and about 160 Myr in the future. Going even further to lower redshifts, the next major merger for another single source is not registered until snapshot 37, which already corresponds to $z = 1.67$ and more than 600 Myr later. This implies that at most three AGN at $z \simeq 2$ are misclassified as mergers. Correcting for this fact, the AGN merger fraction would change only slightly to $f_{\mathrm{m,\,AGN}} \simeq 0.45$, a value still significantly different from the other determinations. For all other false-positive AGN, the time period is too long to even consider them as future mergers in the analysis, since their occurrence at $z \simeq 2$ certainly requires registration as a merger within the next 500 Myr. For completeness, minor mergers are also considered, but only one source is recorded as a merger in the following snapshot, i.e. at $z = 1.9$, while the next source is then registered only at $z = 1.67$.

The same evaluation is performed for the sample of inactive galaxies. Depending on the combination method, the visual analysis yields between 159 and 162 false positives. However, since a source can be a false positive in only one consensus ranking but not in the other two, the selection is not congruent. Therefore, the total number of false positives adds up to 190 inactive galaxies. Overall, these sources show a steady increase in newly registered mergers in each future snapshot, but only from a very low starting point. For example, at $z \simeq 1.9$ (i.e. the next snapshot),

only three new major mergers and three new minor mergers are registered. Considering the total number of false positives, this handful of possibly misclassified sources is negligible. Therefore, it can be ruled out that this small number of objects misclassified as mergers but registered as mergers in the near future has any significant impact on the determined merger fractions or could explain the significantly different AGN merger fraction based on visual classification. This conclusion is independent of whether AGN or control galaxies are concerned.

A Closer Look on the Evolution of Galaxy Properties

Given the results presented in the previous sections, it is still a necessity to find an explanation for the false-positive AGN. Since they appear predominantly perturbed and non-relaxed, it is tested whether the AGN host and control galaxies are indeed inherently different galaxy populations in terms of their evolutionary status. The same analysis is performed for the sources exclusively within the HE AGN sample, separating them into merged and undisturbed classified objects, or into false positives and the remaining active sources.

An initial test evaluates whether AGN sources that are classified as merging in at least one visual consensus ranking are on average younger than the rest of the active sources. This would indicate that these systems may not yet have settled and could explain their conspicuous appearance, which could be misinterpreted as being part of a major merger. As mentioned, these tests also include a comparison with the inactive sources, which in this case are also analyzed separately for merging and non-merging galaxies. The results presented are based on the mass-weighted mean stellar ages within twice the stellar mass half-radius. However, the analysis was also performed for a radius of 30 physical kpc and considering all stars gravitationally bound to the respective galaxy, as well as for luminosity-weighted mean stellar ages based on the R band. Although the absolute values differ, the general conclusion is applicable to all combinations of weighting and radius.

The distributions of the mean stellar ages are shown in Figure 5.9 as stacked histograms for the AGN population and the control sample. The left and middle panels show by the dark and light colors the active and control samples separated into merged and undisturbed classified sources. The right subplot shows a comparison between the two total samples. For both the active and inactive samples, the mean stellar ages of merged and unperturbed galaxies, shown as vertical lines, are not significantly different from each other. However, there is a distinct mean age difference between AGN hosts and the control galaxies. Nevertheless, such a result is not unexpected, since the gas flows that trigger and drive the central SMBH would also be able to support and increase the current and recent star formation on almost all scales, which may lead to a younger mean age of the whole system (Kauffmann et al. 2003a). It is noted here, however,

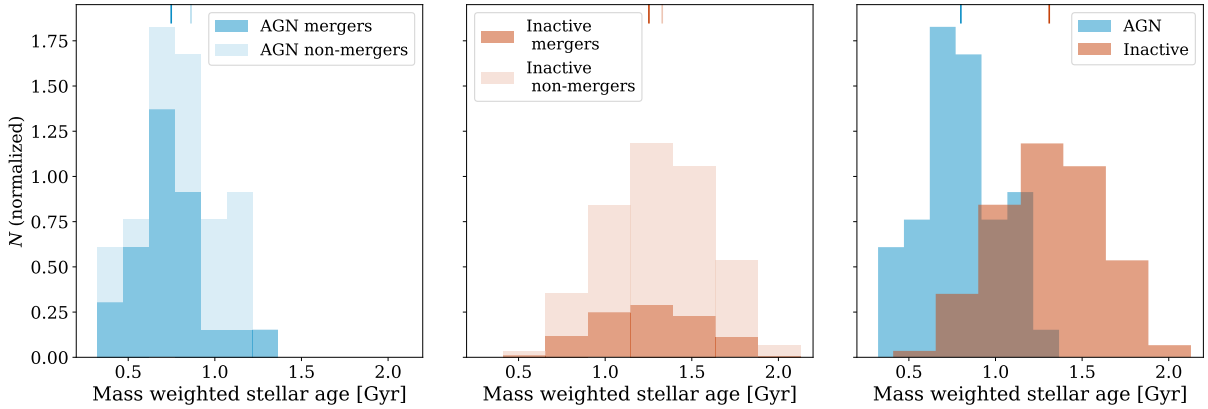

Figure 5.9.: Mass weighted mean stellar ages for AGN and inactive sources classified as mergers and undisturbed, respectively. The left panel shows a stacked histogram for the merging (light blue) and non-merging (dark blue) AGN. In the middle panel the same is shown for the control galaxies. The right panel illustrates a comparison between the complete AGN sample and the total inactive sample. The vertical lines at the top show the respective mean values of the stellar age distributions for each subsample.

that the reverse case is not compulsory. That is, active star formation does not necessarily imply the presence of an AGN. Regarding the analysis of the sources within the AGN sample shows the false positives to be on average of comparable age as the other AGN, disproving the hypothesis that these particular objects are significantly different in terms of their past evolution.

Following up on the analysis of the mean stellar ages, several galactic properties are traced back in time to test whether the galaxies in the active and control samples are from the same galaxy population and have an active or quiescent central SMBH as their only difference at $z \simeq 2$. Again, these parameters are also examined within the AGN sample itself to test whether there is a difference between the false-positive AGN and the remaining active sources that could explain the misclassification. To this end, the merger trees for the respective galaxies at $z \simeq 2$ provide the information to trace back the respective main progenitor branches and determine the corresponding main progenitors for each snapshot up to $z \simeq 4$. All parameter values shown are the true values resulting directly from the simulation.

Finding a pronounced difference in the mean stellar ages between the two HE samples, the most obvious feature to investigate is their star formation histories. Using the stellar masses of all bound stellar particles and the star formation rates of all star-forming gas cells, the specific star formation rates (sSFR) are calculated for all individual sources back to $z \simeq 4$. With a value of $\log(\mathrm{sSFR}) \sim -9[\mathrm{Gyr}^{-1}]$, the mean sSFRs of AGN hosts and inactive galaxies evolve consistently and identically until $z \simeq 2.5$. After this time, the mean sSFR of galaxies hosting an AGN remains

constant until $z \simeq 2$, while the inactive control galaxies appear to be quenched and form fewer and fewer stars until they reach $\log(\mathrm{sSFR}) \sim -10.5[\mathrm{Gyr}^{-1}]$.

As a consistency check, the derived evolution of the sSFR is compared to the catalog presented in Pillepich et al. (2019), which contains classifications of galaxies according to their star-forming activity. These classifications are defined by calculating for each source the log distance $\Delta\log(\mathrm{SFR})$ from the star-forming main sequence at the corresponding stellar mass. For $\Delta\log(\mathrm{SFR}) > -0.5$ and $\Delta\log(\mathrm{SFR}) \leq -1.0$, the respective galaxy is classified as star-forming or quenched. If a target galaxy lies between these values, it is categorized as a transitional galaxy in the green valley.

The first quenched AGN host galaxy does not appear until $z \sim 2.3$, while the galaxies classified as sources in the green valley have their maximum at $z \simeq 2.9$ and account for $\sim 20\%$ of the total AGN at this time. Over the entire studied redshift range of $2 \lesssim z \lesssim 4$, the fraction of star-forming AGN is $\geq 80\%$. This confirms the assessment from the analysis of the sSFR that most of the AGN host galaxies are still actively forming stars. In contrast, for the inactive galaxies, objects appear in all three bins as early as $z \simeq 3.7$. Up to $z \simeq 2.5$ most of them are still classified as star-forming. For lower redshifts, the number of star-forming galaxies decreases rapidly, while the number of quenched galaxies increases steeply, a trend that also agrees excellently with the evolution of the sSFR of these sources. At $z \simeq 2$, only eight of the ~ 1040 inactive galaxies appear to be star-forming, while 989 are classified as quenched. The relatively small number of galaxies in the green valley in both samples, and especially the rapid change in the number of quenched and star-forming galaxies for the control sources, indicate a fairly sharp transition from galaxies that are actively forming new stars to those that are considered "dead." The left panel of Figure 5.10 shows the evolution of the class fractions with redshift. The AGN and control sources are shown in blue and red, respectively, while the solid, dashed, and dot-dashed lines denote star-forming, quenched, and green valley galaxies.

A comparable analysis exclusively for the AGN sample shows no difference for $z \simeq 2$ between the false-positive AGN and the other active sources (Figure 5.10, right panel). Only in the interval of $2.5 \lesssim z \lesssim 3.5$ are the false-positive AGN comparatively less classified as star-forming. The minimum is reached with about $\sim 65\%$ at $z \simeq 2.6$. All other corresponding active sources in this subsample are categorized as galaxies in the green valley. Accordingly, the fraction of this class has its maximum at $\sim 35\%$ at the same redshift. Furthermore, at $z \simeq 2$ only three out of 44 AGN hosts are classified as quenched, corresponding to a fraction of $\sim 7\%$.

As part of the analysis, the evolutions of properties closely related to the sSFR are next studied: the accumulation of stellar mass, the gas content, and the ratio between gas and stellar mass. At $z \simeq 4$, the inactive galaxies appear with an average stellar mass of $M_\star \simeq 10^{10}\mathrm{M}_\odot$ more massive than the AGN host galaxies with $M_\star \simeq 10^{9.5}\mathrm{M}_\odot$. However, while the increase in stellar mass

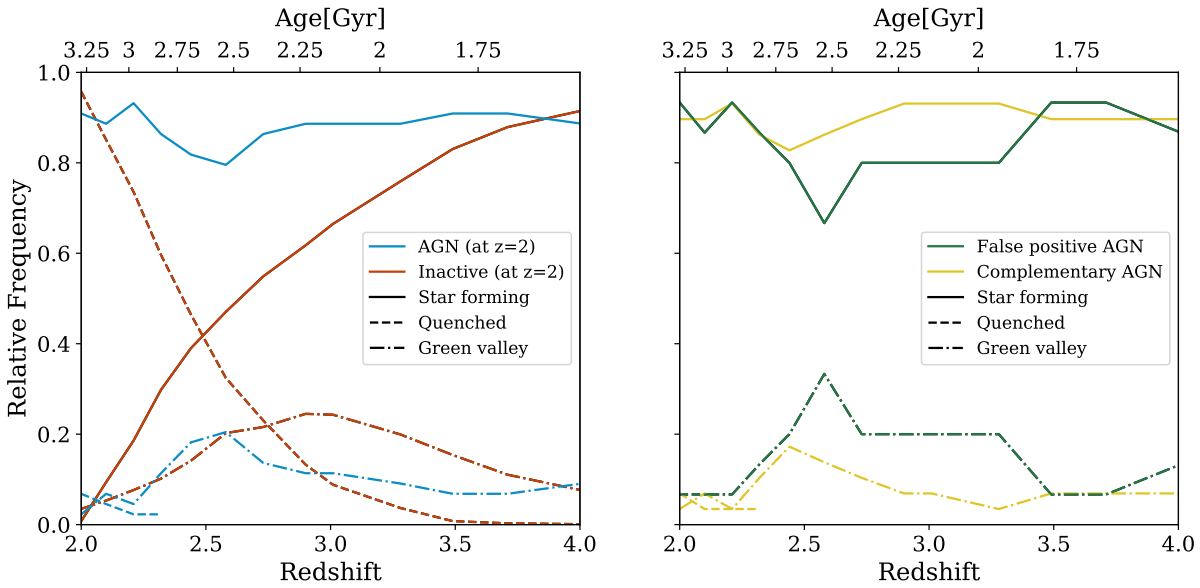

Figure 5.10.: Evolution with redshift of the fractions of galaxies classified as star-forming, quenched, or in the transitional state of a green valley galaxy. In the left panel, the blue and red lines represent the AGN and inactive galaxies, respectively. In the right panel, the AGN sample is divided into false positive classified AGN and the remaining active sources. The style of the lines corresponds to the three different classes.

for the inactive galaxies stops at $z \simeq 2$, the AGN host galaxies have closed the gap and have comparable masses. This is also consistent with the analysis of possible selection effects in the previous Section 5.3.2, where it is noted that the stellar masses of the AGN hosts and the inactive galaxies are similar.

The gas masses at $z \simeq 4$ show a similar distribution to the stellar masses, although the difference between active and inactive galaxies is not as concise. At this redshift, the gas masses for the inactive and active galaxies are $M_{\mathrm{gas}} \simeq 10^{11}\mathrm{M}_{\odot}$ and $M_{\mathrm{gas}} \simeq 10^{10.7}\mathrm{M}_{\odot}$, respectively. Probably one reason for the change in sSFR at $z \simeq 2.5$ is that the median gas mass of the inactive galaxies starts to decrease after this redshift. However, taking into account the uncertainties and an increasing scatter towards $z \simeq 2$, the median gas mass at $z \simeq 2$ can also be interpreted as constant or even increasing. In contrast, the median gas mass of the AGN host galaxies shows a steady increase, exceeding the corresponding median gas mass of the inactive control sample at $z \simeq 2.5$. At $z \simeq 2$, the median gas mass of the AGN host galaxies is $M_{\mathrm{gas}} \simeq 10^{11.4}\mathrm{M}_{\odot}$, while the corresponding value for the inactive galaxies is 0.1–0.2 dex lower.

The gas mass fractions of the AGN host galaxies and the control sources show an identical trend with time, although the AGN have a higher absolute value for a fixed redshift at any given

time. At higher redshifts this is due to the lower stellar mass of the AGN host galaxies, and at lower redshifts it is due to the higher absolute gas mass. For both samples, the gas mass fractions decrease by $\Delta\log[(M_{\rm gas}/M_{\bigstar})] \simeq 0.4$ over the considered timescale. Similar to the sSFR, neither this property nor the stellar or gas masses show a significant difference between the false-positive AGN and the complementary sample of active galaxies.

The last two properties investigated are the BH mass and the Eddington ratio. As in the selection process, only the mass of the most massive BH in each subhalo is used for the BH mass determination of the progenitor sources. For $2 \lesssim z \lesssim 4$, the mean BH mass of the inactive galaxies is consistently higher than that of the AGN. At $z \simeq 4$, the inactive galaxies host a median SMBH with a mass of $M_{\rm BH} \simeq 10^{6.8}{\rm M}_{\odot}$. Compared to the AGN sample, the growth rate is comparatively steeper until it reaches a plateau at $z \simeq 2.5$. Such a trend is similar to the evolution of stellar mass and suggests an identical underlying formation and evolution mechanism of SMBH and host galaxies. As indicated, the AGN host galaxies show a lower mean BH mass at $z \simeq 4$, close to the seeding mass of $M_{\rm BH} \simeq 10^{6}{\rm M}_{\odot}$, and also a slower mass growth. However, at $z \simeq 2$ the difference between the mean BH masses of the AGN and inactive galaxies becomes negligible, while the growth of the SMBHs in the AGN hosts appears to continue.

This different trend in median BH mass for the two HE samples is also reflected in the evolution of the Eddington ratios. While the inactive sources show between $3.5 \lesssim z \lesssim 4$ with $\lambda_{\rm Edd} \simeq 0.5$ a higher median Eddington ratio, this value decreases for lower redshifts until it eventually reaches a negligible value, which brings these systems within the selection limits for control galaxies. In contrast, the AGN show a median Eddington ratio of $\lambda_{\rm Edd} \simeq 0$ for most of the studied cosmic time. Only a few tens of Myr before $z \simeq 2$, the median Eddington ratio rapidly increases to a value of $\lambda_{\rm Edd} \simeq 1$, where it is finally capped by the constraints of the simulation. Although the sSFR and the gas mass of the AGN are constant respectively increasing over the whole studied redshift range, the Eddington ratio increases only shortly before $z \simeq 2$. This means that the actual growth of the SMBH is largely decoupled from the evolution of the host galaxy and requires a process that suddenly provides enough gas to the SMBH to reach such high Eddington ratios. Nevertheless, when a sufficiently large period is considered, it appears that the SMBH and host galaxy evolve simultaneously, as is the case for inactive galaxies, for example. Considering again the false positives and the remaining AGN, the trends of BH mass and Eddington ratio with redshift are identical and provide no apparent explanation for the misclassifications.

Figure 5.11 visualizes the cosmic evolution of all discussed galaxy parameters. The blue and red lines illustrate the median evolution of the corresponding properties for the objects classified as AGN and inactive at $z = 2$. The shaded areas represent the corresponding median absolute deviations. In Figure 5.12, the same properties are shown for AGN only, divided into false

positives and the remaining sources. Clearly evident is the lack of significant difference in all these parameters within the AGN sample.

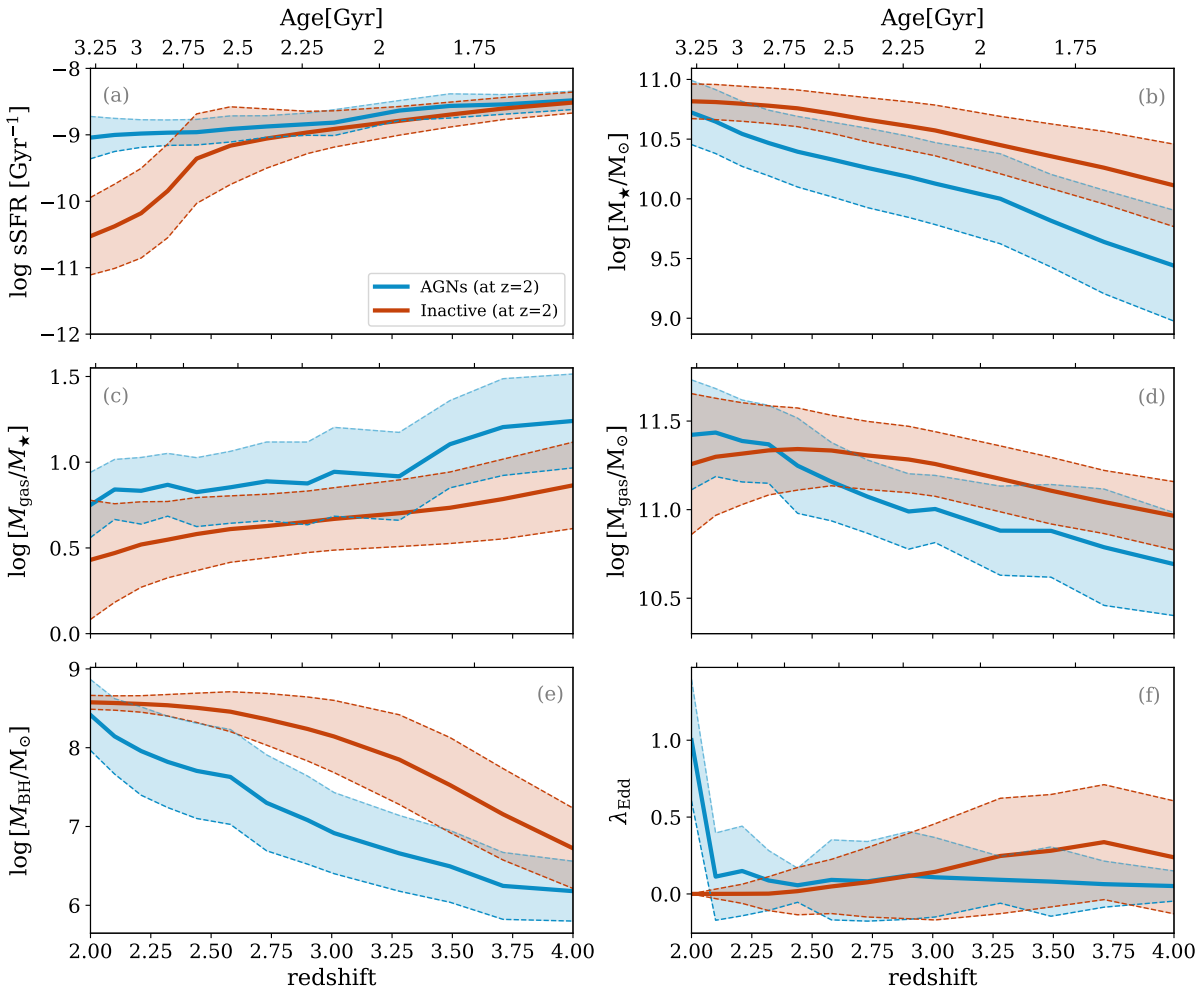

Figure 5.11.: Evolution of different galaxy properties on a median basis in a redshift range of $2 \lesssim z \lesssim 4$ for the AGN (blue) and inactive galaxies (red). The shaded areas show the median absolute deviation for each case. The panels *(a)* - *(f)* show the evolutions of the specific star formation rates (sSFR), stellar masses, gas mass fractions, gas and BH masses, and Eddington ratios.

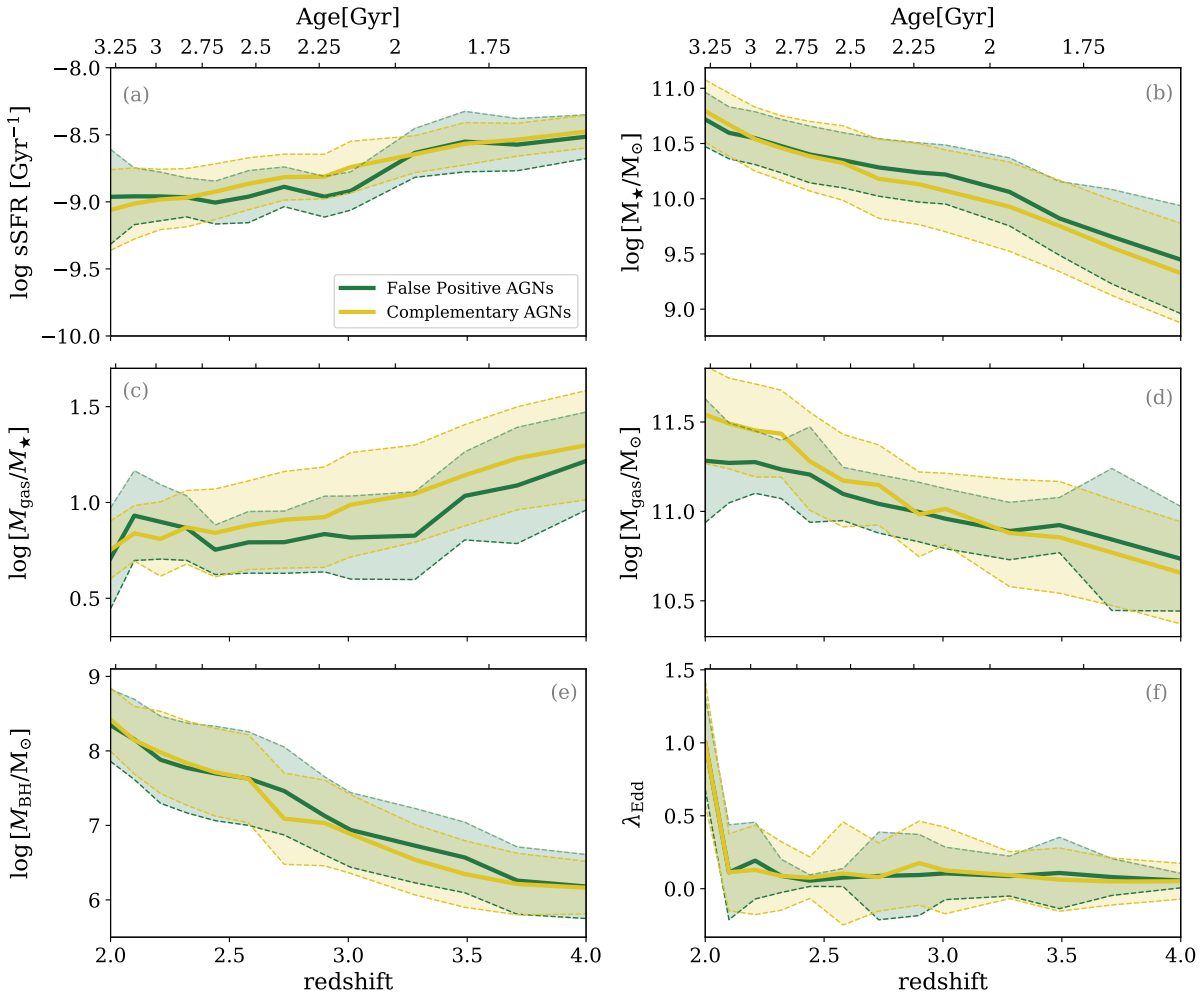

Figure 5.12.: The panels *(a)-(f)* show for a redshift range of $2 \lesssim z \lesssim 4$ the evolution of the specific star formation rate, stellar mass, gas mass fraction, gas mass, BH mass, and Eddington ratio of the false positive and all other AGN, respectively.

5.4. Possible Explanations for the Excess in Visual AGN Merger Fraction

5.4.1. Potential Impact of Obscured AGN

While only type 1 AGN are explicitly studied in the observational study, it is not possible to apply the same criteria to distinguish optically obscured and unobscured AGN in the simulation, since AGN are not modeled as such and thus are not selected or defined by their (spectral) appearance. Rather, the definition of an AGN depends on the interpretation of the simulated properties of

the black hole and surrounding gas particles, such as the accretion rate, bolometric luminosity, or as in this case, the Eddington rate. To estimate the fraction of obscured AGN, one would need to rely on a model that is based on observational results and that takes various parameters into account (Habouzit et al. 2019). While the relative number of obscured AGN is expected to increase with redshift and lower AGN luminosities, it remains unclear how this fraction depends on the properties of the host galaxies.

For example, Merloni et al. (2014) report no dependence on stellar host mass or SFR, while Chang et al. (2017) find that for a given stellar mass and redshift, the host galaxies of obscured AGN are more compact than normal star-forming galaxies. Moreover, for column densities $N_{\mathrm{H}} > 10^{23.5}\,\left[\mathrm{cm}^{-2}\right]$, Buchner & Bauer (2017) argue that the obscuration originates from the core regions rather than being the consequence of Compton-thick gas distributed on galaxy scales. Nevertheless, for column densities in the range of $10^{22} \lesssim N_{\mathrm{H}}\,\left[\mathrm{cm}^{-2}\right] \lesssim 10^{23.5}$, gas on galaxy scales can explain the obscuration values at luminosities similar to those of the AGN studied here. For a comparable luminosity and redshift bin, they present a fraction of $\sim 35\%$ of AGN being obscured, which is also consistent with other works (e.g. Merloni et al. 2014; Buchner et al. 2015; Georgakakis et al. 2017). On the other hand, if the Eddington ratio of the AGN studied in this work is considered, the fraction of obscured AGN appears to be negligible (Ricci et al. 2017). At this point, it should also be noted that the obscuration fraction in principle also depends on the wavelength range investigated, since the sources of obscuration may be different in, for example, the X-ray and optical/IR regions. However, if one considers $N_{\mathrm{H}} = 10^{22}\mathrm{cm}^{-2}$ as the value separating X-ray obscured and unobscured AGN, there is a $\sim$ 80-90% agreement with the optical classification (Hickox & Alexander 2018, and references therein).

Considering now the relatively large number of AGN in this work that are classified as false positives, the question arises whether these sources would in fact be observed, at least in part, as obscured AGN. Since the central AGN source would remain undetected, this would move these sources into the bin of inactive galaxies. As a result, the AGN merger fraction decreases, while the merger fraction of control galaxies remains essentially unchanged due to the existing high number of such sources. Assuming a Compton-thick AGN fraction of 35% would mean that ~ 15 of HE AGN sources would be missed in an observational study. Following the estimates of Farrah et al. (2017), $\sim 75\%$ of these would be classified as mergers. However, they argue that the peculiar morphology is mostly the result of a short luminous AGN phase or a bulge in its earliest stages of formation, and is not due to an actual merger event. Thus, this would be consistent with the interpretation of false-positive AGN in the sense that they appear disturbed but do not actually merge. Taking these estimates into account, the AGN merger fraction would then be $f_{\mathrm{m,\,AGN}} = 0.38 \pm 0.09$. Such a value is still higher than the merger fractions derived

using the other methods, but is within the uncertainties. However, this simplistic approach does not account for uncertainties in the fractions of obscured AGN or perturbed sources within this population. Both of these could drastically alter the resulting AGN merger fraction.

According to e.g. Donley et al. (2012), the SED of obscured AGN shows a significant drop in the UV-optical range. Thus, if the false-positive AGN are indeed predominantly obscured AGN, they should have significantly lower rest frame magnitudes at these wavelengths than the other examined AGN. As a proxy for the respective SEDs, the simulated photometric estimates calculated for the SDSS filter sets, which include the effects of dust obscuration, are used to test this hypothesis (Model C in Nelson et al. 2018).

The distributions of the provided magnitudes in U, G, R, I, Z do not show a significant difference in any of these bands. Quantitatively, the false-positive AGN have the following mean absolute rest frame magnitudes, $\mathrm{mag}_U = 24.4 \pm 0.7$, $\mathrm{mag}_G = 23.6 \pm 0.6$, $\mathrm{mag}_R = 23.5 \pm 0.6$, $\mathrm{mag}_I = 23.3 \pm 0.6$, $\mathrm{mag}_Z = 23.2 \pm 0.6$. The corresponding values for the remaining AGN are $\mathrm{mag}_U = 24.5 \pm 0.9$, $\mathrm{mag}_G = 23.7 \pm 0.8$, $\mathrm{mag}_R = 23.5 \pm 0.8$, $\mathrm{mag}_I = 23.3 \pm 0.8$, and $\mathrm{mag}_Z = 23.2 \pm 0.8$.

These results suggest no difference in SEDs and seemingly confirm the results of Ricci et al. (2017) that for high λ_{Edd}, the fraction of obscured AGN is negligible. Nevertheless, it should be noted that the analysis performed here does not account for the distinction of AGN into types I and II due to geometric effects, nor for obscuration that is primarily confined to the core region. Other studies (Lusso et al. 2011; Pović et al. 2012; Mignoli et al. 2013; Lanzuisi et al. 2015) also report significantly lower values for the fraction of disturbed galaxies containing obscured AGN than the 75% presented by Farrah et al. (2017). In this sense, and due to the small number of false positives in absolute terms, even a small number of obscured AGN eluding an observational study could affect the resulting simulated merger fraction. To accurately estimate the contribution of Compton-thick AGN and their influence on the AGN merger fraction, comprehensive modeling based on the best observational estimates is imperative.

5.4.2. The Effect of Limited Resolution

Another possible explanation for the merger-like appearance of the false-positive AGN attributes the cause to the resolution limit of TNG300 and its effects on the calculation of the mass accretion rates of the BHs. The kernel-weighted accretion rate is derived by averaging the properties of the surrounding gas over a sphere of radius h such that the volume contains a number of cells approximately equal to a predefined number n_{ngb} (Weinberger et al. 2017). For the three realizations TNG100-1, -2, and -3, the number of cells considered is 256, 128, and 64, respectively, with an uncertainty of ± 4 cells. Considering that the highest resolved version of

TNG300 on which this work is based on has the same resolution as TNG100-2, ~ 130 cells are used to calculate the accretion rate.

Quantitatively, the corresponding median radius h for the HE AGN sample yields ~ 1.3 kpc, which is significantly larger than the radius of the sphere of influence of a typical SMBH by a factor of $\sim 10^3$. This means that in TNG300, virtually any modeled galaxy with a sufficiently high gas content on galaxy scales could automatically be defined a priori as an AGN if the gas is suitably distributed. Conversely, this also means that a source with a relatively low gas content is more likely to be classified as inactive.

This fact is also reflected in the HE AGN and the selected control galaxies. As discussed in Section 5.3.3, the sources in the AGN sample still show a continuous growth of stellar mass and thus active star formation, with a significant amount of gas present in these systems. In contrast, the inactive galaxies with a lower median sSFR by 1.5 dex and a possible decreasing gas mass seem to have stopped their buildup of stellar mass. This means that when considering the scale for calculating the accretion rate, the instantaneous accretion rates of the sources classified as AGN are more likely to be affected than those of the control galaxies, leading to potentially biased estimates on an individual basis, especially for high values of the Eddington ratio.

Accordingly, by definition, due to a lower gas abundance and a resulting lower SFR, the inactive galaxies should also have a smoother appearance in the simulations. This fact is confirmed by the low values of M_{20} for the inactive galaxies determined by statmorph. Since the majority have an $M_{20} < -1.6$, they follow the typical description of smooth sources with bright cores (Lee et al. 2013).

Unlike in the simulation, in reality it is not necessary for the SFR to be different between the AGN hosts and the control galaxies. With a high gas abundance on these kpc scales, the probability of an AGN increases, but due to the much smaller sphere of influence of the SMBH, this is not mandatory. It follows that stellar mass growth and AGN activity, while possibly the consequence of the same physical process(es), are not directly causally related (Drouart et al. 2016; McAlpine et al. 2017; Suh et al. 2019; Carraro et al. 2020). Therefore, in contrast to the simulation, the classification into active and inactive sources does not depend on the gas abundance on large scales, but only on the gas content within the central pc and the actual accretion onto the SMBH.

This difference in the physical scales considered for the accretion rate calculation could explain, at least in part, the excess of false positive AGN. Although these AGN do not show a clear difference in h when compared to the other AGN, the strongly asymmetric and patchy appearance is likely the result of a large gas abundance. With the derived value of $h \simeq 1.3$ kpc, a large fraction of this gas is used to calculate the mass accretion rate of the SMBH. In at least some cases, this

could cause sources to erroneously end up within the AGN selection limits. Especially considering, on the one hand, that these sources have Eddington ratios close to or even at the Eddington limit imposed by the simulation and, on the other hand, also considering the relatively limited size of the HE AGN sample, even a few incorrectly selected sources can result in a significantly different merger fraction.

It is highly probable that the cause of the visual misclassifications of AGN is an entanglement of several factors of varying relevance, such as selection effects, the effect of the resolution limit of the simulation, and the inclusion of AGN that would be excluded in an observational study because of their obscuration. However, because of the degeneracy of these factors, it is nearly impossible to pinpoint the actual cause(s). Only through more advanced analyses involving various redshifts as well as BH masses and Eddington ratios could it be possible to potentially quantify the influence of these factors (see also Section 8.2). Also, only then can the effects on the selection and the implications on the derived merger fractions be addressed.

However, due to the rarity of AGN with the highest Eddington ratios, comparatively large simulation boxes are required to analyze this population in a statistically meaningful number. Elaborate zoom-in simulations may resolve the accretion physics, but are far from providing a representative number for the AGN studied in this work. Therefore, the best, but so far unrealistic, solution would be a simulation with a volume similar to TNG300 or larger and a resolution comparable to TNG50 or higher.

Part III.

AGN with the Highest Eddington Ratios in the Local Universe

6. Investigation of the Relation Between Mergers and AGN at Low Redshift

In contrast to $z \simeq 2$, a comparable population of local AGN host galaxies at $\lesssim 0.2$ shows up to a $\sim$ 10 times lower BH activity and star formation rate (Aird et al. 2015). Hence, not only the mean BH accretion rate (Delvecchio et al. 2015; Aird et al. 2019), but also the cold gas fraction (e.g. Santini et al. 2014; Popping et al. 2015) of a galaxy is much lower at $z \lesssim 0.2$ than at $z \simeq 2$. Moreover, only a small fraction ($\lesssim 10\%$) of present-day massive galaxies ($\log(M_\star/\mathrm{M}_\odot) > 10$) may have undergone one or more major merger events since $z \sim$1, with the majority of such galaxies being undisturbed in the last $\sim$ 7 Gyr (López-Sanjuan et al. 2009; Lotz et al. 2011; Xu et al. 2012). As a result, other physical processes may be expected to dominate at such a low redshift, making it necessary to also investigate the role of major mergers in triggering AGN at such a cosmic time. Despite the expected low overall merger rates at low redshifts, especially for the special population of AGN that exhibits the highest Eddington ratio, major mergers may still be the only viable option to supply enough gas to the SMBH to achieve such high specific accretion rates.

The premise is identical to the analysis of AGN at $z \simeq 2$. To test for a causal link between major mergers and AGN, 17 galaxies hosting AGN with $\lambda_{\mathrm{Edd}} > 0.3$ at $z \lesssim 0.2$ and 25 matching inactive control galaxies are visually analyzed with respect to the degree of possible morphological distortions. The results are then in turn validated against possible influences by methodology or systematic effects.

All magnitudes are again given in the AB system (Oke & Gunn 1983) and the same concordance cosmology is assumed as in Chapter 4, with $\Omega_\Lambda = 0.7, \Omega_0 = 0.3$, and $h = 0.7$. At the sample mean redshift of $z \sim 0.15$, *B*- and *V*- roughly correspond to the rest frame *U*- and *B*-bands.

6.1. Data

The sizes of the two samples are based on the goal of identifying, with respect to a matched sample of inactive galaxies, a possible excess of large merger signatures in AGN host galaxies. A merger fraction for the control sample of inactive sources of $f_{\mathrm{m,\,Ina}} = 0.15$ serves as a baseline condition to identify for a merger fraction of the AGN host galaxies of $f_{\mathrm{m,\,AGN}} \geq 0.5$ a significant difference between these two fractions with $\sim 99\%$ confidence. Since this confidence can only increase for smaller values of $f_{\mathrm{m,\,Ina}}$ (or even larger values of $f_{\mathrm{m,\,AGN}}$) and to ensure this desired level of confidence, this rather large value for $f_{\mathrm{m,\,Ina}}$ is used. In contrast, previous works predict rather a value of $f_{\mathrm{m,\,Ina}} < 0.10$ (e.g. Lotz et al. 2011; Man et al. 2016; Mundy et al. 2017). Therefore, this fiducial merger fraction is expected to represent an upper limit on the real merger rate for inactive galaxies in the investigated mass and redshift range.

Since the number of AGN with high Eddington ratios available for observations is limited at $z \lesssim 0.2$, the sample of AGN host galaxies is created first and then the number of inactive galaxies required to meet the confidence criterion is derived. With the final sample sizes, one can then conclude whether or not AGN host galaxies show a significant increase in merger rates, indicating a causal dependence of this particular population of AGN on major mergers.

6.1.1. AGN Host Galaxies

The AGN sample is compiled from the catalogs of the Hamburg/ESO survey (HES, Schulze & Wisotzki 2010), the Palomar Green Survey (PG, Vestergaard & Peterson 2006), and the SDSS DR7 (Shen et al. 2011). The selection of potential targets is restricted to sources with a redshift of $z \lesssim 0.2$. Since an estimate of the central BH mass is required and the focus lies on AGN with the highest specific accretion rates, only unobscured broad line AGN with an Eddington ratio of $\lambda_{\mathrm{Edd}} \geq 0.3$ are selected. BH mass determinations based on single-epoch Hβ measurements and bolometric luminosities are used to derive λ_{Edd}. The latter are determined using the luminosities at 5100 Å and multiplying them by a bolometric correction factor of $k_{\mathrm{bol}} = 9$ (Schulze & Wisotzki 2010; Netzer 2019). Both BH masses and luminosities at 5100 Å are taken from the respective catalogs.

The applied threshold for the minimum BH mass of $\log(M_{\mathrm{BH}}/\mathrm{M}_{\odot}) = 7.7$, leads to a mean BH mass for the AGN sample of $\log(M_{\mathrm{BH}}/\mathrm{M}_{\odot}) \sim 8.0$. Using the $\mathrm{M_{BH}} - \mathrm{M_{bulge}}$ scaling relation of Kormendy & Ho (2013) as a proxy to predict the stellar host galaxy masses, the corresponding mean stellar mass for the AGN host galaxies yields $\log(M_{\bigstar}/\mathrm{M}_{\odot}) \sim 11$. This mass selection leads to feasible exposure times for the inactive galaxies, which must be of equal stellar mass. This also allows to compare the results reported in this chapter with those presented in the previous

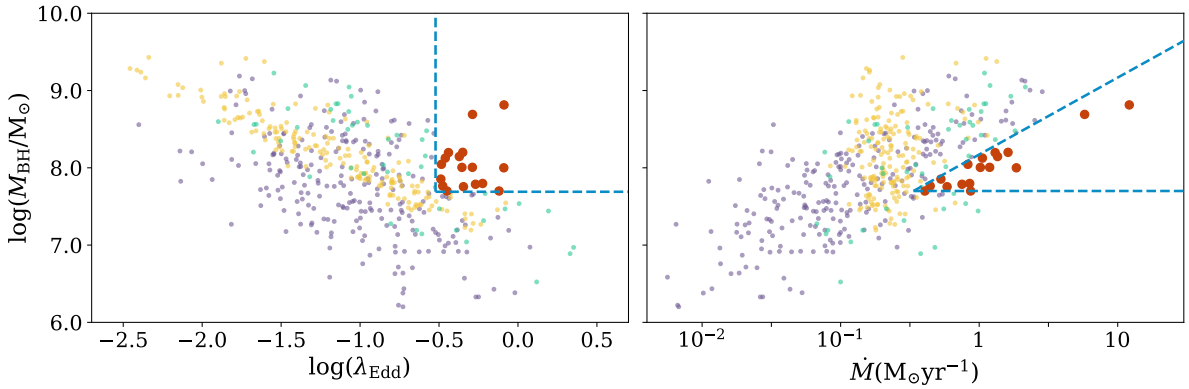

Figure 6.1.: *Left*: Eddington ratio λ_{Edd} vs BH mass M_{BH} for the parent samples and the final selection of AGN at redshift $z \lesssim 0.2$. Given in purple, green, and yellow are the suitable sources from the HES, SDSS DR7, and PG catalogs, respectively. Overplotted are the selection limits in M_{BH} and λ_{Edd} (blue box) and the final selection of AGN (red points). *Right*: BH mass accretion rate $\dot{M}$ vs M_{BH} for the same samples, indicating that the final selection consists of AGN that have the highest specific accretion rates.

Chapters 4 and 5, which have been calculated for similar stellar host masses. In addition, only targets with a declination of $\mathrm{dec} < +15°$ were selected to ensure better visibility with the *VLT*. All these constraints result in a total number of 19 suitable AGN host galaxies, 17 of which are observed with *VLT FORS2* in the *V* and *B* bands (ESO programs 091.B-0672(A), 095.B-0773(A), and 098.A-0241(A), PI: Knud Jahnke). The median redshift of these 17 sources is $z = 0.15$.

The left panel of Figure 6.1 summarizes the selection process. The smaller colored points show the respective parent catalogs (with HES in purple, PG in green, and SDSS in yellow), while the blue box shows the limits set in the parameter space for the final selection of the AGN. The final selection is indicated by the larger red points. Since the AGN have high Eddington ratios ($\lambda_{\mathrm{Edd}} > 0.1$), a possible trend of decreasing radiative efficiency η at low accretion rates (Churazov et al. 2005; Weinberger et al. 2018; Nelson et al. 2019a) does not need to be taken into account and one can derive the BH mass accretion rates $\dot{M}$ (Figure 6.1, right panel) according to Equation (1.8). The right panel of Figure 6.1 highlights that the AGN with the highest specific accretion rates, i.e. those with the highest absolute mass accretion rates relative to their BH masses, are targeted.

Each target was observed with at least three long exposures to detect large-scale distortion features down to *B* and $V \sim 23.4\ \mathrm{mag/arcsec^2}$, and with three short exposures to obtain an unsaturated image of the bright central region. The actual single exposure times are 430 s and 14 s for *B* and 150 s and 8 s for *V*, respectively. Table 6.1 summarizes the properties of the AGN sample and gives the corresponding catalog designations, redshifts, apparent I-band magnitudes,

AGN designation	z	m_{I} mag	L_{5100} erg s^{-1}	L_{bol} log(L$_\odot$)	FWHM Hβ (km s^{-1})	M_{BH} log(M$_\odot$)	λ_{Edd}	$\dot{M}$ M$_\odot$yr^{-1}
(1)	(2)	(3)	(4)	(5)	(6)	(7)	(8)	(9)
HE0119–2836	0.12	14.8	44.92	12.29	3363.00	8.2	0.36	1.3
HE0132–0441	0.15	15.8	44.81	12.18	1719.00	8.0	0.44	1.0
HE0157+0009	0.16	16.1	44.73	12.10	2369.00	7.8	0.60	0.9
HE0444–3449	0.18	16.0	44.83	12.20	1714.00	8.1	0.35	1.1
HE0558–5026	0.14	15.5	44.88	12.25	1583.40	8.0	0.51	1.2
HE1201–2408	0.14	16.8	44.45	11.82	1820.86	7.8	0.33	0.4
HE1226+0219	0.16	13.2	45.89	13.26	3835.03	8.8	0.82	12.1
HE1228+0131	0.12	14.4	44.93	12.31	1866.19	8.1	0.43	1.4
HE2011–6103	0.12	16.3	44.53	11.90	2862.51	7.9	0.32	0.5
HE2152–0936	0.19	14.2	45.56	12.93	2183.42	8.7	0.52	5.8
HE2258–5524	0.14	15.9	44.68	12.05	2419.42	7.8	0.54	0.8
PG1001+054	0.16	16.3	44.74	12.11	1700.00	7.7	0.76	0.9
PG1012+008	0.19	16.2	45.01	12.38	2615.00	8.2	0.45	1.6
PG1211+143	0.09	14.3	45.07	12.44	1817.00	8.0	0.81	1.9
SDSSJ0322+0055	0.18	16.1	44.72	12.09	2440.00	8.0	0.33	0.8
SDSSJ1050+1132	0.13	15.7	44.57	11.94	1906.00	7.8	0.45	0.6
SDSSJ1243+0917	0.19	16.8	44.41	11.78	1979.00	7.7	0.36	0.4

Table 6.1.: Properties of the sampled AGN: columns 1–3, 6, and 7 are taken from the respective catalogs (Vestergaard & Peterson 2006; Schulze & Wisotzki 2010; Shen et al. 2011). The bolometric luminosities L_{bol} in column 5 are calculated by applying a bolometric correction factor of $k_{\mathrm{bol}} = 9$ to L_{5100}(Schulze & Wisotzki 2010; Netzer 2019). Column 6 presents the FWHM of the broad component of Hβ. The Eddington ratios λ_{Edd} and BH mass accretion rates $\dot{M}$ in columns 8 and 9 are calculated by using the bolometric luminosities L_{bol}, the respective BH masses M_{BH}, and a radiative efficiency parameter of $\eta = 0.1$

luminosities at 5100 Å, L_{5100}, and the bolometric luminosities derived by applying a correction factor of $k_{\mathrm{bol}} = 9$ to L_{5100} (Schulze & Wisotzki 2010; Netzer 2019). In addition, the catalog values for the FWHM of the single-epoch measurements of the (broad) $H\beta$ line, the respective BH masses M_{BH}, the calculated Eddington ratios λ_{Edd}, and mass accretion rates $\dot{M}$ are given as well.

6.1.2. Inactive Comparison Sample

Given the size of the AGN sample and the assumptions for the merger fractions for the AGN and control samples ($f_{\mathrm{m,\,AGN}} \geq 0.5$ and $f_{\mathrm{m,\,Ina}} = 0.15$), at least 25 inactive galaxies must be observed to meet the criterion of detecting a difference in these merger fractions with $\sim 99\%$ confidence.

The comparison galaxies are randomly selected from a parent sample of ∼2900 galaxies that are part of the SDSS MPA/JHU catalog (Kauffmann et al. 2003b; Brinchmann et al. 2004). Similar to the AGN, the initial selection restricts sources to declinations of $\mathrm{dec} < 10^{\circ}$ and redshifts of

Galaxy designation	α(J2000) deg	δ(J2000) deg	z	m_{I} mag	$M_{\star}$ log($\mathrm{M}_{\odot}$)
Gal000232	0.164	–0.013	0.08	16.9	11.0
Gal003114	2.083	–0.772	0.16	17.8	11.0
Gal030481	19.605	–9.962	0.11	17.8	11.0
Gal050873	34.151	–8.233	0.18	18.1	11.0
Gal079769	50.365	–6.309	0.16	18.0	11.0
Gal095873	58.093	–6.748	0.09	16.6	11.0
Gal176221	132.158	7.598	0.13	17.9	11.0
Gal185580	133.941	3.320	0.12	17.2	11.0
Gal204260	137.351	9.810	0.16	18.0	11.0
Gal210148	138.539	4.123	0.14	17.3	11.0
Gal221730	140.921	–0.891	0.14	18.5	11.0
Gal270096	150.303	–0.089	0.10	17.5	11.0
Gal286443	153.515	7.057	0.10	17.2	11.0
Gal347112	164.300	6.874	0.14	17.7	11.0
Gal391560	171.878	–2.142	0.10	17.1	11.0
Gal419090	176.075	–1.720	0.11	17.1	11.0
Gal458007	181.927	1.421	0.11	17.5	11.0
Gal498251	188.551	–1.446	0.16	17.7	11.0
Gal510223	190.692	0.540	0.08	17.0	11.0
Gal510224	190.692	0.540	0.08	17.0	11.0
Gal534882	195.327	–0.937	0.19	18.2	11.0
Gal557614	199.167	9.361	0.17	17.8	11.0
Gal656010	215.724	8.849	0.14	17.3	11.0
Gal676011	218.892	0.672	0.11	17.2	11.0
Gal698144	222.606	6.647	0.16	18.0	11.0
Gal782980	236.689	–0.860	0.07	16.1	11.0

Table 6.2.: The designations (column 1), coordinates (columns 2 and 3), redshifts (column 4), k-corrected and dereddened I-band magnitudes (column 5), and photometric median stellar masses taken from the MPA/JHU catalog (Kauffmann et al. 2003b; Brinchmann et al. 2004) of the inactive control galaxies.

$z \lesssim 0.2$, resulting in a median redshift of $z \sim 0.13$ for the control sample. In addition, only sources that possess comparable stellar masses to the AGN host galaxies are selected.

As described in Section 6.1.1, the $\mathrm{M_{BH}} - \mathrm{M_{bulge}}$ scaling relation is adopted from Kormendy & Ho (2013) to infer the mean stellar host masses for the AGN sample from the provided BH masses. Accordingly, the inactive galaxies are constrained to a small range around the mean derived stellar mass of the AGN host galaxies, $\log(M_{\star}/\mathrm{M}_{\odot}) = 11 \pm 0.01$. Finally, all potential sources are vetted against hard X-ray AGN signatures (Baumgartner et al. 2013) to remove all galaxies with an obscured AGN. Taken from the MPA/JHU catalog, Table 6.2 lists the coordinates, redshifts, k-corrected and dereddened I-band magnitudes, and median stellar masses of the comparison galaxies.

With the exception of one source[1], all 25 galaxies in the final sample have been observed in the *B* and *V* bands using an observational setup comparable to that used for the AGN host galaxies. Each target was observed with at least three individual 470 s and 180 s long exposures in *B* and *V*, respectively. This selection and observation approach allows to analyze a sample of AGN hosts and inactive comparison galaxies, respectively, that match in redshift, stellar (host) mass, observational depth, spatial resolution, filter band, and S/N. Thus, a direct comparison can reveal possible relative differences in the merger fractions of the two populations.

6.1.3. Reduction and Post-processing

A seeing of 1″ or better is required to diagnose large-scale merger signatures at a minimum required spatial resolution of ∼2.5 kpc at the mean redshift of the sample. Therefore, before reducing the raw images, the average seeing for each individual exposure is automatically determined by measuring the FWHM of 100 local peaks, using the package astropy photutils (Bradley et al. 2019), and calculating the corresponding median FWHM of all sources. After visually inspecting and remeasuring each individual image with a median FWHM $> 1''$, all individual images with a median FWHM above this threshold are dismissed. Of the total $\sim$ 450 frames, 22 are excluded from the subsequent reduction and analysis. Despite the exclusion of these images, each object is observed with at least three exposures per band.

The data processing pipeline THELI[2] (Erben et al. 2005; Schirmer 2013) is used to perform all initial data reduction steps, i.e. bias and flat field correction, sky background subtraction, astrometry and alignment, and combination of the individual exposures. The resulting pixel scale of 0.″252 corresponds to ∼0.7 kpc at the median redshift of the samples. To generate color images, the respective *B*- and *V*-band observations are combined with MultiColorFits[3] (Cigan 2019).

To ensure that the samples are directly comparable, the appearance of the AGN host galaxies is mimicked in the images of the inactive galaxies by adding a synthetic point source on top of the respective flux centers. To this end, within the central image regions around each inactive galaxy, the 15 brightest unsaturated stars are detected using the DAOStarFinder algorithm within the photutils package. For each galaxy, one of the detected stars is then visually selected, cropped, and upscaled in flux so that it has a central brightness comparable to HE2152–0936, the second brightest source in the AGN sample. As part of this procedure, noise in the outer regions is also scaled down. Since upscaling by a constant factor would result in a noticeable discrepancy in flux between the galaxy and the edge of the artificially enhanced point source, the original point

[1] Due to weather losses, one target was observed only in the *V*-band.
[2] https://www.astro.uni-bonn.de/theli/gui/index.html
https://github.com/schirmermischa/THELI
[3] https://multicolorfits.readthedocs.io

sources are fitted with a two-dimensional Gaussian to determine a circular region with a radius of 5σ around the brightest pixel. This region is then divided into five bins, where the amount by which the pixel values are upscaled depends on which bin they lie in. For the innermost bin, i.e. within 1σ, the total scaling factor is applied, while for the outermost bin, i.e. between 4 and 5σ, a scaling factor lower by 5×10^{-4} is used. For the bins in between, a multiple of the scaling factor is chosen so that the distribution of the scaling factor with radius follows a Gaussian function.

This approach produces point sources that resemble the central regions of AGN host galaxies, but also blend unrecognizably and smoothly into the images of the respective inactive galaxies. After adding these point sources, the appearances of AGN host galaxies and control galaxies are indistinguishable. The point sources are similar in size to the $\sim 1''$ upper limit set for the seeing, while the typical diameter of the galaxies, both AGN and inactive, is on the order of 5–6″. Thus, unlike for the study of strongly accreting AGN at $z \simeq$2, there is no need to model and subtract point sources for the samples at $z \lesssim 0.2$.

Examples of an AGN host galaxy and an inactive comparison galaxy are shown in Figure 6.2. The left (a) and middle columns (b) show the *V* and *B* band images, while the right column (c) depicts the color images. To optimize the visibility of large-scale structures and possible merger signatures while blending out the brightest inner regions, different parameters are chosen for the color cuts and maps for the single band images as well as the color images. Within a set, i.e. *V*-, *B*-band or color images, however, the parameters are constant. Moreover, the Gaussian two-pixel smoothing is applied only to the color images. Given the different visualization of the sources, i.e. single band images at different wavelengths or composite images, one can test whether the subsequent distortion rankings and thus the resulting merger fractions depend on the observed wavelength.

6.2. Morphological Analysis and Merger Fractions

As a result of post-processing, all sources can no longer be visually identified as AGN or inactive. In a next step, both samples are combined, resulting in a final sample of 42 sources in the *V*-band and 41 in the *B*-band or color. Using the same approach as for the study of observed and simulated AGN at $z \simeq 2$, the merger fractions are derived by 19 experts proficient in working with imaging data of galaxies. They perform a visual assessment of the targets and rank them from most to least disturbed, taking into account the occurrence of large-scale distortion features[4].

[4] The ranking was done by Irham Andika, Eduardo Bañados, Vardha Bennert, Seth Cohen, Bernd Husemann, Knud Jahnke, Melanie Kaasinen, Anton Koekemoer, Victor Marian, Masafusa Onoue, Jan-Torge Schindler, Malte Schramm, Andreas Schulze, John Silverman, Irina Smirnova-Pinchukova, Arjen van der Wel, Carolin Villforth, and Rogier Windhorst.

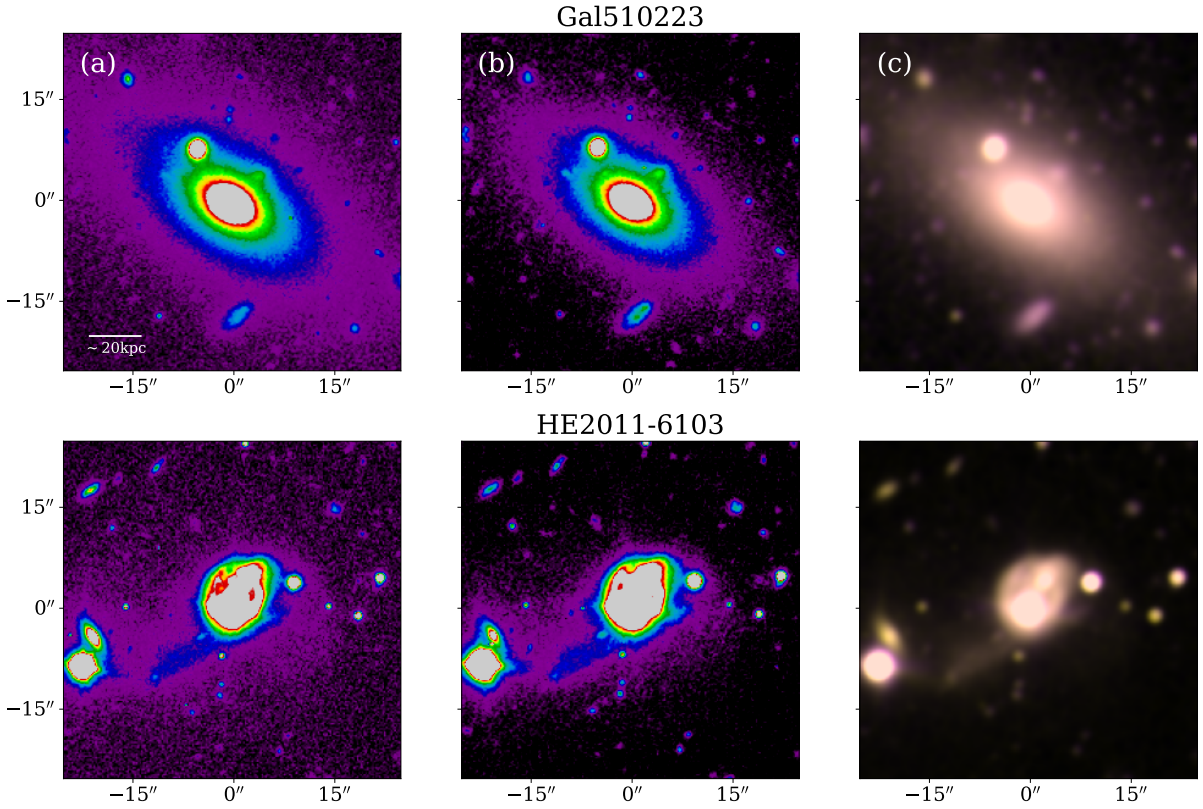

Figure 6.2.: Two sources representative of the objects studied. The top row shows one of the comparison galaxies, while the bottom row presents one of the AGN. From left to right, the columns each show a stamp in the (a) *V* band, (b) *B* band, and (c) in color. Note: To improve visibility, the images are not shown with the same crop and color map parameters.

These features are indicative of ongoing or recent major merger events. Each set of *V*, *B*, and color images is evaluated independently by each expert.

Again, each classifier's individual perception of the classification of a major/minor merger applies equally to AGN host galaxies and comparison galaxies, since the sources are not identifiable as active or inactive in the joint sample. Therefore, in the subsequent analysis, any personal subjectivity in the classification will have the same impact on each of the two subsamples. To further reduce any systematic bias, the data sets provided to each of the 19 ranking experts are randomized. Each classifier is also asked to choose a cutoff rank above which all sources are unambiguously classified as merging or at least show signs of recent gravitational perturbation, such as asymmetries, tidal tails, or binary nuclei. Any galaxy with a rank greater than the cutoff is interpreted as being completely free of perturbations originating from interactions. In the

following, this parameter is used to determine the merger fractions of the two samples. It is also investigated whether these results show a dependence on different cutoff ranks.

The 57 individual rankings (19 experts times three sets) are combined into three consensus sequences for each respective set. The methods introduced in Section 2.1 are used to combine the individual rankings, a task that is repeated for each set, i.e. separately for *B*-, *V*-, and color images. Eventually, by applying all three methods to all three sets, nine overall rankings are obtained. A variety of cutoff ranks are selected, and the combined rankings are again separated into AGN host galaxies and comparison galaxies. Then, for each selected cutoff rank, the merger fractions are derived as before by counting how many active and inactive galaxies are above and below that threshold. Those numbers serve again as input for a and b in the calculation of the respective beta distributions' PDFs.

Figure 6.3 shows the corresponding means and standard deviations for the PDFs of the merger fractions. These values have been calculated for each combination of method and set and for four different cutoffs at ranks 5, 10, 15, and 20. The merger fractions increase with cutoff rank, as this is equivalent to more galaxies being above this threshold and thus being considered a merger. There is no indication that the choice of combination method or set affects the resulting merger fractions. For all combinations, the results for a given sample and cutoff rank are within the error limits or even identical. However, it is also evident that for cutoff ranks $\lesssim$15, the merger fractions for the AGN host galaxies (Figure 6.3, top row) are significantly larger than the fraction of perturbed inactive galaxies (Figure 6.3, bottom row). This is not the case for larger cutoff ranks.

In Figure 6.4, the continuous trend of merger fractions with cutoff rank is now visualized for all combinations of method and set. The AGN host galaxies and the inactive galaxies are shown in blue and red, respectively. The shaded regions denote the 1σ confidence interval from shot and classification noise. Identical to the analysis for the merger fractions at $z \simeq 2$, and as already indicated in Figure 6.3, Figure 6.4 also shows that the choice of method used to combine the individual rankings does not significantly affect the resulting absolute merger fractions or the relative differences between them. Since no discrepancies are found between the results for the *V*, *B*, or the composite set, the same conclusion holds with respect to the choice of set. Since the AGN host galaxies show a significant excess of merger fractions compared to the inactive comparison sample for cutoff ranks $\lesssim$15, this clearly shows that the conclusions depend significantly on the choice of this parameter. The impact that the choice of cutoff rank has on the identified merger fractions and the possible causal relationship between major mergers and the triggering of AGN is discussed in the following section.

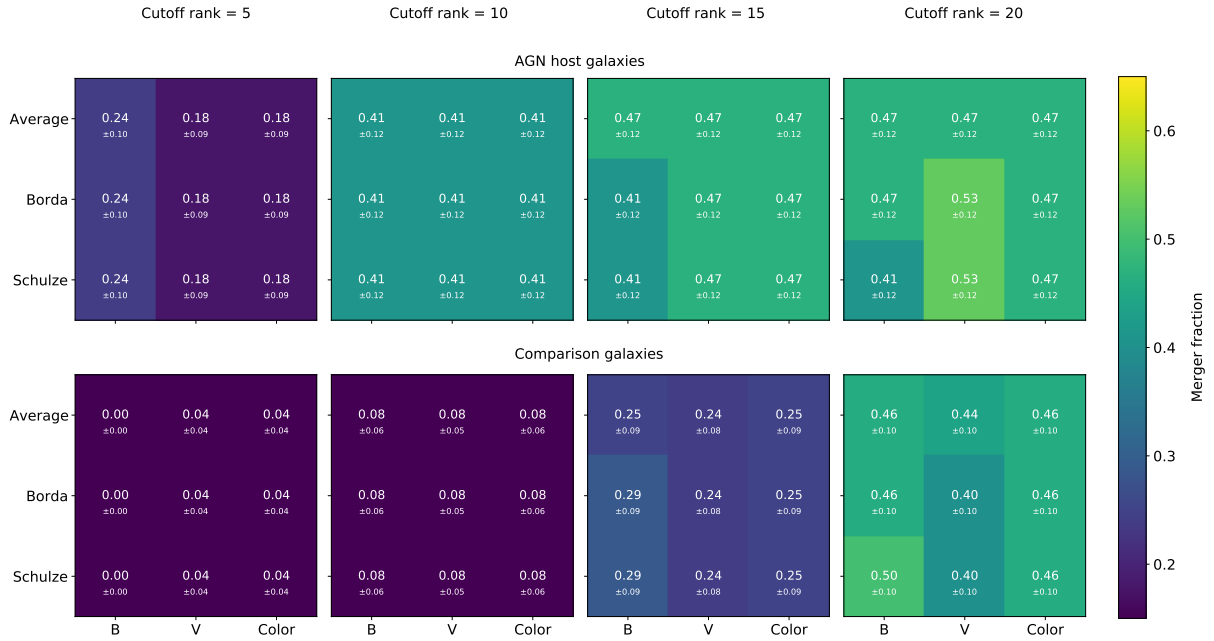

Figure 6.3.: The merger fractions for each set (images in B, V, and color) and aggregation method (average, Borda, Schulze) for four different cutoff ranks. The top row shows the corresponding fractions of perturbed AGN host galaxies, and the bottom row analogously represents the fraction of merging inactive comparison galaxies. The smaller numbers below the actual values of the merger fraction indicate the standard deviations (i.e. 1σ) of the corresponding beta distributions.

6.2.1. Constraining the Absolute Merger Fractions

As mentioned above, the merger fractions for the two samples of 17 AGN host and 25 inactive comparison galaxies depend on the choice of cutoff rank. In the following, two approaches are used to constrain the derived merger fractions. In the first, the choice of cutoff rank is based on the experts' opinion, while in the second method, this limit is constructed so that the resulting merger fraction of the inactive control sample is consistent with the merger rates presented in the literature. For the first approach, the mean values of the individual cutoff ranks chosen by each classifier for each set are calculated. The average cutoff ranks are 21±8, 22±9, and 18±8 for the B, V, and color sets, respectively.

The reason for such high cutoff ranks, which almost bisect the joint samples, is most likely due to the visual determinations of the experts. Since the galaxies are well resolved, smaller asymmetries can be easily identified. However, these do not necessarily have to be the result of a major merger event, but can also be from a minor merger or of secular origin. Nonetheless, this leads classifiers to place these particular sources in the merger bin, i.e. above the cutoff rank, which increases the percentage of galaxies classified as merging. With a corresponding cutoff

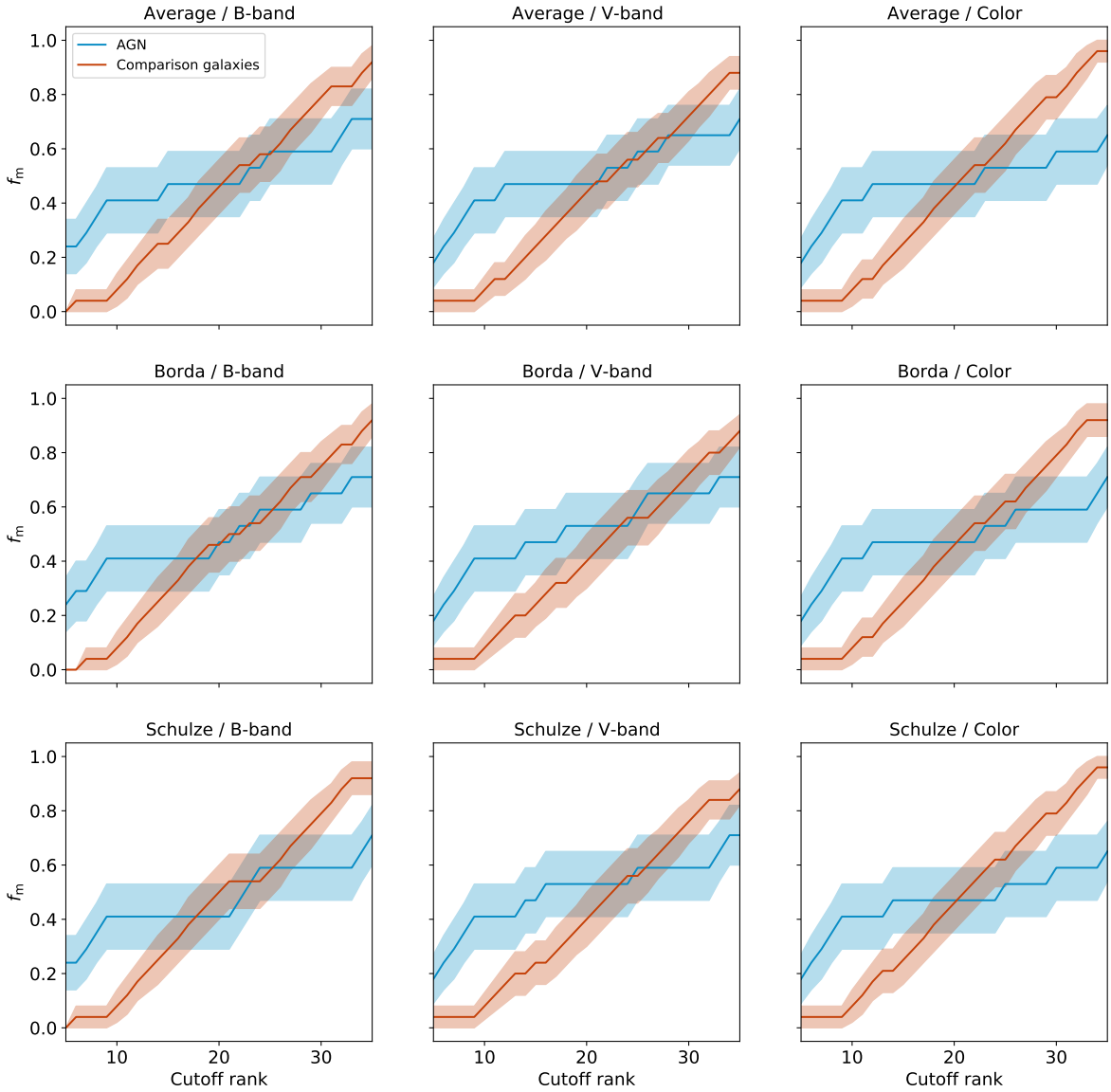

Figure 6.4.: Evolution of the merger fractions for the AGN host galaxies (blue) and inactive galaxies (red) as a function of cutoff rank for each combination of set and method. The shaded regions indicate the 1σ confidence interval.

rank = 20, the merger fractions, depending on the combination method, range from $f_{\mathrm{m,\,AGN}} = 0.41 \pm 0.12$ to $f_{\mathrm{m,\,AGN}} = 0.53 \pm 0.12$ for the AGN sample and $f_{\mathrm{m,\,Ina}} = 0.40 \pm 0.10$ and $f_{\mathrm{m,\,Ina}} = 0.50 \pm 0.10$ for the inactive sample. Therefore, the percentages of disturbed sources in the two samples are not significantly different, which would indicate a negligible contribution of mergers of any strength to the triggering of AGN.

However, the primary goal is to determine the influence of major mergers on the formation of AGN without taking into account the effects of minor gravitational encounters or other processes that shape the morphology of a galaxy. Therefore, the determined merger fractions must be corrected for the contamination from sources with small asymmetries. Such a high merger rate of ~ 40-50% indicates that about half of the population shows evidence of a recent or ongoing gravitational encounter of any strength. This clearly exceeds the original assumption of the major merger rate for the inactive galaxies (see Section 6.1) and also the estimates of previous studies (Lotz et al. 2008b,a, 2011; Bridge et al. 2010; Xu et al. 2012; Casteels et al. 2014; Man et al. 2016; Ventou et al. 2017, 2019; Duncan et al. 2019; O'Leary et al. 2020). Based on these studies, a major merger rate per galaxy of $R_{\mathrm{m}} \sim 0.05\ [\mathrm{Galaxy}^{-1}\,\mathrm{Gyr}^{-1}]$ is assumed. This value represents the number of galaxies that are currently part of a major merger divided by the timescale of the visibility of the associated merger signatures. To obtain an absolute merger fraction representative for the comparison sample, one needs to multiply this rate by the timescale t_{m} in which a major merger is observable. This property depends not only strongly on the mass ratio, individual masses, and gas fractions of the two progenitor galaxies, but also on the depth of the observations. Considering the low redshifts and surface brightnesses of the target galaxies, a comparatively conservative value of $t_{\mathrm{m}} \sim 1.5\,\mathrm{Gyr}$ is chosen, resulting in a major merger fraction of $f_{\mathrm{m}} \sim 0.08$ for galaxies that lie in mass and redshift ranges that are comparable to those of the objects examined in this study. Such a value for the merger fraction for the comparison galaxies corresponds to a cutoff at rank 10. Coincidentally, at this position the respective merger fractions are identical across all sets and methods for each of the two samples (Figure 6.3), yielding $f_{\mathrm{m,\,AGN}} = 0.41 \pm 0.12$ for the AGN host galaxies and $f_{\mathrm{m,\,Ina}} = 0.08 \pm 0.06$ for the control galaxies. This value of $f_{\mathrm{m,\,Ina}}$ is not only in excellent agreement with the major merger rates observed in the 3D-HST survey of Man et al. (2016) for all five fields (AEGIS, COSMOS, GOODS-N, GOODS-S, UDS) found in CANDELS (Grogin et al. 2011; Koekemoer et al. 2011), but also for the major merger fractions identified by MUSE observations (Ventou et al. 2017, 2019). Similarly, studies by Duncan et al. (2019) in CANDELS and by Mundy et al. (2017) in GAMA report comparable values.

The two resulting PDFs of the corresponding beta distributions of the major merger fractions are shown in Figure 6.5, with blue and red representing the AGN sample and the comparison sample, respectively. The shaded regions represent the 1σ intervals and the solid and dotted lines show the corresponding means and modes. Due to the small number of merging control galaxies, the associated PDF appears considerably skewed, with the corresponding mean value deviating considerably from the peak position. Therefore, the merger fraction associated with the mode of this distribution is also given and yields $f_{\mathrm{m,\,Ina}} \sim 0.04$, which is still well within the uncertainties of the mean. Thus, for a cutoff at rank 10, these resulting merger fractions yield

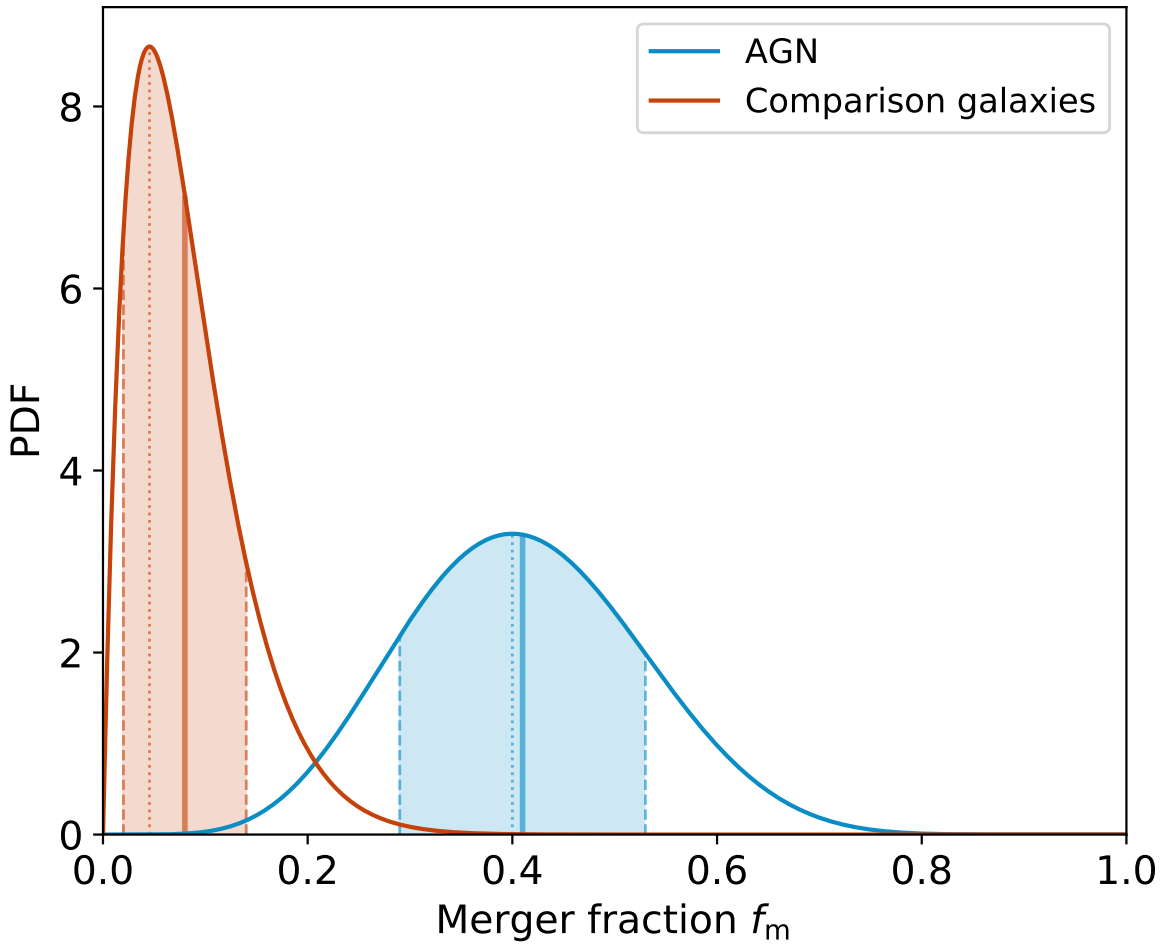

Figure 6.5.: PDFs for the derived merger fractions for AGN with the highest Eddington rates at $z \lesssim 0.2$ (blue) and a comparison sample of inactive galaxies (red). Both PDFs are based on a cutoff rank $= 10$. The solid and dotted lines show the mean and modes of the respective merger fractions, while the dashed lines and shaded regions represent the central 68% confidence intervals. At this particular cutoff rank, the respective merger fractions are identical for all combinations of method and set.

– 7 AGN hosts and

– 2 inactive galaxies showing merger features;

– 10 AGN hosts and

– 23 inactive galaxies showing no merger features.

The order and appearance of the sources in the different consensus rankings is not necessarily congruent. For example, the seven AGN host galaxies classified as merger could vary in the different consensus rankings. However, despite different ranks, the same objects are found at the first eight positions in each combined ranking, with seven of them being the same AGN host galaxies. Of these seven targets, five are from the HES sample, while one each is listed in the SDSS and PG catalogs. Since a total of 11 AGN are selected from the HES catalog and three each from the SDSS and PG catalogs, it is most likely that the parent catalogs from which the AGN host galaxies are drawn do not introduce any bias with respect to the morphological classification. A repeated visual inspection also confirms that a distinction into merging and non-merging systems at this very cutoff rank shows a striking separation into sources with clearly discernible large-scale merger features such as tidal tails and shells and galaxies with significantly less pronounced asymmetries.

Eventually, a singular overall ranking is created by applying the Schulze method to the nine consensus rankings (see Appendices D and E). The same sources that occupy the first eight ranks in the nine initial consensus sequences also populate the highest positions in this final ranking. Therefore, after reapplying a cutoff at rank 10, the results remain unchanged for both merger fractions.

Given the appearance of seven AGN host galaxies among the eight highest ranked sources and the significant excess in major merger fraction for the AGN host galaxies, with a significant difference of $> 2.5\sigma$ with respect to the inactive sample, it can be concluded that major mergers are an essential triggering mechanism for AGN with the highest Eddington ratios at $z \lesssim 0.2$.However, based on the cumulative distribution function (CDF) for the AGN merger fraction, there is only a $\sim 22\%$ probability that the merger fraction is above the threshold of $f_{\mathrm{m,\,AGN}} = 0.5$. This implies that although major mergers at this redshift are indeed an important mechanism in triggering the specific population of AGN, more than half of the SMBHs still need to be activated by other means, such as secular processes or minor mergers. The role of the latter in triggering AGN with the highest specific accretion rates at low redshifts is discussed in the following Section 6.2.2.

6.2.2. The (Un)Importance of Minor Mergers

In the previous Section 6.2.1, it is argued that the initial high merger fraction of the sample of control galaxies is due to the fact that the experts included galaxies in the merger category that exhibit features that are only the consequence of minor merger events. Lotz et al. (2011) state that the minor merger rate is $\sim$ three times the major merger rate, where a minor merger is defined identical to the definition in IllustrisTNG, such that the progenitor galaxies have a mass ratio of 1:4 $< M_{\mathrm{sat}}/M_{\mathrm{primary}} \lesssim$ 1:10. Assuming the major merger fraction for the inactive

galaxies to be correct, the merger fraction that takes major and minor mergers into account yields $f_{\mathrm{m,\,Ina}} = 0.33 \pm 0.09$ for these objects. This would correspond to a cutoff at a rank of 17 and thus to a total merger fraction for the AGN host galaxies of $f_{\mathrm{m,\,AGN}} = 0.47 \pm 0.12$. Evidently, the difference between these two merger rates is much smaller, and indeed, for the singular overall ranking, eight inactive galaxies and eight AGN are above this cutoff .

However, while all classifiers can easily agree on the most distorted galaxies, it should be noted that sources with minor asymmetries are more difficult to categorize. As a result, the rank of a given galaxy with such features may differ greatly across the individual expert rankings, which in turn could also affect to some extent the resulting overall rank and thus the actual number of sources that are considered merging in the final ranking. Nonetheless, this scatter is not expected to be substantial. With only one AGN host but eight inactive galaxies added to the merger category, it appears that only a small fraction of AGN are found in this region of less distorted sources. Therefore, it is evident that the number of AGN host galaxies showing weak perturbation features is much smaller than that of the comparison galaxies. This suggests that minor merging is comparatively unimportant and the rest of the AGN require a different triggering mechanism.

6.3. Testing for a Trend in Luminosity and Potential Time Lags

6.3.1. AGN Merger Fraction and Luminosity

Although the AGN for sources at $z \lesssim 0.2$ can be considered luminous, it is important to note that they are not selected based on absolute luminosity. Rather, the AGN with the highest Eddington ratios, i.e. the sources with the highest accretion rates and luminosities relative to their BH masses, are chosen. With the exception of two AGN – HE1226+0219 and HE2152-0936, which have bolometric luminosities of $\log(L_{\mathrm{bol}}) > 46.5\left[\mathrm{erg\ s^{-1}}\right]$ – all the remaining AGN in the sample have luminosities of $45.3 \lesssim \log(L_{\mathrm{bol}}\left[\mathrm{erg\ s^{-1}}\right]) \lesssim 46$, but at the same time possess the smallest BH masses in this luminosity range ($7.7 < \log(M_{\mathrm{BH}}/\mathrm{M}_{\odot}) < 8.2$).

In fact, ~ 10 more luminous AGN would have been selectable in the three original parent catalogs. In contrast to other studies finding an increased merger rate for luminous AGN, there is no clear trend in the strength of merger features – i.e. rank – with either BH mass or BH mass accretion rate/luminosity within the AGN sample (Figure 6.6). Thus, HE1226+0219 and HE2152–0936, both with significantly higher absolute mass accretion rates compared to the other sampled AGN, only occupy the ranks ~ 30 and ~ 25 in all consensus rankings and clearly do not exhibit significant merger features. However, since the selection of AGN is based on a combination of BH mass and Eddington ratio, it is notable that apart from the two most luminous

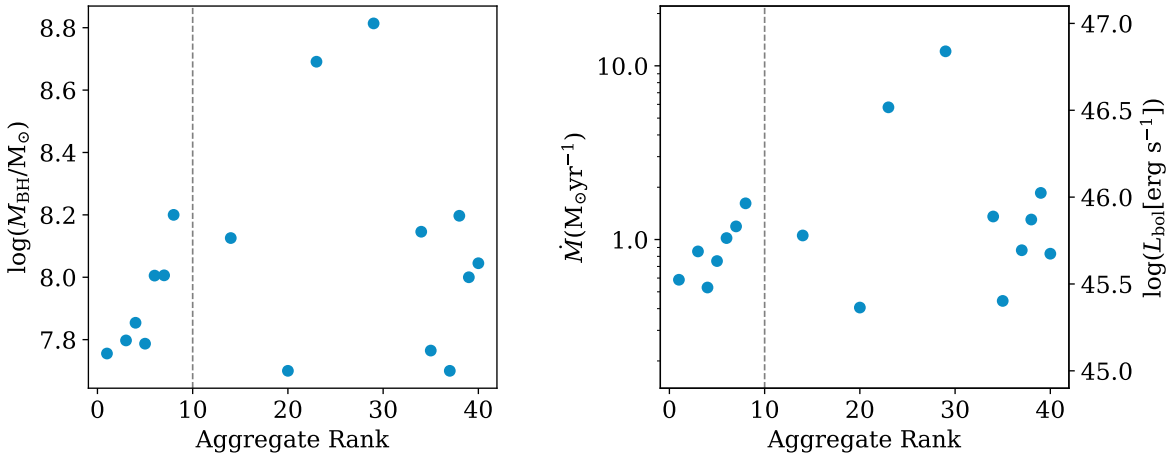

Figure 6.6.: Consensus rank of the examined AGN vs. BH mass M_{BH} (*left*) and mass accretion rate $\dot{M}$ as well as bolometric luminosity L_{bol} (*right*). The vertical dashed line visualizes a cutoff at rank 10 that is used in the analysis.

AGN mentioned above, the sources cover a relatively narrow luminosity range. Nevertheless, because of the lack of an obvious correlation of the merger fraction with AGN luminosity, the results require an alternative explanation – especially since the existence of such a trend has not yet been clearly proven. Although some studies have found evidence for such a correlation between merger rate and luminosity (Treister et al. 2012; Fan et al. 2016; Goulding et al. 2018), others have not (Villforth et al. 2014, 2017; Hewlett et al. 2017).

6.3.2. Estimation of Recent AGN in Mergers

Since major mergers trigger only a maximum of $\sim 50\%$ of the AGN examined in this study, the question remains open as to which other process(es) is (are) responsible for triggering AGN with high Eddington rates at $z \lesssim 0.2$. With this question in mind, a possible influence of different time scales is considered. Previous studies that found no significant difference in the distortion fractions of AGN and a matched sample of control galaxies analyzed a possible disparity in the lifetimes of AGN and mergers as an explanation for their results (Cisternas et al. 2011; Mechtley et al. 2016). The unanimous conclusion is consistent with the estimates presented in Section 4.3.1 that the difference in the lifetimes of merger features and AGN is not sufficient to explain the lack of excess in merger rates because the time scale over which merger features are observable is significantly longer than the lifetimes of the respective AGN. In Section 4.3.1, the same conclusion is drawn for the highly accreting AGN at $z \simeq 2$. However, since this study shows a significant

difference in the merger fractions of the AGN host galaxies and the control galaxies, respectively, it is reasonable to repeat this calculation in a reverse fashion.

A scenario is considered in which some of the galaxies that do not host a visible AGN and have only minor distortions are actually the result of a major merger event that also led to a past phase of active SMBH growth. However, since the lifetimes of AGN can be much shorter compared to those of major merger features, small asymmetries would be the only detectable remnants of such a gravitational encounter. This implies that, if the cumulative fractions of minor and major mergers that are derived in Section 6.2.2 are used, a fraction of the $33 \pm 9\%$ inactive galaxies showing distortions of different strengths have indeed hosted an AGN triggered by a major merger in the past. As a result, the AGN major merger fraction of $f_{\mathrm{m,\,AGN}} = 0.41 \pm 0.12$ would increase, suggesting that major mergers are not only an essential but perhaps even the dominant mechanism for triggering high Eddington rate AGN at $z \lesssim 0.2$.

Following the scenario outlined by Goulding et al. (2018), the number of intermittent AGN is also estimated (see Section 4.3.2 for the definition of such AGN). It should be noted that one cannot distinguish between such AGN and past AGN that are not reignited. However, since only the eventual increase in the AGN merger fraction is important, the origin of this increase is irrelevant.

Equation (4.1) is used to constrain the fraction $f_{\mathrm{m,\,Ina\,\&\,AGN}}$ of distorted inactive galaxies that have hosted an AGN in the recent past or currently host an intermittent AGN. Again, t_{AGN} and f_{AGN} represent the lifetime and the fraction of the studied AGN, with respect to the total galaxy population in the examined redshift and mass range. The time scale at which the merger features are observable is given by t_{m}, while $f_{\mathrm{m,\,AGN}}$ describes the total merger fraction of the specific AGN population. As for the AGN at $\simeq 2$, f_{AGN} is derived by using the number densities based on the stellar mass and quasar bolometric luminosity functions at $z \sim 0$, taking into account the studied stellar mass range and the mean bolometric AGN luminosity.

Using the respective median I-band luminosities, this yields $\log\Phi \sim -2.9$ Mpc^{-3} mag^{-1} for the total galaxy population (Hirschmann et al. 2014; Henriques et al. 2015; Furlong et al. 2015; Lacey et al. 2016; Pillepich et al. 2018b) and $\log\Phi \sim -5.8$ Mpc^{-3} mag^{-1} for the particular population of AGN (Hopkins et al. 2007; Fanidakis et al. 2012; Hirschmann et al. 2014; Sijacki et al. 2015), resulting in $f_{\mathrm{AGN}} \sim 1.3 \times 10^{-3}$. This estimate is in excellent agreement with the value reported by Schulze & Wisotzki (2010) for the fraction of active BHs that have a redshift $z < 0.3$ and a mass of $\log(M_{\mathrm{BH}}/\mathrm{M}_{\odot}) \sim 8$, similar to the properties of the SMBHs studied here. For $f_{\mathrm{m,\,AGN}}$, the derived value of $f_{\mathrm{m,\,AGN}} = 0.47 \pm 0.12$ is used, but calculations for $f_{\mathrm{m,\,AGN}} = 0.30$ and 0.70 are performed as well. In addition to the initial estimate of $t_{\mathrm{m}} = 1.5 \times 10^{9}$ yr (see Section 6.2.1), $t_{\mathrm{m}} = 10^{9}$ yr is adopted for comparison. Finally, in agreement with previous studies, the AGN

lifetime t_{AGN} is constrained to be between 10^6 and 10^8 yr (Martini 2004; Hopkins et al. 2005; Shen et al. 2007; Hopkins & Hernquist 2009; Conroy & White 2013; Cen & Safarzadeh 2015).

Since one cannot distinguish between merging inactive galaxies that have already gone through their AGN phase, will only host an AGN in the future, or are currently hosting an intermittent AGN, it is not necessary to consider a time lag (Hopkins et al. 2006b; Wild et al. 2010; McAlpine et al. 2020) between the onset of the actual phase of active BH growth and the beginning/coalescence of the merger. Thus, from a timescale perspective, the result depends only on the relative difference between AGN and merger lifetimes, and thus the fraction of inactive merging galaxies that have already hosted an AGN can only be considered as an upper limit. However, a visual follow-up revealed only a small number of galaxies with asymmetries that actually have a close companion. Therefore, it appears that most of the distorted galaxies are already in the late stages of their merger process, suggesting that, if anything, they have already experienced a potential AGN phase where the probability of an AGN becoming active again is low.

The total merger fraction of inactive galaxies, i.e. $f_{\mathrm{m,\,Ina}} \sim 0.35$, serves as an upper bound for $f_{\mathrm{m,\,Ina\,\&\,AGN}}$. If both parameters are equal, this would mean that all distorted inactive galaxies have hosted (or will host) an AGN. Conversely, $f_{\mathrm{m,\,Ina\,\&\,AGN}} = 0$ would mean that no such galaxy has ever hosted (or will host) an AGN. Figure 6.7 shows the results of the calculations for different $f_{\mathrm{m,\,AGN}}$ and $t_{\mathrm{m}} = 10^9$ yr (left) and 1.5×10^9 yr (right). The blue lines and shaded regions represent the results for the determined AGN merger fraction and the corresponding 1σ intervals, while the purple and yellow lines represent the trend for $f_{\mathrm{m,\,AGN}} = 0.30$ and 0.70, respectively. The fraction of merging inactive galaxies hosting an AGN at some point during the merger process increases with shorter AGN lifetimes. Moreover, for a given period of AGN activity, this fraction grows with longer merger timescales and larger AGN merger fractions, both due to an increased probability of finding a distorted galaxy that actually hosts an AGN. Depending on the merger timescale and assuming that the lower limit on the AGN merger fraction is correct, one can derive a lower bound on the AGN lifetime by considering each inactive distorted galaxy as a host for an AGN, i.e. $f_{\mathrm{m,\,Ina\,\&\,AGN}} \equiv f_{\mathrm{m,\,Ina}}$. The lifetime of an AGN then corresponds to a minimum of 1.3×10^6 yr and 1.9×10^6 yr for merger timescales of 10^9 yr and 1.5×10^9 yr, respectively (Figure 6.7, dotted lines).

Again based on the current best estimates for accretion rate histories (Di Matteo et al. 2005; Johansson et al. 2009a,b; Hopkins & Quataert 2010; Jung et al. 2018), the time period during which an AGN is above $\lambda_{\mathrm{Edd}} > 0.3$ is assumed to be on the order of $t_{\mathrm{AGN}} = 10^7$ yr. Note that this value is a factor of 10 larger than in the similar study at $z \simeq 2$ because the cumulative duration of an AGN observed at $\lambda_{\mathrm{Edd}} \gtrsim 0.3$ is expected to be longer than for $\lambda_{\mathrm{Edd}} \gtrsim 0.7$.

The derived fractions of inactive merging galaxies that also host an AGN at any time then yield $f_{\mathrm{m,\,Ina\,\&\,AGN}} = 0.06^{+0.01}_{-0.02}$ and $0.09^{+0.02}_{-0.02}$ for $t_{\mathrm{m}} = 10^9$ yr and 1.5×10^9 yr, respectively (Figure 6.7,

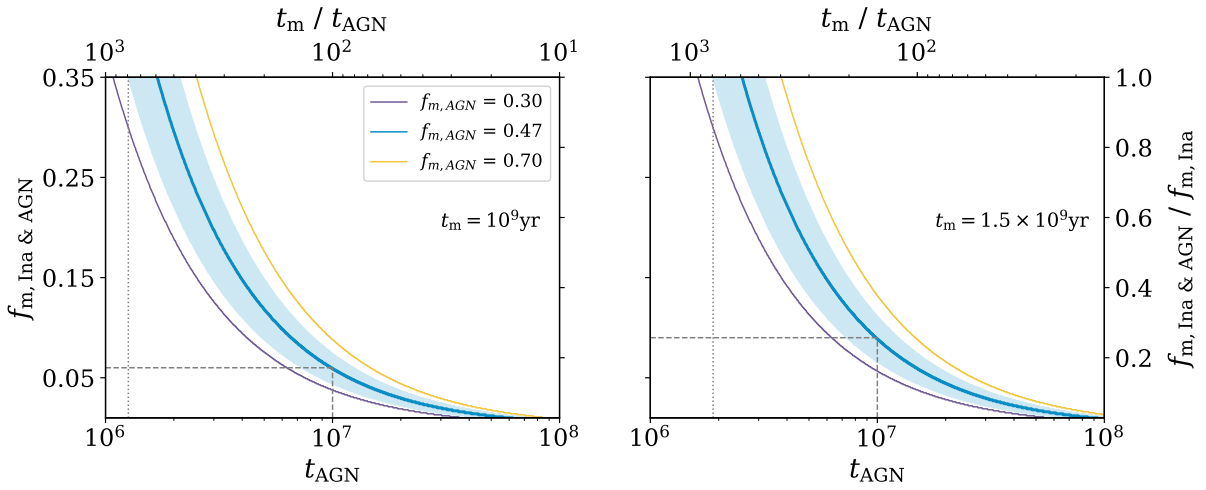

Figure 6.7.: Total fraction of merging inactive galaxies that hosted an AGN in the recent past $f_{\mathrm{m,\,Ina\,\&\,AGN}}$ as a function of AGN lifetime t_{AGN} for a merger timescale t_{m} of 10^9 yr (left) and t_{m} =1.5 $times10^9$ yr (right). The blue line enclosing the shaded area represents the result of the AGN merger fraction of $f_{\mathrm{m,\,AGN}}$ = 0.47 ±0.12, which accounts for major and minor mergers. The purple and yellow lines correspond to $f_{\mathrm{m,\,AGN}}$ = 0.30 and 0.70, respectively. The dotted line corresponds to a lower limit of t_{AGN}, and the dashed lines show the resulting $f_{\mathrm{m,\,Ina\,\&\,AGN}} \sim 0.09$ for an assumed $t_{\mathrm{AGN}} = 10^7$.

dashed lines). Thus, adding even the upper limit of this fraction to the AGN major merger rate derived in Section 6.2.1 yields only a revised fraction just above the threshold of 0.5. This result still leaves $\sim 50\%$ of AGN of unknown origin. Only by assuming a much lower AGN duty cycle of $t_{\mathrm{AGN}} \sim 10^6$ yr, and thus considering almost every distorted inactive galaxy to host an AGN, one can obtain AGN major merger fractions of $\sim 80\%$, which then leaves no doubt about the role of major mergers in triggering AGN with high Eddington rates at $z \lesssim 0.2$. Therefore, it is reasonable to conclude that neither a difference in the time scales of AGN and merger nor the possible presence of intermittent AGN significantly affect the inferred AGN merger rate. This conclusion is also consistent with the finding above that only a negligible number of AGN are hosted by galaxies with minor asymmetries. If a difference in timescales were important, then a substantial number of AGN should be expected to reside in host galaxies that show only the fading features of a past major merger event, i.e. minor distortions. However, just the opposite is true. Either most AGN are in highly disturbed or completely undisturbed sources. As for $z \simeq 2$, more detailed simulations predicting, in particular, AGN timescales as a function of accretion rate are imperative to better constrain the derived estimates.

Part IV.

Discussion and Conclusions

7. Consolidation of Results

This work focuses on the role of major mergers in triggering AGN with the highest Eddington ratios at $z \simeq 2$ and $z \lesssim 0.2$. Observations and subsequent visual morphological classifications of suitable AGN and matched samples of inactive control galaxies are used to determine the impact of such major mergers on SMBH growth. In addition, a comparable analysis is performed on simulated AGN to assess the validity of the observational results at $z \simeq 2$.

In the observational study at $z \simeq 2$, the derived major merger fractions yield $f_{\mathrm{m,\,AGN}} = 0.24 \pm 0.09$ and $f_{\mathrm{m,\,Ina}} = 0.19 \pm 0.04$, respectively. By using the extensive data set of IllustrisTNG, the merger fractions of comparable samples of AGN and control galaxies at $z \simeq 2$ are evaluated. Whereas the analyses of the true merger histories and an automatic classification of the galaxy morphologies lead to major merger fractions that are in excellent agreement with the observations, the same visual approach that is used in the observational inspection leads to deviating results. The reason for this divergence is not yet clear and requires further investigation. Besides the influence of selection effects or obscured AGN, the limited resolution of the simulation most likely plays a significant role. Although the resolution is sufficiently high to resolve large-scale distortions, its limit may affect the calculations of the instantaneous accretion rates and hence the selection considerably. However, the primary goal of studying the merger fractions produced by a cosmological simulation is to determine how well the observations can recover the true merger rates. In this sense, a comparison with simulated merger fractions that account for observational uncertainties and are based on the true merger histories is most appropriate. Such an approach for comparable samples at $z \simeq 2$ yields $f_{\mathrm{m,\,AGN}} = 0.27 \pm 0.07$ and $f_{\mathrm{m,\,Ina}} = 0.22 \pm 0.01$ and is in excellent agreement with the observational results. Examination of the local AGN counterparts at $z \lesssim 0.2$ shows a significant increase in the major merger fraction when compared to a control sample, yielding $f_{\mathrm{m,\,AGN}} = 0.41 \pm 0.12$ and $f_{\mathrm{m,\,Ina}} = 0.08 \pm 0.06$.

Figure 7.1 summarizes the main results of this work by showing the probability density distributions of the found merger fractions. Since it serves as a reference point for the other studies, the middle panel shows the PDFs of merger fractions derived in the observational study at $z \simeq 2$. For comparison, the left and right panels show the merger fractions found by examining the low-redshift sources and the results obtained by applying different methods to the IllustrisTNG

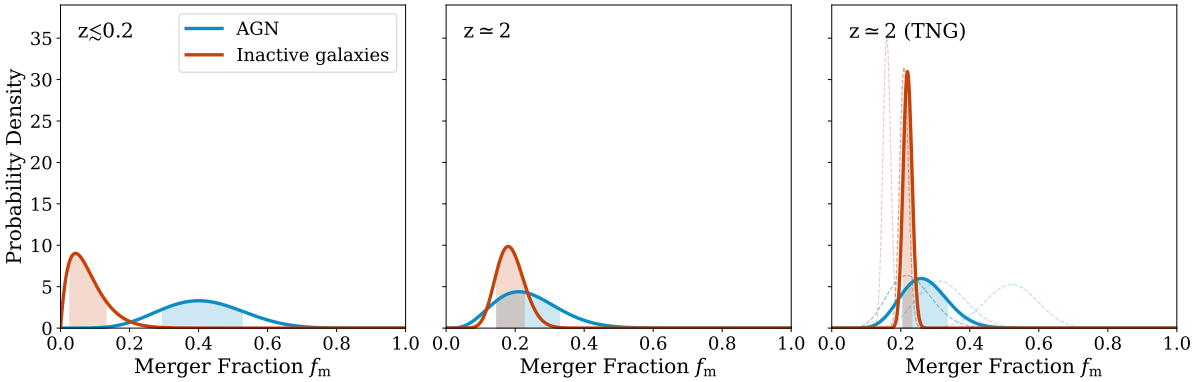

Figure 7.1.: From left to right, the panels show the PDFs for the major merger fractions of the sources at $z \lesssim 0.2$, the galaxies at $z \simeq 2$, and the simulated comparison samples at $z \simeq 2$, respectively. The AGN host galaxies are shown in blue, while the red lines represent the matched control galaxies. The highlighted PDFs in the panel showing the result of the IllustrisTNG simulation are based on the iteratively sampled merger histories after accounting for typical uncertainties from SDSS observations.

data, respectively. The blue and red lines represent the results for the corresponding AGN sources and samples of inactive galaxies, respectively. The highlighted distributions in the panel showing the IllustrisTNG results are based on the iteratively sampled merger histories after accounting for characteristic observational uncertainties. The remaining PDFs visualize the results derived via the other methods discussed in Section 5.2. The shaded regions represent the intervals from the 16th to 84th percentiles.

In all three separate studies, the methods used to aggregate the individual visual classifications do not affect the final results, which are in excellent agreement with each other. Also, the choice of the cutoff that separates the joint samples into merging and undisturbed objects within the final consensus visual classifications results in merger fractions for the inactive galaxies that reproduce the merger rates of the general galaxy population at similar stellar masses and redshifts. Finally, possible time delays between mergers and the presence of AGN, as well as potential intermittent AGN, do not fundamentally affect any of the derived results.

7.1. Interpreting the Difference in AGN Major Merger Fractions

Regardless of the redshift, the underlying data, or the applied methodology, the excellent agreement between the major merger fractions of the inactive galaxies is visible in Figure 7.1. The same conclusion can be drawn for the AGN major merger fractions at $z \simeq 2$. With the exception of the result based on the visual classification of the IllustrisTNG sources, all calculations lead to similar results. This not only confirms that the results of the observational

study are not affected by any observational limitations, but also that the major merger fractions of AGN with the highest Eddington ratios at $z \simeq 2$ and of mass- and redshift-matched inactive galaxies are not significantly different. Consequently, major mergers are not the dominant cause of SMBH growth at cosmic noon. In contrast, the $z \lesssim 0.2$ AGN studied in this work show a significant excess of major merger fraction when compared to a control sample of inactive galaxies. This suggests that major mergers play a more pronounced role in triggering the AGN with the highest Eddington ratios at low redshifts.

Neglecting for a moment the results of the study of the simulated AGN that confirm the observational results, consideration is now given to the different epochs of the studied AGN and the possible observational features associated with them that might explain the difference in the absolute AGN merger fractions at $z \simeq 2$ and $z \lesssim 0.2$. One factor to keep in mind is certainly surface brightness dimming and the impact it has on the detection of possible weak morphological distortion features. With a drop in surface brightness of $\sim$5 mag/arcsec^2 at $z \simeq 2$, merger features observed at $z \lesssim 0.2$ will be missed at this redshift. This effect may be enhanced by the fact that galaxies at $z \simeq 2$ are on average more compact than at $z = 0$ (e.g. van der Wel et al. 2014).

Furthermore, if the triggering of an AGN immediately follows a starburst caused by a galaxy merger, the resulting potentially extensive amount of dust may more easily obscure the starburst at $z \simeq 2$ than at $z \lesssim 0.2$. In the lower redshift case, the starburst can equally occur in the outer spiral arms and tidal streams of the galaxy, while the starburst in a galaxy at $z \simeq 2$ is much more confined to the central region due to its more compact nature. Therefore, in addition to the difference in surface brightness dimming between $z \simeq 2$ and $z \lesssim 0.2$, a more complex situation is possible where the visibility of an AGN host galaxy at $z \simeq 2$ is reduced not only by surface brightness dimming but also by obscuring dust.

Thus, the AGN merger fraction at $z \simeq 2$ could be significantly underestimated, which could explain the discrepancy in the derived AGN major merger rates. Consequently, this would lead to the conclusion that a substantial proportion of AGN with the highest Eddington rates at $z \simeq 2$ are actually also triggered by major mergers. However, in this study, the main conclusions are drawn by comparing the respective AGN samples with matched control samples of inactive galaxies at the same redshifts and determining primarily the relative differences between the respective merger fractions. Thus, the relevance of major mergers for the growth of SMBHs can be determined independently of the absolute values.

Under the reasonable assumption that the mechanisms causing the detectable morphological features are identical between the respective AGN host galaxies and their corresponding inactive counterparts, the merger fractions at $z \simeq 2$ are equally affected by surface brightness dimming. As a consequence, this effect need not be taken into account if one focuses only on the relative

differences in the merger fractions. Similarly, a merger-driven starburst that produces a large amount of obscuring dust can occur in both an inactive galaxy and a system that will host an AGN triggered by this merger event. Therefore, the dust would only affect the results at $z \simeq 2$ if the dust obscured the actual AGN, leading to a misclassification of these particular sources as inactive galaxies. However, the assessment of the relevance of hidden and intermittent AGN at $z \simeq 2$ performed in this work, which would implicitly include such sources, does not yield a significant effect on the resulting merger rates. Furthermore, only Type I AGN were selected for both observational studies, minimizing the likelihood that sources obscured by dust would affect the reported results. Therefore, similar to the surface brightness dimming, the effect of obscuring dust can be neglected when primarily considering the relative difference in merger fractions at $z \simeq 2$.

The major merger fractions for both observational samples of inactive galaxies at $z \simeq 2$ and $z \lesssim 0.2$ are consistent with previous findings on major merger rates for galaxies at comparable redshifts and masses (Man et al. 2016). In particular, for the study at $z \simeq 2$, the choice of cutoff is not tuned to the published merger rates. Prior to the analysis performed in this work, the overall merger fraction of galaxies at $z \simeq 1$ has been expected to be about a factor of 2 higher than at $z = 0$ (e.g. Lin et al. 2004; Bridge et al. 2010). Towards larger redshifts, simulations have predicted a further increase proportional to $(1+z)^2$ (Fakhouri & Ma 2008), leading to an estimated merger fraction of $\sim 20\%$ for the inactive galaxies. Despite the lack of any constraints, the result for $f_{\mathrm{m,\,Ina}}$ at $z \simeq 2$ is in excellent agreement with these expectations and also previous studies.

For instance, Snyder et al. (2019) obtain in their study comparable values by using synthetic images from the original ILLUSTRIS simulation and comparing them with CANDELS observations. In addition, Ventou et al. (2017, 2019) report similar values using spectroscopic *Multi Unit Spectroscopic Explorer (MUSE)* observations in the MUSE deep fields by applying close pair counts. For their subsample of massive galaxies ($\log(M_\star/\mathrm{M}_\odot) > 9.5$), whose mass range is almost identical to that of the samples studied in this work, they find merger fractions of $0.232^{+0.112}_{-0.056}$ and $0.195^{+0.142}_{-0.081}$ for the redshift ranges $1 \leq z \leq 2$ and $2 \leq z \leq 4$, respectively. Thus, although the goal was not to obtain consistent absolute values for the merger fractions, but rather to determine a possible relative difference between AGN and control galaxies, the estimated merger fractions of the inactive galaxies are clearly consistent with these other recent observations and simulations.

These agreements confirm the results presented in this work and suggest that surface brightness dimming or dust does not indeed significantly affect the merger fractions at $z \simeq 2$. Thus, even without validation of the observational results through the simulated data, it can be ruled out that observational effects are the reason for the discrepant results, necessitating an alternative

explanation for the excess in the merger fraction for the studied subpopulation of AGN at low redshift.

In addition to the mean BH accretion rate/bolometric luminosity and Eddington ratio of an AGN (Schulze et al. 2015), in particular, the cold gas fraction of a galaxy at $z \lesssim 0.2$ is significantly smaller than for a counterpart at $z \simeq 2$ (e.g. Santini et al. 2014; Popping et al. 2015). Since the AGN in both redshift samples have comparable Eddington ratios, but the sources at lower redshifts have a substantially smaller intrinsic gas reservoir, it is reasonable to assume that at $z \simeq 2$ enough gas is still present to fuel the central supermassive BH via mechanisms other than major mergers, while at $z \lesssim 0.2$ this process is essential to trigger AGN with the highest specific accretion rates. A similar observation is made by Silva et al. (2021). They attribute the similar fractions of AGN in merging and non-merging galaxies at high redshift to the higher abundance of cold gas. Finally it should be noted, however, that despite the excess of major merger fraction for the local AGN host galaxies, $\gtrsim 50\%$ of the sample nevertheless do not appear to be triggered by such an event.

7.2. Results in Context with Previous Studies

Similarly to this work, the majority of previous studies addressing the role of (major) mergers in the triggering and fueling of AGN are based on observations in the optical/IR wavelength range and an evaluation of neighborhood counts or the respective morphology of the observed host galaxies by means of non-parametric diagnostics, such as asymmetry, concentration, G, and M_{20}, or visual inspection, usually after considering and subtracting the central point source.

Particularly luminous AGN still seem to follow the decades-old paradigm that SMBH growth is primarily a causal consequence of major mergers. Corresponding results are reported by Treister et al. (2012), Hong et al. (2015), and Goulding et al. (2018), who analyze luminous AGN ($\log(L_{\mathrm{bol}}) > 45 \left[\mathrm{erg\ s^{-1}}\right]$) in a combined redshift range of $0 \lesssim z \lesssim 3$. Especially, with a merger fraction of $\sim\ 44\%$ for luminous AGN at $z \lesssim 0.3$ and with comparable bolometric luminosities, the results published in Hong et al. (2015) are highly consistent with the distortion rate found for the local sample of AGN studied in this work. Similar results are also reported by Gao et al. (2020) for their sample of AGN at $0 < z < 0.6$, who derive a merger fraction of $\sim 40\%$ and an overall increase in the distortion incidence with stellar mass.

In addition to luminous AGN, obscured AGN also appear more likely to be connected with major merger events. It should be noted, however, that this is to be expected, as focusing on obscured sources most likely introduces a bias towards merging systems, as this obscuration may be caused by dust within a merging (U)LIRG-like host. With this caveat in mind, Glikman et al.

(2015), Fan et al. (2016), and Donley et al. (2018) all detect merger fractions $> 50\%$ for such reddened or obscured AGN sources at $z \sim 2$, $z \sim 3$, and $0 < z < 5$, respectively. Although with $f_{\mathrm{m,\,AGN}} = 0.20^{+0.07}_{-0.05}$ and $f_{\mathrm{m,\,Ina}} = 0.04^{+0.02}_{-0.01}$ smaller in absolute terms, Cotini et al. (2013) also find evidence for a higher incidence of mergers in their X-ray study of obscured AGN. The findings of Weston et al. (2017) and Urbano-Mayorgas et al. (2019) also suggest a merger induced SMBH growth for obscured AGN at lower redshifts. Similarly, and while only $\sim 1\%$ of their control sources exhibit merger features, Koss et al. (2010) and Koss et al. (2018) report an increased AGN merger fraction of $\sim 18\%$ for their sample of moderately luminous AGN detected in hard X-ray light at $z \lesssim 0.07$.

In contrast, Schawinski et al. (2012), Zakamska et al. (2019), and Zhao et al. (2019a) find in their studies of obscured AGN in a redshift range of $0 \lesssim z \lesssim 3$ no evidence that mergers are the predominant triggering mechanism of such AGN. Similarly, Cisternas et al. (2011), Hewlett et al. (2017), and Villforth et al. (2017) detect no excess of AGN merger fractions in their studies for their selection of luminous AGN with bolometric magnitudes of $\log(L_{\mathrm{bol}}) > 44\big[\mathrm{erg\ s^{-1}}\big]$. For their objects in a redshift range of $0.3 \lesssim z \lesssim 2$, they instead consistently report AGN merger fractions of $\sim 15 - 20\%$, a value identical to the results presented in this paper for both the observed and simulated AGN at $z \simeq 2$.

As for lower luminosities, numerous works draw the same conclusion. For example, Grogin et al. (2005), Gabor et al. (2009), and Böhm et al. (2013) evaluate neighboring counts and/or various morphological indices, e.g., asymmetry A, concentration C, Gini coefficient G, and M_{20} index, but find no significant causality between major mergers and AGN. Similarly, Allevato et al. (2011), Schawinski et al. (2011), and Rosario et al. (2015) detect no redshift evolution of the morphological properties for similar AGN up to $z \simeq 2.5$. In particular, the derived value of $16.7^{+5.3}_{-3.5}\%$ of moderately luminous strongly disturbed AGN at $z \simeq 2$ published by Kocevski et al. (2012), is in excellent agreement with the merger fraction for AGN at this redshift presented here. For a wide range of luminosities, Villforth et al. (2014) find no increase in merger signatures with luminosity and also report consistent distortion fractions between the AGN and the comparison galaxies for their sample of observed low and intermediate luminosity AGN ($41 \lesssim L_X[\mathrm{erg\ s^{-1}}] \lesssim 44.5$) at $0.5 \lesssim z \lesssim 0.8$. In contrast, Silverman et al. (2011) find an enhanced merger prevalence for AGN of moderate X-ray luminosity in spectroscopic pairs at $z \lesssim 1$. However, their rate of $17.8^{+8.4}_{-7.4}\%$ is still consistent with the absolute values obtained in this work for AGN at $z \simeq 2$.

With respect to more specific AGN populations, Mechtley et al. (2016) find at $z \simeq 2$ a similar incidence of mergers for 19 galaxies hosting the most massive SMBH ($9 < \log(M_{\mathrm{BH}}/\mathrm{M}_{\odot}) < 10$) and a sample of 84 matched inactive galaxies. In fact, their merger fraction ratio of $f_{\mathrm{m,\,AGN}}/f_{\mathrm{m,\,Ina}} =$

1.30 ± 0.33 is identical to the result of both studies at $z \simeq 2$ presented in this paper. Also, AGN that are in their earliest stages of evolution do not show a dominant connection with major mergers (Villforth et al. 2019).

Finally, other studies approached the question from the opposite direction by investigating the occurrence of AGN in mergers. While Ellison et al. (2019) and Secrest et al. (2020) identify an excess of AGN in mergers at low redshifts ($z \lesssim 0.2$), Silva et al. (2021) find in their study for a wide redshift interval of $0.3 \lesssim z \lesssim 2.5$ with $16.4^{+5.0}_{-3.1}\%$ and $15.4 \pm 0.6\%$ comparable fractions for AGN in mergers and undisturbed systems, respectively. At best, a small enhancement of AGN is also presented in Shah et al. (2020) for the analysis of spectroscopic galaxy pairs at $0.5 \lesssim z \lesssim 3$.

As contradictory as the results of the observations are, so are the findings from the analyses of various simulations. Using the cosmological simulations ROMULUS25 and ROMULUSC, Ricarte et al. (2019) detect no obvious connection between SMBH growth and mergers, regardless of timescale or redshift. Similar to the analysis and results of the ILLUSTRIS-TNG300 sources at $z \simeq 2$ presented in this work, Sharma et al. (2021) investigate the AGN merger connection for massive galaxies in 30 high-resolution zoom-in cosmological hydrodynamical simulations. They produce *HST*/WFC3 F160W mock observations for suitable objects in a redshift range of $0.5 \lesssim z \lesssim 3$ and evaluate the morphologies by measuring the concentration C, asymmetry A, Gini coefficient G, and $M20$. A subsequent comparison between the simulated AGN activity, the synthetic images, and an observational sample from the CANDELS survey shows that AGN are not more likely to be in merging systems. This is also true if only major mergers, i.e. mergers with a mass ratio $> 1:4$, or the most luminous AGN ($L_{\rm bol} > 10^{45}\,[\mathrm{erg\ s^{-1}}]$) are considered.

A more complex conclusion, in excellent agreement with the overall results derived in this paper, is presented by McAlpine et al. (2018, 2020). For their analysis of SMBH growth in the EAGLE simulation, they find that major mergers - while not important at high redshifts - play a significant role at low redshifts and derive a consistent major merger fraction of $\sim 40\%$ for rapidly growing BHs at $z \sim 0$. Similar results are reported by Bhowmick et al. (2020) for an analysis of BH pairs at scales of $0.01, 0.1,$ and $1 h^{-1}$Mpc in ILLUSTRIS-TNG100. They find an increased likelihood of AGN residing in systems with small separation and also find a trend of Eddington ratio with distance, both suggesting a connection with galaxy interactions. Nevertheless, they report that only at maximum $\sim 40\%$ of the AGN with the highest Eddington ratios live in close pairs, with this fraction decreasing for larger distances and lower Eddington ratios. Finally, by analyzing two realizations of the MAGNETICUM simulation for given AGN luminosities and stellar masses, Steinborn et al. (2018) find an excess in the merger rates by a factor of up to three compared to a sample of control galaxies. Nevertheless, their overall result shows that regardless of luminosity, mergers play only a minor role in the fueling of AGN.

Thus, even if there is no unanimous opinion among the observations and simulations neither on the strength of a potential enhancement in AGN merger fractions, nor on the relevance of major mergers, practically all of these previous studies find AGN merger fractions below 50%. An assessment that is consistent with the results presented in this paper and that necessitates a continuing research focusing on the triggering mechanisms of AGN.

8. Conclusions and Outlook

8.1. Summary

This work summarizes the first studies specifically targeting AGN with the highest specific accretion rates to test the merger–AGN connection over cosmic time for this particular subpopulation of AGN. The first study focuses on the investigation and comparison of 21 AGN host galaxies and 92 matched inactive control galaxies at $z \simeq 2$. Both samples are based on observations with *HST*/WFC3. Point source components and Sérsic profiles are modeled simultaneously to derive the best fit for the AGN components embedded in each galaxy center. To create a sample of inactive galaxies with comparable residuals, synthetic point sources are added at the respective flux centers and the fitting process is repeated. The resulting joint sample of 113 indistinguishable host galaxies is then visually ranked from most to least distorted by 10 experts. To assess the impact of the methodology, a total of three different methods are used to aggregate these classifications, resulting in three consensus classifications. All are then divided into galaxies that show features of a recent or ongoing merger event, and another subset that shows no particular features. A subsequent comparison and analysis of the resulting merger fractions of AGN hosts and control galaxies leads to the following results:

– No significant increase in merger incidence is found for the AGN host galaxies with respect to a sample of matched inactive galaxies. The corresponding merger fractions are $f_{\mathrm{m,\,AGN}} = 0.24 \pm 0.09$ and $f_{\mathrm{m,\,Ina}} = 0.19 \pm 0.04$ for the AGN sample and control galaxies, respectively.

– Neither the choice of cutoff rank nor the method used to combine each rank affects the derived merger fractions.

– Within the selection, the merger fractions for both samples do not depend strongly on the stellar mass.

– The Sérsic indices of the AGN host galaxies and the inactive galaxies show a negligible difference. Both samples have a comparable fraction of disk-dominated galaxies.

- Considering all these observations in combination with results from other studies, the conclusion is that even for AGN at $z \simeq 2$ with the highest specific accretion rates, major mergers are not the dominant trigger.

- Considering the time scale of both the AGN activity and the merger visibility, it is unlikely that the lack of AGN merger enhancement in this study is due to a time lag that washes out merger features before the AGN phase ends.

- The influence of intermittent AGN that have exhibited and will again exhibit high accretion rates but are currently inactive, or at least appear so, is considered. With the best estimates, only $\sim 20\%$ within the population of merging and inactive galaxies would actually host such an intermittent AGN.

- Considering the respective number densities and the resulting AGN timescales, even post-starburst galaxies showing significant merger features and enhanced star formation rates do not appear to be predominantly associated with AGN.

The observations of AGN host galaxies at $z \simeq 2$ pushed *HST* to its limits in terms of resolution and available wavelength range. To test the validity of these observational results, a pilot study is performed by repeating the analysis with identical methodology on simulated samples of comparable AGN and control galaxies from the hydrodynamic cosmological TNG300 simulation, which is part of the IllustrisTNG project. For a consistent comparison with the observational results, typical observational uncertainties in BH mass and Eddington ratio are added to the simulated values. In addition, the morphologies of both AGN host galaxies and inactive sources are determined by deriving the characteristic parameters concentration C, (shape) asymmetry A_S, Gini coefficient G, and M_{20}. For these analyses, *HST*/WFC3 F160W, mock observations are created and processed to reflect the real data used in the observational study.

To assess the accuracy of both methods, the resulting merger fractions are compared with the corresponding merger fractions predicted by the true simulated merger histories of the respective sources. To test for any trend with BH mass, the simulated merger histories are also analyzed for two other AGN samples with the same Eddington limits but lower BH masses, and are also compared to two matched control samples. The merger fractions based on the merger histories are derived three times, each time using a slightly different approach with respect to the galaxies considered and thus their merger histories. First, only the merger histories from the originally selected galaxies are considered. Second, the merger fractions are averaged over 1000 iterations of re-sampling the simulated galaxies, with uncertainties randomly selected in each iteration, thus resulting in ever-slightly different samples for each step. In theory, this approach should

best reproduce the observational results. Third, the galaxies are selected based on their true simulated values without considering the observational uncertainties.

The findings are summarized as follows:

- Independent of BH mass, time passed since the last merger, merger mass ratio, and the consideration of characteristic observational uncertainties, AGN host galaxies show at most an excess of $\sim 10\%$ compared to a corresponding matched control sample.
- Considering a time of < 1 Gyr since the last merger, all derived major and minor merger fractions for the studied AGN yield values of $f_{\mathrm{m,\,AGN}} \lesssim 40\%$.
- The best estimates based on the merger histories for AGN host systems and control galaxies give $f_{\mathrm{m,\,AGN}} = 0.27 \pm 0.07$ and $f_{\mathrm{m,\,Ina}} = 0.22 \pm 0.01$, respectively. Such values are in excellent agreement with the results of the observational study.
- Similar merger fractions are found using the classification of galaxies based on the measurements of automatically derived morphological parameters.
- The same visual classification approach used in the observational study leads to a consistent merger fraction for the inactive galaxies, but also to a significantly higher merger incidence for the studied AGN. This is most likely not due to uncoalesced mergers or the study of galaxies with a different evolutionary history. While an influence of selection effects or obscured AGN that are not part of an observational study cannot be ruled out, this finding is most likely the result of a systematic effect introduced by the resolution limit of TNG300. However, further studies are needed to verify this hypothesis.
- Considering the evolution of sSFR, gas mass and Eddington ratio over a redshift range of $2 \lesssim z \lesssim 4$, it appears that the SMBH growth is decoupled from the evolution of its host galaxy. As a consequence a process is required that provides the SMBH in a few Myr with a sufficient amount of gas to trigger an AGN phase.

The third study again investigates a possible direct correlation between AGN, which specifically have the highest Eddington ratios, and major mergers, but this time at $z \lesssim 0.2$. A total of 17 AGN host galaxies and 25 comparison galaxies matched in mass, redshift, filter, and S/N are analyzed in *V*, *B*, and color images based on *VLT/FORS2* observations. The process of adding artificial point sources to the flux centers of the control galaxies yields two indistinguishable samples, which are combined into a randomized total sample of 42 targets. As in the observational study at $z \simeq 2$, the resulting total sample is ranked by the presence of merger features (from most to least distorted) by 19 experts. By applying again three different methods, the individual rankings of each set, i.e.

V, *B*, and color, are then combined, resulting in a total of nine consensus rankings. This allows to determine any bias that could be a consequence of the visual classification of the galaxies at different wavelengths or the algorithm that combines the individual classifications. Finally, an overall sequence is created by combining the nine initial consensus rankings. By choosing specific cutoff ranks, all rankings are separated into galaxies with distinct merger features and objects that show no sign of gravitational disruption. As a last step, the respective merger fractions are then derived.

The results strongly depend on the choice of the distinction between merging and unperturbed systems. In order to analyze how the choice of cutoff rank affects the results, two approaches are employed. First, it is based on the experts' assessments and second, it is chosen so that the merging rate of the comparison sample matches published major merging fractions of galaxies in the same mass and redshift range. Considering the first method, the averages of the cutoff rank determinations of the classifiers are calculated. As a result, about half of both populations show evidence of a recent or current merger event, suggesting that there is no causal link between major mergers and the triggering of this particular population of AGN.

However, since this first approach also accounts for asymmetries or signatures that most likely arise from processes other than a major merger event, the major merger fraction of inactive galaxies is adjusted to match the findings of recent simulations and observations. The result is a substantial excess in the major merger fraction of the AGN sample with respect to the inactive galaxies. Coincidentally, separation at the appropriate cutoff rank also leads to a clear distinction between highly perturbed galaxies and galaxies with either low or no merger signatures, confirming the classification. The results can be summarized as follows:

- The merger fractions of the AGN host galaxies and the comparison galaxies are $f_{\mathrm{m,\,AGN}} = 0.41 \pm 0.12$ and $f_{\mathrm{m,\,Ina}} = 0.08 \pm 0.06$, respectively.

- As in the other studies presented in this paper, the choice of combination method does not affect the derived merger fractions. Similarly, there is no dependence on the wavelength range studied.

- For AGN, with the highest Eddington ratios at $z \lesssim 0.2$, major mergers are an essential mechanism to trigger BH growth.

- Minor mergers appear to play an insignificant role in triggering this particular subpopulation of AGN.

– In contrast to the findings at high redshifts, the limited amount of cold gas within a galaxy at low redshift, could be a possible explanation for the more prominent role of major mergers.

– Considering AGN and merger lifetimes, as well as AGN variability induced by an ongoing merger event, the best estimate results in $\sim 50\%$ of this AGN population being still of unknown origin.

Although focusing explicitly for the first time on AGN with the highest Eddington ratios, and although deriving different absolute AGN merger fractions for sources at $z \lesssim 0.2$ and $z \simeq 2$, all results are consistent with the pivotal conclusion that *in the grand scheme of things, major mergers play at most a subdominant role in triggering and fueling AGN.*

8.2. Future work

With each new scientific result, more questions arise. The finding that mergers play only a limited role in SMBH growth is no different and leads, for example, to the following partially interdependent questions. Does the relevance of large mergers in triggering and driving AGN depend on AGN properties such as redshift and luminosity? What other possible mechanisms exist to explain the existence of $\gtrsim 50\%$ of AGN? How important are minor mergers, bars, or secular processes, and to what extent does their role depend on AGN properties? How significant are the environments of AGN host galaxies? How can AGN and merger timescales be better constrained? Could a multi-wavelength approach provide more insight? How well do simulations agree with observations and with each other? Can automatic and self-learning clustering algorithms, applied to upcoming data from the new generation of telescopes, reveal new information in the form of distinct subpopulations? Of course, these questions do not claim to be exhaustive and with every answer to one of these questions, new ones are sure to follow. Thus, the possibilities for future research in this field are numerous and manifold. The following paragraphs are intended to provide a selection of possible answers to the questions mentioned above.

Certainly one of the most essential questions is whether and how much the major merger fractions vary with redshift and AGN properties such as luminosity, accretion rate, or Eddington ratio. All previous studies, as well as this work, already provide clues to the answers to this question. Nevertheless, all these studies can also be interpreted only as individual pieces of a large puzzle whose unveiling is still pending. In particular, this may take the form of an all-encompassing study that examines AGN both over a large cosmic time period and over a wide range of an AGN property, such as luminosity. Apart from an unprecedented observational

campaign, this is currently only possible through the study of cosmological simulations. The closest to this goal at the moment are probably the studies of McAlpine et al. (2018, 2020), Steinborn et al. (2018), and Sharma et al. (2021). However, when performing such an analysis, one must of course be aware of the limitations that in particular large-scale simulations entail when modeling BHs and AGN.

Another obvious problem is to determine the alternative mechanisms leading to SMBH growth. For example, although initial studies attribute a rather minor role to bars (Cheung et al. 2015; Cisternas et al. 2015; Goulding et al. 2017), all potentially triggering processes must be considered with reference to a variety of AGN populations and also to redshift. For example, bars could play a more important role for low-luminosity AGN, while even minor mergers could have a significant impact on AGN in dwarf galaxies. Similarly, secular processes could be more essential at high redshifts, while major mergers are more dominant in the local Universe. Of course, both topics are compounded by the complicating issue of the environment and the consideration of different timescales. Both circumstances add another layer of complexity.

Regardless of these ambitious projects, there are also more realistic, immediate studies to be carried out. In addition to the usual desire for larger samples, one of these would be to study a new or even previously studied sample of (local) AGN like the one in this paper using Integral Field Spectroscopy observations. Estimating the strength of possible past merger events by examining the high-resolution gas dynamics and stellar populations could also reveal other processes, such as secular gas flows. Another potential project that could be realized without delay would be to continue the analyses of the IllustrisTNG simulation in the form of a study of a broader spectrum of AGN at different redshifts using the extensive data set provided by this suite of cosmological simulations. To further take advantage of a simulation and analyze the relevance of inclination, one could also perform a classification of synthetic images showing the same samples from multiple, different perspectives. Both the study of the extended parameter space and an analysis of the influence of the viewing angle would also potentially solve the puzzle of the significantly different visually derived AGN merger fraction presented in this work.

Finally, comparing the merger–AGN connection in different cosmological simulations, such as IllustrisTNG and EAGLE, would be an appealing and worthwhile endeavor. With respect to the $M_{\mathrm{BH}} - M_{\star}$ scaling relation and the BH mass function, this has already been performed by Habouzit et al. (2020). However, a comparative analysis focusing on the role of major mergers in SMBH growth has not yet been published. Such a study would be able to filter out most of the systematic effects that might be inherent in each of the simulations, and would therefore tighten the predictions for the AGN merger fractions over a wide range of redshifts and AGN properties.

As mentioned before, the observational analysis at $z \simeq 2$ has exhausted the capabilities of *HST*. The next logical step would be to exploit the extraordinary facilities of the *James Webb Space Telescope (JWST)*. The higher resolution and sensitivity allow the AGN host galaxies to be studied up to $z \simeq 7$ by applying, for example, PSFMC, the same modeling algorithm used in this work (Marshall et al. 2020, 2021). Still, what needs to be considered in any case at such high redshifts is the significance of the derived merger fractions based on morphology. Not only is (for a given stellar mass) the evolution of the merger fractions up to $z \sim 5 - 7$ not yet entirely clear (Duncan et al. 2019; O'Leary et al. 2020), but galaxies at this cosmic age also have increasingly clumpy, more compact and irregular appearance, which is not necessarily the result of a merger (Jiang et al. 2013; Conselice 2014; Genel et al. 2014; Shibuya et al. 2015; Bowler et al. 2017). Similarly, the question arises as to the added value of higher resolution images of galaxies at lower redshifts, given that large-scale major mergers, already detectable with *HST* up to $z \simeq 2$, have been largely discarded as the dominant mechanism for SMBH growth. Nevertheless, a repeated analysis of the AGN studied in this work would be very compelling. Among other things, this would allow to determine whether visual inspection of higher-resolution images, which could already provide evidence for minor mergers, would yield the same results.

When it comes to visual classification, of course, one cannot ignore the growing field of automatic classification using machine learning – a field that will most likely bring about a profound change in the way astronomical data are analyzed in the near future. As data sets continue to grow, and also to ensure objectivity and reproducibility, such methods will certainly become increasingly common in the work of astrophysicists. In the last three years, more and more promising approaches and analyses have emerged demonstrating the suitability of AGN detection and morphological classification by various machine learning algorithms (Goulding et al. 2018; Bottrell et al. 2019; Cheng et al. 2019; Snyder et al. 2019; Zhao et al. 2019b; Cheng et al. 2020; Ciprijanović et al. 2020; Clarke et al. 2020; Ferreira et al. 2020; Ghosh et al. 2020; Hausen & Robertson 2020; Margalef-Bentabol et al. 2020; Pfister et al. 2020; Storey-Fisher et al. 2020; Vega-Ferrero et al. 2020; Wang et al. 2020; Chen et al. 2021; Livet et al. 2021; Sharma et al. 2021). Immediate applications include a repetition of the analysis of previously studied AGN samples in order to detect systematic effects introduced by human perception, or visual inspection of synthetic images based on simulations. In the (hopefully near) future, the observations provided by *JWST* or *Euclid* will also be the subject of such investigations. Considering the sheer number of objects these two telescopes in particular will observe, automated analyses are likely inevitable.

Finally, an investigation at other wavelength ranges would also be a worthwhile task. One could thereby determine the merger fractions for obscured AGN by selecting in the infrared or X-ray domain. However, one should not forget that obscuration leads to an unavoidable bias

with respect to merging systems. In contrast, a further study of possibly already investigated (local) AGN in the submillimeter and radio range could provide more accurate information about the gas content and dynamics. For example, it could confirm visual classifications or provide evidence for the presence of other mechanisms.

Considering the multitude of all previous findings, including those presented in this work, it is evident that the assessment of the role of major mergers in SMBH growth is much more complex than expected. It appears that the importance of major mergers in SMBH growth depends on redshift and, considering previous works, possibly also on luminosity. Given AGN and a matched sample of control galaxies in a given stellar mass range, examining a possible plane spanned by merger fraction, luminosity, and redshift could provide deeper insights into the possible causal relationship between major mergers and AGN.

In summary, despite many new insights, especially within the last decade, the question of the origin of an AGN cannot be answered conclusively. As with many other astronomical questions, the hope is that new simulations with larger volumes and higher resolution, as well as a multi-wavelength approach using the new generation of observatories that explore the X-ray (*Lynx*, *AXIS*, *Athena*), optical/IR (*ELT*, *GMT*, *TMT*, *Rubin Observatory*, *Euclid*, *JWST)*, and submillimeter (*ALMA*) ranges will provide a more complete picture.

Appendix

A. Modeling of AGN Host Galaxies at $z \simeq 2$

Similar to Figure 4.3, Figure A.1 depicts the remaining 20 AGN examined at $z \simeq 2$. The AGN host galaxies classified as being in a merging state are labeled accordingly with the term 'merger' after their respective SDSS designation.

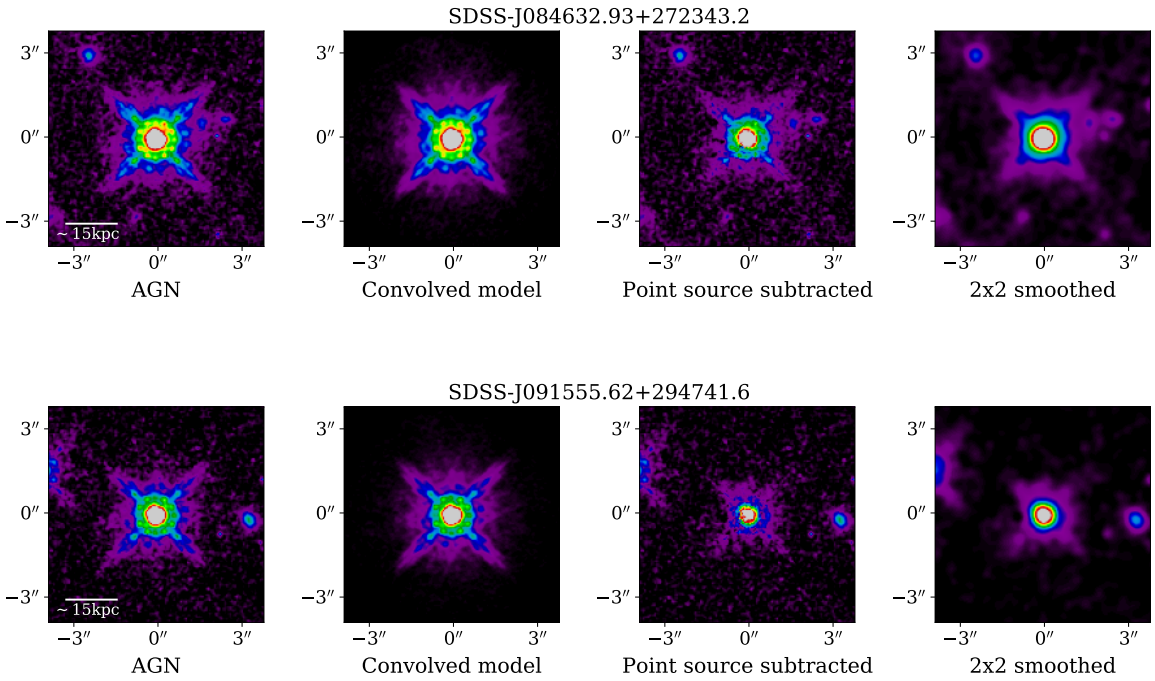

Figure A.1.: Different steps of the AGN/host galaxy modeling process for all remaining AGN. From left to right: the original processed *HST*/WFC3 image, the PSF convolved point source model, and the host galaxy after point source subtraction with the original sampling or smoothed by a σ=2 px Gaussian. All images are shown with the same arcsinh scaling.

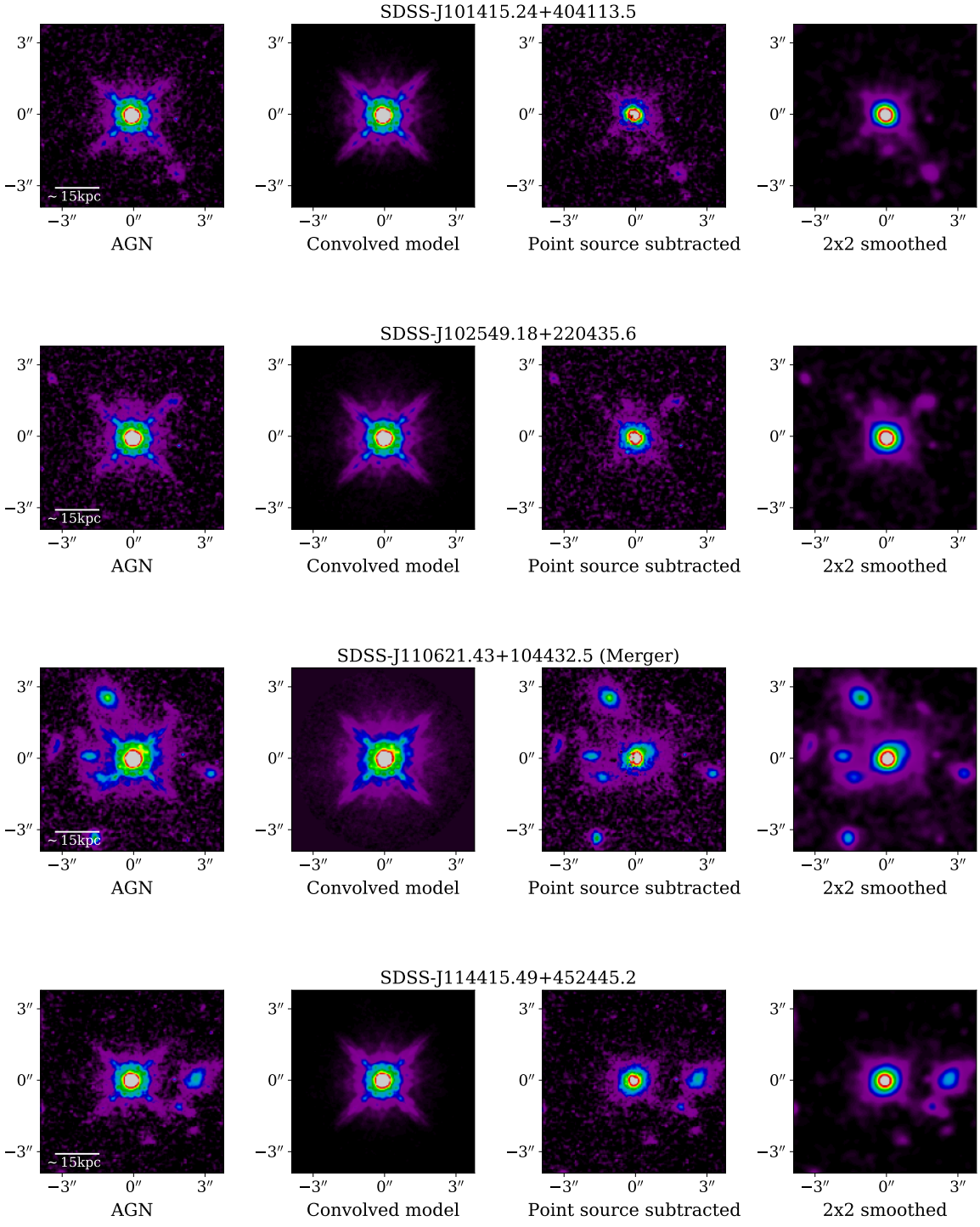

Figure A.1.: (Continued.)

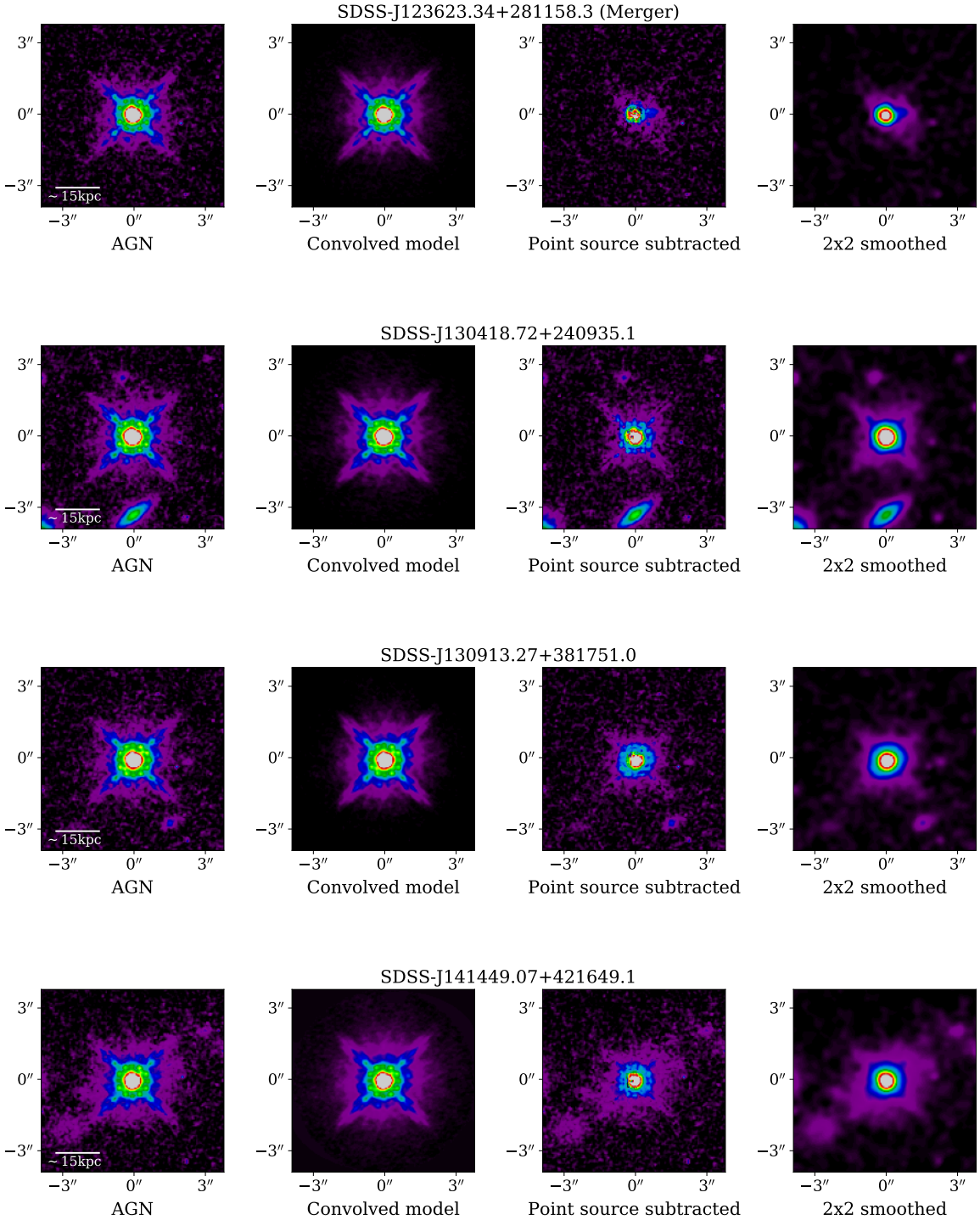

Figure A.1.: (Continued.)

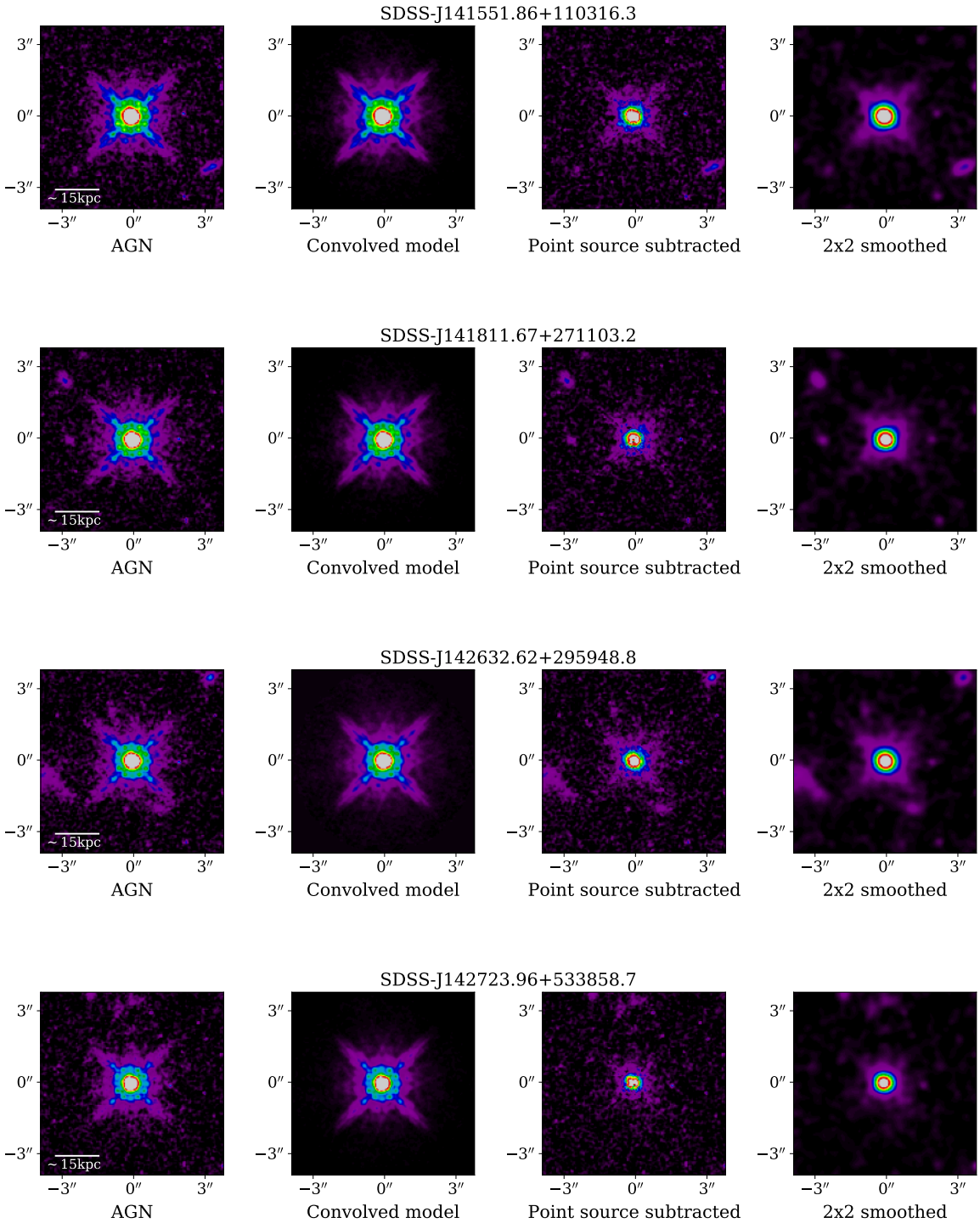

Figure A.1.: (Continued.)

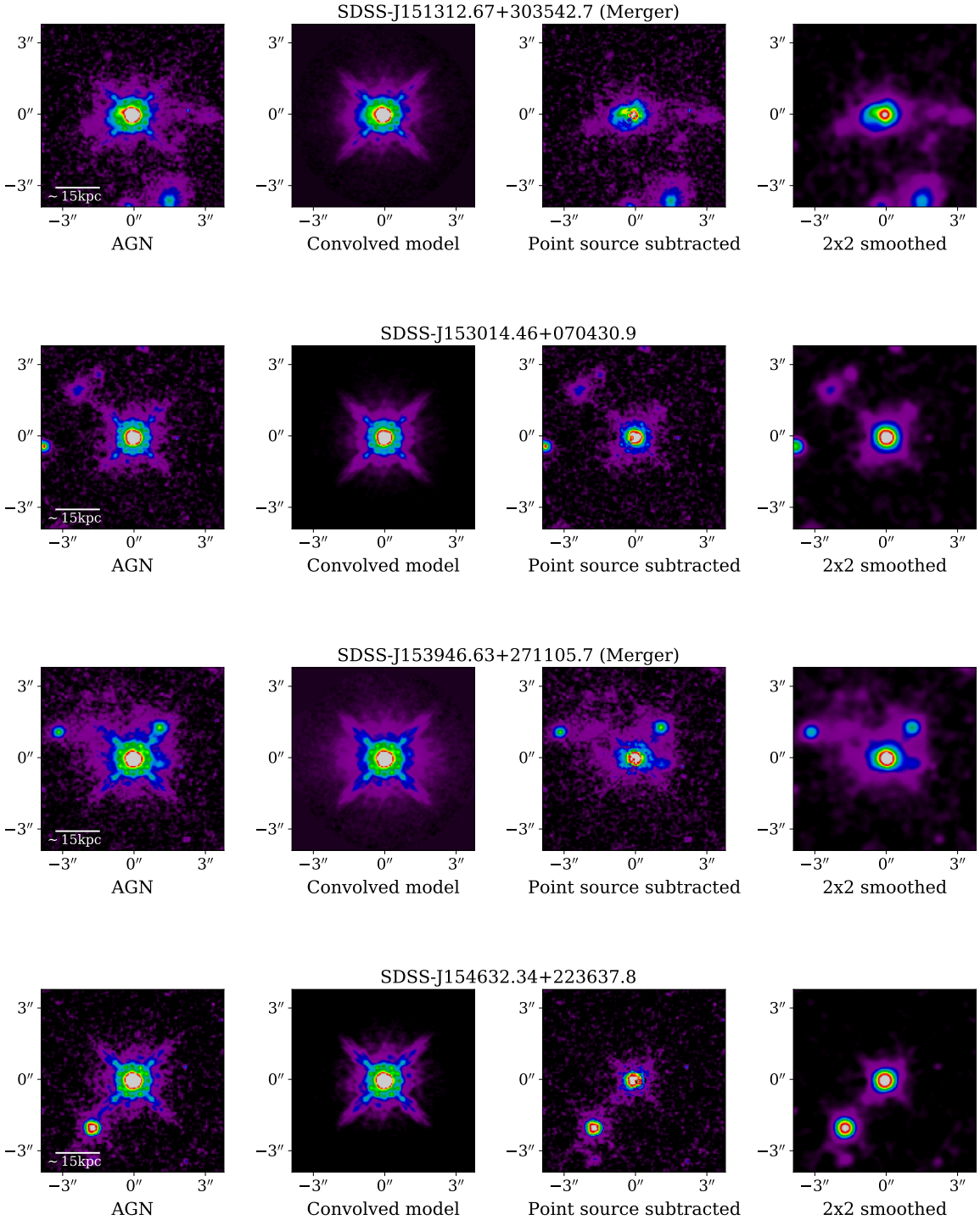

Figure A.1.: (Continued.)

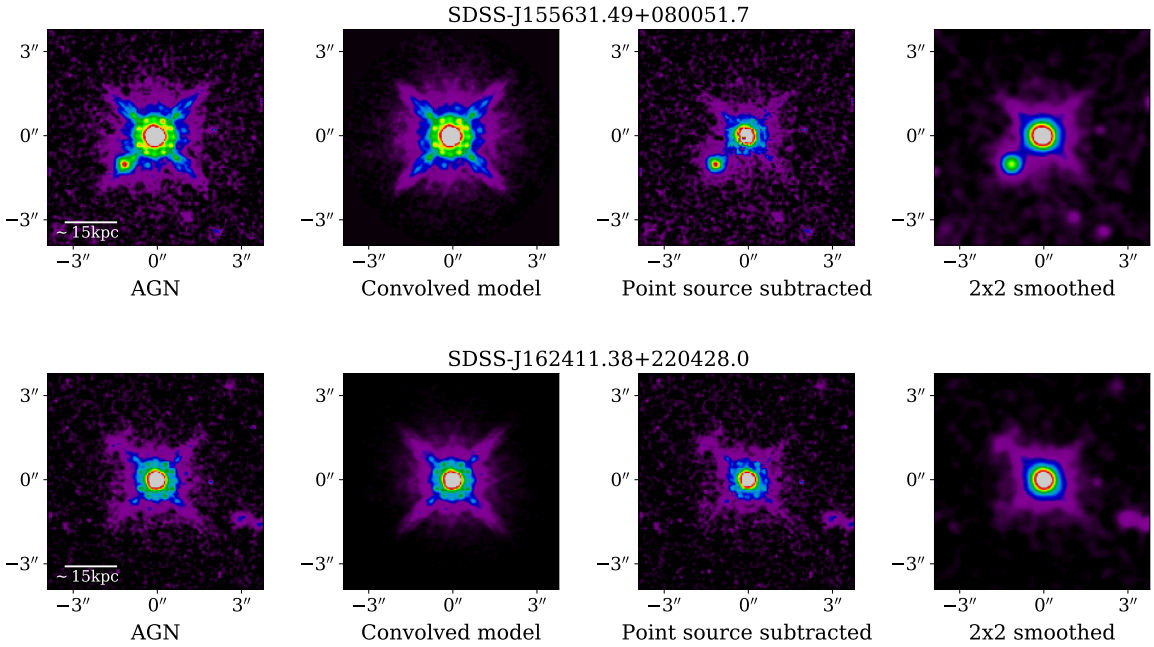

Figure A.1.: (Continued.)

B. Modeling of Inactive Galaxies at $z \simeq 2$

Similar to the Appendix A, Figure B.1 shows the modeling process for a selection of 21 inactive galaxies. In addition to all 11 galaxies classified as mergers in all three consensus rankings, 10 additional random unperturbed sources are included for comparison purposes (see Section 4.2). Galaxies classified as merging are labeled accordingly by the term 'merger' after their respective designation. In contrast to Figures 4.3 and A.1, Figure B.1 shows in the second column not the PSF convolved point source model, but the original image of the respective inactive galaxy that is shown in the first column, after adding a synthetic point source. In this sense, the second panels from the left in Figure B.1 are similar to the first ones in Figures 4.3 and A.1.

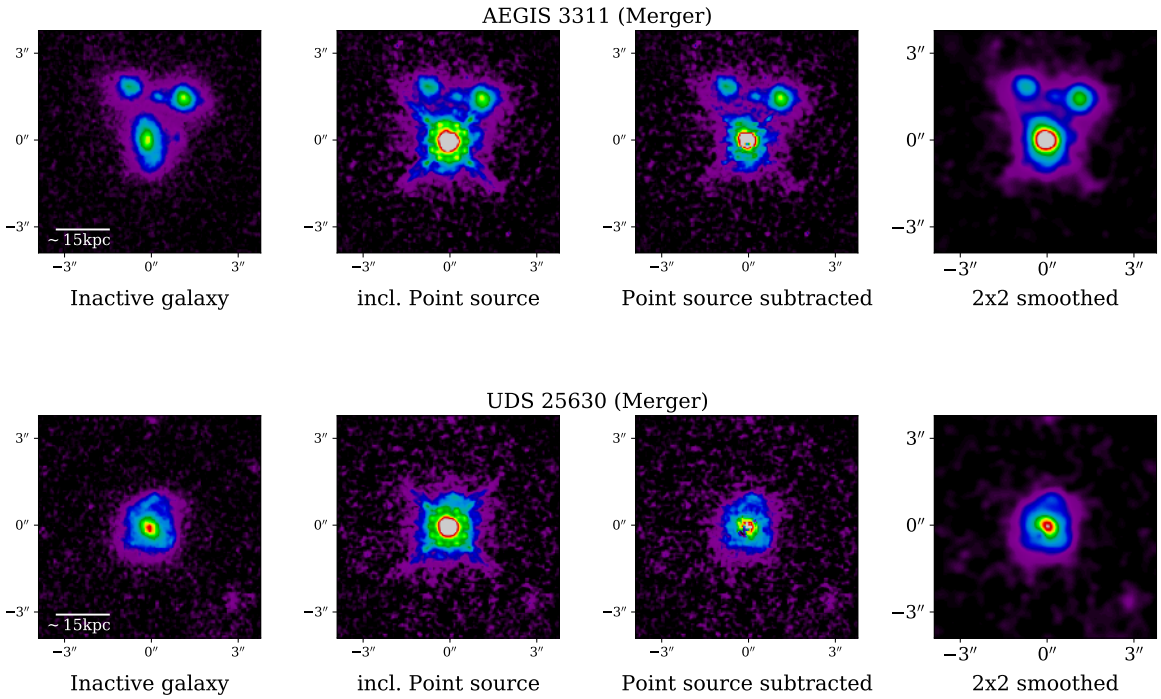

Figure B.1.: From left to right the original processed *HST*/WFC3 image, the same image with the synthetic point source added on top of the flux center, and the galaxies after point source subtraction with the original sampling or smoothed by a $\sigma = 2$ px Gaussian are shown. All images are shown with the same arcsinh scaling.

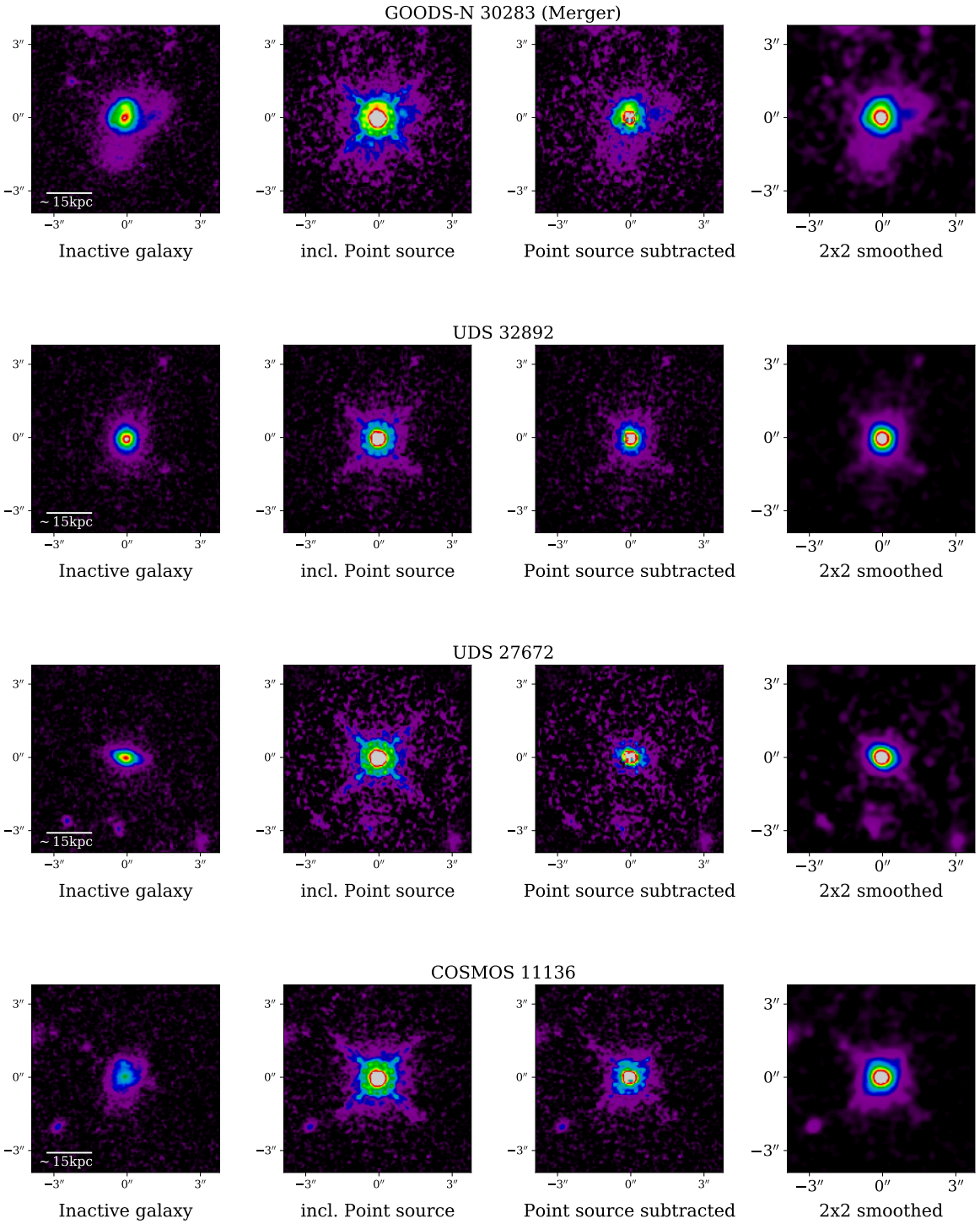

Figure B.1.: (Continued.)

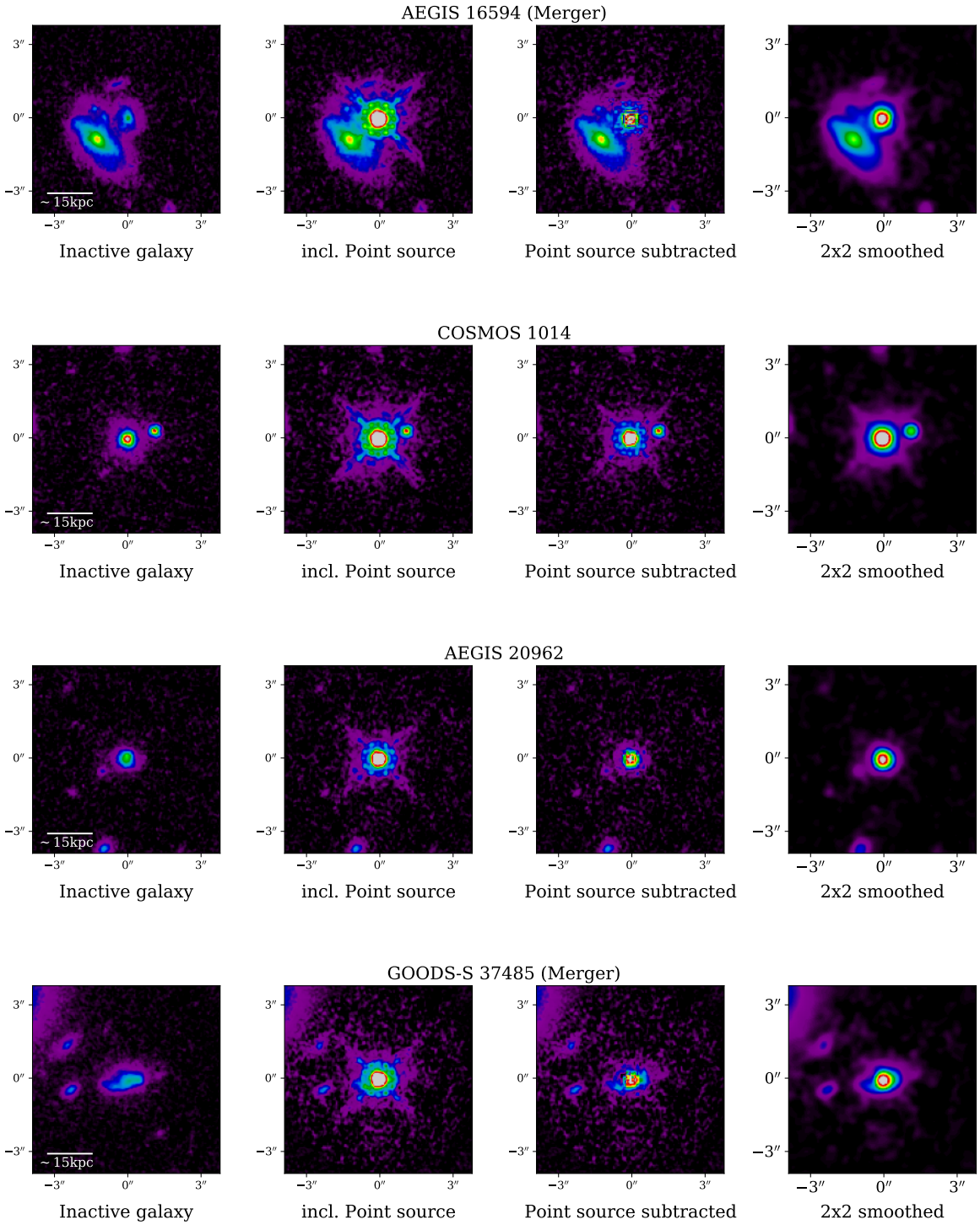

Figure B.1.: (Continued.)

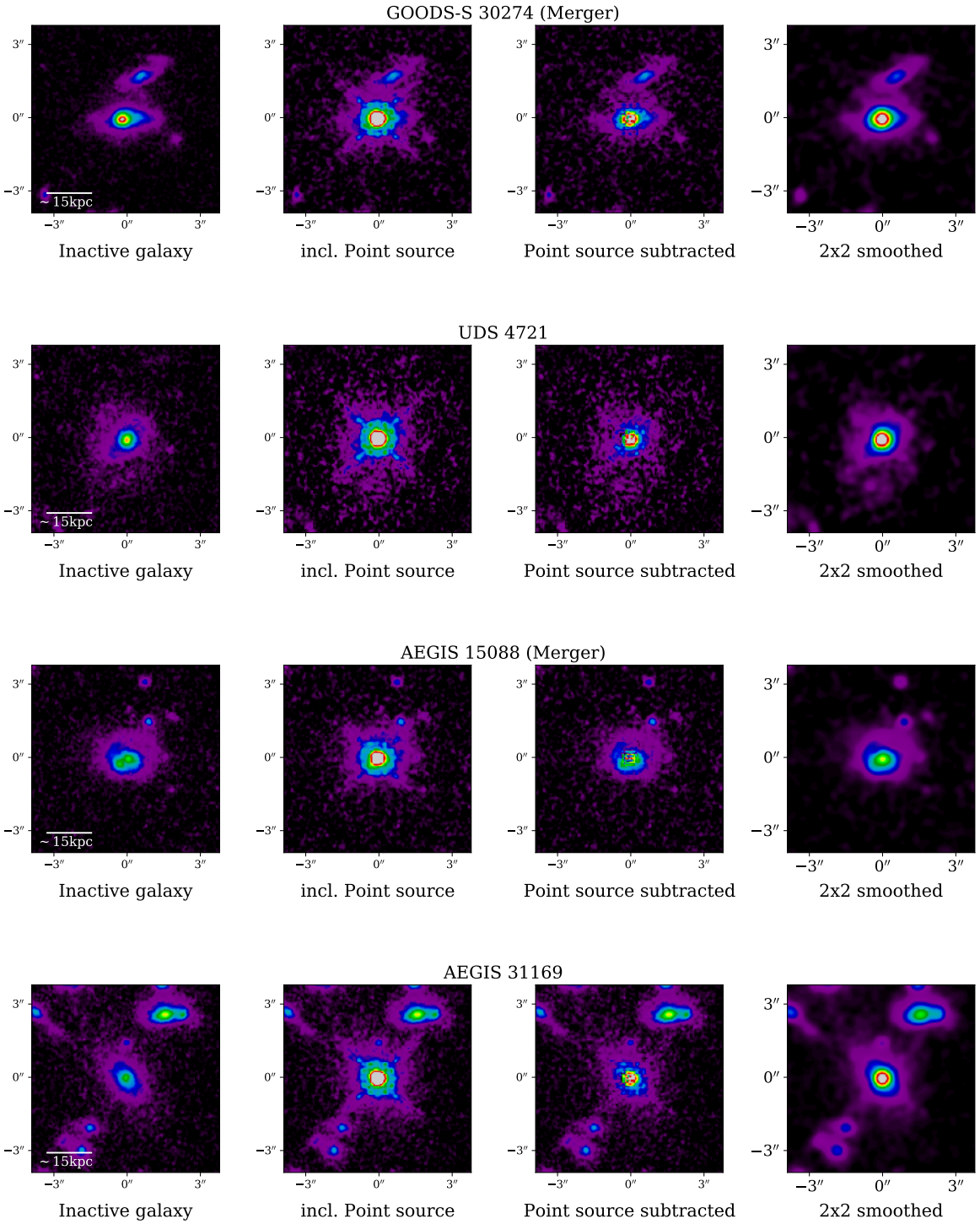

Figure B.1.: (Continued.)

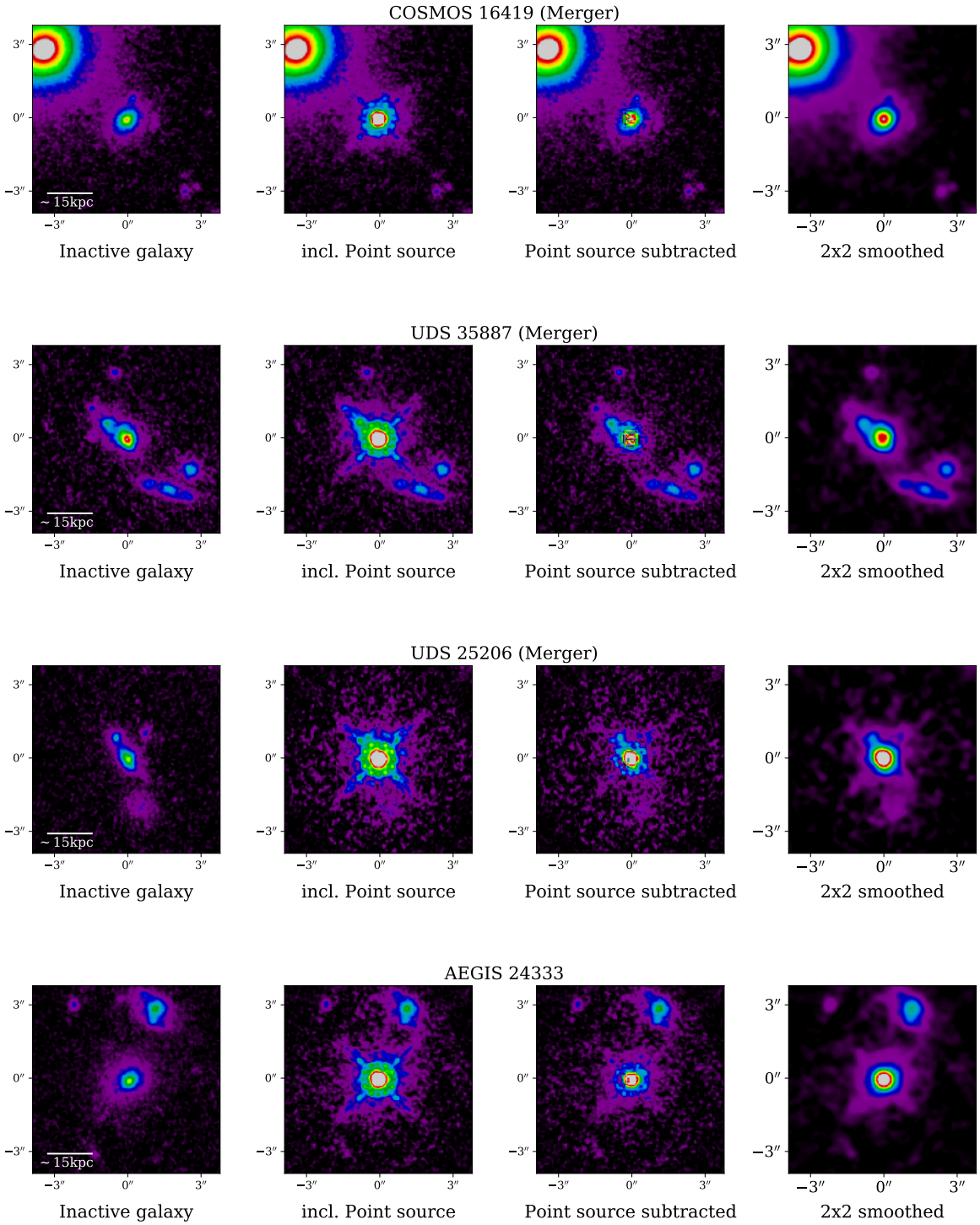

Figure B.1.: (Continued.)

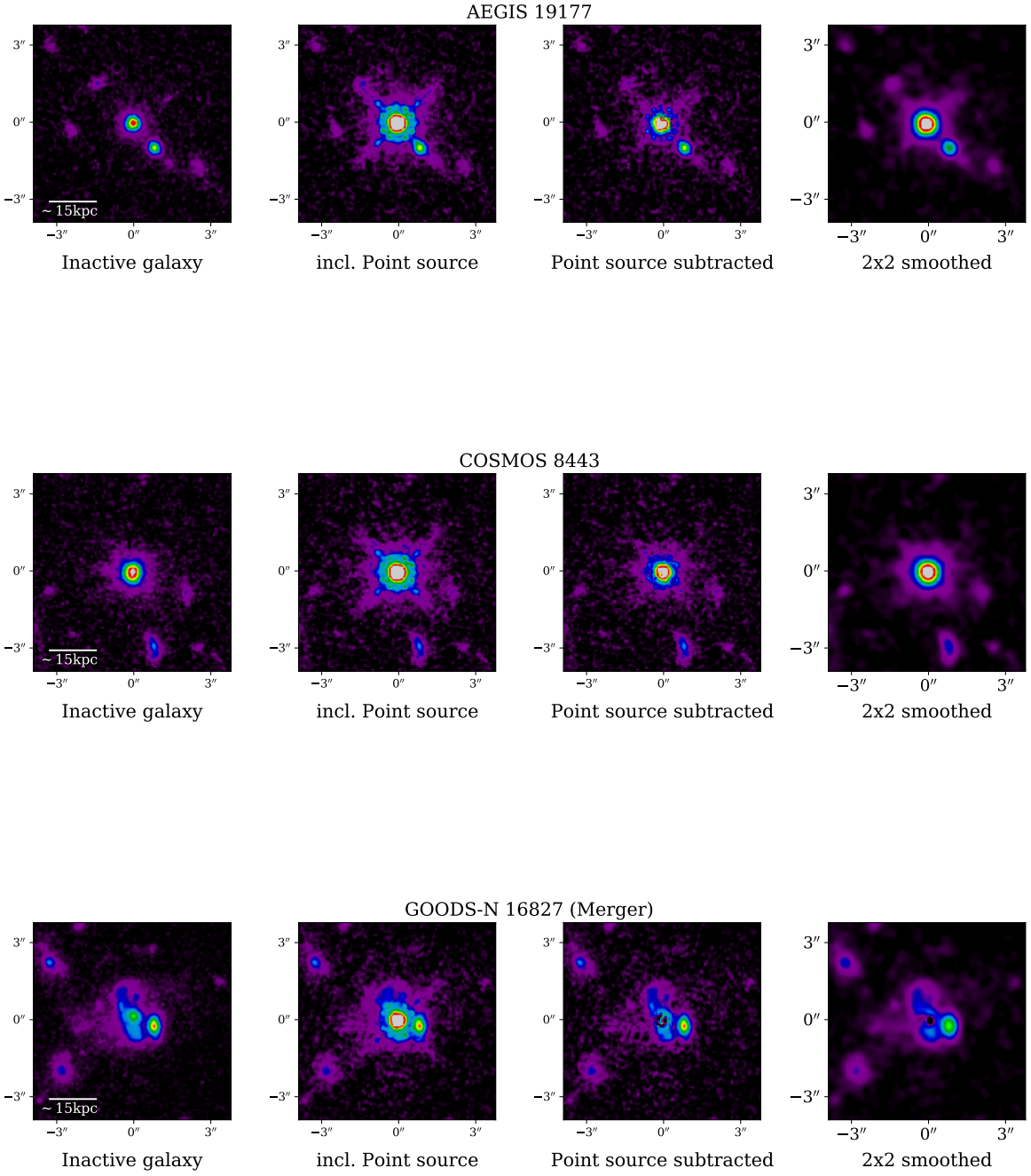

Figure B.1.: (Continued.)

C. Relative Differences of Simulated Merger Fractions

Similar to Figures 5.2, 5.3, and 5.8, Figure C.1 shows the relative differences in merger fractions for each combination of sample, merger type, and lookback time based on the 1000 times resampled merger histories of the simulated sources (see Section 5.2.1). It should be noted that although the absolute values indicate at first glance mostly a slightly increased merger fraction for the AGN sources, the corresponding uncertainties also include for many cases a relative difference equal to 0. Moreover, even for the cases with a lookback time of $t_{\mathrm{lb}} < 1\,\mathrm{Gyr}$ that actually yield an excess in the merger fraction for the AGN hosts, the absolute values are still well below 50%, indicating the need for alternative mechanisms to trigger AGN with the highest Eddington ratios at $z \simeq 2$.

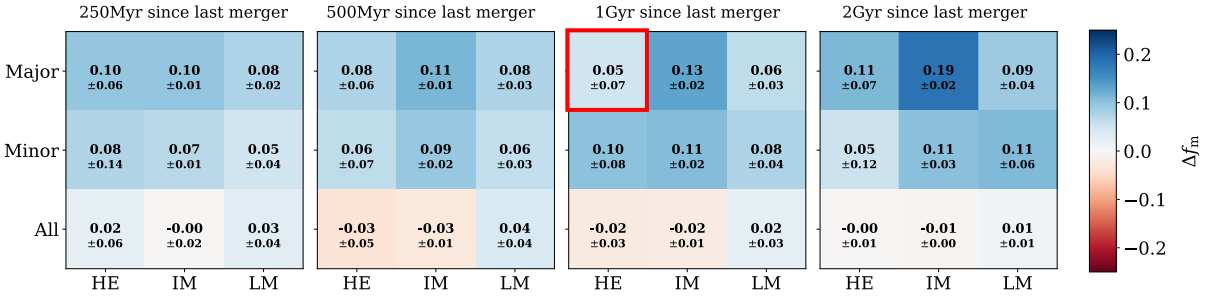

Figure C.1.: Relative difference in derived merger fractions based on resampled simulated merger histories. Again, the most suitable combination of subsample, mass ratio, and lookback time is highlighted for comparison with the observational study.

D. Visual Consensus Ranking for Sources at $z \lesssim 0.2$

To obtain a 'meta' singular consensus sequence, the Schulze method (see Sections 6.2 and 2.1) is applied to the final nine overall rankings, which are the result of the calculations for each combination of set and method. Figure D.1 presents all sources in the resulting order, and for completeness also includes the objects already shown in Figure 6.2. The respective rank for each object is given in parentheses next to its name. It should be noted that Gal176221 occupies only the last rank because it was observed only in the *V* band and therefore appears only in the three corresponding consensus rankings. In these three respective rankings it is always positioned at rank 14. Clearly visible is the drop in strong merger features at a cutoff rank $\gtrsim$10.

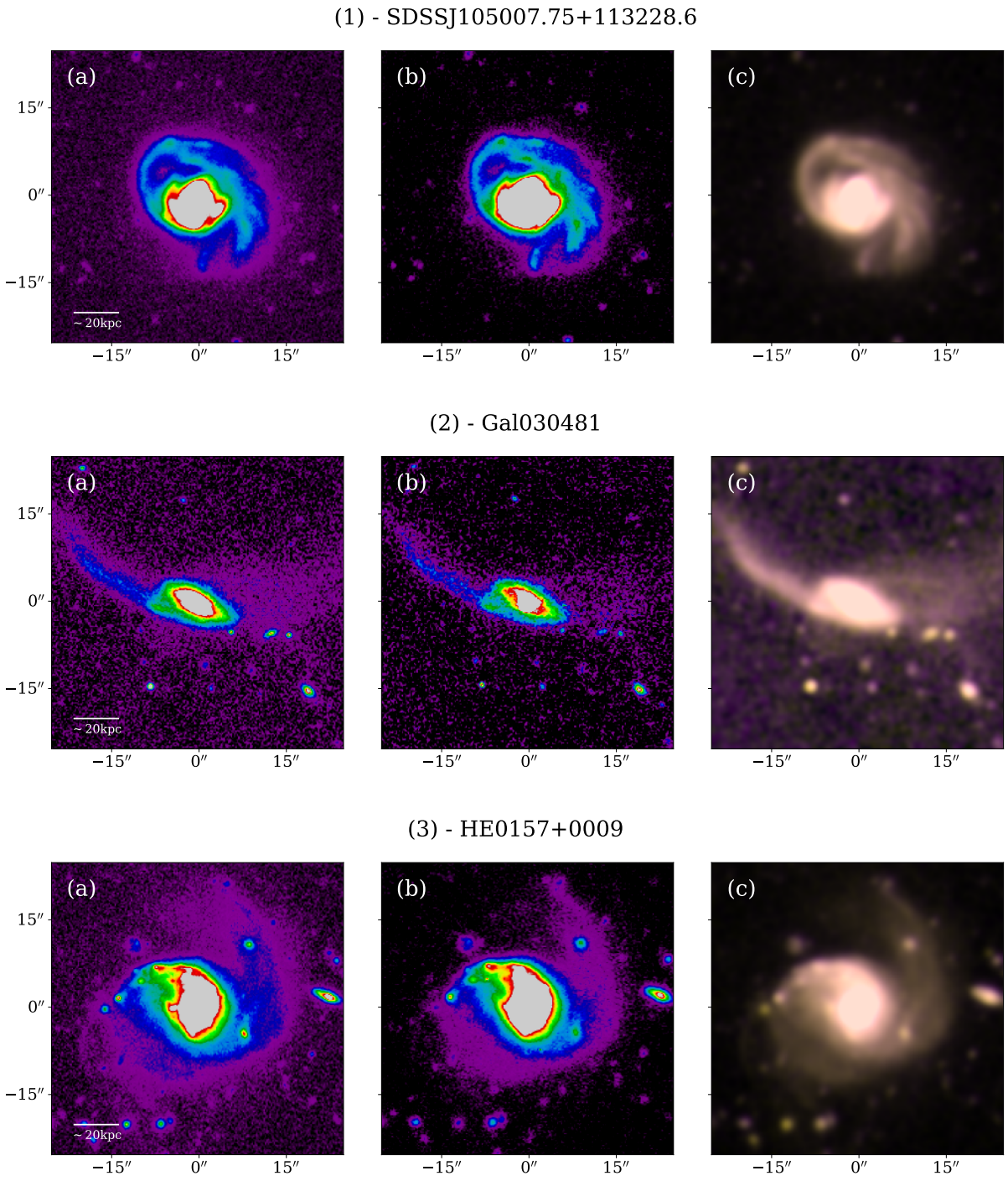

Figure D.1.: From left to right the panels display a postage stamp in (a) *V*-band, (b) *B*-band and (c) color, respectively. Note: In order to enhance the visibility the images are not shown with the same cuts and color map parameters.

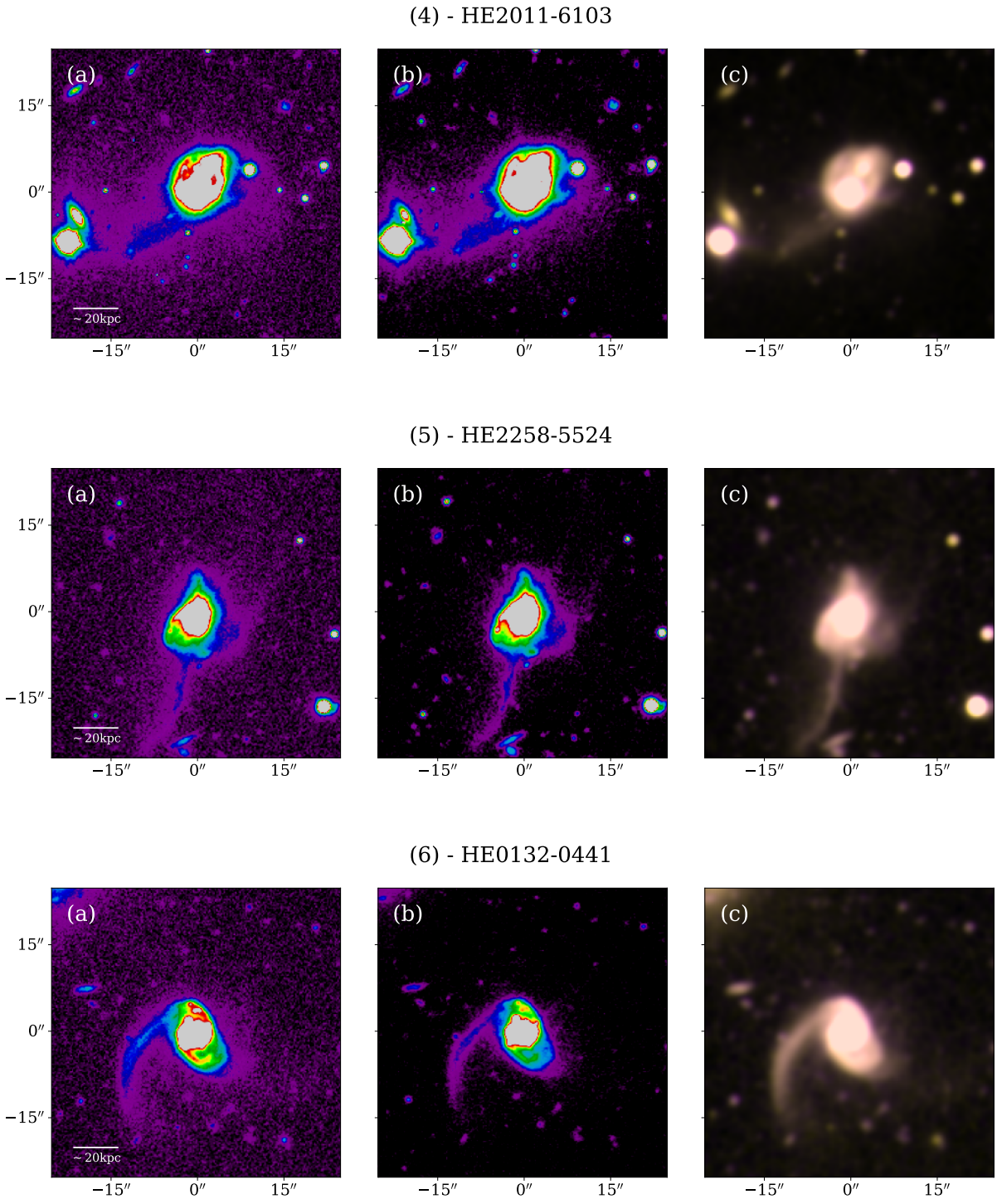

Figure D.1.: (Continued.)

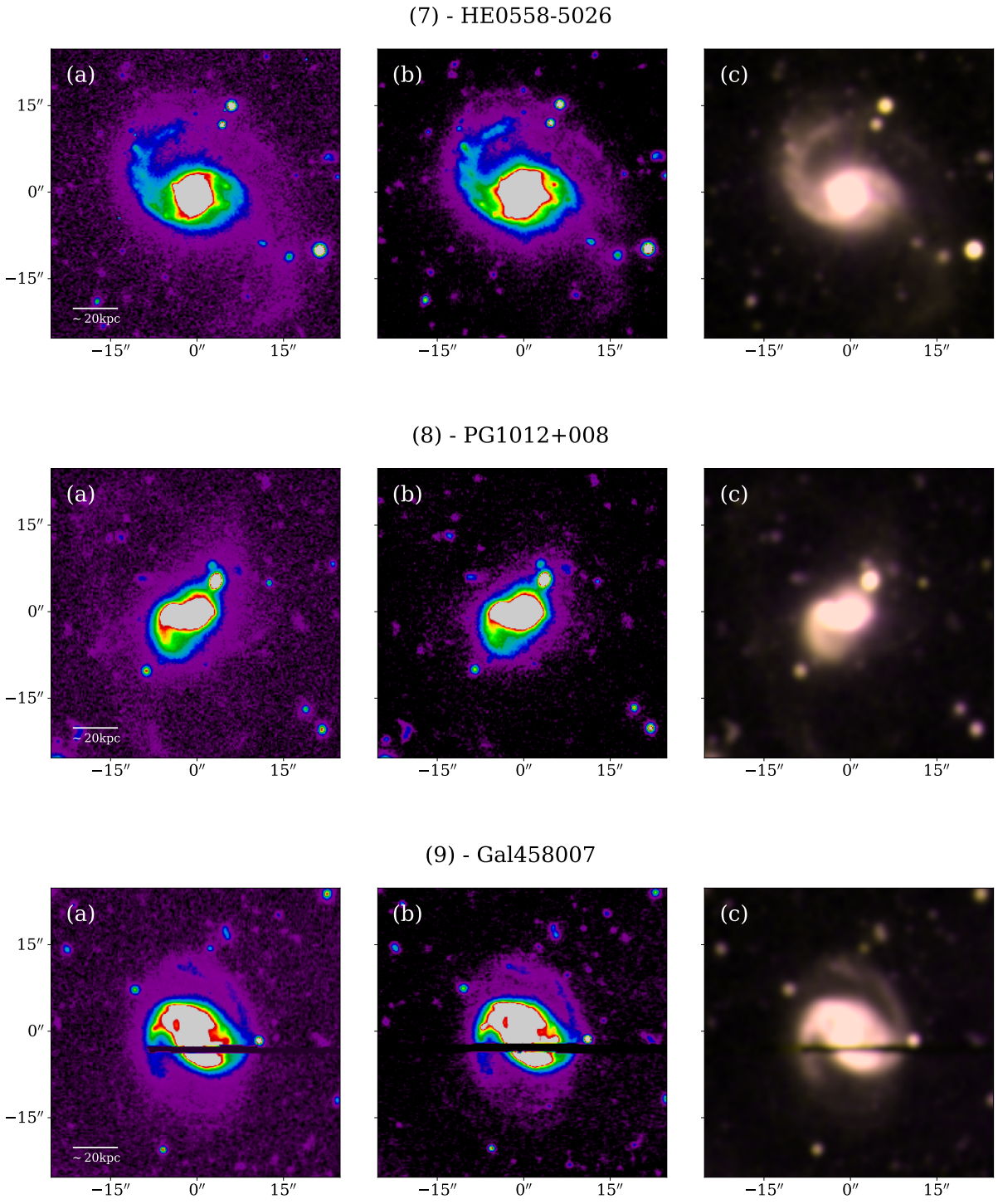

Figure D.1.: (Continued.)

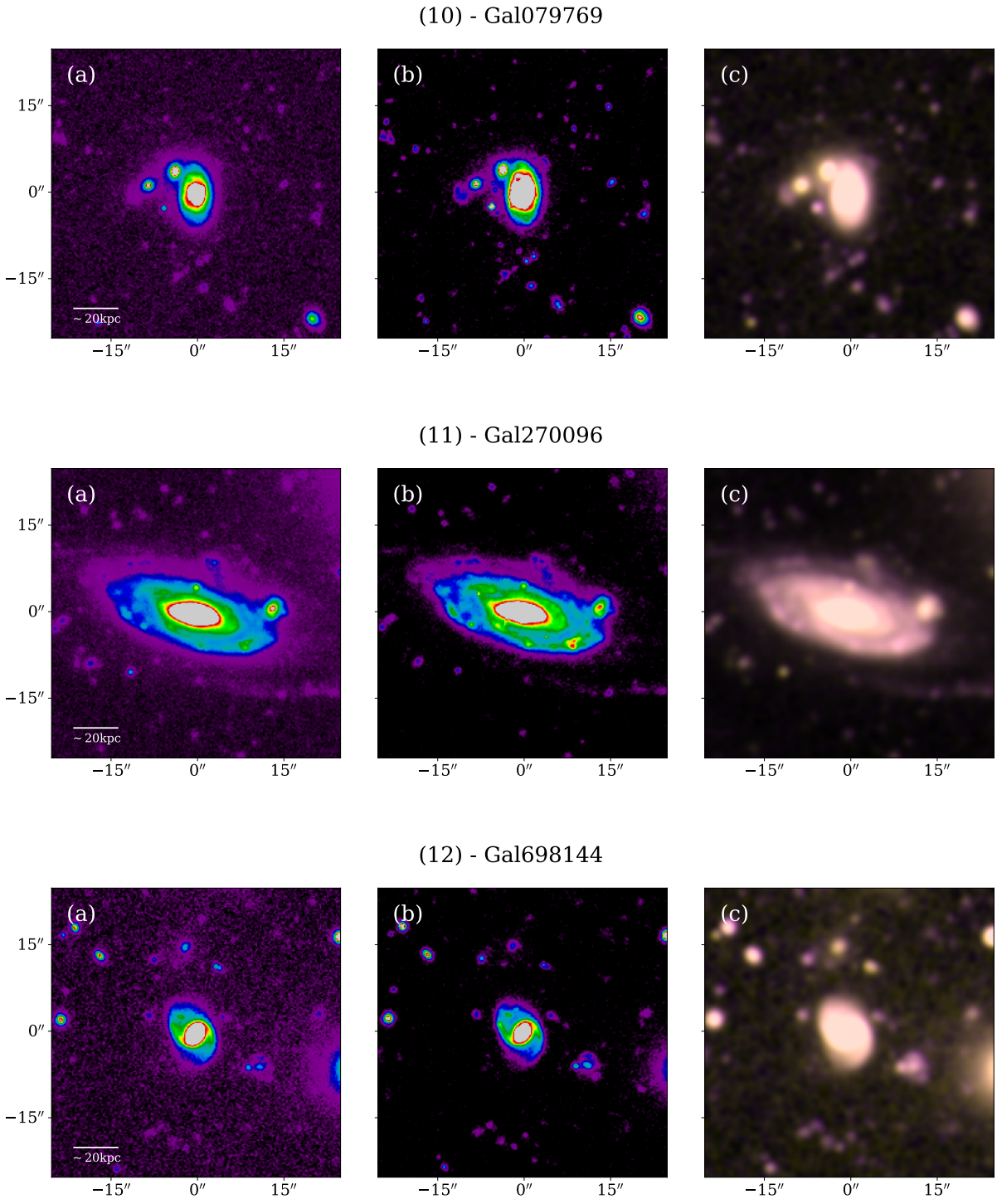

Figure D.1.: (Continued.)

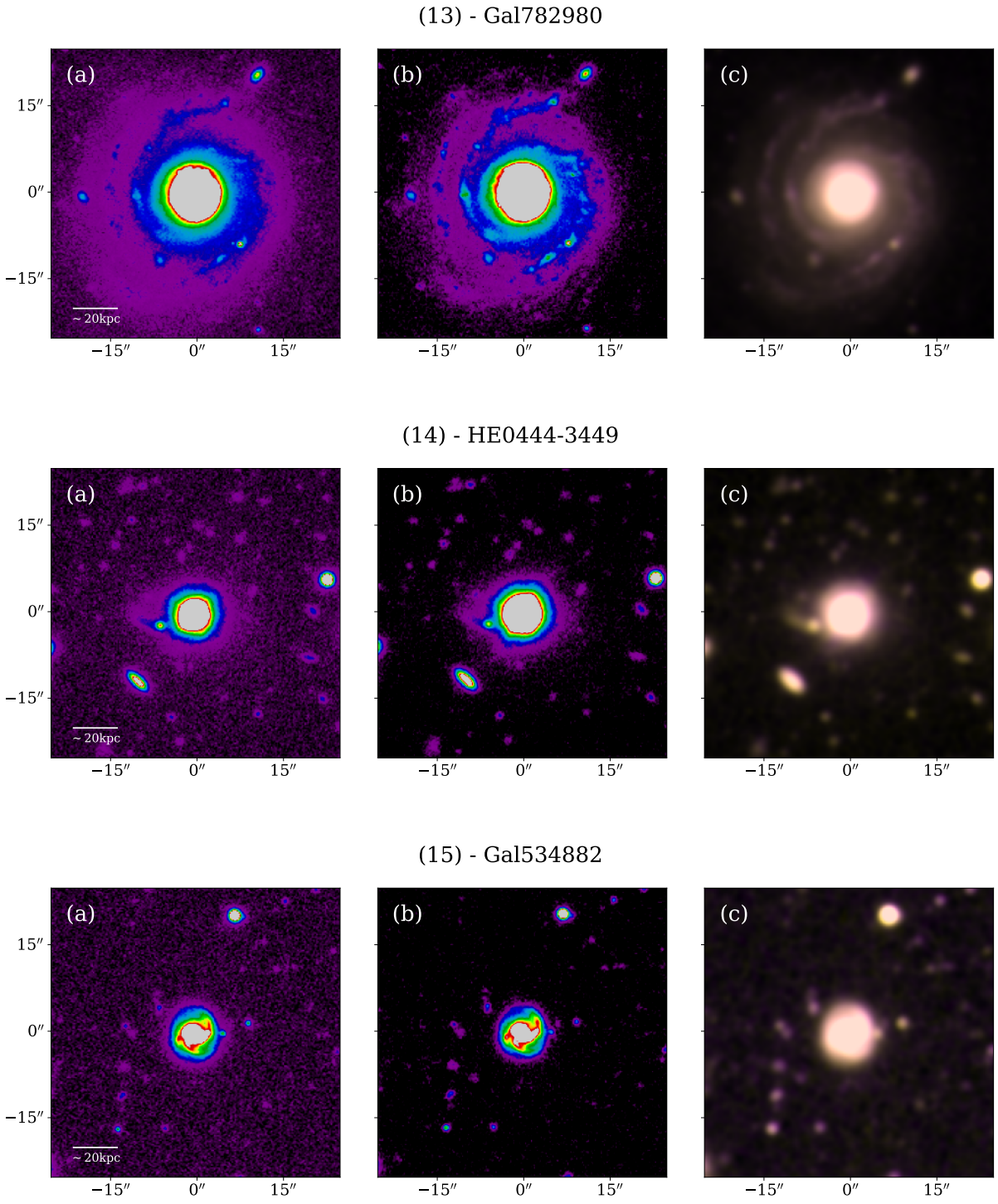

Figure D.1.: (Continued.)

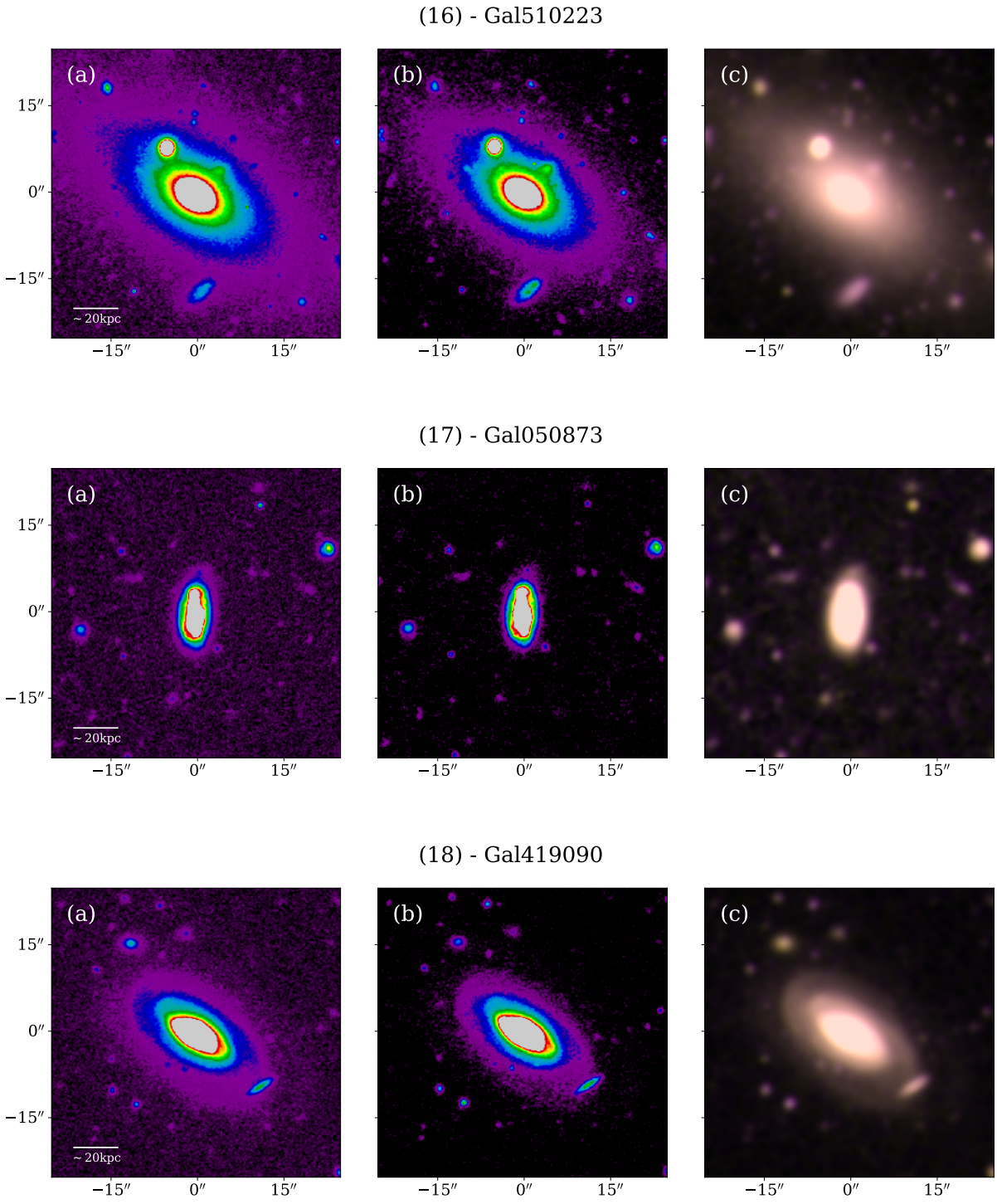

Figure D.1.: (Continued.)

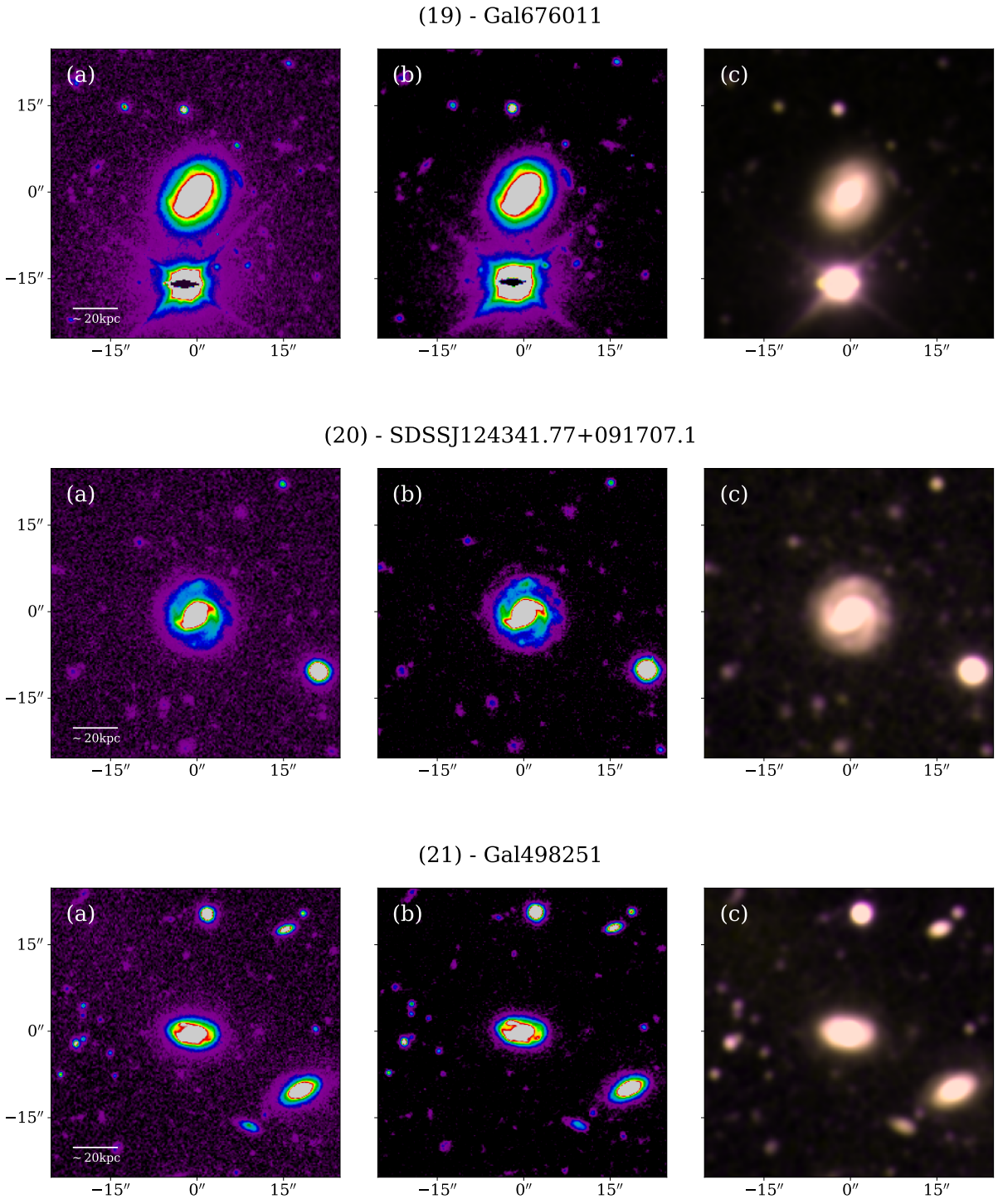

Figure D.1.: (Continued.)

(22) - Gal286443

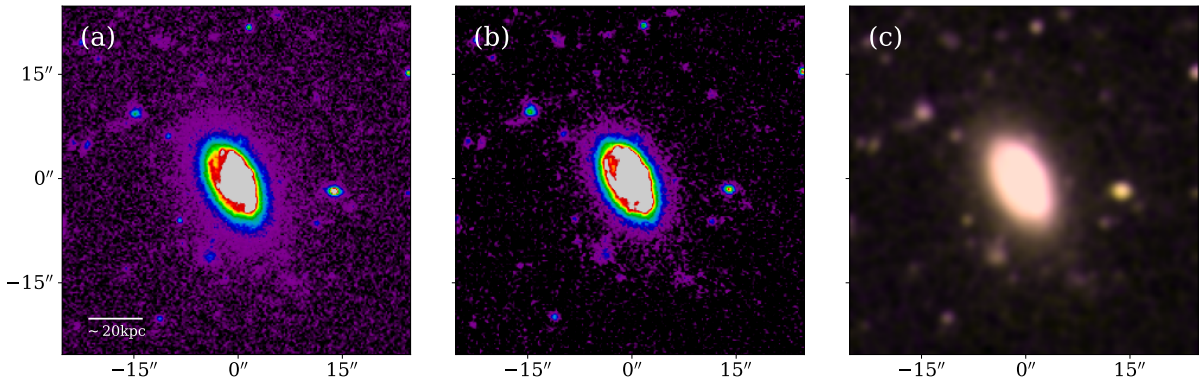

(23) - HE2152-0936

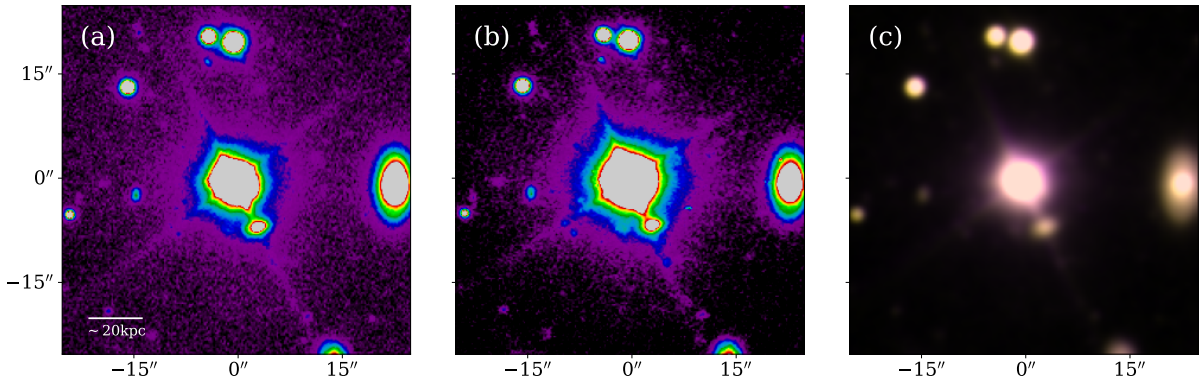

(24) - Gal185580

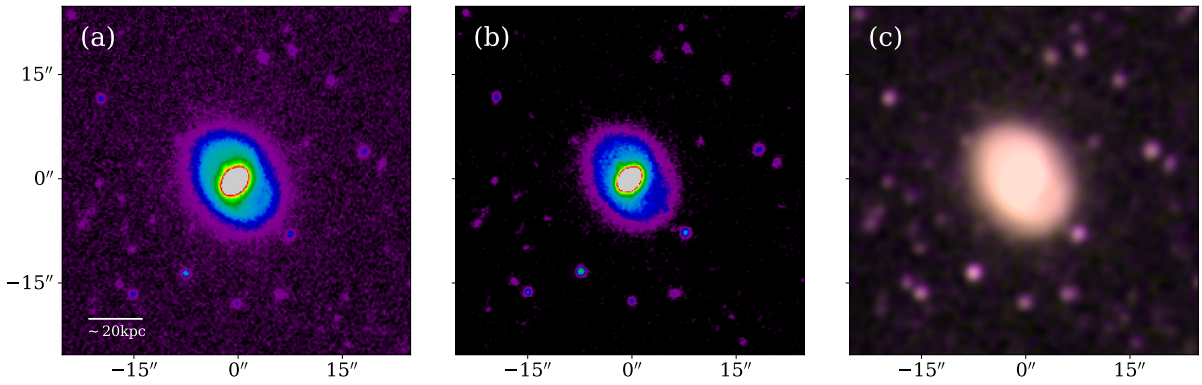

Figure D.1.: (Continued.)

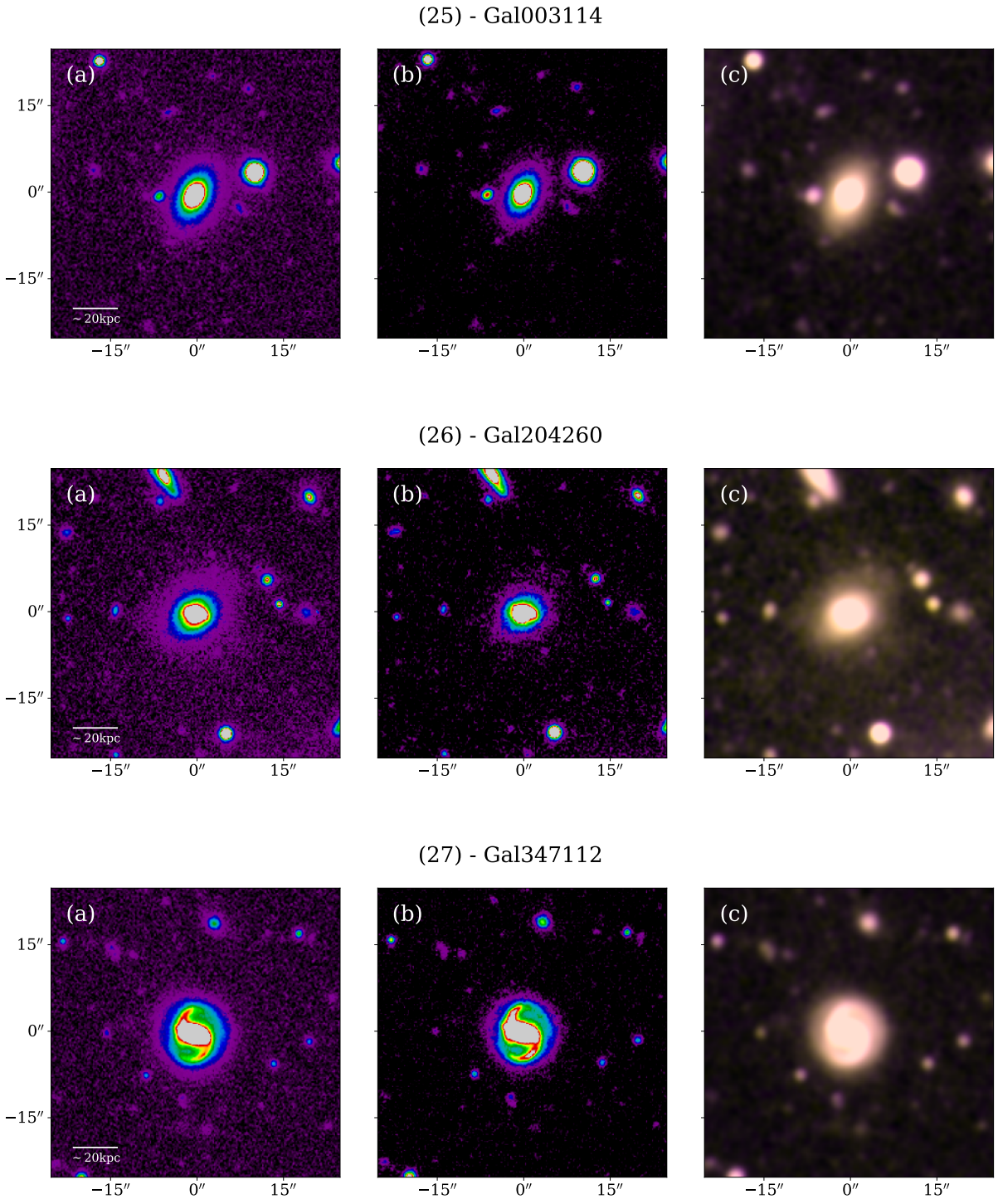

Figure D.1.: (Continued.)

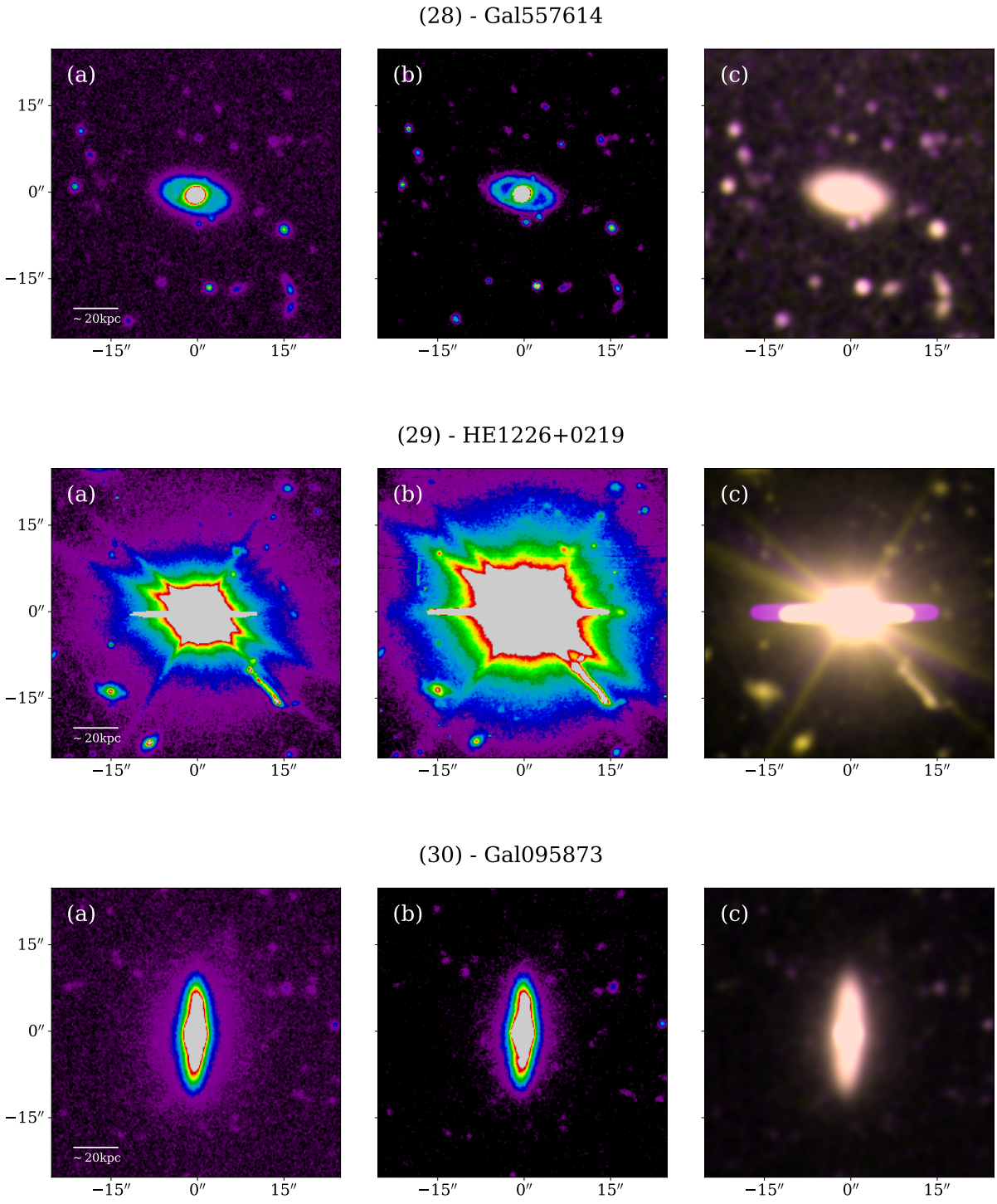

Figure D.1.: (Continued.)

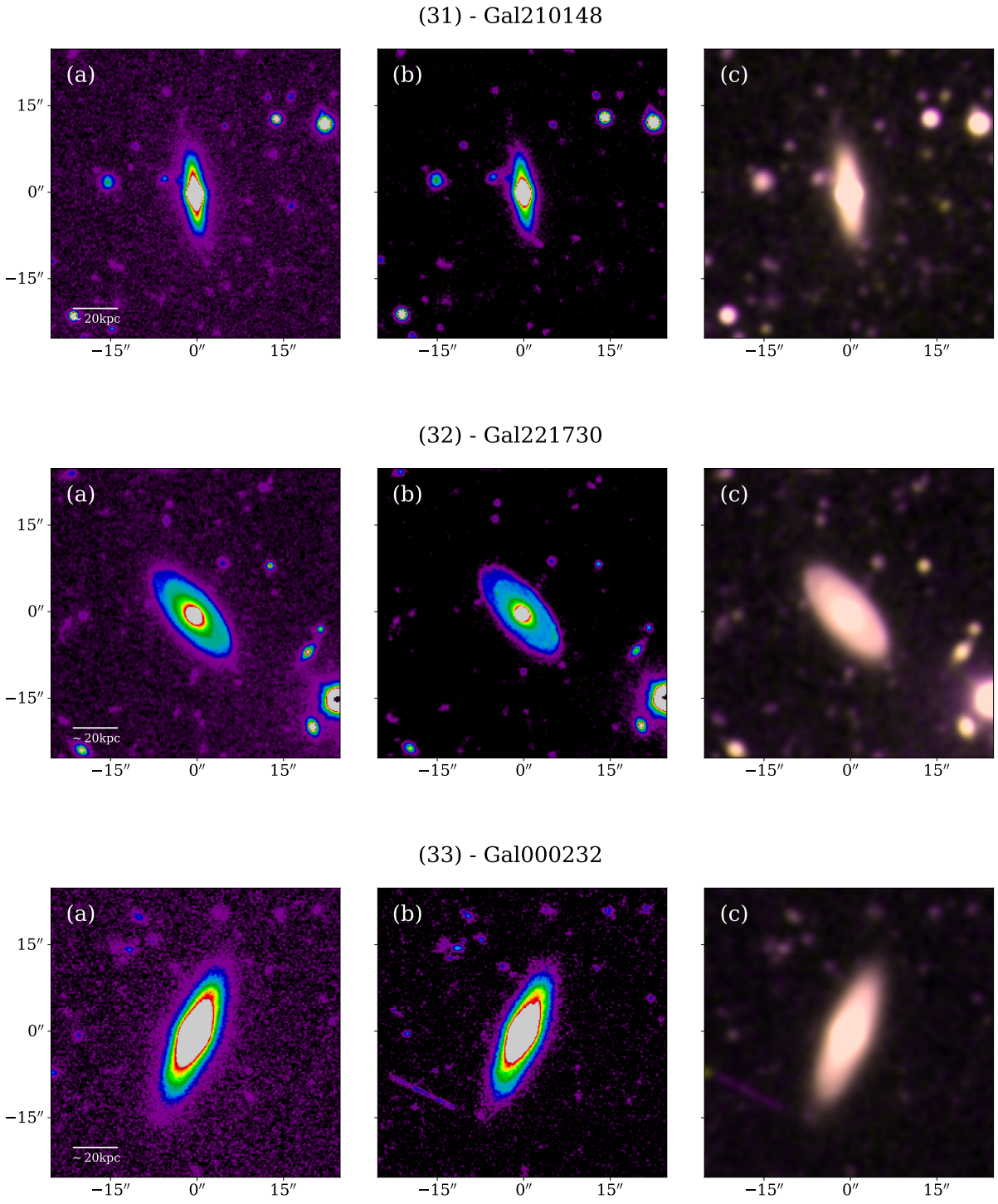

Figure D.1.: (Continued.)

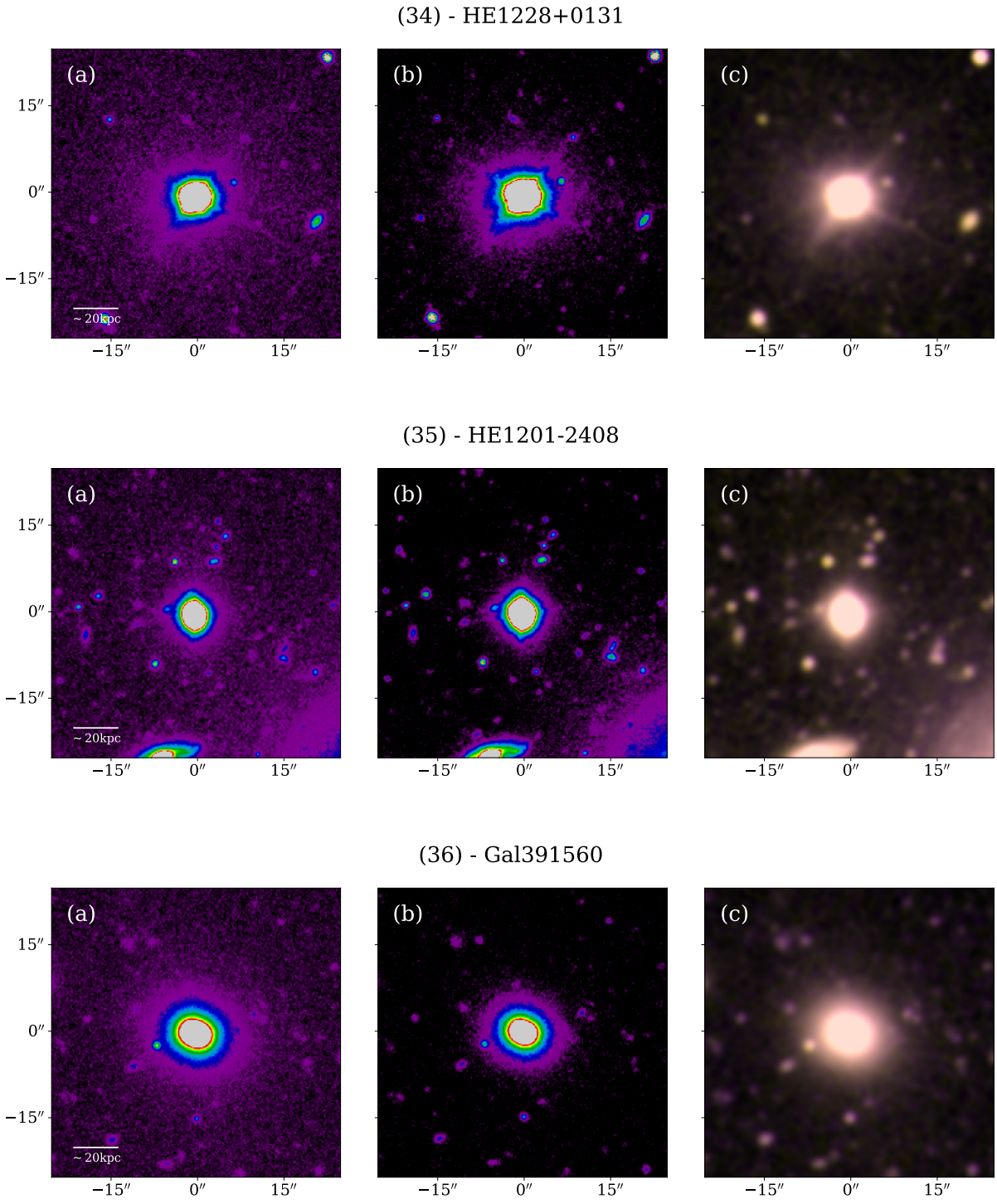

Figure D.1.: (Continued.)

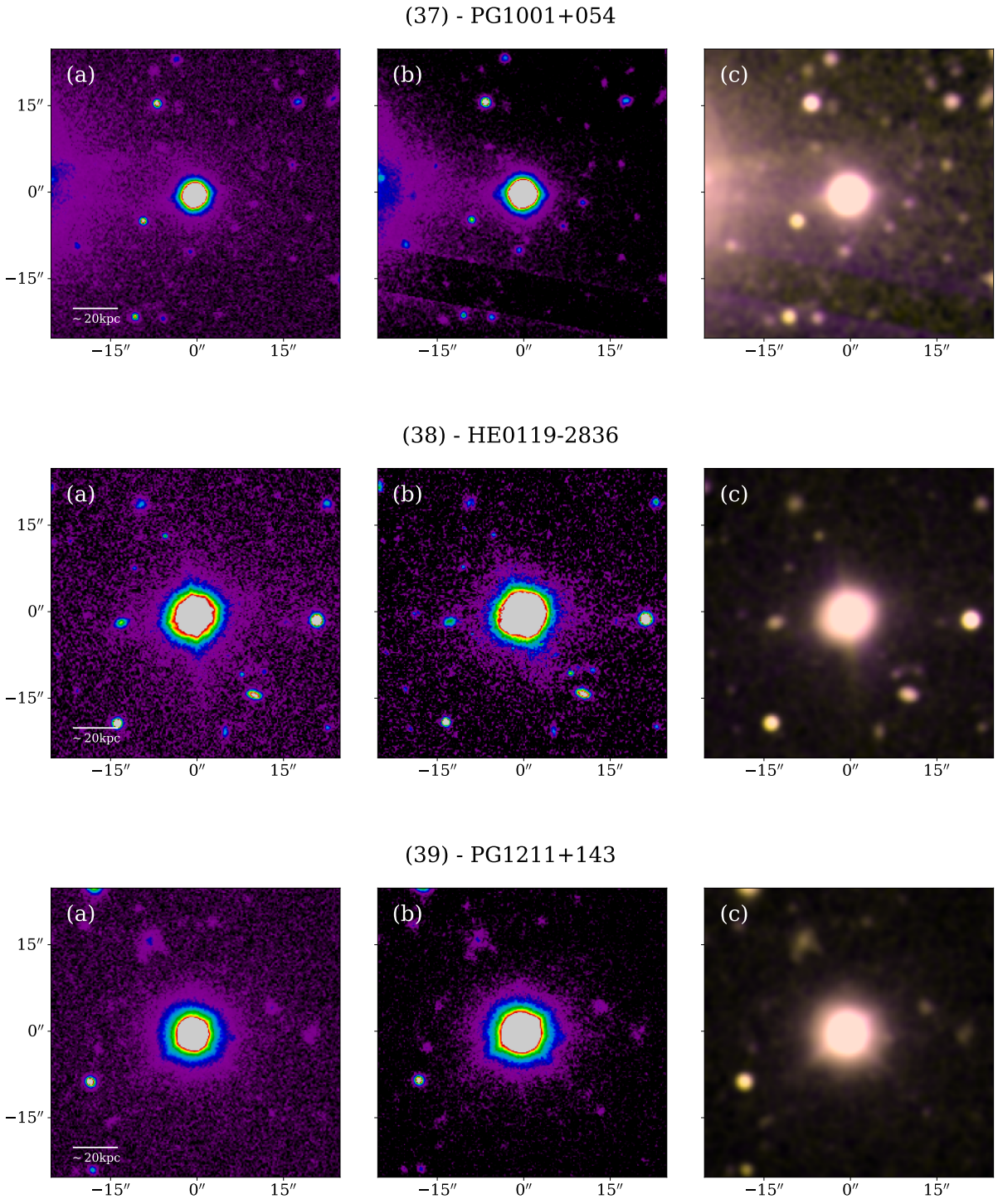

Figure D.1.: (Continued.)

(40) - SDSSJ032213.89+005513.4

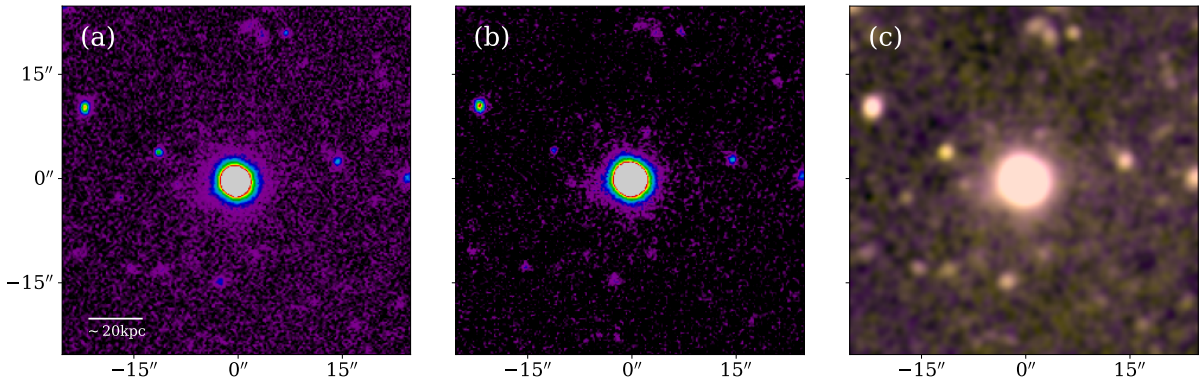

(41) - Gal656010

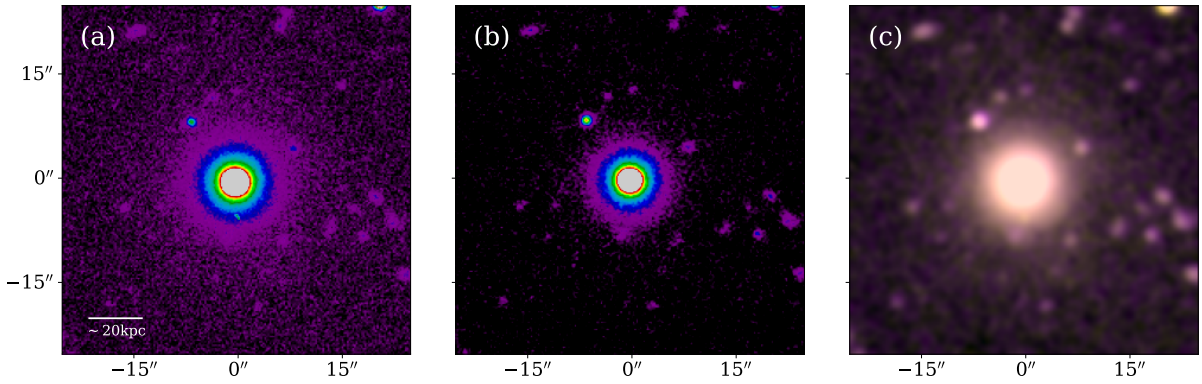

(42) - Gal176221

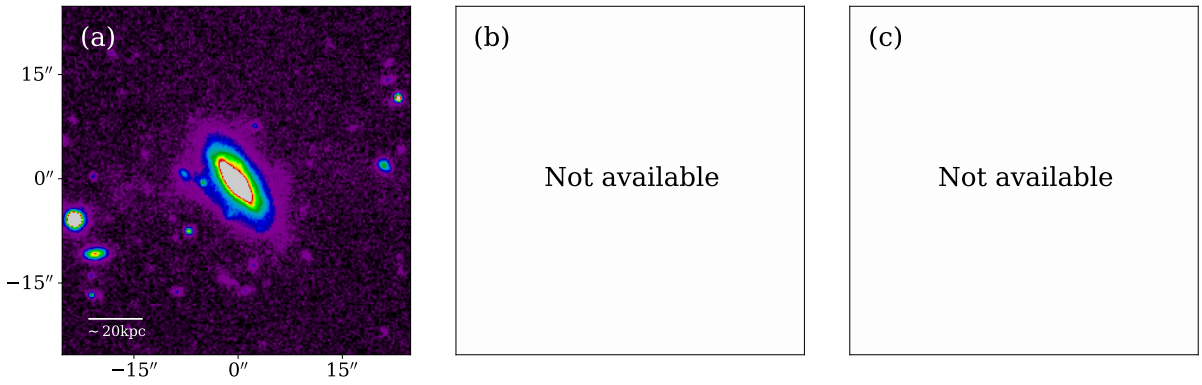

Figure D.1.: (Continued.)

E. Tabular Summary of the Ranks of the Sources at $z \lesssim 0.2$

Supplementing Appendix D and for reference, this section presents the consensus ranks for each target for all permutations of set and combination method. As in Appendix D, the sources are sorted by their respective positions in the 'meta' consensus ranking, i.e. the combined rank of the nine overall rankings (see Section 6.2.1).

Target	Borda Rank			Average Rank			Schulze Rank		
	V-band	B-band	Color	V-band	B-band	Color	V-band	B-band	Color
SDSS-J105007.75+113228.6	1	3	3	1	4	4	1	3	5
Gal030481	4	6	1	2	5	1	2	5	1
HE0157+0009	3	1	4	3	1	6	3	1	6
HE2011-6103	2	2	5	4	2	5	4	2	4
HE2258-5524	5	4	2	6	6	2	5	4	2
HE0132-0441	7	7	6	5	7	3	6	7	3
HE0558-5026	6	5	8	7	3	8	7	6	8
PG1012+008	8	8	7	8	8	7	8	8	7
Gal458007	10	11	9	9	10	9	9	10	10
Gal079769	12	10	10	13	9	13	10	9	9
Gal270096	11	12	12	10	11	12	11	11	11
Gal698144	18	13	13	15	12	10	18	12	12
Gal782980	9	9	15	12	13	16	12	13	16
HE0444-3449	13	21	11	11	22	11	13	21	13
Gal534882	15	16	16	20	19	18	17	17	15
Gal510223	19	14	21	17	15	19	22	14	19
Gal050873	20	17	17	19	20	17	19	18	17
Gal419090	22	22	18	18	18	15	20	16	18
Gal676011	23	15	20	23	16	21	23	15	20
SDSS-J124341.77+091707.1	17	19	22	21	14	22	15	22	24
Gal498251	21	18	26	22	17	25	21	19	22
Gal286443	16	20	27	16	21	26	16	20	23
HE2152-0936	24	23	37	24	24	35	24	23	35
Gal185580	26	30	14	25	29	14	25	28	14

Gal003114	28	24	29	28	23	27	27	24	26
Gal204260	31	26	19	29	26	20	30	29	21
Gal347112	30	29	23	26	27	23	26	26	27
Gal557614	27	27	24	30	28	24	28	27	25
HE1226+0219	25	28	25	27	31	29	33	33	29
Gal095873	29	31	32	31	30	31	29	30	32
Gal210148	33	25	35	33	25	33	31	25	33
Gal221730	34	33	28	32	33	28	35	32	31
Gal000232	36	34	30	37	34	32	34	31	30
HE1228+0131	35	32	33	34	32	37	36	34	36
HE1201-2408	37	38	34	35	36	34	32	36	34
Gal391560	38	39	31	36	39	30	38	35	28
PG1001+054	32	36	41	38	35	40	37	37	39
HE0119-2836	40	37	39	39	37	38	39	38	38
PG1211+143	39	35	38	40	38	39	40	39	41
SDSS-J032213.89+005513.4	41	40	40	41	40	41	42	40	40
Gal656010	42	41	36	42	41	36	41	41	37
Gal176221	14	–	–	14	–	–	14	–	–

Table E.1.: The final ranks for each source depending on combination method (Borda, average or Schulze) and set (*B*, *V* or color images. The targets are sorted by a repeated use of the Schulze method on this nine overall rankings resulting in a singular consensus sequence. Since Gal176221 has been only observed in *V*-band, it is ranked last by the algorithm.

Bibliography

Abazajian, K. N., Adelman-McCarthy, J. K., Agüeros, M. A., et al. 2009, ApJS, 182, 543

Aird, J., Coil, A. L., & Georgakakis, A. 2019, MNRAS, 484, 4360

Aird, J., Coil, A. L., Georgakakis, A., et al. 2015, MNRAS, 451, 1892

Allevato, V., Finoguenov, A., Cappelluti, N., et al. 2011, ApJ, 736, 99

Almaini, O., Wild, V., Maltby, D. T., et al. 2017, MNRAS, 472, 1401

Almeida, C. R. & Ricci, C. 2017, NatAs, 1, 679

Antonucci, R. 1993, ARA&A, 31, 473

Arrow, K. J. 1950, JoPE, 58, 58

Astropy Collaboration, Price-Whelan, A. M., Sipöcz, B. M., et al. 2018, AJ, 156, 123

Astropy Collaboration, Robitaille, T. P., Tollerud, E. J., et al. 2013, A&A, 558, A33

Baes, M., Verstappen, J., Looze, I. D., et al. 2011, ApJS, 15

Baldassare, V. F., Dickey, C., Geha, M., & Reines, A. E. 2020, ApJL, 898, L3

Barnes, J. E. & Hernquist, L. 1992, ARA&A, 30, 705

Bassini, L., Rasia, E., Borgani, S., et al. 2019, A&A, 630, A144

Baumgartner, W. H., Tueller, J., Markwardt, C. B., et al. 2013, ApJS, 207, 19

Beifiori, A., Courteau, S., Corsini, E. M., & Zhu, Y. 2012, MNRAS, 419, 2497

Bennert, V. N., Auger, M. W., Treu, T., Woo, J.-H., & Malkan, M. A. 2011, ApJ, 742, 107

Bennert, V. N., Treu, T., Ding, X., et al. 2021, arXiv: 2101.10355

Bennert, V. N., Treu, T., Woo, J.-H., et al. 2010, ApJ, 708, 1507

Bentz, M. C., Peterson, B. M., Pogge, R. W., Vestergaard, M., & Onken, C. A. 2006, ApJ, 644, 133

Berrier, J. C., Davis, B. L., Kennefick, D., et al. 2013, ApJ, 769, 132

Bhowmick, A. K., Blecha, L., & Thomas, J. 2020, ApJ, 904, 150

Blanton, E. L., Clarke, T. E., Sarazin, C. L., Randall, S. W., & McNamara, B. R. 2010, PNAS, 107, 7174

Bottrell, C., Hani, M. H., Teimoorinia, H., et al. 2019, MNRAS, 490, 5390

Bournaud, F., Dekel, A., Teyssier, R., et al. 2011, ApJ, 741, L33

Bowler, R. A. A., Dunlop, J. S., McLure, R. J., & McLeod, D. J. 2017, MNRAS, 466, 3612

Boyle, B. J., Shanks, T., Croom, S. M., et al. 2000, MNRAS, 317, 1014

Bradley, L., Sipőcz, B., Robitaille, T., et al. 2019, astropy/photutils: v0.7.2

Brammer, G. B., van Dokkum, P. G., Franx, M., et al. 2012, ApJS, 200, 13

Bridge, C. R., Carlberg, R. G., & Sullivan, M. 2010, ApJ, 709, 1067

Brinchmann, J., Charlot, S., White, S. D. M., et al. 2004, MNRAS, 351, 1151

Bruzual, G. & Charlot, S. 2003, MNRAS, 344, 1000

Buchner, J. & Bauer, F. E. 2017, MNRAS, 465, 4348

Buchner, J., Georgakakis, A., Nandra, K., et al. 2015, ApJ, 802, 89

Burkert, A. & Tremaine, S. 2010, ApJ, 720, 516

Böhm, A., Wisotzki, L., Bell, E. F., et al. 2013, A&A, 549, A46

Caglar, T., Burtscher, L., Brandl, B., et al. 2020, A&A, 634, A114

Camps, P. & Baes, M. 2015, A&C, 9, 20

Camps, P. & Baes, M. 2020, A&C, 31, 100381

Carraro, R., Rodighiero, G., Cassata, P., et al. 2020, A&A, 642, A65

Casteels, K. R. V., Conselice, C. J., Bamford, S. P., et al. 2014, MNRAS, 445, 1157

Cen, R. & Safarzadeh, M. 2015, ApJL, 798, L38

Chang, Y.-Y., Le Floc'h, E., Juneau, S., et al. 2017, MNRAS, 466, L103

Chen, B. H., Goto, T., Kim, S. J., et al. 2021, MNRAS, 501, 3951

Chen, Y.-M., Wang, J.-M., Yan, C.-S., Hu, C., & Zhang, S. 2009, ApJ, 695, L130

Cheng, T.-Y., Conselice, C. J., Aragón-Salamanca, A., et al. 2019, arXiv:1908.03610

Cheng, T.-Y., Huertas-Company, M., Conselice, C. J., et al. 2020, arXiv: 2009.11932

Cheung, E., Trump, J. R., Athanassoula, E., et al. 2015, MNRAS, 447, 506

Chowdhury, R. K., Chatterjee, S., Lonappan, A. I., Khandai, N., & DiMatteo, T. 2019, arXiv:1911.07824

Churazov, E., Sazonov, S., Sunyaev, R., et al. 2005, MNRAS, 363, L91

Cigan, P. 2019, MultiColorFits

Ciprijanović, A., Snyder, G. F., Nord, B., & Peek, J. E. G. 2020, A&C, 32, 100390

Cisternas, M., Jahnke, K., Inskip, K. J., et al. 2011, ApJ, 726, 57

Cisternas, M., Sheth, K., Salvato, M., et al. 2015, ApJ, 802, 137

Clarke, A. O., Scaife, A. M. M., Greenhalgh, R., & Griguta, V. 2020, A&A, 639, A84

Condorcet, J.-A.-N. d. C. .-. . m. d. A. d. t. 1785, Essai sur l'application de l'analyse à la probabilité des décisions rendues à la pluralité des voix (de l'Impr. royale (Paris))

Condorcet, J.-A.-N. d. C., Sommerlad, F., McLean, I., University of Oxford, & Faculty of Social Studies. 1989, The political theory of Condorcet (Oxford: University of Oxford, Faculty of Social Studies)

Conroy, C. & White, M. 2013, ApJ, 762, 70

Conselice, C. J. 2003, ApJS, 147, 1

Conselice, C. J. 2006, ApJ, 638, 686

Conselice, C. J. 2014, ARA&A, 52, 291

Conselice, C. J., Wilkinson, A., Duncan, K., & Mortlock, A. 2016, ApJ, 830, 83

Cotini, S., Ripamonti, E., Caccianiga, A., et al. 2013, MNRAS, 431, 2661

Cox, C. & Niemi, S.-M. 2011, Evaluation of a temperature- based HST Focus Model, STScI

Dashyan, G., Choi, E., Somerville, R. S., et al. 2019, MNRAS, 487, 5889

Davies, J. J., Crain, R. A., Oppenheimer, B. D., & Schaye, J. 2020, MNRAS, 491, 4462

Davis, B. L., Graham, A. W., & Cameron, E. 2018, ApJ, 869, 113

Davis, B. L., Graham, A. W., & Cameron, E. 2019, ApJ, 873, 85

Davis, B. L., Graham, A. W., & Seigar, M. S. 2017, MNRAS, 471, 2187

Davis, M., Efstathiou, G., Frenk, C. S., & White, S. D. M. 1985, ApJ, 292, 371

De Lucia, G. & Blaizot, J. 2007, MNRAS, 375, 2

de Nicola, S., Marconi, A., & Longo, G. 2019, MNRAS, 490, 600

Delvecchio, I., Lutz, D., Berta, S., et al. 2015, MNRAS, 449, 373

Di Matteo, T., Springel, V., & Hernquist, L. 2005, Nat, 433, 604

Ding, X., Silverman, J., Treu, T., et al. 2020, ApJ, 888, 37

Dolag, K., Borgani, S., Murante, G., & Springel, V. 2009, MNRAS, 399, 497

Donley, J. L., Kartaltepe, J., Kocevski, D., et al. 2018, ApJ, 853, 63

Donley, J. L., Koekemoer, A. M., Brusa, M., et al. 2012, ApJ, 748, 142

Drouart, G., Rocca-Volmerange, B., De Breuck, C., et al. 2016, A&A, 593, A109

Duncan, K., Conselice, C. J., Mundy, C., et al. 2019, ApJ, 876, 110

Ellison, S. L., Viswanathan, A., Patton, D. R., et al. 2019, MNRAS, 487, 2491

Emerson, P. 2013, Social Choice and Welfare, 40, 353

Erben, T., Schirmer, M., Dietrich, J. P., et al. 2005, Astron. Nachr., 326, 432

Fakhouri, O. & Ma, C.-P. 2008, MNRAS, 386, 577

Fan, L., Han, Y., Fang, G., et al. 2016, ApJ, 822, L32
Fanaroff, B. L. & Riley, J. M. 1974, MNRAS, 167, 31P
Fanidakis, N., Baugh, C. M., Benson, A. J., et al. 2012, MNRAS, 419, 2797
Farrah, D., Petty, S., Connolly, B., et al. 2017, ApJ, 844, 106
Fath, E. A. 1909, Lick Observatory Bulletin, 5, 71
Ferrarese, L. & Ford, H. 2005, Space Sci. Rev., 116, 523
Ferrarese, L. & Merritt, D. 2000, ApJL, 539, L9
Ferreira, L., Conselice, C. J., Duncan, K., et al. 2020, ApJ, 895, 115
Ferreras, I., Pasquali, A., Khochfar, S., et al. 2012, AJ, 144, 47
Freeman, P. E., Izbicki, R., Lee, A. B., et al. 2013, MNRAS, 434, 282
Furlong, M., Bower, R. G., Theuns, T., et al. 2015, MNRAS, 450, 4486
Gabor, J. M., Impey, C. D., Jahnke, K., et al. 2009, ApJ, 691, 705
Gao, F., Wang, L., Pearson, W. J., et al. 2020, A&A, 637, A94
Gebhardt, K., Bender, R., Bower, G., et al. 2000, ApJL, 539, L13
Genel, S., Vogelsberger, M., Springel, V., et al. 2014, MNRAS, 445, 175
Genzel, R., Eisenhauer, F., & Gillessen, S. 2010, RvMP, 82, 3121
Georgakakis, A., Coil, A. L., Laird, E. S., et al. 2009, MNRAS, 397, 623
Georgakakis, A., Salvato, M., Liu, Z., et al. 2017, MNRAS, 469, 3232
Ghez, A. M., Klein, B. L., Morris, M., & Becklin, E. E. 1998, ApJ, 509, 678
Ghez, A. M., Salim, S., Weinberg, N. N., et al. 2008, ApJ, 689, 1044
Ghosh, A., Urry, C. M., Wang, Z., et al. 2020, ApJ, 895, 112
Gilli, R., Comastri, A., & Hasinger, G. 2007, A&A, 463, 79
Giommi, P., Padovani, P., Polenta, G., et al. 2012, MNRAS, 13
Glikman, E., Simmons, B., Mailly, M., et al. 2015, ApJ, 806, 218
Gonzaga, S. & et al. 2012, STScI, The DrizzlePac Handbook
Goulding, A. D., Greene, J. E., Bezanson, R., et al. 2018, PASJ, 70
Goulding, A. D., Matthaey, E., Greene, J. E., et al. 2017, ApJ, 843, 135
Graham, A. W. 2007, MNRAS, 379, 711
Graham, A. W. 2016, Galactic Bulges, 263
Graham, A. W. & Driver, S. P. 2005, Publ. Astron. Soc. Australia, 22, 118
Graham, A. W. & Driver, S. P. 2007, ApJ, 655, 77
Graham, A. W. & Scott, N. 2013, ApJ, 764, 151

Greenstein, J. L. & Matthews, T. A. 1963, AJ, 68, 279
Grogin, N. A., Conselice, C. J., Chatzichristou, E., et al. 2005, ApJ, 627, L97
Grogin, N. A., Kocevski, D. D., Faber, S. M., et al. 2011, ApJS, 197, 35
Gültekin, K., Richstone, D. O., Gebhardt, K., et al. 2009, ApJ, 698, 198
Habouzit, M., Genel, S., Somerville, R. S., et al. 2019, MNRAS, 484, 4413
Habouzit, M., Li, Y., Somerville, R. S., et al. 2020, arXiv: 2006.10094
Harris, G. L. H. & Harris, W. E. 2011, MNRAS, 410, 2347
Harrison, C. M., Costa, T., Tadhunter, C. N., et al. 2018, NatAs, 2, 198
Hastings, W. K. 1970, Biometrika, 57, 97
Hausen, R. & Robertson, B. E. 2020, ApJS, 248, 20
Henriques, B. M. B., White, S. D. M., Thomas, P. A., et al. 2015, MNRAS, 451, 2663
Hewlett, T., Villforth, C., Wild, V., et al. 2017, MNRAS, 470, 755
Hickox, R. C. & Alexander, D. M. 2018, ARA&A, 56, 625
Hirschmann, M., Dolag, K., Saro, A., et al. 2014, MNRAS, 442, 2304
Hong, J., Im, M., Kim, M., & Ho, L. C. 2015, ApJ, 804, 34
Hopkins, P. F. & Hernquist, L. 2009, ApJ, 698, 1550
Hopkins, P. F., Hernquist, L., Cox, T. J., et al. 2006a, ApJS, 163, 1
Hopkins, P. F., Hernquist, L., Cox, T. J., & Kereš, D. 2008, ApJS, 175, 356
Hopkins, P. F., Hernquist, L., Martini, P., et al. 2005, ApJ, 625, L71
Hopkins, P. F. & Quataert, E. 2010, MNRAS, 407, 1529
Hopkins, P. F., Richards, G. T., & Hernquist, L. 2007, ApJ, 654, 731
Hopkins, P. F., Somerville, R. S., Hernquist, L., et al. 2006b, ApJ, 652, 864
Hoyle, F. & Fowler, W. A. 1963, MNRAS, 125, 169
Huertas-Company, M., Pérez-González, P. G., Mei, S., et al. 2015, ApJ, 809, 95
Husemann, B. & Harrison, C. M. 2018, NatAs, 2, 196
Häring, N. & Rix, H.-W. 2004, ApJL, 604, L89
Hönig, S. F. 2019, ApJ, 884, 171
Jahnke, K., Bongiorno, A., Brusa, M., et al. 2009, ApJ, 706, L215
Jahnke, K., Kuhlbrodt, B., & Wisotzki, L. 2004a, MNRAS, 352, 399
Jahnke, K. & Macciò, A. V. 2011, ApJ, 734, 92
Jahnke, K., Sanchez, S. F., Wisotzki, L., et al. 2004b, ApJ, 614, 568
Ji, I., Peirani, S., & Yi, S. K. 2014, A&A, 566, A97

Jiang, L., Egami, E., Fan, X., et al. 2013, ApJ, 773, 153
Johansson, P. H., Burkert, A., & Naab, T. 2009a, ApJ, 707, L184
Johansson, P. H., Naab, T., & Burkert, A. 2009b, ApJ, 690, 802
Jung, M., Illenseer, T. F., & Duschl, W. J. 2018, A&A, 614, A105
Karouzos, M., Jarvis, M. J., & Bonfield, D. 2014, MNRAS, 439, 861
Kaspi, S., Maoz, D., Netzer, H., et al. 2005, ApJ, 629, 61
Kaspi, S., Smith, P. S., Netzer, H., et al. 2000, ApJ, 533, 631
Kauffmann, G., Heckman, T. M., Tremonti, C., et al. 2003a, MNRAS, 346, 1055
Kauffmann, G., Heckman, T. M., White, S. D. M., et al. 2003b, MNRAS, 341, 33
Kaviraj, S., Cohen, S., Ellis, R. S., et al. 2013, MNRAS, 428, 925
Kocevski, D. D., Barro, G., Faber, S. M., et al. 2017, ApJ, 846, 112
Kocevski, D. D., Faber, S. M., Mozena, M., et al. 2012, ApJ, 744, 148
Koekemoer, A. M. & et al. 2002, HST Dither Handbook, STScI
Koekemoer, A. M., Faber, S. M., Ferguson, H. C., et al. 2011, ApJS, 197, 36
Kormendy, J. & Ho, L. C. 2013, ARA&A, 51, 511
Kormendy, J. & Richstone, D. 1995, ARA&A, 33, 581
Koss, M., Mushotzky, R., Veilleux, S., & Winter, L. 2010, ApJ, 716, L125
Koss, M. J., Blecha, L., Bernhard, P., et al. 2018, Nat, 563, 214
Kotilainen, J. K., Falomo, R., Labita, M., Treves, A., & Uslenghi, M. 2007, ApJ, 660, 1039
Kumar, P. & Johnson, J. L. 2010, MNRAS, 404, 2170
Lacey, C. G., Baugh, C. M., Frenk, C. S., et al. 2016, MNRAS, 462, 3854
Lanzuisi, G., Ranalli, P., Georgantopoulos, I., et al. 2015, A&A, 573, A137
Lauer, T. R., Tremaine, S., Richstone, D., & Faber, S. M. 2007, ApJ, 670, 249
Lee, B., Giavalisco, M., Williams, C. C., et al. 2013, ApJ, 774, 47
Li, Y., Gendron-Marsolais, M.-L., Zhuravleva, I., et al. 2020a, ApJ, 889, L1
Li, Y., Habouzit, M., Genel, S., et al. 2020b, ApJ, 895, 102
Lin, L., Koo, D. C., Willmer, C. N. A., et al. 2004, ApJ, 617, L9
Livet, F., Charnock, T., Le Borgne, D., & de Lapparent, V. 2021, arXiv:2102.01086
Lotz, J. M., Davis, M., Faber, S. M., et al. 2008a, ApJ, 672, 177
Lotz, J. M., Jonsson, P., Cox, T. J., et al. 2011, ApJ, 742, 103
Lotz, J. M., Jonsson, P., Cox, T. J., & Primack, J. R. 2008b, MNRAS, 391, 1137
Lotz, J. M., Primack, J., & Madau, P. 2004, AJ, 128, 163

Lusso, E., Comastri, A., Vignali, C., et al. 2011, A&A, 534, A110

Lynden-Bell, D. 1969, Nat, 223, 690

López-Sanjuan, C., Balcells, M., Pérez-González, P. G., et al. 2009, A&A, 501, 505

Madau, P. & Dickinson, M. 2014, ARA&A, 52, 415

Magorrian, J., Tremaine, S., Richstone, D., et al. 1998, AJ, 115, 2285

Man, A. W. S., Zirm, A. W., & Toft, S. 2016, ApJ, 830, 89

Man, Z.-y., Peng, Y.-j., Kong, X., et al. 2019, MNRAS, 488, 89

Marconi, A. & Hunt, L. K. 2003, ApJL, 589, L21

Marconi, A., Risaliti, G., Gilli, R., et al. 2004, MNRAS, 351, 169

Margalef-Bentabol, B., Huertas-Company, M., Charnock, T., et al. 2020, MNRAS, 496, 2346

Marinacci, F., Vogelsberger, M., Pakmor, R., et al. 2018, MNRAS, 480, 5113

Marshall, M. A., Mechtley, M., Windhorst, R. A., et al. 2020, ApJ, 900, 21

Marshall, M. A., Wyithe, J. S. B., Windhorst, R. A., et al. 2021, arXiv: 2101.01219

Martin-Navarro, I., Burchett, J. N., & Mezcua, M. 2019, ApJ, 884, L45

Martini, P. 2004, Coevolution of Black Holes and Galaxies, QSO Lifetimes, 169

McAlpine, S., Bower, R. G., Harrison, C. M., et al. 2017, MNRAS, 468, 3395

McAlpine, S., Bower, R. G., Rosario, D. J., et al. 2018, MNRAS, 481, 3118

McAlpine, S., Harrison, C. M., Rosario, D. J., et al. 2020, MNRAS, 494, 5713

McConnell, N. J. & Ma, C.-P. 2013, ApJ, 764, 184

McLure, R. J. & Dunlop, J. S. 2002, MNRAS, 331, 795

McLure, R. J. & Dunlop, J. S. 2004, MNRAS, 352, 1390

Mechtley, M., Jahnke, K., Windhorst, R. A., et al. 2016, ApJ, 830, 156

Mechtley, M. R. 2014, Markov Chain Monte Carlo Modeling of High-Redshift Quasar Host Galaxies in Hubble Space Telescope Imaging, (PhD Thesis)

Merloni, A., Bongiorno, A., Brusa, M., et al. 2014, MNRAS, 437, 3550

Merritt, D. 2004, Coevolution of Black Holes and Galaxies, 263

Merritt, D. & Ferrarese, L. 2001, ApJ, 547, 140

Metropolis, N., Rosenbluth, A. W., Rosenbluth, M. N., Teller, A. H., & Teller, E. 1953, JChPh, 21, 1087

Mignoli, M., Vignali, C., Gilli, R., et al. 2013, A&A, 556, A29

Momcheva, I. G., Brammer, G. B., van Dokkum, P. G., et al. 2016, ApJS, 225, 27

Mortlock, A., Conselice, C. J., Hartley, W. G., et al. 2013, MNRAS, 433, 1185

Mundy, C. J., Conselice, C. J., Duncan, K. J., et al. 2017, MNRAS, 470, 3507
Naiman, J. P., Pillepich, A., Springel, V., et al. 2018, MNRAS, 477, 1206
Nelson, D., Pillepich, A., Springel, V., et al. 2019a, MNRAS, 490, 3234
Nelson, D., Pillepich, A., Springel, V., et al. 2018, MNRAS, 475, 624
Nelson, D., Springel, V., Pillepich, A., et al. 2019b, ComAC, 6, 2
Netzer, H. 2015, ARA&A, 53, 365
Netzer, H. 2019, MNRAS, 488, 5185
Oke, J. B. & Gunn, J. E. 1983, ApJ, 266, 713
O'Leary, J. A., Moster, B. P., Naab, T., & Somerville, R. S. 2020, arXiv:2001.02687
Onken, C. A., Ferrarese, L., Merritt, D., et al. 2004, ApJ, 615, 645
Oppenheimer, B. D., Davies, J. J., Crain, R. A., et al. 2020, MNRAS, 491, 2939
Padovani, P., Alexander, D. M., Assef, R. J., et al. 2017, ARA&A, 25, 2
Pakmor, R. & Springel, V. 2013, MNRAS, 432, 176
Pawlik, M. M., Wild, V., Walcher, C. J., et al. 2016, MNRAS, 456, 3032
Peebles, P. J. E. 1972, ApJ, 178, 371
Peng, C. Y., Ho, L. C., Impey, C. D., & Rix, H.-W. 2002, AJ, 124, 266
Peng, C. Y., Ho, L. C., Impey, C. D., & Rix, H.-W. 2010, AJ, 139, 2097
Peterson, B. M., Ferrarese, L., Gilbert, K. M., et al. 2004, ApJ, 613, 682
Pfister, H., Dotti, M., Laigle, C., Dubois, Y., & Volonteri, M. 2020, MNRAS, 493, 922
Phipps, F., Bogdán, A., Lovisari, L., et al. 2019, ApJ, 875, 141
Pillepich, A., Nelson, D., Hernquist, L., et al. 2018a, MNRAS, 475, 648
Pillepich, A., Nelson, D., Springel, V., et al. 2019, MNRAS, 490, 3196
Pillepich, A., Springel, V., Nelson, D., et al. 2018b, MNRAS, 473, 4077
Planck Collaboration, Ade, P. A. R., Aghanim, N., et al. 2016, A&A, 594, A13
Popping, G., Caputi, K. I., Trager, S. C., et al. 2015, MNRAS, 454, 2258
Pović, M., Sánchez-Portal, M., Pérez García, A. M., et al. 2012, A&A, 541, A118
Ramos Almeida, C., Levenson, N. A., Alonso-Herrero, A., et al. 2011, ApJ, 731, 92
Reilly, B. 2002, International Political Science Review, 23, 355
Reines, A. E. & Volonteri, M. 2015, ApJ, 813, 82
Ricarte, A., Tremmel, M., Natarajan, P., & Quinn, T. 2019, MNRAS, 489, 802
Ricci, C., Trakhtenbrot, B., Koss, M. J., et al. 2017, Nat, 549, 488
Richards, G. T., Fan, X., Newberg, H. J., et al. 2002, AJ, 123, 2945

Richards, G. T., Strauss, M. A., Fan, X., et al. 2006, AJ, 131, 2766
Rodriguez-Gomez, V., Genel, S., Vogelsberger, M., et al. 2015, MNRAS, 449, 49
Rodriguez-Gomez, V., Snyder, G. F., Lotz, J. M., et al. 2019, MNRAS, 483, 4140
Rosario, D. J., McIntosh, D. H., van der Wel, A., et al. 2015, A&A, 573, A85
Ross, N. P., McGreer, I. D., White, M., et al. 2013, ApJ, 773, 14
Sabater, J., Best, P. N., & Argudo-Fernández, M. 2013, MNRAS, 430, 638
Sadoun, R. & Colin, J. 2012, MNRAS, 426, L51
Sahu, N., Graham, A. W., & Davis, B. L. 2019a, ApJ, 876, 155
Sahu, N., Graham, A. W., & Davis, B. L. 2019b, ApJ, 887, 10
Salpeter, E. E. 1964, ApJ, 140, 796
Sanchez, S. F., Jahnke, K., Wisotzki, L., et al. 2004, ApJ, 614, 586
Sanders, D. B. & Mirabel, I. F. 1996, ARA&A, 34, 749
Sanders, D. B., Soifer, B. T., Elias, J. H., et al. 1988, ApJ, 325, 74
Sani, E., Marconi, A., Hunt, L. K., & Risaliti, G. 2011, MNRAS, 413, 1479
Santini, P., Maiolino, R., Magnelli, B., et al. 2014, A&A, 562, A30
Schawinski, K., Simmons, B. D., Urry, C. M., Treister, E., & Glikman, E. 2012, MNRAS, 425, L61
Schawinski, K., Treister, E., Urry, C. M., et al. 2011, ApJ, 727, L31
Schirmer, M. 2013, ASCL, ascl:1308.013
Schmidt, M. 1963, Nat, 197, 1040
Schneider, D. P., Richards, G. T., Hall, P. B., et al. 2010, AJ, 139, 2360
Schramm, M., Wisotzki, L., & Jahnke, K. 2008, A&A, 478, 311
Schulze, A., Bongiorno, A., Gavignaud, I., et al. 2015, MNRAS, 447, 2085
Schulze, A. & Gebhardt, K. 2011, ApJ, 729, 21
Schulze, A. & Wisotzki, L. 2010, A&A, 516, A87
Schulze, A. & Wisotzki, L. 2011, A&A, 535, A87
Schulze, M. 2011, Social Choice and Welfare, 36, 267
Schulze, M. 2018, arXiv:1804.02973
Schutte, Z., Reines, A. E., & Greene, J. E. 2019, ApJ, 887, 245
Secrest, N. J., Ellison, S. L., Satyapal, S., & Blecha, L. 2020, MNRAS, 499, 2380
Seigar, M. S., Kennefick, D., Kennefick, J., & Lacy, C. H. S. 2008, ApJL, 678, L93
Sexton, R. O., Canalizo, G., Hiner, K. D., et al. 2019, ApJ, 878, 101
Seyfert, C. K. 1943, ApJ, 97, 28

Shah, E. A., Kartaltepe, J. S., Magagnoli, C. T., et al. 2020, ApJ, 904, 107

Shankar, F., Allevato, V., Bernardi, M., et al. 2019, arXiv:1910.10175

Shankar, F., Bernardi, M., Sheth, R. K., et al. 2016, MNRAS, 460, 3119

Shankar, F., Weinberg, D. H., Marsden, C., et al. 2020, MNRAS, 493, 1500

Sharma, R. S., Choi, E., Somerville, R. S., et al. 2021, arXiv:2101.01729

Shen, S., Mo, H. J., White, S. D. M., et al. 2003, MNRAS, 343, 978

Shen, Y. 2013, BASI, 41, 61

Shen, Y., Greene, J. E., Strauss, M. A., Richards, G. T., & Schneider, D. P. 2008, ApJ, 680, 169

Shen, Y., Richards, G. T., Strauss, M. A., et al. 2011, ApJS, 194, 45

Shen, Y., Strauss, M. A., Oguri, M., et al. 2007, AJ, 133, 2222

Shibuya, T., Ouchi, M., & Harikane, Y. 2015, ApJS, 219, 15

Shields, G. 1999, PASP, 111, 661

Sijacki, D., Vogelsberger, M., Genel, S., et al. 2015, MNRAS, 452, 575

Silk, J. & Rees, M. J. 1998, A&A, 331, 4

Silva, A., Marchesini, D., Silverman, J. D., et al. 2021, arXiv:2101.05000

Silverman, J. D., Kampczyk, P., Jahnke, K., et al. 2011, ApJ, 743, 2

Skelton, R. E., Whitaker, K. E., Momcheva, I. G., et al. 2014, ApJS, 214, 24

Smethurst, R. J., Simmons, B. D., Lintott, C. J., & Shanahan, J. 2019, MNRAS, 489, 4016

Snyder, G. F., Lotz, J., Moody, C., et al. 2015, MNRAS, 451, 4290

Snyder, G. F., Rodriguez-Gomez, V., Lotz, J. M., et al. 2019, MNRAS, 486, 3702

Solanes, J. M., Perea, J. D., & Valentí-Rojas, G. 2018, A&A, 614, A66

Soltan, A. 1982, MNRAS, 200, 115

Somerville, R. S., Hopkins, P. F., Cox, T. J., Robertson, B. E., & Hernquist, L. 2008, MNRAS, 391, 481

Spinoglio, L. & Fernández-Ontiveros, J. A. 2019, arXiv:1911.12176

Springel, V. 2010, MNRAS, 401, 791

Springel, V., Di Matteo, T., & Hernquist, L. 2005, MNRAS, 361, 776

Springel, V., Pakmor, R., Pillepich, A., et al. 2018, MNRAS, 475, 676

Springel, V., White, S. D. M., Tormen, G., & Kauffmann, G. 2001, MNRAS, 328, 726

Steinborn, L. K., Hirschmann, M., Dolag, K., et al. 2018, MNRAS, 481, 341

Storey-Fisher, K., Huertas-Company, M., Ramachandra, N., et al. 2020, arXiv:2012.08082

Suh, H., Civano, F., Hasinger, G., et al. 2019, ApJ, 872, 168, tex.ids: suh_multi-wavelength_2019-1

Suh, H., Civano, F., Trakhtenbrot, B., et al. 2020, ApJ, 889, 32

Sérsic, J. L. 1963, Boletin de la Asociacion Argentina de Astronomia La Plata Argentina, 6, 41

Sérsic, J. L. 1968, Atlas de Galaxias Australes, (Cordoba: Observatorio Astronomico)

Terrazas, B. A., Bell, E. F., Pillepich, A., et al. 2020, MNRAS, 493, 1888

Thorne, K. S. 1974, ApJ, 191, 507

Torrey, P., Vogelsberger, M., Marinacci, F., et al. 2019, MNRAS, 484, 5587

Treister, E., Schawinski, K., Urry, C. M., & Simmons, B. D. 2012, ApJ, 758, L39

Tremaine, S., Gebhardt, K., Bender, R., et al. 2002, ApJ, 574, 740

Trump, J. R., Impey, C. D., Kelly, B. C., et al. 2011, ApJ, 733, 60

Truong, N., Pillepich, A., Werner, N., et al. 2020, MNRAS, 494, 549

Urbano-Mayorgas, J. J., Villar Martín, M., Buitrago, F., et al. 2019, MNRAS, 483, 1829

Urrutia, T., Lacy, M., & Becker, R. H. 2008, ApJ, 674, 80

Urry, C. 2004, ASP Conf. Ser., 311, 49

Urry, C. M. & Padovani, P. 1995, PASP, 107, 803

Valentini, M., Murante, G., Borgani, S., et al. 2020, MNRAS, 491, 2779

van der Wel, A., Franx, M., van Dokkum, P. G., et al. 2014, ApJ, 788, 28

van Dokkum, P. G. & Brammer, G. 2010, ApJ, 718, L73

van Dokkum, P. G., Nelson, E. J., Franx, M., et al. 2015, ApJ, 813, 23

Vega-Ferrero, J., Sánchez, H. D., Bernardi, M., et al. 2020, arXiv:2012.07858

Ventou, E., Contini, T., Bouché, N., et al. 2017, A&A, 608, A9

Ventou, E., Contini, T., Bouché, N., et al. 2019, A&A, 631, A87

Vestergaard, M., Fan, X., Tremonti, C. A., Osmer, P. S., & Richards, G. T. 2008, ApJ, 674, L1

Vestergaard, M. & Osmer, P. S. 2009, ApJ, 699, 800

Vestergaard, M. & Peterson, B. M. 2006, ApJ, 641, 689

Vika, M., Driver, S. P., Cameron, E., Kelvin, L., & Robotham, A. 2012, MNRAS, 419, 2264

Villforth, C., Hamann, F., Rosario, D. J., et al. 2014, MNRAS, 439, 3342

Villforth, C., Hamilton, T., Pawlik, M. M., et al. 2017, MNRAS, 466, 812

Villforth, C., Herbst, H., Hamann, F., et al. 2019, MNRAS, 483, 2441

Vogelsberger, M., Genel, S., Springel, V., et al. 2014a, Nat, 509, 177

Vogelsberger, M., Genel, S., Springel, V., et al. 2014b, MNRAS, 444, 1518

Volonteri, M., Natarajan, P., & Gültekin, K. 2011, ApJ, 737, 50

Wang, L., Pearson, W. J., & Rodriguez-Gomez, V. 2020, A&A, 644, A87

Weigel, A. K., Schawinski, K., Treister, E., Trakhtenbrot, B., & Sanders, D. B. 2018, MNRAS, 476, 2308

Weinberger, R., Springel, V., Hernquist, L., et al. 2017, MNRAS, 465, 3291

Weinberger, R., Springel, V., Pakmor, R., et al. 2018, MNRAS, 479, 4056

Weston, M. E., McIntosh, D. H., Brodwin, M., et al. 2017, MNRAS, 464, 3882

Wild, V., Almaini, O., Dunlop, J., et al. 2016, MNRAS, 463, 832

Wild, V., Heckman, T., & Charlot, S. 2010, MNRAS, 405, 933

Wyithe, J. S. B. 2006a, MNRAS, 371, 1536

Wyithe, J. S. B. 2006b, MNRAS, 365, 1082

Xu, C. K., Zhao, Y., Scoville, N., et al. 2012, ApJ, 747, 85

Yu, Q. & Tremaine, S. 2002, MNRAS, 335, 965

Yue, M., Fan, X., Schindler, J.-T., McGreer, I. D., & Huang, Y.-H. 2019, ApJ, 883, 141

Zakamska, N. L., Sun, A.-L., Strauss, M. A., et al. 2019, MNRAS, 489, 497

Zel'dovich, Y. B. 1964, Soviet Physics Doklady, 9, 195

Zhao, D., Ho, L. C., Zhao, Y., Shangguan, J., & Kim, M. 2019a, ApJ, 877, 52

Zhao, Y., Ge, J., Yuan, X., et al. 2019b, MNRAS, 487, 801

Zhu, P., Ho, L. C., & Gao, H. 2021, ApJ, 907, 6

Publications

The following publications are included in this Thesis:

- **Marian V.**, Jahnke K., Pillepich A., Rodriguez-Gomez V., Andika I., Koekemoer A.M., Mechtley M., Onoue M., van der Wel A. & Villforth C., (2021),
  The Significance of Major Galaxy Mergers in Triggering AGN with the Highest Eddington Ratios at $z \simeq 2$ in IllustrisTNG,
  In prep.

- **Marian V.**, Jahnke K., Andika I., Bañados E., Bennert V.N., Cohen S., Husemann B., Kaasinen M., Koekemoer A.M., Mechtley M., Onoue M., Schindler J.T., Schramm M., Schulze A., Silverman J.D., Smirnova-Pinchukova I., van der Wel A., Villforth C. & Windhorst R.A., (2020),
  A Significant Excess in Major Merger Rate for AGN with the Highest Eddington Ratios at $z < 0.2$,
  ApJ, 904, 79

- **Marian V.**, Jahnke K., Mechtley M., Cohen S. Husemann B., Jones V., Koekoemoer A.M., Schulze A., van der Wel A., Villforth C. & Windhorst R.A., (2019),
  Major Mergers Are Not the Dominant Trigger for High-accretion AGN at $z \simeq 2$,
  ApJ, 882, 141

Additional publications that are not part of this Thesis:

- Andika I., Jahnke K., Onoue M., Bañados E., Mazzucchelli C., Novak M., Eilers A.C., Venemans B.P., Schindler J.T., Walter F., Neeleman M., Simcoe R.A., Decarli R., Farina E.P., **Marian V.**, Pensabene A., Cooper T.M. & Rojas A.F., (2020),
  Probing the Nature of High-redshift Weak Emission Line Quasars: A Young Quasar with a Starburst Host Galaxy,
  ApJ, 903, 34

- Marshall M.A., Mechtley M., Windhorst R.A., Cohen S., Jansen R.A., Jiang L., Jones V., Wyithe J.S.B., Fan X., Hathi N.P., Jahnke K., Keel W.C., Koekemoer A.M., **Marian V.**, Ren K., Robinson J., Röttgering H.J.A., Ryan R.E., Scannapieco E., Schneider D.P., Schneiger G., Smith B.M. & Yan H., (2020),
  Limits to Rest-frame Ultraviolet Emission from Far-infrared-luminous $z \simeq 6$ Quasar Hosts,
  ApJ, 900, 21

- Gibbs A., Bixel A., Rackham B.V., Apai D., Schlecker M., Espinoza N., Mancini L., Chen W., Henning T., Gabor P., Boyle R., Perez Chavez J., Mousseau A., Dietrich J., Jay Socia Q., Ip W., Ngeow C., Tsai A., Bhandare A., **Marian V.**, Baehr H., Brown S., Häberle M., Keppler M., Molaverdikhani K. & Sarkis P., (2020),
  EDEN: Sensitivity Analysis and Transiting Planet Detection Limits for Nearby Late Red Dwarfs,
  AJ, 159, 169

- **Marian V.**, Ziegler B., Kuchner U. & Verdugo M., (2018),
  Color gradients reflect an inside-out growth in early-type galaxies of the cluster MACS J1206.2-0847,
  A&A, 617, A34

Glossary

AEGIS	All-wavelength Extended Groth strip International Survey
AGN	Active Galactic Nucleus/Nuclei
BLR	Broad Line Region
BH	Black Hole
CANDELS	Cosmic Assembly Near-Infrared Deep Extragalactic Legacy Survey
CDF	Cumulative Distribution Function
COSMOS	Cosmic Evolution Survey
DR	Data Release
FORS	FOcal Reducer and low dispersion Spectrograph
FWHM	Full Width Half Maximum
GOODS (-S/-N)	Great Observatories Origins Deep Survey (-South/-North)
HES	Hamburg/ESO Survey
HST	Hubble Space Telescope
JWST	James Webb Space Telescope
MCMC	Markov Chain Monte Carlo
NLR	Narrow Line Region
PDF	Probability Density Function
PG	Palomar-Green
PSF	Point Spread Function
SDSS	Sloan Digital Sky Survey
SED	Spectral Energy Distribution
SMBH	SuperMassive Black Hole
S/N	Signal-to-Noise
UDS	(CANDELS) Ultra Deep Survey
VLT	Very Large Telescope
WFC3	Wide Field Camera 3

Acknowledgments

First of all, I would like to thank Knud Jahnke for his supervision and guidance. His (virtual) door was always open for me to discuss scientific but also everyday topics. He sets the bar very high for all future supervisors I will have in my further career path. I also thank him for reviewing my thesis and for being part of the examination committee. For both I also thank Luca Amendola and I also extend my thanks to Björn Malte Schäfer and Christian Fendt for completing the examination committee.

A big thank you for the warm and stimulating atmosphere also goes to all the staff, post docs, PhD students etc. of the MPIA. First and foremost, I would like to thank those who have livened up the sometimes dry scientific routine with stimulating discussions and humorous diversions. In particular, I would like to mention Manuel, my go-to guy for Austrian nostalgia, Steffi, my PoGo buddy, as well as Felix and Melanie, who among other things raised this work to a higher level by proofreading parts of it. I also appreciate all those who came together for the soccer matches and of course the Outreachies. Unfortunately, we had breakfast together far too rarely and were forced by external circumstances to stop communicating our enthusiasm for the Universe.

Ich danke auch Christian und Lisy. Ihr habt immer ein offenes Ohr, wenn mal wieder ein wenig Dampf abgelassen werden muss und taucht immer wieder in eure alte Lebenswelt ein, wenn ihr Texte, wie diesen hier, Korrekturlesen "dürft". Unser Interesse für Astronomie hat unsere Lebenswege kreuzen lassen und auch wenn sich diese wieder etwas voneinander entfernt haben, so hoffe ich, dass wir auch zukünftig die engen Freunde bleiben, die wir bis heute sind.

Nicht zuletzt möchte ich mich natürlich auch bei meinen Eltern bedanken. Nicht nur einmal habt ihr mir unter die Arme gegriffen, vor allem in den Anfängen, als mein Ehrgeiz wohl etwas zu wünschen übrig ließ. Und nicht zuletzt, Tanja, Vincent und Krümelchen. So wie ein Blick in den unendlichen Nachthimmel für mich alles wieder in die richtige Perspektive rückt, so gilt das auch für euch. Jede noch so große Sorge wird durch ein Lächeln und einer eurer geliebten Umarmungen vergessen. Jeder Frust ist durch einen Augenblick mit euch verschwunden. Und auch wenn, wie jetzt, immer wieder spannende und aufregende Zeiten bevorstehen, eines weiß ich für immer gewiss: Ihr seid mein Anker, mein Ruhepol und mein Lebensmittelpunkt!